ENCAPSULATION OF METAL SULFIDE AND OXIDE CLUSTERS IN MoS_2 AND WS_2 AND CHARACTERIZATION OF RESTACKED MoS_2 AND WS_2

By

Joy Marie Heising

A DISSERTATION

Submitted to
Michigan State University
in partial fulfillment of the requirements
for the degree of

DOCTOR OF PHILOSOPHY

Department of Chemistry

1999

ABSTRACT

ENCAPSULATION OF METAL SULFIDE AND OXIDE CLUSTERS IN MoS_2 AND WS_2 AND CHARACTERIZATION OF RESTACKED MoS_2 AND WS_2

By

Joy Marie Heising

The synthesis of $[Al_{13}O_4(OH)_{24}(H_2O)_{12}]_xMS_2$ (M = Mo,W; x = 0.02 - 0.05; d spacing = 16.0Å) was accomplished by a precipitative encapsulation technique in which a suspension of single MS_2 layers in H_2O was added to an aqueous solution of the $[Al_{13}O_4(OH)_{24}(H_2O)_{12}]^{7+}$ cluster. One-dimensional electron density mapping and Rietveld refinement revealed that the cluster is oriented with its C_3 axis perpendicular to the layers. Thermal analysis of the samples indicate that the layers remain expanded up to 100°C and partially expanded to 300°C, but surface area measurements reveal that void space (if any) in the material is inaccessible.

The synthesis of $[Fe_6S_8(PEt_3)_y]_xMS_2$ (x = 0.05-0.2; y = 2-3; d-spacing = 10.5 -1 1.4 Å) and $[Ni_9S_9(PEt_3)_6]_xMS_2$ (x = 0.04-0.077; d-spacing = 14.0 - 14.2 °) is similar but a solution of the cluster in a non-aqueous, water miscible solvent is used. $[Co_6S_8(PPh_3)_6]_{0.02}MoS_2$ (d-spacing = 15.3 Å) was synthesized by the addition of a solution of the $Co_6S_8(PPh_3)_6$ cluster in

CH_2Cl_2 to an aqueous suspension of single MoS_2 layers. Thermal analysis reveals that the volatile product in all samples is phosphine sulfide. The hydrodesulfurization (HDS) activity of $[Co_6S_8(PPh_3)_6]_{0.02}MoS_2$ is comparable to that of commercially available catalysts; the activity of $[Ni_9S_9(PEt_3)_6]_xMS_2$ is inferior.

The structure of restacked MS_2 (M = Mo,W) was solved by electron crystallographic studies. Using two-dimensional *hk0* data indexed to a $\sqrt{3}a$ x a orthorhombic unit cell, Patterson projections were calculated which revealed a severe distortion in the Mo/W plane, forming infinite zig-zag chains. The projection of the structure suggests M-M distances of 2.92 Å and 2.74 Å for MoS_2 and WS_2, respectively. Least squares refinement from the single crystal data gives R_1=13.3% for WS_2 and R_1=15.3% for MoS_2, and reveals a WTe_2 type structure.

The relationship between charge and structure in restacked MS_2 has been probed by encapsulation of alkali cations, forming $A_x(H_2O)_yMS_2$ (x = 0.15-0.25; y = 0.3-0.45) and chemical oxidation with I_2 and Br_2. Chemical oxidation results in a change in the structure of restacked MoS_2, giving rise to a $\sqrt{3}a$ x $\sqrt{3}a$ superlattice. Differential Scanning Calorimetry studies show an irreversible exothermic transition to 2H-MS_2 which shifts in temperature with oxidation. Thermopower measurements indicate that restacked MoS_2 and WS_2 are p-type metallic conductors.

ACKNOWLEDGMENTS

Nothing presented here would have been possible without the support, enthusiasm, patience, and guidance of my advisor, Professor Mercouri Kanatzidis, for which I am deeply grateful. I would also like to thank Professor Pinnavaia for his helpful advice, for allowing me to use his equipment, and his comments as a second reader. Much thanks to Professor McCracken and Professor Baker for serving as members of my graduate committee as well. I thank Dr. Chris Marshall and Dr. Jim Brenner for HRTEM and HDS studies, Dr. Eric Prouzet for EXAFS measurements, and Dr. Duck-Young Chung for thermopower measurements.

I owe a great deal to Dr. John Heckman, who taught me to use a TEM and offered many useful suggestions throughout my studies. I would also like to thank the members of the Kanatzidis group for their kindness and all that I have learned from them, especially Rabin Bissessur, Wakgari Hirpo, Hui-Lien Tsai, Lei Wang, Jason Hanko, and Rhonda Patschke. Much thanks also to the chemistry department staff. Thanks to my friends, especially Dean Lantero and Carl Iverson for help with the NMR and Gary Lavine for just listening. Finally, I thank my family for their support.

TABLE OF CONTENTS

LIST OF TABLES viii

LIST OF FIGURES ix

ABBREVIATIONS xiv

CHAPTER 1
Introduction 1
1.1 Insertion Reactions 2
1.2 Open Framework Materials 5
1.3 MoS_2 and WS_2 as hosts 10
1.4 Pillaring agents 17
References 26

CHAPTER 2
Encapsulation and Rietveld Structural Characterization of the $[Al_{13}O_4(OH)_{24}(H_2O)_{12}]^{7+}$ cluster into MoS_2 and WS_2. 35
2.0 Abstract 36
2.1 Introduction 37
2.2 Experimental 38
2.2.1 Synthesis 38
2.2.2 Characterization 40
2.3 Results and Discussion 41
2.3.1 Evidence of Cluster Encapsulation 41
2.3.2 One-Dimensional Electron Density Mapping 49
2.3.3 One-Dimensional Rietveld Refinement 57
2.3.4 Thermal Stability and Absorption Measurements 60
2.4 Conclusions 63
References 65

CHAPTER 3
Encapsulation of Neutral and Cationic Metal Chalcogenide Clusters in MoS_2 and WS_2 68
3.0 Abstract 69
3.1 Introduction 71
3.2 Experimental 72
3.2.1 Synthesis 72
3.2.2 Characterization 75

3.3 Results and Discussion 77
3.3.1 Evidence of Cluster Encapsulation 77
3.3.2 Thermal Analysis 90
3.3.3 HDS Activity 101
3.4 Conclusions 109
References 113

CHAPTER 4
Structure of Restacked MoS_2 and WS_2 Elucidated by Electron Crystallography 117
4.0 Abstract 118
4.1 Introduction 119
4.2 Experimental 124
4.3 Results and Discussion 125
4.3.1 Data Collection 125
4.3.2 Structure solution from the "triplet" crystal of WS_2 128
4.3.3 Dynamic Scattering: Two-Beam Approximation 136
4.3.4 Structure solution from "single" crystals of WS_2. 146
4.3.5 Dynamic Range Correction 153
4.3.6 Structure Solution from "single" crystals of MoS_2. 155
4.3.7 Dynamic scattering: n-beam approximation. 160
4.3.8 Electron Crystallographic Studies of an alternate superlattice in MoS_2 168
4.4 Conclusions 174
References 175

CHAPTER 5
Exfoliated and Restacked MoS_2 and WS_2: Ionic or Neutral Species? Encapsulation and Ordering of Hard Electropositive Cations 179
5.0 Abstract 180
5.1 Introduction 181
5.2 Experimental 184
5.2.1 Synthesis 184
5.2.2. Characterization. 191
5.3 Results and Discussion 192
5.3.1 Cation encapsulated MS_2. 192
5.3.2 Electron diffraction studies of $(cation)_xMS_2$. 194
5.3.3 Modeling the cation ordering. 202
5.3.4. Oxidation state of M (M = Mo,W) and the charge of the layers. 209
5.3.5 Oxidation reactions of $LiMS_2$. 212
5.3.6 X-ray diffraction studies of oxidized MS_2. 218

5.3.7 DSC studies of oxidized MS_2. 225
5.3.8 Acid restacked MS_2. 231
5.3.9 Thermopower measurements. 237
5.4 Conclusions 241
References 246

LIST OF TABLES

Table 2.1. $|F(l)_{obs}|$ and $F(l)_{calc}$ for $[Al_{13}O_4(OH)_{24}(H_2O)_{12}]_{0.05}MoS_2$. 52
Table 2.2 $|F(l)_{obs}|$ and $F(l)_{calc}$ for $[Al_{13}O_4(OH)_{24}(H_2O)_{12}]_{0.055}WS_2$. 53
Table 2.3. Rietveld refinement summary of $[Al_{13}O_4(OH)_{24}(H_2O)_{12}]_{0.055}WS_2$ 59

Table 3.1. HDS catalytic activity and surface area (SA) of selected samples and references. 103

Table 4.1. Crystal data and structure refinement for restacked WS_2. 134
Table 4.2. Preliminary atomic coordinates (x 10^4) and equivalent isotropic displacement parameters (A^2 x 10^3) for restacked WS_2. 135
Table 4.3. Refinement for WS_2 as a function of data correction methods. 141
Table 4.4. Crystal data and structure refinement for crystals of WS_2. 150
Table 4.5. Atomic coordinates (x 10^4) and equivalent isotropic displacement parameters (A^2 x 10^3) of restacked "single" and "triple" WS_2. 151
Table 4.6. Crystal data and structure refinement of restacked MoS_2. 158
Table 4.7. Atomic coordinates (x 10^4) and equivalent isotropic displacement parameters (A^2 x 10^3) in restacked MoS_2. 159
Table 4.8. A comparison of simulated dynamic electron diffraction data to the experimental data for MoS_2 and WS_2 as a function of layer thickness. 167

LIST OF FIGURES

Figure 1.1. The chemical insertion of Li atoms into TaS_2. 2
Figure 1.2. Projection of 2H-MoS_2 (A) in the *ab* plane (one layer) and (B) along the *c* axis. 2H-WS_2 is isostructural. 11
Figure 1.3. Structure of 1T-TiS_2 viewed (A) in the *ab* plane and (B) along the *c* axis. 13
Figure 1.4. Illustration of the exfoliation and flocculation process used to encapsulate neutral and cationic species. 15
Figure 1.5. (A) the $[Al_{13}O_4(OH)_{24}(H_2O)_{12}]^{7+}$ cluster. (B) A trimer of edge-sharing octahedral Al^{3+} ions with a common vertex (open circle). 19
Figure 1.6. (A) M_6Q_8 core of $Co_6S_8(PPh_3)_6$. (B) M_6Q_8 core with phosphine ligands. 21
Figure 1.7. (A) Ni_3S_3 units which are stacked in a staggered fashion to form (B), the $[Ni_9S_9(PEt_3)_6]^{2+}$ cluster. 24

Figure 2.1. X-ray diffraction patterns of (A) $[Al_{13}O_4(OH)_{24}(H_2O)_{12}]_{0.05}MoS_2$ and (B) $[Al_{13}O_4(OH)_{24}(H_2O)_{12}]_{0.055}WS_2$ used for electron density maps and Rietveld refinements. 42
Figure 2.2. Three possible orientations of the $[Al_{13}O_4(OH)_{24}(H_2O)_{12}]^{7+}$ cluster between the layers. 43
Figure 2.3. Solid State MAS-NMR ^{27}Al spectra of (A) $[Al_{13}O_4(OH)_{24}(H_2O)_{12}]_{0.03}MoS_2$ and (B) $Na[Al_{13}O_4(OH)_{24}(H_2O)_{12}](SO_4)_2$. 46
Figure 2.4. HRTEM Micrographs of (A) $[Al_{13}O_4(OH)_{24}(H_2O)_{12}]_{0.03}MoS_2$ and (B) $[Al_{13}O_4(OH)_{24}(H_2O)_{12}]_{0.04}WS_2$. 47
Figure 2.5. One-dimensional electron density maps of (A) $[Al_{13}O_4(OH)_{24}(H_2O)_{12}]_{0.05}MoS_2$ and (B) $[Al_{13}O_4(OH)_{24}(H_2O)_{12}]_{0.055}WS_2$. 54
Figure 2.6. (A) Electron density maps calculated from $[Al_{13}O_4(OH)_{24}(H_2O)_{12}]_{0.055}WS_2$ $F(l)_{obs}$ data using 12-19 *00l* reflections (a-h). (B) Maps calculated from theoretical data for a) a W atom and b) a W atom and a S atom, illustrating the Fourier truncation error and the dynamic range problem. 56
Figure 2.7. (A) TGA of $[Al_{13}O_4(OH)_{24}(H_2O)_{12}]_{0.03}MoS_2$ under nitrogen, showing gradual weight loss with an inflection point near 300°C. (B) XRD patterns of the material (a) at room temperature (b) after heating to 120°C and (c) after heating to 300°C. 62

Figure 3.1. X-ray diffraction patterns of (A) $[Co_6S_8(PPh_3)_6]_{0.24}MoS_2$ and restacked MoS_2, showing an expansion of 15.4 Å upon encapsulation of the cluster (B) $[Co_6S_8(PPh_3)_6]_{0.96}MoS_2$, showing only 4 *00l* reflections. 78
Figure 3.2. The $Co_6S_8(PPh_3)_6$ cluster oriented with its (A) C_3 axis perpendicular to the layers and its (B) C_4 axis perpendicular to the layers. 79
Figure 3.3. HRTEM micrographs of $[Co_6S_8(PPh_3)_x]_{0.02}MoS_2$. (A) Region with lamellar features showing expanded and unexpanded layers. Expansion suggests that PPh_3 ligands have been removed. Small (B) Region showing in-plane structure. 80
Figure 3.4. X-ray diffraction patterns of (A) $[Fe_6S_8(PEt_3)_2]_{0.096}MoS_2$ (Δ = 10.5 Å) and (B) $[Fe_6S_8(PEt_3)_3]_{0.20}WS_2$ (Δ = 11.4 Å). 84
Figure 3.5. HRTEM micrograph of $[Fe_6S_8(PEt_3)_3]_{0.20}WS_2$ showing highly ordered in-plane structure. 85
Figure 3.6. X-ray diffraction patterns of (A) $[Ni_9S_9(PEt_3)_6]_{0.07}MoS_2$ (Δ = 14.2 Å) and (B) $[Ni_9S_9(PEt_3)_6]_{0.077}WS_2$ (Δ = 14.0 Å). 88
Figure 3.7. A view of the $[Ni_9S_9(PEt_3)_6]^{2+}$ cluster with its Ni_3S_3 planes (A) parallel to and (B) perpendicular to the MS_2 layers 89
Figure 3.8. TGA of (A) $Co_6S_8(PPh_3)_6$. (B) $[Co_6S_8(PPh_3)_6]_{0.22}MoS_2$. 91
Figure 3.9. An illustration of the original plan to create a microporous sulfide: encapsulation of the cluster with phosphine ligands acting as "spacers", followed by thermal treatment to remove the phosphine ligands. 92
Figure 3.10. An illustration of the observed data: encapsulation of the cluster with phosphine ligands acting as "spacers", followed by thermal treatment. The phosphine ligands attack the layers as they depart, forming SPR_3 species and possible S^{2-} anion vacancies. 93
Figure 3.11. X-ray diffraction patterns upon thermal treatment of $[Co_6S_8(PPh_3)_6]_{0.24}MoS_2$. 94
Figure 3.12. TGA of (A) $[Fe_6S_8(PEt_3)_6](BPh_4)_2$, (B) $[Fe_6S_8(PEt_3)_2]_{0.096}MoS_2$ (solid line) and $[Fe_6S_8(PEt_3)_3]_{0.20}WS_2$ (dashed line). 97
Figure 3.13. X-ray diffraction patterns upon thermal treatment of $[Fe_6S_8(PEt_3)_2]_{0.096}MoS_2$. 98
Figure 3.14. TGA of (A) $[Ni_9S_9(PEt_3)_6](ClO_4)_2$. (B) TGA of $[Ni_9S_9(PEt_3)_6]_{0.047}WS_2$. 100
Figure 3.15. HRTEM micrograph of $[Co_6S_8(PPh_3)_6]_{0.02}MoS_2$ after HDS. 105
Figure 3.16. Illustration of the "rim-edge" model for (A) unpillared and (B) pillared MoS_2. 107

Figure 4.1. Schematic illustrating the proposed superstructures of restacked/1T-MoS_2. 121
Figure 4.2. BFI and SAED of "triple" and "single" WS_2. 126
Figure 4.3. (A) Relationship between the *2a x a* and $\sqrt{3}a$ *x a* lattice. (B) Illustration of how three $\sqrt{3}a$ *x a* patterns can be overlapped to form a *2a x 2a* pattern. 127
Figure 4.4. Illustration of the "Gel Plotting Macro" in NIH Image 1.60. 130
Figure 4.5. Two-dimensional Pattersons along the *c*-axis: (A) 1T-MS_2 (theoretical), (B) restacked WS_2 with background subtraction and Lorentz correction, (C) restacked WS_2 with only Lorentz correction, (D) restacked WS_2 with no corrections. 131
Figure 4.6. Schematic illustrating (A) kinematic scattering and (B) dynamic scattering. 137
Figure 4.7. Graph of the function $K(A_3Q)$. 139
Figure 4.8. The intersection of the Ewald sphere with the reciprocal lattice at an accelerating voltage of (A) ~50kV and (B) ~100kV. 143
Figure 4.9. (A) The limit of detectable reflections (in a perfectly oriented crystal) as a function of the thickness (t) of the sample ($q = 1/t$), the radius of the Ewald sphere (r), and angle γ. (B) An illustration of secondary scattering. 144
Figure 4.10. Selected Area Electron Diffraction of "single" WS_2 patterns used to generate Patterson contour plots. 148
Figure 4.11. Two-dimensional Patterson projections along *c*-axis: (A) ideal MS_2 and (B-D) three "single" WS_2 data sets. 149
Figure 4.12. (A) Two-dimensional projection of a restacked MS_2 layer and one WTe_2 layer. (B) View of WTe_2 parallel to *c*-axis. 152
Figure 4.13. Surface plots of the *(3-10)* and the *(-2-20)* reflections from the patterns in Figures 4.2d and 4.11a. 154
Figure 4.14. Bright Field images and Selected Area Diffraction Patterns of "single" crystal restacked MoS_2. 156
Figure 4.15. Two-dimensional Patterson projections of restacked MoS_2. 157
Figure 4.16. Simulated dynamic Electron Diffraction patterns of restacked WS_2. 162
Figure 4.17. Patterson projections calculated from the data in 4.16. 165
Figure 4.18. Simulated Patterson projections for WS_2 calculated as a function of thickness. 166
Figure 4.19. Selected Area Electron Diffraction pattern of alternate MoS_2 superlattice. 171
Figure 4.20. Two-dimensional Patterson projections calculated for (A) an ideal MoS_2 lattice and (B) from experimental data 172

Figure 4.21. Simulated Patterson projections of alternate MoS_2 superlattice. 173

Figure 5.1. (A) X-ray diffraction pattern of $Na_{0.18}(H_2O)_{0.45}WS_2$. (B) TGA of $Na_{0.18}(H_2O)_{0.45}WS_2$, $K_{0.21}(H_2O)_{0.40}WS_2$, and $Rb_{0.24}(H_2O)_{0..}$ 193
Figure 5.2. Selected Area Electron Diffraction patterns of (A) $Cs_{0.23}MoS_2$ and (B) $Cs_{0.13}WS_2$. 196
Figure 5.3. Selected Area Electron Diffraction patterns of (A) $K_{0.23}MoS_2$; (B) $K_{0.23}MoS_2$; (C) $Rb_{0.15}MoS_2$; and (D) $K_{0.23}MoS_2$. 199
Figure 5.4. Selected Area Electron Diffraction patterns from (A) a thick crystal of Li_xWS_2 and (B) a thin crystal of $Rb_{0.15}MoS_2$. 200
Figure 5.5. (A) Structural model and (B) simulated electron diffraction pattern to explain the observed patterns in Figures 5.2-5.3. 203
Figure 5.6. Selected Area Electron Diffraction patterns of (A) $Ba_{0.08}MoS_2$ and (B) $Na_{0.14}MoS_2$. 207
Figure 5.7. (A) Structural model and (B) simulated electron diffraction pattern to explain the observed Selected Area Electron Diffraction patterns in Figure 5.5. 208
Figure 5.8. Selected Area Electron Diffraction pattern of $LiMoS_2$ oxidized with Br_2 in MeCN. 214
Figure 5.9. (A) Patterns which show only the alternate superlattice. (B) Selected Area Electron Diffraction pattern of $LiMoS_2$ oxidized with Br_2 in MeCN over a longer period of time with sonication. 215
Figure 5.10. Selected Area Electron Diffraction pattern of a minority phase formed upon oxidation of $LiWS_2$ with Br_2 in MeCN. 216
Figure 5.11. Transmission X-ray diffraction (XRD) pattern of $LiMoS_2$ oxidized in MeCN with increasing time. 219
Figure 5.12. Transmission XRD pattern of $LiWS_2$ oxidized with Br_2 in MeCN. The black circle marks a peak at 2.55 Å which does not appear to be an *hk0* reflection of any of the three expected lattices. The asterisk marks a contribution from the Saran™ wrap substrate. 220
Figure 5.13. Transmission XRD pattern of $LiWS_2$ oxidized with Br_2 (A) before and (B) after heating. 224
Figure 5.14. Differential Scanning Calorimetry (DSC) plots of restacked MoS_2 and $LiMoS_2$ oxidized with Br_2. 226
Figure 5.15. DSC plots showing the irreversible exothermic phase transition to 2H-WS_2. 227
Figure 5.16. Transmission XRD pattern of (A) $LiWS_2$ and (B) H_xMoS_2 obtained from $LiMoS_2$ exfoliated in concentrated HCl. 232
Figure 5.17. DSC plots of H_xWS_2 obtained from the reaction of HCl with (A) $LiWS_2$ (155°C) and $Li_{1-n}(H_2O)_xWS_2$ (191°C). 233

Figure 5.18. Schematic illustrating (A) an ideal 1T-MS_2 lattice, (B) a $\sqrt{3}a$ x a lattice with infinite zig-zag metal chains, (C) a $\sqrt{3}a$ x $\sqrt{3}a$ lattice with trimers, and (D) a $2\sqrt{3}a$ x $2\sqrt{3}a$ lattice with possible tetramers formed due to M-M distortions. 236
Figure 5.19. Schematic band diagram illustrating the distortion of an ideal octahedral system to form zig-zag chains. 239
Figure 5.20. Thermopower measurements of restacked MoS_2 and WS_2. 240
Figure 5.21. Reaction scheme illustrating the different phases obtained with various treatment of (A) MoS_2 and (B) WS_2. 243

ABBREVIATIONS

BET: Brunauer, Emmett, and Teller (Surface Area)

BFI: Bright Field Image

DSC: Differential Scanning Calorimetry

EDS: Energy Dispersive Spectroscopy

EXAFS: Extended X-ray Absorption Fine Structure

HDS: Hydrodesulfurization

HRTEM: High Resolution Transmission Electron Microscopy

MAS-NMR: Magic Angle Spinning Nuclear Magnetic Resonance

SAED: Selected Area Electron Diffraction

SEM: Scanning Electron Microscope

TEM: Transmission Electron Microscope

TGA: Thermogravimetic Analysis

XRD: X-ray Diffraction

PEt_3: triethyl phosphine

PPh_3: triphenyl phosphine

$Al_{13}O_{40}$: $[Al_{13}O_4(OH)_{24}(H_2O)_{12}]^{7+}$

CHAPTER 1

Introduction

1.1 Insertion Reactions

The demand for materials with new and unique combinations of properties has required scientists to adopt many clever synthetic strategies. One approach is to alter the properties of two existing materials by combining them. For example, the combination of nylon-6 with clays results in nanocomposites with enhanced thermal stability and mechanical properties relative to those of the individual components.[1] Materials which are mixed on a molecular level are of particular interest to chemists, and can be synthesized through processes such as encapsulation and insertion.

In insertion or encapsulation reactions, a guest species is incorporated into a host species, resulting in a net gain in the energy of the system. The "host" is usually a one-dimensional, two-dimensional, or three-dimensional material[2,3] and the "guest" includes molecular species which range from a proton[4] to large clusters[92] or polymers.[15,16] An example is the chemical or electrochemical insertion of Li atoms into the layered compound TaS_2:[5]

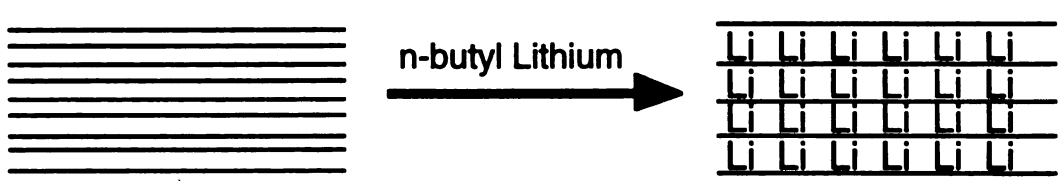

Figure 1.1. The chemical insertion of Li atoms into TaS_2.

An insertion is said to be "topotactic" or "topochemical" when the structure of the host framework is not significantly altered by the insertion process. Layered materials have been explored perhaps most extensively as hosts because their structure is sufficiently robust to allow topotactic insertion, but flexible enough to allow species of many different sizes to be inserted. Intercalation, a special kind of insertion process, is a very popular example of host/guest chemistry. In the most general chemical sense, "intercalation" refers to a reversible insertion. The word "intercalation" is sometimes loosely employed in the literature to describe irreversible insertion reactions as well.

The driving force for the insertion process is the net gain in energy of the system, which can be realized through a variety of mechanisms. One of the most common ways is through electron transfer from the guest species to the host species. For example, in the insertion of the Li atoms into TaS_2 the layers are reduced and the lithium atoms are oxidized.[5] Another frequently encountered insertion mechanism is ion-exchange, which has been used to replace gallery Na^+ ions in smectite clays with other cations such as tetramethyl or tetraethylammonium.[6] This is accomplished by swelling the clay with water, then exposing it to a solution with an excess of the cation which is to be intercalated. A third manner is through coordination of the guest species to the host, which is observed when alcohols replace coordinated water in vanadyl phosphonates.[7] Other

methods exist, and some layered hosts, such as V_2O_5, can undergo insertion through more than one method.[8] The variety in mechanisms through which guest species can be inserted, coupled with the large number of known layered structures, has resulted in an enormous body of literature on the subject of the insertion of guest species in lamellar materials.[2,3,9,10] The earliest reports of intercalation involve graphite as a host material.[11] Layered hosts which can undergo insertion reactions also include smectite clays[18]; double hydroxides[12]; metal oxides[8,16], oxyhalides[15], and halides[9]; transition metal phosphates, phosphonates, and sulfophosphonates[13]; and transition metal dichalcogenides.[3,5,10] Even the high temperature superconducting cuprates can undergo insertion reactions.[14]

The diversity of available layered hosts and guest species has led to the study of these systems for many applications. One of the most important applications which has been explored for those systems which undergo insertion via redox reactions is their use as solid state battery cathodes. In particular, the insertion of alkali metals in the transition metal dichalcogenides both chemically and electrochemically has been studied extensively due to the interesting electronic properties of the chalcogenides, which can be affected by the intercalation reaction.[2-5,10] Related to this is the study of polymers as guest species, desirable because they lead to an increase in ion mobility in the lattice. Studies have not been limited to the layered dichalcogenides, but include hosts such as clays, V_2O_5, FeOCl, and

MoO_3. Strategies to incorporate polymers have included insertion of the monomer followed by polymerization[15] or direct incorporation of the polymer.[16] Another important application for layers which undergo insertion processes is as ion-exchange materials[17] or open framework catalysts.[18] The layers in smectite clays can be separated by solvation, called swelling, which allows ion exchange.[19] When larger cations are used, void spaces may be created.[6]

1.2 Open Framework Materials

The demand for open framework structures, which originates from their application as size selective molecular sieves and catalysts, has inspired the discovery and characterization of a vast array of materials in the last fifty years. Those with accessible void spaces in the range 3 - 20 Å are called microporous; compounds with larger void spaces (up to 500 Å) are mesoporous. The most widely used open framework materials are the aluminosilicate zeolites, which possess three dimensional structures with pore sizes in the range 3-9 Å[20], and zeolite-like aluminophosphates, which contain micropores up to 14 Å.[21] Applications for zeolites include ion exchange[17] and a variety of size selective catalytic processes.[22] Zeolites with larger void spaces are desirable but have not been discovered. A breakthrough in the synthesis of mesoporous materials was the discovery of

MCM-41 in 1992. The synthesis involves the polymerization of silicate around micelles of long-chain alkylammonium cations, followed by calcination, and results in a material which has uniform channels with accessible void space.[23] The dimensions of these channels can be controlled synthetically by adjusting the micelles, allowing the pore size to range from 16 - 100 Å.

Prior to MCM-41, one strategy for attaining pore sizes larger than 14 Å was the "pillaring" of smectite clays with large cations, creating materials with accessible void space. Typically void space is quantified through surface area values measured by N_2 absorption. The exchange of small gallery cations for larger cations requires an expansion of the layers, and is possible in smectites due to their ability to swell and even delaminate in water. The first example of pillaring was reported by Barrer and MacLeod in 1955, and involved the exchange of Na^+ for tetramethyl and tetraethyl ammonium in smectite clays.[6] These cations are small pillars, however, and interest in pillared clays only began to develop in the 1970's, particularly with the discovery that pillaring with polynuclear metal hydroxyl cations such as $Al_{13}O_4(OH)_{24}(H_2O)_{12}^{7+}$ and $Zr_4(OH)_{12}^{4+}$ results in materials with thermal stability above 500°C and moderately high surface area values.[77] These pillars convert to metal oxide clusters upon calcination, resulting in a material which retains the layer expansion. Other pillaring agents have included bicyclic amine cations[24], metal and

silicon chelate complexes[25], metal halide clusters such as $Nb_6Cl_{12}^{2+}$,[18a] and imogolite, a large tubular structure.[26]

Unfortunately open framework silicates are insulators. The chalcogenides, however, usually have semiconducting or metallic properties, which, when combined with porosity, could result in a unique new class of materials with interesting practical applications which include use as chemical sensors or catalysts. For this reason many researchers are using a variety of techniques in an effort to synthesize open framework chalcogenides.[27]

A logical approach is hydrothermal synthesis, as it is the method used to make zeolites. An important breakthrough came in 1989, when Bedard and coworkers discovered $A_2Sn_3S_7$ (A = alkyl ammonium cation) and $A_2MGe_4S_{10}$.[28,34] Perhaps the most exhaustively studied open framework chalcogenide is $A_2Sn_3S_7$, which has a layered structure with large pores in the basal plane. The solution precursors have been isolated and a mechanism of formation proposed.[29] The effects of progressive selenium substitution and included water upon the band gap have been reported.[30] Unfortunately, adjustment of the layer stacking to minimize the void space in the basal plane occurs when organic cations of various sizes are used in the synthesis.[31] The tremendous flexibility of the framework seems to confound efforts to maximize void space in the structure. The materials are only stable to 250-350°C (depending on the identity of the organic

cation), and microporous behavior is only observed when CO_2 is used in the absorption studies.[32] Cesium sulfide and selenide analogs have been isolated, but the selenide analog is fairly air sensitive and the sulfide analog contains an S_8 molecule included in the structure which cannot be removed.[33]

Most other open framework chalcogenides are not so thoroughly investigated. Members of the family $A_2MGe_4Q_{10}$ (M = transition metal; Q = S, Se) are perhaps the second most reported and characterized compounds.[34] Some interesting antimony sulfides and selenides have also been published.[35] Molten salt synthesis has resulted in KBi_3S_5, a three dimensional material with channels, and $(Ph_4P)[M(Se_6)_2]$ (M = Ga, In, Tl), a two-dimensional framework with void spaces in the basal plane occupied by tetraphenylphosphonium cations.[36] Perhaps the most promising recent development in the search for chalcogenide analogs of zeolites are the hydrothermally synthesized indium sulfide frameworks ASU-31 and ASU-32, but no absorption studies are reported.[37]

Concurrent with the hydrothermal self-assembly approach to synthesize microporous chalcogenides is an effort to create mesoporous chalcogenides through supramolecular assembly, as in the synthesis of MCM-41. The polymerization reaction about the micelles is accomplished by the linkage of $Ge_4Q_{10}^{4-}$ clusters with transition metals. Preliminary results indicate that structures with wormholes and channels are formed;

however, the thermal stability of the materials is poor and no absorption studies are reported.[38]

As hydrothermal synthesis and supramolecular assembly are both synthetic techniques developed for the silicates, a logical extension is the application of pillaring to the chalcogenides as well. Pillaring has been extended to other non-silicate layered materials with some success. Pillared phosphonates have been reported, but these are not synthesized by an insertion process.[39] The layered materials which are most obvious candidates for pillaring by insertion are ones which can undergo ion exchange, as this is the mechanism for pillaring in clays. Hydrotalcite has been pillared with polyoxometallates in this manner.[12] The cations $[Bi_6(OH)_{12}]^{6+}$ $[Al_{13}O_4(OH)_{24}(H_2O)_{12}]^{7+}$ have been inserted in MoO_3, and the latter cation into V_2O_5 as well, by ion exchange.[80-82] Insertion of large molecules via a redox reaction has been observed, however, in the insertion of $[Fe_4(\eta\text{-}C_5H_4Me)_4(\mu^3\text{-}S)_4]$ and $[Mo_4(\eta\text{-}C_5H_4Pr^i)_4(\mu^3\text{-}Se)_4]$ into MoO_3 and FeOCl.[40]

As mentioned previously, the layered dichalcogenides undergo intercalation chemistry and have been explored extensively as battery cathode materials due to their ability to accept alkali metal cations through redox intercalation.[2-5,10] Redox intercalation has also been used to insert larger molecules such as pyridine[41] and phthalocyanine dye derivatives[42] in TaS_2. Also by redox chemistry, metallocenes can be inserted into group IV

and V layered dichalcogenides[43] and into SnS_2 and $SnSe_2$.[44] Redox insertion is limited, however, in that the pillaring agent must be capable of reducing the host. An important development in the pillaring of the layered dichalcogenides was the insertion of $[Al_{13}O_4(OH)_{24}(H_2O)_{12}]^{7+}$ and $[Fe_6S_8(PEt_3)_6]^{2+}$ into $Na_x(H_2O)_yTaS_2$ by ion exchange.[81,92] The layers were dispersed (similar to delamination) in a mixture of n-methylformamide and water and the clusters introduced, resulting in layer flocculation. The use of ion exchange to pillar TaS_2 expands the identity of guest species which can be incorporated to include species which cannot be inserted by redox chemistry, which encompasses most of the pillaring agents used in clays.

1.3 MoS_2 and WS_2 as hosts

Unlike the group IV and V chalcogenides, MoS_2 was notorious for its resistance to intercalation until 1983, when it was discovered that redox insertion is possible but induces a transformation in the coordination environment of the metal.[47] MoS_2 is found in nature as the mineral molybdenite. The structure, first solved in 1923 by Dickinson and Pauling,[45] consists of a layer of Mo atoms sandwiched by layers of sulfur atoms such that the coordination environment of the Mo atom is trigonal prismatic. The stacking of the MoS_2 layers is staggered (Figure 1.2).

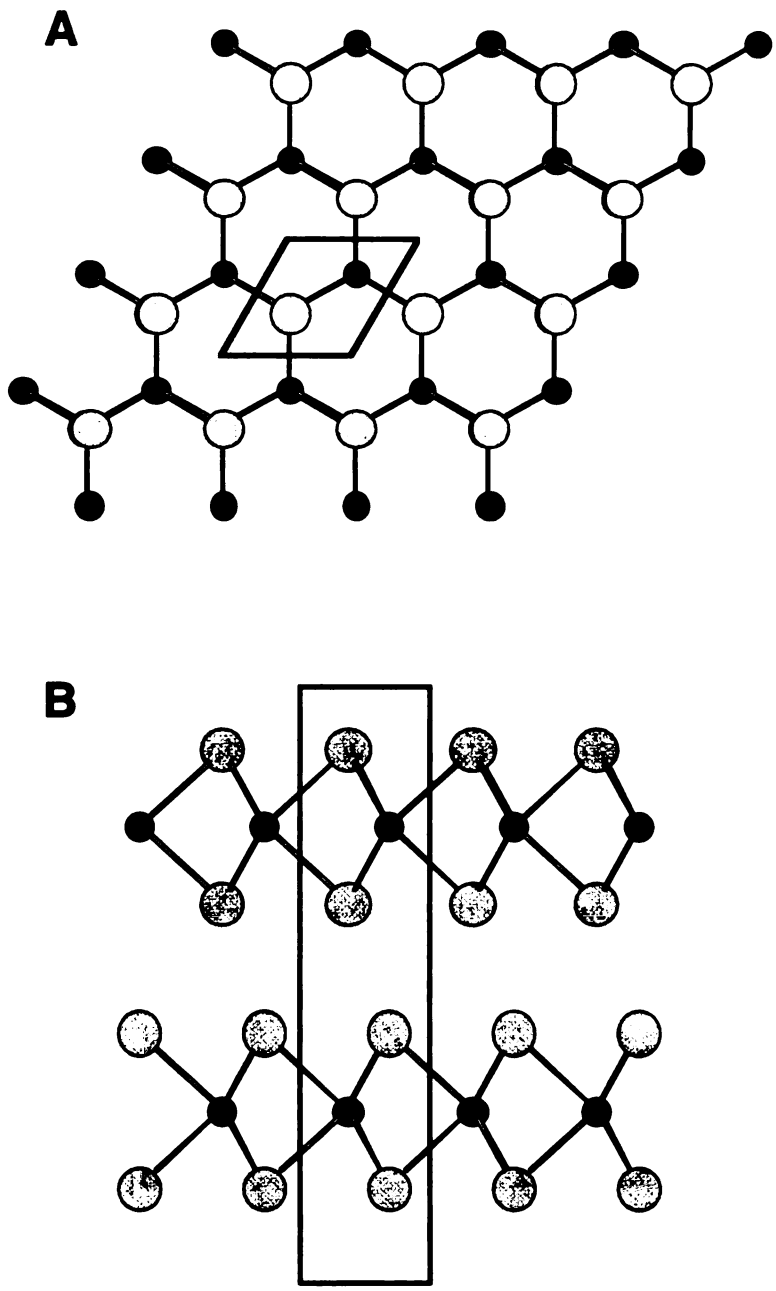

Figure 1.2. Projection of 2H-MoS_2 (A) in the *ab* plane (one layer) and (B) along the *c* axis. 2H-WS_2 is isostructural.

Each MoS_2 layer has only van der Waals interactions with the neighboring MoS_2 layers. This allows the layers to slide with respect to one another with relative ease; as such, other polytypes of MoS_2 can be found with trigonal prismatic coordination of Mo, but a different stacking arrangement. Using a simple system of prefixes for naming the polytypes, molybdenite is called 2H-MoS_2 because there are two layers per unit cell and the crystal has hexagonal symmetry. Another polytype, 3R-MoS_2, has three layers per unit cell and rhombohedral symmetry. The structure and polytypes of WS_2 are analogous to MoS_2.[46]

As mentioned previously, it was discovered that upon intercalation of MoS_2 and WS_2 with lithium a structural transformation takes place in which the metal coordination environment changes from trigonal prismatic to octahedral.[47] The new structure, denoted 1T-MoS_2 (and WS_2), has been called analogous to the structure type observed for TiS_2 (Figure 1.3).[48]

The practical applications for MoS_2 (and to a lesser extent WS_2) are diverse, and include use as a high temperature lubricant.[49] Cobalt and nickel supported MoS_2 and WS_2 are among the commercially available catalysts for hydrodesulfurization.[50] Exfoliated MoS_2 has also been explored as a catalyst for coal liquefaction[51] and methanation of CO.[52] 2H-MoS_2 is a semiconductor with a band gap of 1.1 eV. Because it is found in nature, molybdenite is a relatively inexpensive material.

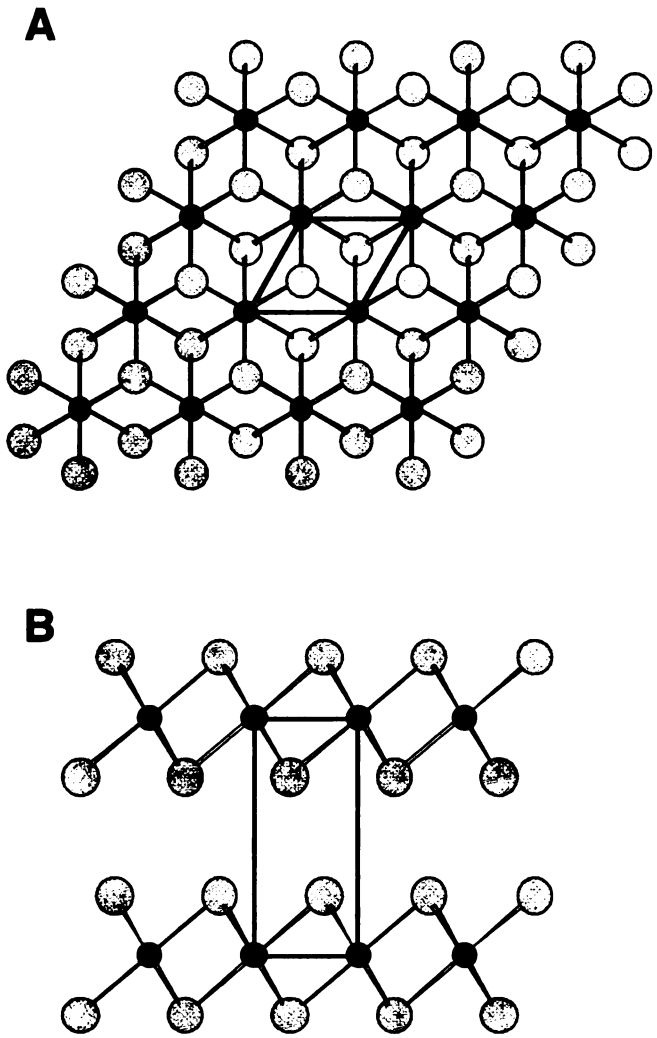

Figure 1.3. Structure of 1T-TiS_2 viewed (A) in the *ab* plane and (B) along the *c* axis. Restacked MoS_2 and WS_2 are resemble this structure type if distortions due to metal-metal associations are neglected.

Electrochemical studies of Li insertion in MoS_2 for solid state battery applications have been conducted,[53] but a more important development in the behavior of $LiMoS_2$ was the discovery in 1986 that it exfoliates in water, much like the delamination of clays. The following redox reaction with water was proposed: [54]

$$LiMoS_2 + H_2O \text{ --> } MoS_2 \text{ (single layers)} + LiOH + 1/2\ H_2(g) \qquad \text{Eq. (1.1)}$$

The suspension of MoS_2 layers can be recovered to a lamellar form by centrifugation, evaporation, or filtration. Furthermore, the layers can encapsulate guest molecules in the restacking process. This is accomplished by first washing away the LiOH generated in the exfoliation reaction, then introducing a water-immiscible solvent such as benzene. An emulsion is formed, and eventually the MoS_2 begins to collect at the water/solvent interface. If a guest species is dissolved in the organic solvent, it can be incorporated in this manner (Figure 1.4).[55] Subsequent studies have shown that some species can also be incorporated without the presence of the organic solvent.[56] It is remarkable that it is possible to incorporate neutral species in this manner. Neutral species of all sizes have been encapsulated and include organic molecules,[55] polymers,[55a,56] ferrocene,[55a,57] fullerenes,[58] and metal chalcogenide clusters.[87a] The behavior of WS_2 is similar.[59,60]

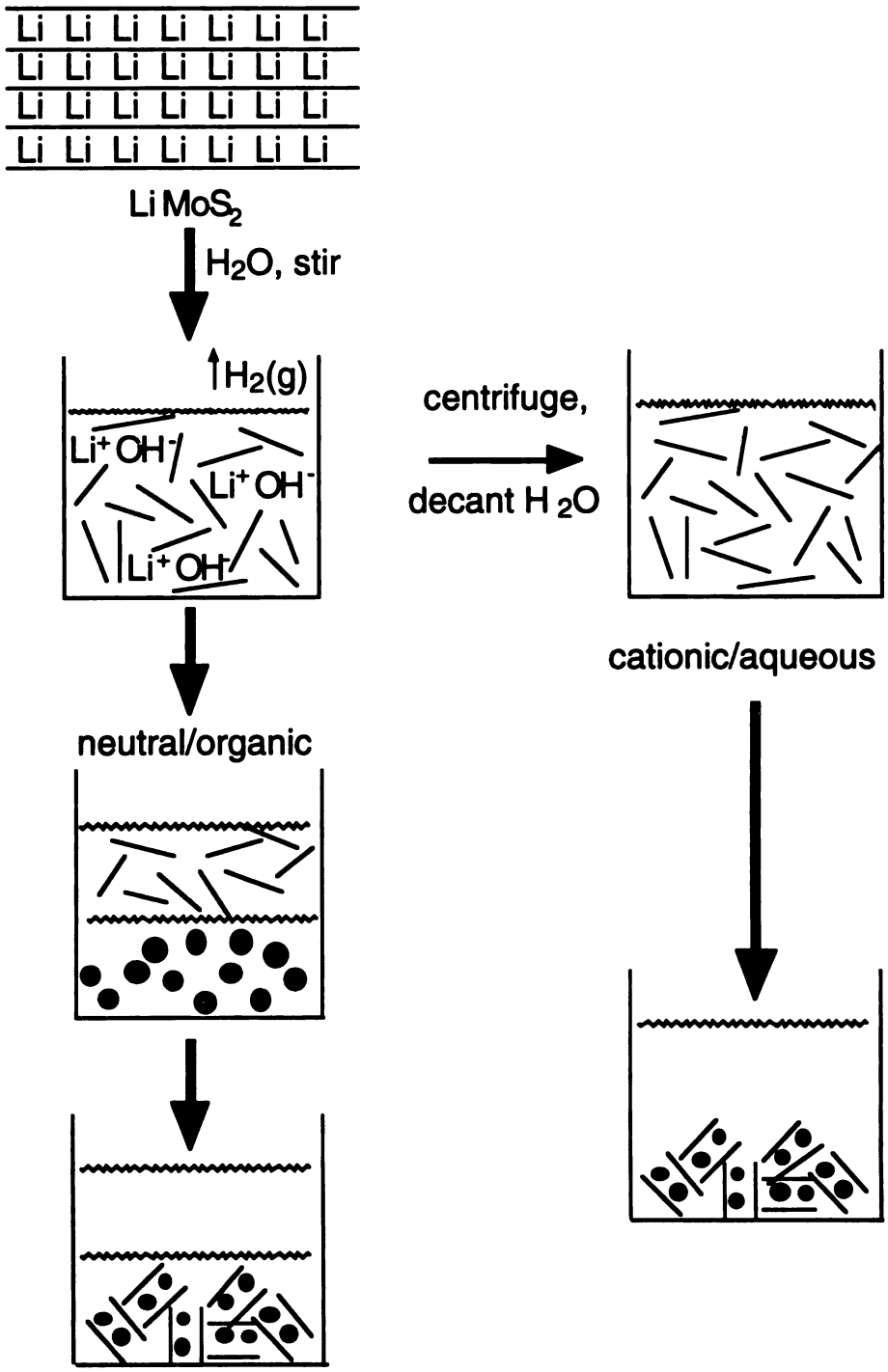

Figure 1.4. Illustration of the exfoliation and flocculation process used to encapsulate neutral and cationic species.

Due to the ability of MoS_2 to encapsulate neutral species, it was believed by many scientists that the oxidation of MoS_2 in the exfoliation process was complete, resulting in neutral layers in suspension. An increasing number of studies have revealed that it is possible to incorporate cationic species as well, without the detectable presence of co-encapsulated anions. Transition metals[61] and small alkyl ammonium cations,[62] along with larger cations such as protonated phenanthroline,[63] iron porphyrins,[64] dihexadecyldimethyl ammonium,[65] and poly(allylamine hydrochloride)[66] have been incorporated by the exfoliation/encapsulative precipitation method. These results suggest that MoS_2 (and WS_2) may in fact retain some negative charge. The results of the studies reported in Chapters 2 and 3 support this assertion. Experiments designed specifically to address the issue of charge on the MS_2 layers are reported in Chapter 5.

The octahedral coordination environment, induced by the lithiation reaction, appears to be retained in restacked MoS_2 and WS_2.[67, 59] However, there are several superlattices which have been observed in lithiated, restacked, and oxidized MoS_2 (and WS_2) due to metal-metal associations which cause a deviation from the ideal 1T structure type depicted in Figure 2. Initially a *2a x 2a* superlattice was reported based on transmission X-ray diffraction patterns.[67,59] Other researchers found evidence for a *2a x a* lattice by Scanning Tunneling Microscopy (STM).[68] Still others have

observed a $\sqrt{3}a \times \sqrt{3}a$ lattice by X-ray diffraction and STM.[69] The layered metal dichalcogenides are prone to these kinds of structural distortions due to the formation of charge density waves (CDWs).[70] The structural distortion in restacked MoS_2 and WS_2 will be discussed in detail in Chapter 4.

1.4 Pillaring agents

Due to the unique ability of exfoliated MoS_2 and WS_2 to accept both neutral and cationic species, there are an enormous variety of metal chalcogenide, metal oxide, metal halide, and metal pnictide clusters which could be used as pillaring agents.[71,72,73] Obviously, metal chalcogenide clusters are requisite for the synthesis of an open framework chalcogenide. The four clusters selected for this work were chosen for their history as a successful pillaring agent in other layered materials and/or the desirability of their chemical composition for potential catalytic materials.

$[Al_{13}O_4(OH)_{24}(H_2O)_{12}]Cl_7$. The aqueous Al^{3+} ion exhibits diverse coordination chemistry at various pH.[74] It was known for years that soluble polynuclear species are formed at pH just below 7[75] before the $[Al_{13}O_4(OH)_{24}(H_2O)_{12}]^{7+}$ cluster, sometimes abbreviated as $[Al_{13}O_{40}]^{7+}$, was crystallized from solution as a sulfate salt.[76] The structure of the cation is a distorted version of a Keggin ion structure observed in polyoxometallates,[73a,74] in which twelve octahedrally coordinated Al^{3+} ions surround one tetrahedrally coordinated Al^{3+} ion (Figure 1.5a). The octahedral Al^{3+} ions may be broken into four groups of edge-sharing trimers, each with a common vertex (Figure 1.5b). These trimers are linked to one another through edge sharing, forming a cluster with tetrahedral symmetry. The tetrahedral Al^{3+} ion at the center is coordinated by the common vertex of each of the four trimers. The cluster is approximately 10 Å in its smallest projection (visible in Figure 1.5a) and nearly 13 Å in its largest dimension.

Polynuclear hydroxy aluminum species, particularly the $[Al_{13}O_{40}]^{7+}$ cluster, have been explored by many as pillaring agents for clays.[77,78] Solution and solid state ^{27}Al NMR have proved useful tools in the identification of the cluster in solution and in the intercalated samples.[79] The thermal stability of clays pillared with this species permits activity as a

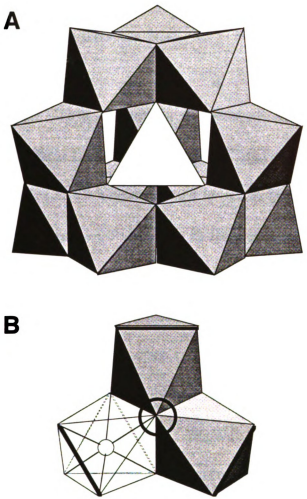

Figure 1.5. (A) the $[Al_{13}O_4(OH)_{24}(H_2O)_{12}]^{7+}$ cluster. The tetrahedral Al^{3+} polyhedron is shown in white. (B) A trimer of edge-sharing octahedral Al^{3+} ions with a common vertex (open circle). Four of these trimers are linked together though edge sharing (black lines) to form the cluster.

molecular sieve and acid catalyst.[78] The cluster has also been used as a pillaring agent for MoO_3[80], TaS_2[81], and V_2O_5.[82] The encapsulation of this cluster will be described in Chapter 2.

$Co_6S_8(PPh_3)_6$. This cluster is a member of a large family of compounds of the general formula $Co_6Q_8(PR_3)_6^{n+}$ (Q = S, Se, Te; R = ethyl, butyl, phenyl; n = 0,1,2).[83,84] The structure is comprised of a cube of eight chalcogen atoms containing a cobalt atom in the center of each face (Figure 1.6a). To each cobalt atom is ligated one phosphine group (Figure 1.6b).

This M_6Q_8 core appears frequently in metal chalcogenide cluster chemistry.[71] The size of the Co_6S_8 core is about 5 Å along the faces of the cube and 7.5 Å along the body diagonal. The overall dimensions of the cluster, including the phosphine ligands, range from 14 - 15.5 Å.

Research involving molecular clusters such as $Co_6S_8(PPh_3)_6$ is motivated (at least in part) by the hope that they might be used as molecular precursors to extended solids.[84a] One particularly interesting feature of the $Co_6Q_8(PR_3)_6^{n+}$ clusters is their structural and compositional similarity to catalytic materials. As mentioned previously, cobalt supported MoS_2 is used as a catalyst in hydrodesulfurization (HDS), but the mechanism of the activity is not well understood.[50] One theory to explain the activity, called the "contact synergy" model, involves separate Co_9S_8

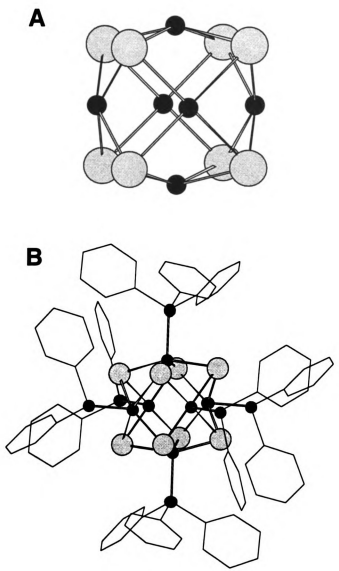

Figure 1.6. (A) M_6Q_8 core (M, black circles, Q, gray circles) of $Co_6S_8(PPh_3)_6$. (B) M_6Q_8 core with phosphine ligands (P, dark gray circles).

clusters and MoS_2 domains.[85] Another group of HDS catalysts, called the Chevrel phases, are ternary compounds containing a three dimensional array of linked Mo_6Q_8 (Q = S, Se, Te) units.[86]

The encapsulation of neutral members of the $Co_6Q_8(PR_3)_6$ family into MoS_2 was initiated in the Kanatzidis laboratory by Bissessur.[87] Surface area measurements and magnetic properties were reported, but HDS activity was not explored. The $Co_6S_8(PPh_3)_6$ cluster was selected for further studies due to the relative ease of the cluster synthesis, the large expansion afforded by the bulky ligands, and the relatively high thermal stability of the unencapsulated cluster. The encapsulation of this cluster will be discussed in Chapter 3.

$[Fe_6S_8(PEt_3)_6]^{2+}$. In addition to the possible use for metal chalcogenide clusters as molecular precursors to extended solids, the synthesis of many such clusters, particularly iron chalcogenide clusters, is motivated by a need for models of compositionally and structurally similar redox centers in biological systems.[88] Because they are of interest to materials scientists as well as bioinorganic chemists, the family of $[Fe_6Q_8(PR_3)_6]^{n+}$ (Q = S, Se, Te; R = methyl, ethyl; n = 0 - 4) compounds is also fairly large. [89,90,91] $[Fe_6S_8(PEt_3)_6]^{2+}$ is isostructural to $Co_6S_8(PPh_3)_6$ with similar core dimensions (4.5 Å across faces and 7.5 Å down the body diagonal), but smaller overall dimensions due to the smaller phosphine

ligands (10 - 12 Å). The $[Fe_6S_8(PEt_3)_6]^{2+}$ cluster was successfully used as a pillaring agent for TaS_2 but little was reported beyond the structural characterization of the material.[81,92] The encapsulation of this cluster will be discussed in Chapter 3.

$[Ni_9S_9(PEt_3)_6]^{2+}$. Polynuclear nickel chalcogenide species with the M_6Q_8 structure have not been observed; rather, a prismane structure is found in $Ni_6Se_5(PPh_3)_6$.[72,93] In general, nickel chalcogenide cluster chemistry seems to be dominated by the linkage of nickel trimers to form larger clusters. The $[Ni_9S_9(PEt_3)_6]^{2+}$ cluster is assembled from three Ni_3S_3 units (Figure 1.7a) stacked in alternating directions.[94] The coordination environment of the nickel atoms in the top and bottom trimers is completed by triethyl phosphine ligands (Figure 1.7b). The dimensions of the core are 6 Å perpendicular to and 6.8 Å parallel to the Ni_3S_3 planes. The overall dimensions of $[Ni_9S_9(PEt_3)_6]^{2+}$ range from 11.5 Å to 13 Å.

This cluster has not been used as a pillaring agent for any lamellar material. Ni supported MoS_2 and WS_2, however, are active HDS catalysts; hence, a nickel chalcogenide pillaring agent is desirable. The encapsulation of this cluster will be discussed in Chapter 3.

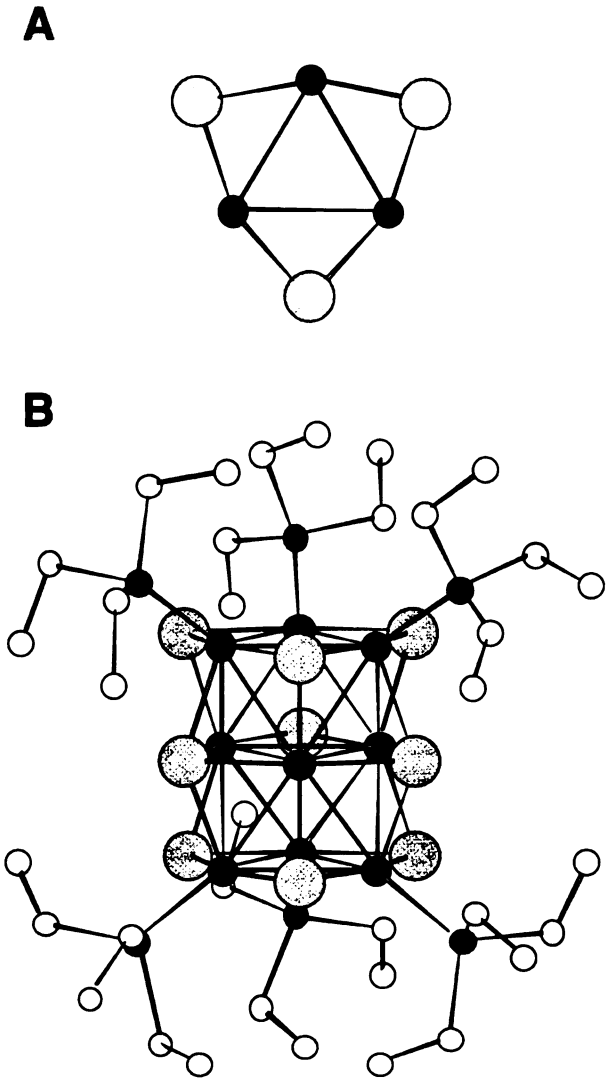

Figure 1.7. (A) Ni_3S_3 units (Ni = black circles, S = gray circles) which are stacked in a staggered fashion to form (B), the $[Ni_9S_9(PEt_3)_6]^{2+}$ cluster. The top and bottom trimers are ligated by triethyl phosphine (P = dark gray circles, C = open circles).

The insertion of metal sulfide and metal oxide clusters into the layered dichalcogenides is a step toward open framework sulfides. The hosts MoS_2 and WS_2 are particularly well suited for this task due to their remarkable ability to exfoliate in water, allowing the encapsulation of large guest molecules between the layers. The clusters $[Al_{13}O_4(OH)_{24}(H_2O)_{12}]^{7+}$ (Chapter 2); $Co_6S_8(PPh_3)_6$, $[Fe_6S_8(PEt_3)_6]^{2+}$, and $[Ni_9S_9(PEt_3)_6]^{2+}$ (Chapter 3) have been incorporated and characterized. The structure of the layered hosts MoS_2 and WS_2 has been solved by electron crystallography (Chapter 4), and studies regarding the oxidation state of the layers have been conducted (Chapter 5).

References

1. a) Fukushima, Y.; Okada, A.; Kawasumi, M.; Kurachi, T.; Kamigaito, O. *Clay Minerals,* 1988, **23**, 27. b) Okada, A.; Kawakado, M. *Japanese Patent Application* 1985, No. SHO 60-217396.

2. Schöllhorn, R. *Comments Inorg. Chem.,* 1983, **2**, 271.

3. Whittingham, M.S. *Prog. Solid St. Chem.,* 1978, **12**, 41.

4. Murphy, D.W.; DiSalvo, F.J.; Hull, G.W., Jr.; Waszczak, J.V.; Mayer, S.F.; Steward, G.R.; Early, S.; Acrivos, J.V.; Geballe, T.H. *J. Chem. Phys.,* 1975, **62**, 967.

5. a) Dines, M.B. *Mater. Res. Bull.,* 1975, **10**, 287. b) Murphy, D.W.; DiSalvo, F.J.; Hull, G.W., Jr., Waszczak, J.V. *Inorg. Chem.,* 1976, **15**, 17. c) Hung, P. L.-K.; Sundararajan, G.; San Filippo, J., Jr. *Organometallics,* 1982, **1**, 957.

6. Barrer, R.M.; MacLeod, D.M. *Trans. Faraday Soc.,* 1955, **51**, 1290.

7. a) Johnson, J.W.; Jacobson, A.J.; Butler, W.M.; Rosenthal, S.E.; Brody, J.F.; Lewandowski, J.T. *J. Am. Chem. Soc.,* 1989, **111**, 381. b) Gendraud, P.; de Roy, M.E.; Besse, J.P. *J. Solid State Chem.,* 1993, **106**, 577.

8. a) Bouhaouss, A.; Aldebert, P.; *Mater. Res. Bull.,* 1983, **18**, 1247. b) Aldebert, P.; Baffier, N.; Gharbi, N.; Livage, J. *Mater. Res. Bull.,* 1981, **16**, 949.

9. O'Hare, D. *New J. Chem.,* 1994, **18**, 989.

10. Rouxel, J. *Comprehensive Supramolecular Chemistry,Vol. 7.,* Alberti, G.; Bein, T., Eds. Pergamon Press, New York, 1996, 77-105.

11. a) Fredenhagen, K.; Cadenbach, G. *Z. Anorg. Allg. Chem.,*1926, **158**, 249. b) Schafhäutl, C. *J. Prakt. Chem.,* 1840, **3**, 129.

12. a) Li, L.; Ma, S.; Liu, X.; Yue, Y.; Hui, J.; Xu, R.; Bao, Y.; Rocha, J. *Chem. Mater.,* 1996, **8**, 204. b) Drezdzon, M.A.; *Inorg. Chem.,* 1988, **27**, 4628.

13. Clearfield, A. *Prog. Inorg. Chem.,* 1998, **47**,371.

14. a) Choy, J.-H.; Park, N.-G.; Kin, Y.-I.; Hwang, S.-H.; Lee, J.-S.; Yoo, H.-I. *J. Phys. Chem.,* 1995, **99**, 7845. b) Choy, J.-H.; Park, N-G.; Hwang, S.-J.; Kim, D.-H. *J. Am. Chem. Soc.,* 1994, **116**, 11564.

15. a) Kanatzidis, M.G.; Marcy, H.O.; McCarthy, W.J.; Kannewurf, C.R.; Marks, T.J. *Solid State Ionics,* 1989, **32/33**, 594. b) Bissessur, R.; DeGroot, D.C.; Schindler, J.L.; Kannewurf, C.R.; Kanatidis, M.G. *J. Chem. Soc., Chem. Commun.,* 1993, 687.

16. a) Wang, L.; Schindler, J.; Kannewurf, C.R.; Kanatzidis, M.G. *J. Mater. Chem.,* 1997, **7**, 1277. b) Liu, Y.-J.; Schindler, J.L.; DeGroot, D.C.; Kannewurf, C.R.; Hirpo, W.; Kanatzidis, M.G. *Chem. Mater.,* 1996, **8**, 525.

17. Sherry, H.S., *Ion Exchange,* **2**, J. A. Marinsky, Ed., Marcel Dekker, New York, 1969.

18. a) Pinnavaia, T.J. *Science,* 1983, **220**, 365. b) Figueras, F. *Catal. Rev. -Sci. Eng.,* 1988, **30**, 457.

19. Walker, G.F.; Garret, W.G. *Science,* 1967, **156**, 385.

20. a) Barrer, R.M. *Hydrothermal Chemistry of Zeolites,* Academic Press, New York, 1972. b) Breck, D.W. *Zeolite Molecular Sieves,* Wiley, New York, 1984.

21. a) Davis, M.E. *Acc. Chem. Res.,* 1993, **26**, 111. b) Bu, X.; Feng, P.; Stucky, G.D. *Science,* 1997, **278**, 2080.

22. a) Vaughan, D.E.W., *Chem. Eng. Prog.,* 1988, 25. b) Chen, N.Y.; Garwood, W.E.; Dwyer, F.G. *Shape Selective Catalysis in Industrial Applications,* Marcel Dekker, New York, 1989.

23. Kresge, C.T.; Leonowicz, M.E.; Roth, W.J.; Vartuli, J.C.; Beck, J.S. *Nature*, 1992, **359**, 710.

24. Mortland, M.M.; Berkheiser, V.E. *Clays Clay Miner.,* 1976, **24**, 60.

25. a) Knudson, M.I.; McAtee, J.L. *Clays Clay Miner.,* 1973, **21**, 19. b) Pinnavaia, T.J. *Clays Clay Miner.,* 1978, **26**, 319.

26. Johnson, I.D.; Werpy, T.A.; Pinnavaia, T.J. *J. Am. Chem. Soc.,* 1988, **110**, 8545.

27. Bowes, C.L.; Ozin, G.A. *Adv. Mater.,* 1996, **8**, 13.

28. Bedard, B.L.; Wilson, s.T.; Vail, L.D.; Bennet, J.M.; Flanigen, E.M. *Zeolites, Facts, Figures, Future.* Jacobs, P.A.; van Santen, R.A.; Eds. Elsevier Science Publishers B., Amsterdam, the Netherlands, 1989, 375.

29. Jiang, T.; Lough, A.; Ozin, G.A.; Bedard, R.L. *J. Mater. Chem.,* 1998, **8**, 733.

30. a) Ahari, H.; Ozin, G.A.; Bedard, R.L.; Petrov, S.; Young, D. *Adv. Mater.,* 1995, **7**, 370. b) Ahari, H.; Bowes, C.L.; Jiang, T.; Lough, A.; G.A. Ozin, Bedard, R.L.; Petrov, S.; Young, D. *Adv. Mater.,* 1995, **7**, 375.

31. Jiang, T.; Lough, A.; Ozin, G.A.; Bedard, R.L.; Broach, R. *J. Mater. Chem.,* 1998, **8**, 721.

32. Bowes, C.L.; Petrov, s.; Vovk, G.; Young, D.; Ozin, G.A.; Bedard, R.L. *J. Mater. Chem.,* 1998, **8**, 711.

33. a) Sheldrick, W.S.; Braunbeck, H.-G. *Z. Naturforsch,* 1990, **45b**, 1643. b) Marking, G.A.; Kanatzidis, M.G. *Chem. Mater.,* 1995, **7**, 1915.

34. a) Yaghi, O.M.; Sun, Z.; Richardson, D.A.; Groy, T.L. *J. Am. Chem. Soc.,* 1994, **116**, 807. b) Tan, K.; Darovsky, A.; Parise, J.B. *J. Am. Chem. Soc.,* 1995, **117**, 7039. c) Ahari, H.; Garcia, A.; Kirkby, S.; Ozin, G.A.; Young, D.; Lough, A.J. *J. Chem. Soc., Dalton Trans.,* 1998, 2023.

35. a) Parise, J.B. *Science,* 1991, **251**, 293. b) Hanko, J.A.; Kanatzidis, M.G. *Angew. Chem. Int. Ed.,* 1998, **37**, 342. c) Stephan, H.-O.; Kanatzidis, M.G. *J. Am. Chem. Soc.,* 1996, **118**, 12226.

36. a) McCarthy, T.J.; Tanzer, T.A.; Kanatzidis, M.G. *J. Am. Chem. Soc.,* 1995, **117**, 1294. b) Dhingra, S.; Kanatzidis, M.G. *Science,* 1992, **258**, 1769.

37. Li, H.; Laine, A.; O'Keefe, M.; Yaghi, O.M. *Science,* 1999, **283**, 1145.

38. a) Wachhold, M.; Rangan, K.K.; Billinge, S.J.L.; Petkov, V.; Heising, J.; Kanatzidis, M.G. submitted for publication. b) MacLachlan, M.J.; Coombs, N.; Ozin, G.A. *Nature,* 1999, **397**, 681.

39. Dines, M.D.; DiGiacomo, P.M.; Callahan, K.P.; Griffith, P.C.; Lane, R.H.; Cooksey, R.E. *Chemically Modified Surfaces in Catalysis and Electrocatalysis,* Miller, J.S., Ed., *Amer. Chem. Soc. Symp. Ser.* , 1982, **192**, Washington, D.C., Chapter 12.

40. Chatakondu, K.; Green, M.L.H.; Qin, J.; Thompson, M.E.; Wiseman, P.J. *J. Chem. Soc., Chem. Commun.,* 1988, 223.

41. Gamble, F.R.; DiSalvo, F.J.; Klemm, R.A.; Geballe, T.H. *Science,* 1970, **168**, 568.

42. Preobazhensky, V.B.; Zhernova, A.Ja.; Babichev, A.P.; Kobrin, I.K. *Solid State Commun.,* 1978, **27**, 127.

43. a) Dines, M. B. *Science,* 1975, **188**, 1210. b) Clement, R.P.; Davies, W.B.; Ford, K.A.; Green, M.L.H.; Jacobson, A.J. *Inorg. Chem.,* 1978, **17**, 2754.

44. a) O'Hare, D.; Jaegermann, W.; Williamson, D.L.; Ohuchi, F.S.; Parkinson, B.A. *Inorg. Chem.,* 1988, **27**, 1537. b) Formstone, C.A.; FitzGerald, E.T.; O'Hare, D.; Cox, P.A.; Kurmoo, M.; Hodby, J.W.; Lillicrap, D.; Goss-Custard, M. *J. Chem. Soc., Chem. Commun.,* 1990, 501.

45. a) Dickinson, R.G.; Pauling, L. *J. Am. Chem. Soc.,* 1923, **45**, 1466. b) Bronsema, K.D.; de Boer, J.L.; Jellinek, F. *Z. Anorg. Allg. Chem.,* 1986, **540/541**, 15.

46. a) Wildervanck, J.C.; Jellinek, F. *Z. Anorg. Allg. Chem.,* 1964, **328**, 309. b) Glemser, O.; Sauer, H.; König, P. *Z. Anorg. Chem.,* 1948, **257**, 241. c) van Arkel, A.E., *Rec. Trav., Chim., Pays-Bas,* 1925, **45**, 437. d) Ehrlich, P.; *Z. Anorg. Chem.,* 1948, **257**, 247.

47. Py, M.A.; Haering, R. R. *Can. J. Phys.,* 1983, **61**, 76.

48. Chianelli, R.R.; Scanlon, J.C.; Thompson, A.H. *Mater. Res. Bull.*, 1975, **10**, 1379.

49. Fleischauer, P.D. *Thin Solid Films,* 1987, **154**, 309.

50. a) Chianelli, R.R.; Ruppert, A.F.; José-Yacamán, M.; Vázquez-Zavala, A. *Catal. Today.*, 1995, **23**, 269. b) Topsøe, H.; Clausen, B.S. *Catal. Rev. -Sci. Eng.*, 1984, **26**, 395. c) Weisser, O.; Landa, S. *Sulfided Catalysts, their Properties and Applications.* Pergamon Press, New York, 1973.

51. Bockrath, B.C.; Parfitt, D.S. *Catal. Lett.*, 1995, **33**, 201.

52. Miremadi, B.K.; Morrison, S.R. *J. Catal.*, 1987, **103**, 334.

53. a) Mulhern, P.J. *Can. J. Phys.*, 1989, **67**, 1049. b) Julien, C. *Microionics: Solid State Integrable Batteries.* Balkanski, M., Ed. Elsevier Science, 1991, New York, 309.

54. Joensen, P.; Frindt, R.F..; Morrison, S.R. *Mater. Res. Bull.*, 1986, **21**, 547.

55. a) Divigalpitiya, W.M.R.; Frindt, R.F.; Morrison, S.R. *Science,* 1989, **246**, 369. b) Zhou, X.; Yang, D.; Frindt, R.F. *J. Phys. Chem. Solids,* 1996, **57**, 1137. c) Kosidowski, L.; Powell, A.V. *Chem. Commun.*, 1998, 2201.

56. a) Divigalpitiya, W.M.R.; Frindt, R.F.; Morrison, S.R. *J. Mater. Res.*, 1991, **6**, 1103. b) Ruiz-Hitzky, E.; Jimenes, R.; Casal, B.; Manriquez, v.; Santa Ana, A.; Gonzalez, G. *Adv. Mater.*, 1993, **5**, 738. c) Kanatzidis, M.G.; Bissessur, R.; DeGroot, D.C.; Schindler, J.L.; Kannewurf, C.R. *Chem. Mater.*, 1993, **5**, 595. d) Bissessur, R.; Kanatzidis, M.G.; Schindler, J.L.; Kannewurf, C.R. *J. Chem. Soc., Chem. Commun.*, 1993, 1582. e) Lemmon, J.P.; Lerner, M.M. *Chem. Mater.*, 1994, **6**, 207. f) Wang, L.; Schindler, J.; Thomas, J.A.; Kannewurf, C.R.; Kanatzidis, M.G. *Chem. Mater.*, 1995, **7**, 1753. g) Oriakhi, C.O.; Nafshun, R.L.; Lerner, M.M. *Mater. Res. Bull.*, 1996, **31**, 1513.

57. Tagaya, H.; Hashimoto, T.; Karasu, M.; Izumi, T.; Chiba, K. *Chem. Lett.*, 1991, 2113.

58. Divigalpitiya, W.M.R.; Frindt, R.F.; Morrison, S.R. *Mater. Res. Symp. Proc.,* 1992, Boston.

59. a) Yang, D.; Frindt, R.F. *J. Phys. Chem. Solids,* 1996, **57**, 1113. b) Tsai, H.-L.; Heising, J.; Schindler, J.L.; Kannewurf, C.R.; Kanatzidis, M.G. *Chem. Mater.,* 1997, **9**, 879.

60. a) Wang, L. Ph.D. Dissertation, Michigan State University, 1999. b) Tsai, H.-L.; Kanatzidis, M.G., to be published.

61. a) Danot, M.; Manson, J.L.; Golub, A.S.; Protzenko, G.A.; Fabritchnyi, P.B.; Novikov, Yu.N.; Rouxel, J. *Mater. Res. Bull.,* 1994, **29**, 833. b) Golub, A.S.; Payen, c.; Protzenko, G.A.; Novikov, Yu.N.; Danot, M. *Solid State Commun.,* 1997, **102**, 419. c) Gash, AE.; Spain, A.L.; Dysleski, L.M.; Flaschenreim, C.J.; Kalaveshi, A.; Dorhout, P.K.; Strauss, S.H. *Environ. Sci. Tech.,* 198, **32**, 1007. d) Golub, A.S.; Shumilova, I.B.; Zubavichus, Y.V.; Jahncke, M.; Süss-Fink, G.; Danot, M.; Novikov, Y.N. *J. Mater. Chem.,* 1997, **7**, 163. e) Gee, M.A.; Frindt, R.F.; Joensen, P.; Morrison, S.R. *Mater. Res. Bull.,* 1986, **21**, 543.

62. Golub, A.S.; Protsenko, G.A.; Bumileva, L.V.; Buyanovskaya, A.G.; Novikov, Yu.N. *Russ. Chem. bull.,* 1993, **42**, 632.

63. Golub, A.S.; Shumilova, I.B.; Novikov, Yu.N.; Mansot, J.L.; Danot, M. *Solid State Ionics,* 1996, **91**, 307.

64. Nakagaki, S.; Mangrich, A.S.; Wypych, F. *Inorg. Chim. Acta,* 1997, **254**, 213.

65. Taguchi, Y.; Kimura, R.; Azumi, R.; Tachibana, H.; Koshizaki, N.; Shimomura, M.; Momozawa, N.; Sakai, H.; Abe, M.; Matsumoto, M. *Langmuir,* 1998, **14**, 6550.

66. Ollivier, P.J.; Kovtyukhova, N.I.; Keller, S.W.; Mallouk, T.E. *Chem. Commun.,* 1998, 1563.

67. Yang, D.; Sandoval, S.J.; Divigalpitiya, W.M.R.; Irwin, J.C.; Frindt, R.F. *Phys. Rev. B.,* 1991, **43**, 12053.

68. Qin, X.R.; Yang, R.; Frindt, R.F.; Irwin, J.C. *Ultramicroscopy,* 1992, **42-44**, 630.

69. a) Wypych, F.; Schöllhorn, R. *J. Chem. Soc., Chem. Commun.*, 1992, 1386. b) Wypych, F.; Weber, Th.; Prins, R. *Chem. Mater.*, 1998, **10**, 723.

70. a) Wilson, J.A.; DiSalvo, F.J.; Mahajan, s. *Adv. Phys.*, 1975, **10**, 1379. b) Wilson, J.A.; DiSalvo, F.J.; Mahajan, S. *Phys. Rev. Lett.*, 1974, **32**, 882.

71. Dance, I.; Fisher, K. *Prog. Inorg. Chem.*, 1994, **41**, 637.

72. Fenske, D.; Ohmer, J.; Hachgenei, J.; Merzweiler, K. *Angew. Chem. Int. Ed. Engl.*, 1988, **27**, 1277.

73. a) Pope, M.T. *Heteropoly and Isopoly Oxometallates.* Springer-Verlag, New York, New York, 1983. b) Fleming, P.B.; Mueller, L.A.; McCarley, B.E. *Inorg. Chem.*, 1967, **6**, 1. c) Koknat, F.W.; Adaway, T.J.; Erzerum, S.I.; Syet, S. *Inorg. Nucl. Chem. Lett.*, 1980, **16**, 307.

74. Cotton, F.A.; Wilkinson, G. *Advanced Inorganic Chemistry, 5th Ed.* John Wiley and Sons, New York, 1988, 215-217; 813-819.

75. a) Kohlschütter, H.W.; Hantelmann, P. *Z. Anorg. All. Chem.*, 1941, **248**, 319. b) Broset, C.; Biedermann, G.; Sillén, L.G. *Acta. Chem. Scand.*, 1954, **8**, 1917.

76. a) Johansson, G.; Lundgren, G.; Sillén, L.G.; Soderquist, R. *Acta. Chem. Scand.*, 1960, **14**, 769. b) Johansson, G. *Acta. Chem. Scand.*, 1960, **14**, 771. c) Tsai, P.P.; Hsu, P.H. *Soil Sci. Soc. Am. J.*, 1985, **49**, 1060.

77. a) Brindley, G.W.; Sempels, R.E. *Clay Miner.*, 1977, **12**, 229. b) Lahav, N.; Shani, U.; Shabtai, J. *Clays Clay Miner.*, 1978, **26**, 107. c) Singh, S.S.; Kodama, H. *Clays Clay Miner.*, 1988, **36**, 397. d) Schoonheydt, R.A.; van den Eynde, J.; Tubbax, H.; Leeman, H.; Stuyckens, M.; Lenotte, I.; Stone, W.E.E. *Clays Clay Miner.*, 1993, **41**, 598. e) Coelho, A.V.; Poncelet, G. *Appl. Catal.*, 1991, **77**, 303. f) Bukka, K.; Miller, J.D.; Shabtai, J. *Clays Clay Miner.*, 1992, **40**, 92. g) Malla, P.B.; Komarneni, S. *Clays Clay Miner.*, 1993, **41**, 472.

78. a) Vaughan, D.W. E.; Lussier, R.J.; Magee, J.S. U.S. Patent 4,176,090 (1979). b) Vaughan, D.W. E.; Lussier, R.J.; Magee, J.S. U.S. Patent 4,271,043 (1981). c) Shabtai, J.; U.S. Patent 4,238,364 (1980).

79. a) Bottero, J.Y.; Cases, J.M.; Flessinger,F.; Poirier, J.E. *J. Phys. Chem.*, 1980, **84**, 2933. b) Akitt, J.W.; Farthing, A.; *J. Chem. Soc., Dalton Trans.*, 1981, 1617. c) Plee, D.; Borg, F.; Gatineau, L.; Fripiat, J.J. *J. Am. Chem. Soc.*, 1985, **107**, 2362.

80. a) Lerf, A.; Lalik, E.; Kolodziejski, W.; Klinowski, J. *J. Phys. Chem.*, 1992, **96**, 7389. b) Nazar, L.F.; Liblong, W.S.; Yin, X.T. *J. Am. Chem. Soc.*, 1991, **113**, 5889. c) Nazar, L.F.; Yin, X.T.; Zinkweg, D.; Zhang, Z.; Liblong, S. *Mat. Res. Soc. Symp. Proc.*, 1991, **210**, 417.

81. Nazar, L.F.; Jacobson, A.J. *J. Mater. Chem.*, 1994, **4**, 149.

82. Mori, M.; Isobe, T.; Senna, M. *Solid State Ionics*, 1995, **81**, 157.

83. a) Hong, M.; Huang, Z.; Lei, X.; Wei, G.; Kang, B.; Liu, H. *Inorg. Chim. Acta*, 1989, **159**, 1. b) Jiang, F.; Huang, X.; Cao, R.; Hong, M.; Liu, H. *Acta Cryst. C.*, 1995, 1275. c) Hong, M.; Huang, Z.; Lei, X.; Wei, G.; Kang, B.; Liu, H. *Polyhedron*, 1991, **10**, 927.

84. a) Stuczynski, S.M.; Kwon, Y.-U.; Steigerwald, M.L. *J. Organomet. Chem.*, 1993, **449**, 167. b) Steigerwald, M.L.; Siegrist, T.; Stuczynski, S.M. *Inorg. Chem.*, 1991, **30**, 2256. c) Cecconi, F.; Ghilardi, C.A.; Midollini, S.; Orlandini, A.; Bencini, A. *J. Chem. Soc., Dalton Trans.*, 1996, 3991. d) Cecconi, F.; Ghilardi, C.A.; Midollini, S.; Orlandini, A. *Inorg. Chim. Acta*, 1983, **76**, L183. e) Cecconi, F.; Ghilardi, C.A.; Midollini, S.; Orlandini, A.; Zanello, P. *Polyhedron*, 1986, **5**, 2021.

85. Delmon, B. *Prepr. Am. Chem. Soc. Div. Pet. Chem.*, 1977, **22**, 503.

86. a) Chevrel, R.; Sergent, M.; Prigent, J. *J. Solid State Chem.*, 1971, **3**, 515. b) Chevrel, R.; Hirrien, M.; Sergent, M. *Polyhedron*, 1986, **5**, 87. c) McCarty, K.F.; Anderegg, J.W.; Schrader, G.L. *J. Catal.*, 1985, **93**, 375.

87. a) Bissessur, R.; Heising, J.; Hirpo, W.; Kanatzidis, M.G. *Chem. Mater.*, 1996, **8**, 318. b) Bissessur, R. "Synthesis and Characterization

of Novel Intercalation Compounds of Molybdenum Trioxide and Molybdenum Disulfide." Ph.D. Dissertation, Michigan State University, 1994.

88. a) Holm, R.H. *Chem. Soc. Rev.*, 1981, **10**, 455. b) Coucouvanis, D. *Acct. Chem. Res.*, 1981, **14**, 201.

89. Steigerwald, M.L.; Siegrist, T.; Gyorgy, E.M.; Hessen, B.; Kwon, Y.-U., Tanzler, S.M. *Inorg. Chem.*, 1994, **33**, 3389.

90. a) Cecconi, F.; Ghilardi, C.A.; Midollini, S.; Orlandini, A. *Inorg. Chim. Acta,* 1997, **254**, 387. b) Agresti, A.; Bacci, M.; Cecconi, F.; Ghilardi, C.A.; Midollini, S. *Inorg. Chem.*, 1985, **24**, 689. c) Cecooni, F.; Ghilardi, C.A.; Midollini, S.; Orlandini, A.; Zanello, P. *J. Chem. Soc., Dalton Trans.*, 1987, 831. d) Cecooni, F.; Ghilardi, C.A.; Midollini, S. *J. Chem. Soc., Chem. Commun.*, 1981, 640.

91. Goddard, C.A.; Long, J.R.; Holm, R.H. *Inorg. Chem.*, 1996, **35**, 4347.

92. Nazar, L.F.; Jacobson, A.J. *J.Chem. Soc., Chem. Commun.*, 1986, 570.

93. Fenske, D.; Ohmer, J. *Angew. Chem. Int. Ed. Engl.*, 1987, **26**, 148.

94. a) Cecconi, F.; Ghilardi, C.A.; Midollini, S. *Inorg. Chem.*, 1983, **22**, 3802. b) Ghilardi, C.A.; Midollini, S.; Sacconi, L. *J. Chem. Soc., Chem. Commun.*, 1981, 47.

CHAPTER 2

Encapsulation and Rietveld Structural Characterization of the $[Al_{13}O_4(OH)_{24}(H_2O)_{12}]^{7+}$ cluster into MoS_2 and WS_2.

2.0 Abstract

The synthesis of $[Al_{13}O_4(OH)_{24}(H_2O)_{12}]_xMS_2$ (x=0.02-0.05, M=Mo, x=0.02-0.055, M=W) was accomplished by a precipitative encapsulation technique using single layers of MS_2. The products were characterized by powder X-ray diffraction, energy dispersive spectroscopy (EDS), thermogravimetric analysis (TGA), ^{27}Al Magic Angle Spinning Nuclear Magnetic Resonance (MAS-NMR), High Resolution Transmission Electron Microscopy (HRTEM), room temperature electrical conductivity measurements, and surface area measurements. Powder X-ray diffraction patterns show an expansion of approximately 9.9Å. ^{27}Al MAS-NMR indicates that the cluster is intact between the MS_2 layers. One-dimensional electron density mapping and Rietveld refinement performed on the powder diffraction data shows that the cluster is oriented with its C_3 symmetry axis perpendicular to the layers. The samples exhibit conductivity values from 3-14 S/cm. TGA shows that the layers remain expanded to 100°C, and partially expanded to 300°C. Surface area measurements suggest that the space between the clusters is not accessible.

2.1 Introduction

Since Barrer and MacLeod reported the first pillared species in 1955[1], much effort has gone into the development of microporous materials for use as size selective molecular sieves and as catalysts. Zeolites and pillared clays have been studied extensively for these applications[2,3]; however, these materials are insulators. Because WS_2 and MoS_2 have interesting electronic and optical properties, pillared WS_2 and MoS_2 may be useful for unique applications similar to but distinct from the applications for zeolites and pillared clays. The availability and relatively low cost of MoS_2 make it an especially desirable chalcogenide host.

The practical applications of MoS_2 itself are quite diverse. These include use as a solid lubricant[4], a catalyst[5], and as a host material for solid state batteries.[6] MoS_2 has been intercalated with a variety of compounds which include polymers[7,8], small organic molecules[9], and inorganic complexes such as ferrocene[10] and the cobalt clusters $Co_6Q_8(PR_3)_6$ (Q=S, Se, Te; R=alkyl)[11]. WS_2 is isostructural to MoS_2, with similar intercalation chemistry, although less well explored.[12]

Despite the considerable intercalation history of layered dichalcogenides, microporous pillared chalcogenides have not been reported to date. The intercalation of TaS_2 with $[Al_{13}O_4(OH)_{24}(H_2O)_{12}]^{7+}$ and the iron cluster $[Fe_6S_8(PEt_3)_6]^{2+}$ has been achieved, but no information about the

porosity of these materials is reported.[13] Intercalation of the $Co_6S_8(PPh_3)_6$ clusters into MoS_2 increase the surface area three or fourfold, but TEM studies show that the lamellar expansion due to the clusters is localized.[14] We have chosen to explore $[Al_{13}O_4(OH)_{24}(H_2O)_{12}]^{7+}$ as a pillaring agent for MoS_2 because of its successful history as a pillaring agent for clays[3,15] and because alumina-supported MoS_2 is used as a catalyst for hydrodesulfurization.[5]

2.2 Experimental

2.2.1 Synthesis

MoS_2 was purchased from Cerac and WS_2 from Alfa Aesar. $LiBH_4$, n-Butyl lithium, hexane, and $AlCl_3$ were purchased from Aldrich. $BaCl_2 \cdot 2H_2O$, $Na_2SO_4 \cdot 10H_2O$, and NaOH were purchased from J.T. Baker. All compounds were used as received except hexane, which was dried over CaH_2 (Aldrich).

$LiMS_2$[16]. $LiMoS_2$ was prepared by a) stirring 2H-MoS_2 in threefold excess of n-butyl lithium in dry hexane for 2 days or b) heating with $LiBH_4$ at 300°C for 2 days. $LiWS_2$ was prepared by the latter method at 350°C.

MS_2 aqueous suspension. $LiMS_2$ was exfoliated[17] in deionized, deoxygenated H_2O via a redox reaction, generating single layers, lithium hydroxide, and hydrogen gas.

$$LiMS_2(s) + H_2O(l) \text{ ---> } MS_{2\ (\text{single layers})} + LiOH(aq) + 0.5H_2\ (g) \quad \text{Eq. (2.1)}$$

Eq. 2.1 has been proposed for the exfoliation of MS_2 by Divigalpitiya et al.[9] The exfoliated suspension (pH>12) was centrifuged for 0.5 hr and rinsed with deionized, deoxygenated H_2O three times in order to reduce the pH of the solution to about 7 (pH ~12, pH ~9, and pH ~7 after each rinse). The product was then re-suspended in H_2O and stirred 0.5 hr prior to use.

$[Al_{13}O_4(OH)_{24}(H_2O)_{12}]Cl_7$ solution.[18] The $[Al_{13}O_4(OH)_{24}(H_2O)_{12}]^{7+}$ was prepared by the slow addition of 500 ml of NaOH (0.24M) to 500 ml of an aqueous $AlCl_3$ solution (0.1M) at 80°C with stirring. It was then crystallized as the sulfate salt $Na[Al_{13}O_4(OH)_{24}(H_2O)_{12}](SO_4)_2$ in order to isolate it from any other soluble Al-containing species. It was then redissolved by stirring in excess $BaCl_2$ solution, and the $BaSO_4$ precipitate removed by filtration. This method results in excess Ba^{2+} ions also present in the solution.

$[Al_{13}O_4(OH)_{24}(H_2O)_{12}]_xMS_2$. The aqueous MS_2 suspension was added to various amounts of a 0.03M solution (approximately) of $[Al_{13}O_4(OH)_{24}(H_2O)_{12}]Cl_7$ in H_2O.[19] After stirring for several hours the product was isolated via centrifuge, rinsed, and dried on a glass slide. The product was a shiny film which could be scraped off the glass and ground to a fine black powder.

2.2.2 Characterization

Powder X-ray diffraction patterns were recorded using a Rigaku-Denki/RW400F2 (Rotaflex) rotating anode X-ray diffractometer using Cu-$K\alpha$ radiation. HRTEM micrographs were acquired using a JEOL 4000EX II at Argonne National Laboratory, operating at 400kV. Energy Dispersive Spectroscopy (EDS) was used to determine the ratios of Al to Mo (or W) on a JEOL-JSM-6400V at an accelerating voltage of 20kV with samples mounted on non-aluminum stubs using carbon paint or carbon tape, equipped with a Tracor Northern 5500 X-ray microanalysis attachment. Solid state ^{27}Al MAS-NMR measurements were performed using a Varian 400MHz instrument tuned to 130.4 MHz pulse frequency, and at MAS frequencies of 4 and 6.2 MHz. Thermogravimetric measurements were obtained with a Shimadzu TG 50 instrument using oxygen or nitrogen flow and a heating rate of 5°C or 2°C/min. BET surface area measurements were performed on a Quantasorb Jr. Sorption System using ultra-pure nitrogen gas as the adsorbate and ultra-pure helium gas as the carrier. The surface areas of the samples were calculated using the BET equation.[20] Conductivity measurements of the materials at room temperature were obtained for a pressed pellet using the four prong probe and a Keithley 236 source measure unit.

2.3 Results and Discussion

2.3.1 Evidence of Cluster Encapsulation

The predominance of the *00l* reflections in the X-ray powder diffraction pattern indicate that the layers are well oriented, with a d-spacing of about 16 Å (see Figure 2.1). Restacked MoS_2 has a d-spacing of 6.2 Å, so the expansion of the layers is about 9.9 Å. This value is consistent with the dimensions of the cluster, which are about 10.2 Å along the C_3 symmetry axis, 12.8 Å along one C_2 symmetry axis and 11.5 Å along the other C_2 axis (average diameter 11.5 Å) (see orientations (A), (B), and (C), respectively, in Figure 2.2). Our observed expansion suggests that the cluster is oriented with its C_3 axis perpendicular to the layers.

Loadings of the cluster were calculated using Energy Dispersive Spectroscopy (EDS) to quantitate an Al:Mo (or Al:W) ratio. Conversion to oxides by heating to 650°C under a stream of O_2 prior to quantitation was necessary for MoS_2-containing samples because the X-ray emission lines (for EDS) of Mo and S overlap completely, hindering quantitative analysis. The observed values ranged from $[Al_{13}O_4(OH)_{24}(H_2O)_{12}]_{0.02}MoS_2$ to $[Al_{13}O_4(OH)_{24}(H_2O)_{12}]_{0.05}MoS_2$. The theoretical maximum loading of the

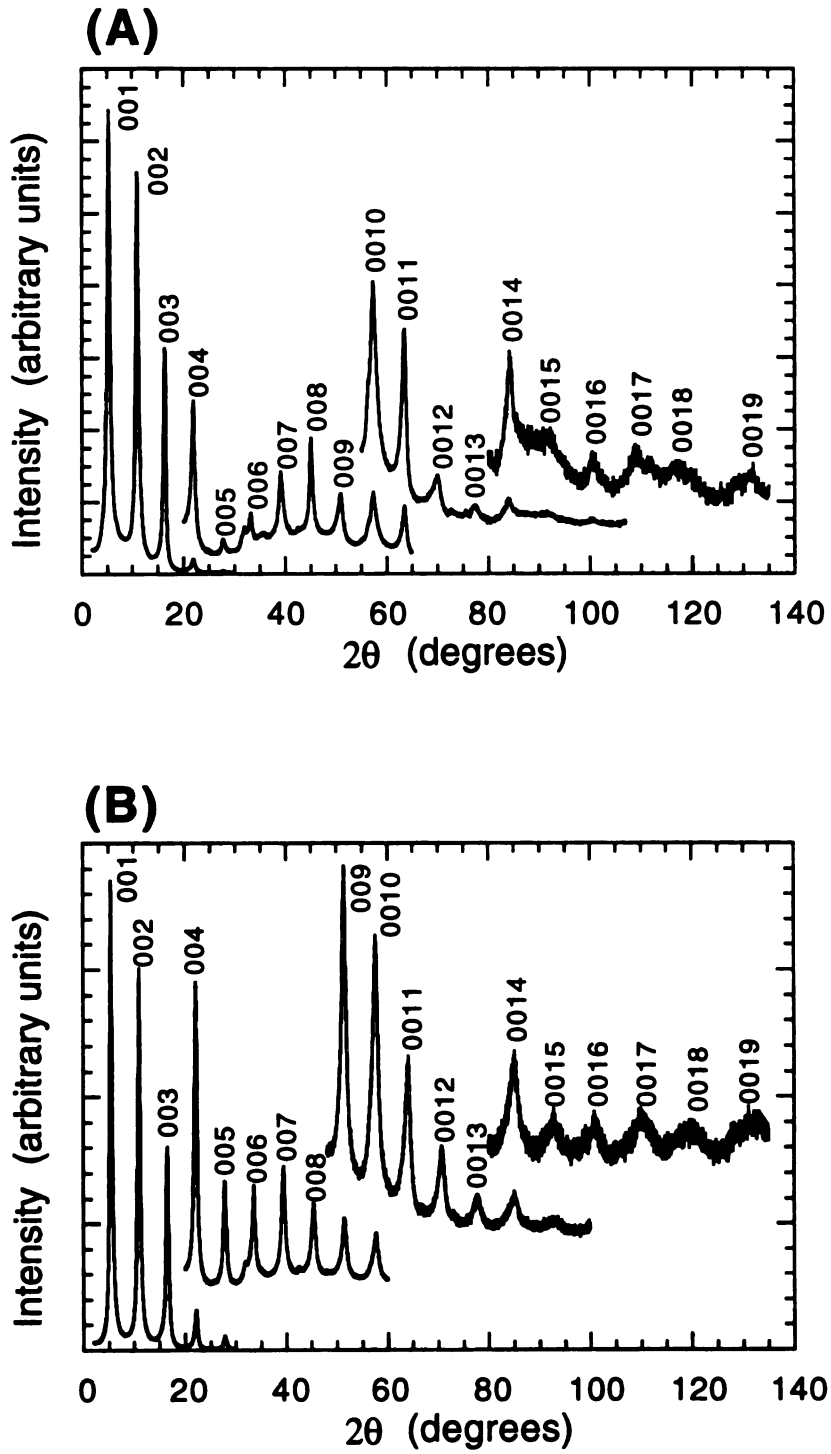

Figure 2.1. X-ray diffraction patterns of (A) $[Al_{13}O_4(OH)_{24}(H_2O)_{12}]_{0.05}MoS_2$ and (B) $[Al_{13}O_4(OH)_{24}(H_2O)_{12}]_{0.055}WS_2$ used for electron density maps and Rietveld refinements. Strong preferred orientation of the samples leads to the predominance of the *00l* reflections.

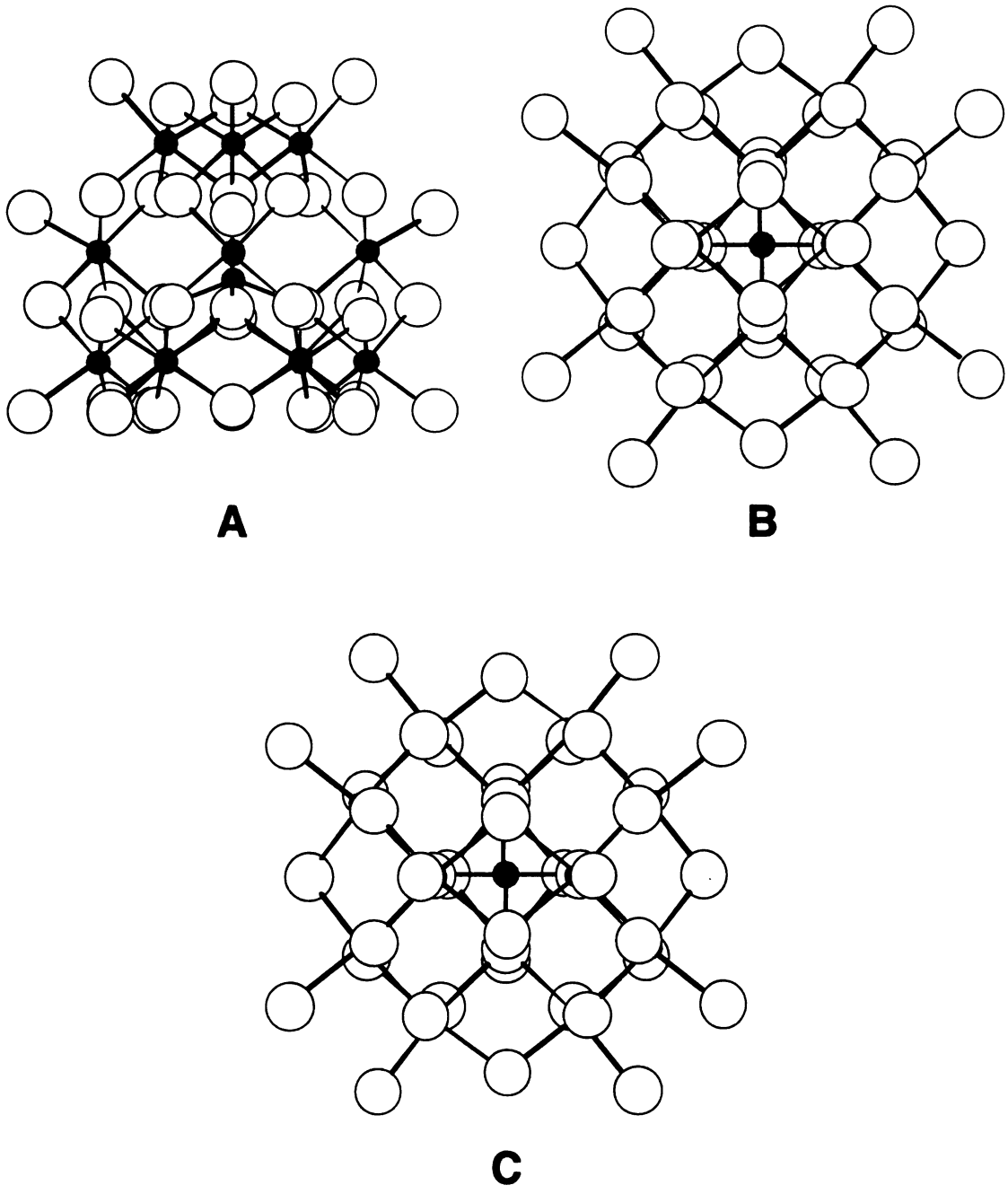

Figure 2.2. Three possible orientations of the $[Al_{13}O_4(OH)_{24}(H_2O)_{12}]^{7+}$ cluster between the layers. The gray circles represent Al atoms, open circles are O atoms. H atoms are omitted for clarity.

cluster (if one assumes hcp packing of the spheres) is $[Al_{13}O_4(OH)_{24}(H_2O)_{12}]_{0.06}MoS_2$. Conversion to oxide was not necessary for samples containing WS_2, and comparable stoichiometries (up to $[Al_{13}O_4(OH)_{24}(H_2O)_{12}]_{0.055}WS_2$) were observed by EDS. The stoichiometry of selected samples was confirmed by elemental analysis.

Lithiated and exfoliated MoS_2 was presumed to be neutral because it is possible to intercalate neutral molecules.[9] One surprising discovery was that no chloride is detected in the samples by EDS. It appears that this cation intercalates without its chloride anion. The strong intensity of reflections, the relatively high degree of order, and the ease of encapsulation of the cation seems to indicate that the MoS_2 and WS_2 have some negative charge. This would explain the driving force for the intercalation. We have observed intercalation of other cations without anions, consistent with a negative charge on the layers.[21] The observed loadings of the cluster, presuming no change in its charge, suggest that the negative charge on the layers is between 0.1 and 0.4. This wide range of possible negative charge suggests that the charge on the aluminum cluster may vary, depending on the loading. Another surprising result is that the excess Ba^{2+} ions found in solution with the cluster do not appear to be encapsulated. The layers appear to favor the soft $[Al_{13}O_4(OH)_{24}(H_2O)_{12}]^{7+}$ ion over the hard, electropositive Ba^{2+} ion. Studies to probe the ionicity of the layers in detail are described in Chapter 5.

MAS-NMR ^{27}Al spectra of several samples with various loadings of cluster exhibited a peak at about 64 ppm corresponding to the tetrahedral aluminum at the center of the cluster (Figure 2.3). This peak has been observed by others who have intercalated the cation into various hosts and is found in the sulfate salt of the unintercalated cluster.[10,15] The spectra also exhibit a broad peak centered around 0 ppm which can be attributed to octahedral aluminum. Intermediate coordination environments may contribute to the broad signal found between the two peaks in $[Al_{13}O_4(OH)_{24}(H_2O)_{12}]_{0.03}MoS_2$. This suggests that, although some of the cluster is clearly intact, there may be some decomposition products encapsulated as well.

An effort was made to image the encapsulated clusters, or at least the lamellar expansion, by HRTEM. HRTEM studies of thin sectioned $[Al_{13}O_4(OH)_{24}(H_2O)_{12}]^{7+}$-pillared clays revealed a lamellar expansion (the cluster, as it is comprised of light atoms, apparently does not scatter sufficiently to be directly visible); however, it was smaller than the expansion indicated by the powder X-ray diffraction patterns.[22] The authors attributed this to dehydration of the cluster in the high vacuum of the electron microscope. Rather than thin sectioning, $[Al_{13}O_4(OH)_{24}(H_2O)_{12}]_{0.03}MoS_2$ and $[Al_{13}O_4(OH)_{24}(H_2O)_{12}]_{0.03}WS_2$ were dusted on a carbon supported copper grid and images were acquired at the edges

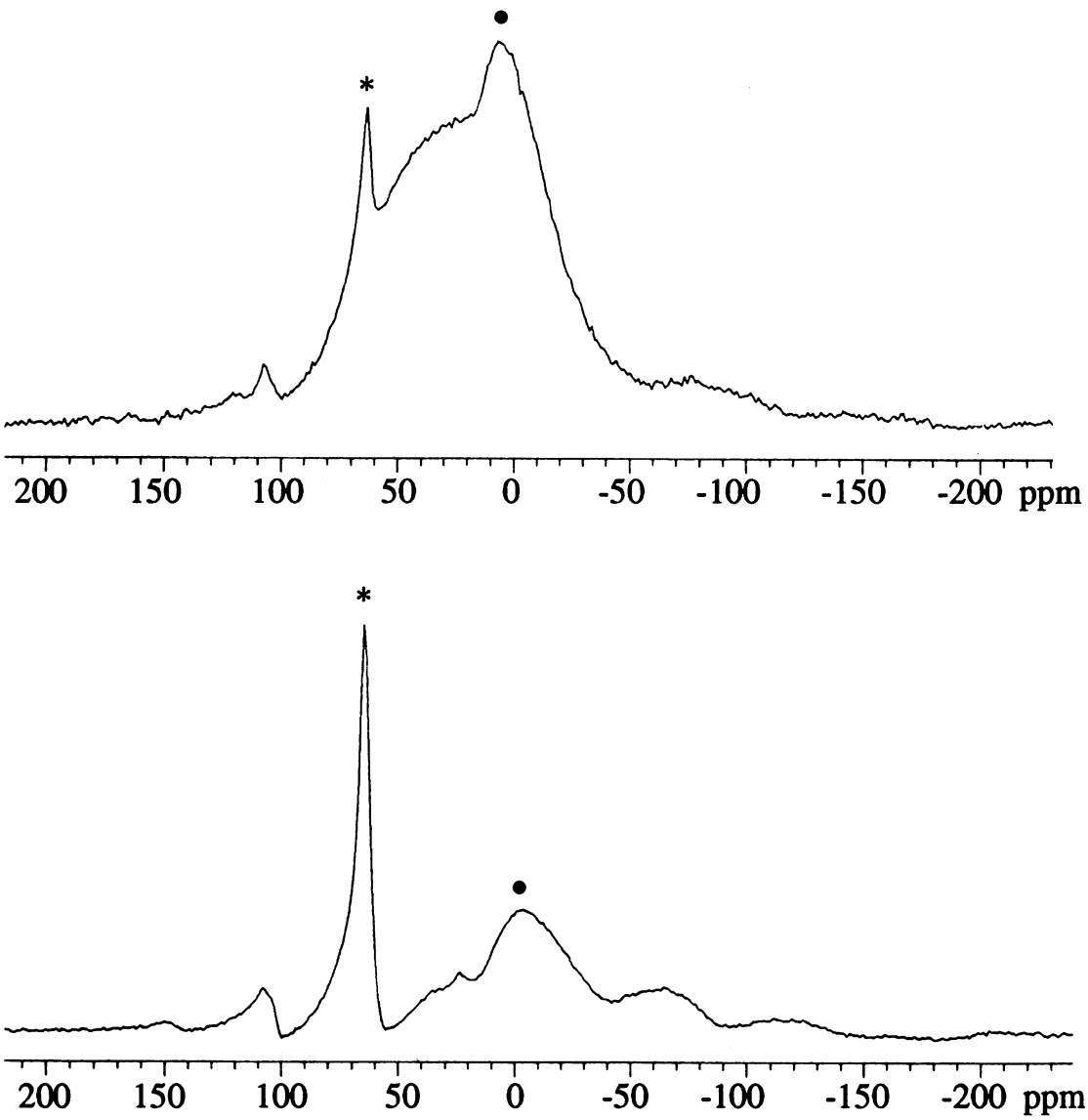

Figure 2.3. Solid State MAS-NMR ^{27}Al spectra of (A) $[Al_{13}O_4(OH)_{24}(H_2O)_{12}]_{0.03}MoS_2$ and (B) $Na[Al_{13}O_4(OH)_{24}(H_2O)_{12}](SO_4)_2$. The peak at 64 ppm (asterisk) is attributed to the tetrahedral Al^{3+} atom at the center of the cluster; the broad peak at 0 ppm (circle) is attributed to octahedral Al^{3+}.

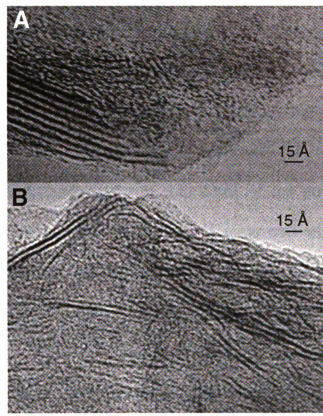

Figure 2.4. HRTEM Micrographs of (A) $[Al_{13}O_4(OH)_{24}(H_2O)_{12}]_{0.03}MoS_2$ and (B) $[Al_{13}O_4(OH)_{24}(H_2O)_{12}]_{0.04}WS_2$. Lamellar regions are visible in both; however, d-spacings are the same as the collapsed material, suggesting a "calzone"-like structure.

of the particles. A view parallel to the layers is visible in Figure 2.4. In contrast to the powder X-ray diffraction pattern, a more reliable method which probes the bulk of the material, the layers do not appear to be expanded. Figure 2.4b contains regions in which the layers appear to be locally expanded, but scattering centers due to the cluster are not visible, and regions of unexpanded WS_2 are also found in the micrograph. This suggests that the interior of the particle is pillared, but at the edges the layers are mostly collapsed, resembling a "calzone".

The electrical conductivity of thin films of the materials, dried on glass microscope slides, were measured. If measured within twenty four hours of the exfoliation, the conductivity of the cluster intercalated MoS_2 ranges from 3-14 S/cm. In contrast, the room temperature conductivity of 2H-MoS_2 is only ~10^{-5} S/cm. The metallic properties of these samples can be attributed to a phase transition in MoS_2 upon lithiation.[23]

2.3.2 One-Dimensional Electron Density Mapping

In order to probe the structure and orientation of the encapsulated cluster, one-dimensional electron density mapping calculations were carried out on samples of the cluster in MoS_2 and in WS_2 prepared using excess cluster to generate particularly well ordered materials (see Figure 2.1).[24] The integrated intensities (I) of the *00l* reflections in the X-ray powder diffraction patterns were extracted and converted to structure factors by the following relation:

$$|F(l)_{obs}| = (I/Lp)^{1/2} \qquad \text{Eq. (2.2)}$$

in which $F(l)_{obs}$ is the structure factor for each reflection and Lp, a Lorentz-polarization correction, is

$$Lp = (1 + \cos^2 2\theta)/(\sin^2\theta\cos\theta) \qquad \text{Eq. (2.3)}$$

Sixteen *00l* reflections were used in the calculations for the sample containing MoS_2 and eighteen *00l* reflections for the sample containing WS_2.

In order to calculate an electron density map it is necessary to know the signs [(+) or (-) for a centrosymmetric structure] as well as the magnitudes of the $F(l)_{obs}$ values. The recovery of these signs is the essence of (centrosymmetric) single crystal structure determination. In order to recover the signs of the $F(l)_{obs}$ values, an assumption is made that the contribution of the $[Al_{13}O_4(OH)_{24}(H_2O)_{12}]^{7+}$ cluster to each structure factor

is small relative to the contribution from the MoS_2 and WS_2 layers. Therefore, we can calculate the structure factors for the expanded, empty layers and apply the signs of these structure factors ($F(l)_{calc}$) to the $|F(l)_{obs}|$ values. This is a reasonable assumption because the cluster is comprised of light atoms which will not scatter nearly as well as the heavy atoms found in the MoS_2 and WS_2 layers. Subsequent calculations including the cluster (computed for modeling purposes) resulted in no changes in the signs of the structure factors.

Calculation of $F(l)_{calc}$ for the expanded, empty layers is more tedious than calculation of $|F(l)_{obs}|$ because one must first calculate the atomic scattering factors (f) for Mo (or W) and S by the following equation:

$$f(\theta) = [\sum_{i=1}^{4} a_i e^{(-b_i \lambda^2 \sin^2 \theta)} + c] e^{(-B \sin^2 \theta / \lambda^2)} \qquad \text{Eq. (2.4)}$$

where a_i, b_i, and c are a series of nine coefficients which describe an exponential decay that is specific to each element (in this case Mo, W, or S), θ is the Bragg angle, λ is the wavelength of the radiation (1.54184 Å for Cu K_a), and B is the temperature factor (B = 2 in these calculations). The value of (f) for each element varies as a function of θ, and as such will be different for each $F(l)_{calc}$.

Once $f(\theta)$ for each atom is known, each $F(l)_{calc}$ can be calculated:

$$F(l)_{calc} = \sum_{j=1}^{N} 2f_j \cos(2\pi l z_j) \qquad \text{Eq. (2.5)}$$

where, if there are N atoms in the structure, f_j is the scattering factor of atom j (at the particular θ value associated with each $F(l)_{calc}$), l is the *00l* index, and z_j is the fractional coordinate of atom j on the *c*-axis. The signs of these $F(l)_{calc}$ are then applied to the corresponding $|F(l)_{obs}|$ values, and electron density (ρ) is calculated:

$$\rho(z) = (1/c)[2\sum_{l} F(l)_{obs} \cos(2\pi l z)] \qquad \text{Eq.(2.6)}$$

where *c* is the *c*-axis, l is the *001* index, and z is a fractional coordinate along the *c*-axis (varied from -0.2 to 1.2 in increments of 0.01 in the calculation to create a "map" of the electron density).

In order to interpret a one-dimensional electron density map, it is necessary to compare it to at least one structural model. The $[Al_{13}O_4(OH)_{24}(H_2O)_{12}]^{7+}$ cluster is a polyhedral species with well-defined faces; as such, it may prefer to "sit" in certain orientations over a completely random arrangement in the gallery. Three plausible orientations for the cluster are depicted in Figure 2.2. Orientation (A), in which the C_3 axis of the cluster is perpendicular to the layers, seems the most plausible on the basis of the observed d-spacing in the X-ray powder

Table 2.1. $|F(l)_{obs}|$ and $F(l)_{calc}$ for $[Al_{13}O_4(OH)_{24}(H_2O)_{12}]_{0.05}MoS_2$.

(hkl)	d_{obs} (Å)	d_{calc} (Å)	F_{obs}	F_{calc}(A)	F_{calc}(B)	F_{calc}(C)
(001)	16.699	16.065	26.646	274.22	270.41	271.51
(002)	8.1199	8.032	52.606	247.67	266.53	257.94
(003)	5.4380	5.355	58.736	171.17	146.79	160.11
(004)	4.0530	4.016	19.715	74.776	78.750	72.375
(005)	3.2148	3.213	8.7890	44.046	50.528	50.806
(006)	2.6945	2.678	13.220	63.536	62.353	75.002
(007)	2.3010	2.295	24.328	131.01	147.03	108.80
(008)	2.0115	2.008	35.250	152.74	117.28	161.35
(009)	1.7940	1.785	27.271	188.86	212.96	186.74
(0010)	1.6069	1.606	30.300	186.01	186.74	207.76
(0011)	1.4650	1.460	36.311	166.52	157.87	129.79
(0012)	1.3438	1.339	22.789	121.93	121.44	141.82
(0013)	1.2338	1.236	14.951	56.119	69.016	65.835
(0014)	1.1507	1.148	18.734	59.011	46.407	38.087
(0015)	1.0717	1.071	10.520	18.270	13.598	28.652
(0016)	1.0026	1.004	10.942	26.389	45.069	30.572

Table 2.2 $|F(l)_{obs}|$ and $F(l)_{calc}$ for $[Al_{13}O_4(OH)_{24}(H_2O)_{12}]_{0.055}WS_2$.

(hkl)	d_{obs} (Å)	d_{calc} (Å)	F_{obs}	F_{calc}(A)	F_{calc}(B)	F_{calc}(C)
(001)	16.127	15.957	41.993	233.64	229.81	231.01
(002)	8.0412	7.978	78.622	235.87	254.44	245.44
(003)	5.3510	5.319	87.163	192.42	169.80	183.48
(004)	4.0043	3.989	49.378	130.21	131.42	124.92
(005)	3.2001	3.191	36.795	108.94	117.22	117.33
(006)	2.6653	2.660	37.353	127.78	124.82	138.89
(007)	2.2829	2.280	59.930	176.82	196.28	155.88
(008)	1.9977	1.995	57.041	178.46	139.94	185.13
(009)	1.7754	1.773	60.342	189.72	214.66	187.26
(0010)	1.5973	1.596	68.732	172.88	173.03	197.09
(0011)	1.4524	1.451	54.920	152.13	145.55	114.76
(0012)	1.3310	1.330	44.387	116.22	112.17	133.66
(0013)	1.2279	1.227	33.418	64.414	80.720	76.615
(0014)	1.1406	1.140	42.592	83.899	70.454	63.151
(0015)	1.0645	1.064	25.648	56.567	50.907	65.094
(0016)	1.0004	0.997	26.249	64.253	82.880	69.740
(0017)	0.93866	0.939	30.428	83.784	71.011	74.567
(0018)	0.89063	0.887	23.845	80.485	82.466	84.517

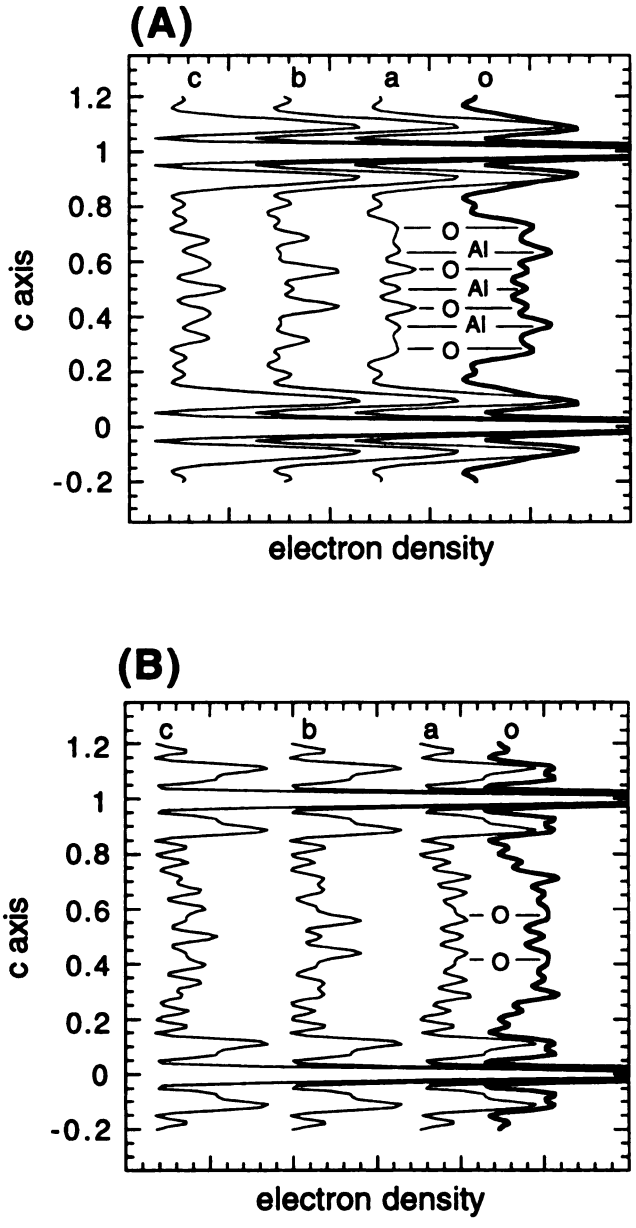

Figure 2.5. One-dimensional electron density maps of (A) $[Al_{13}O_4(OH)_{24}(H_2O)_{12}]_{0.05}MoS_2$ and (B) $[Al_{13}O_4(OH)_{24}(H_2O)_{12}]_{0.055}WS_2$. The patterns labeled (O) were generated from the X-ray diffraction data (Figure 2.1). The remaining patterns were calculated from three possible orientations of the cluster depicted in Figure 2.2. Orientation (A) matches best with the experimental data for both samples.

diffraction pattern. Theoretical electron density maps were generated for these three orientations by computing $F(l)_{calc}$ values for each of these models in the same way that $F(l)_{calc}$ values were generated for the expanded, empty layers (Eq. 2.4 and Eq. 2.5), and then calculating the electron density map for each (Eq. 2.6).

Comparison of the observed data (O) to theoretical data for the intercalated cluster in three possible orientations for both samples supports the initial supposition that the cluster is oriented with its C_3 axis oriented perpendicular to the layers in both hosts (see Figure 2.5). In this orientation, which has been observed in clays with an expansion of 9.6 Å,[25] qualitatively one would expect to see four peaks for the four planes containing oxygen atoms interspersed with three, somewhat weaker peaks corresponding to the less densely occupied aluminum containing planes. The electron density map calculated from the diffraction data for MoS_2 (Figure 2.5a, pattern (O)) matches the calculated pattern for orientation (A) (Figure 2.5a, pattern (A)) in shape and location of peaks (although two peaks from the aluminum planes seem enhanced, and two of the oxygen planes seem weak) in the experimental pattern. Both the locations and intensities of the peaks for orientations (B) and (C) do not match the pattern calculated from the diffraction data.

The data from the cluster in WS_2 also matches orientation (A), but in

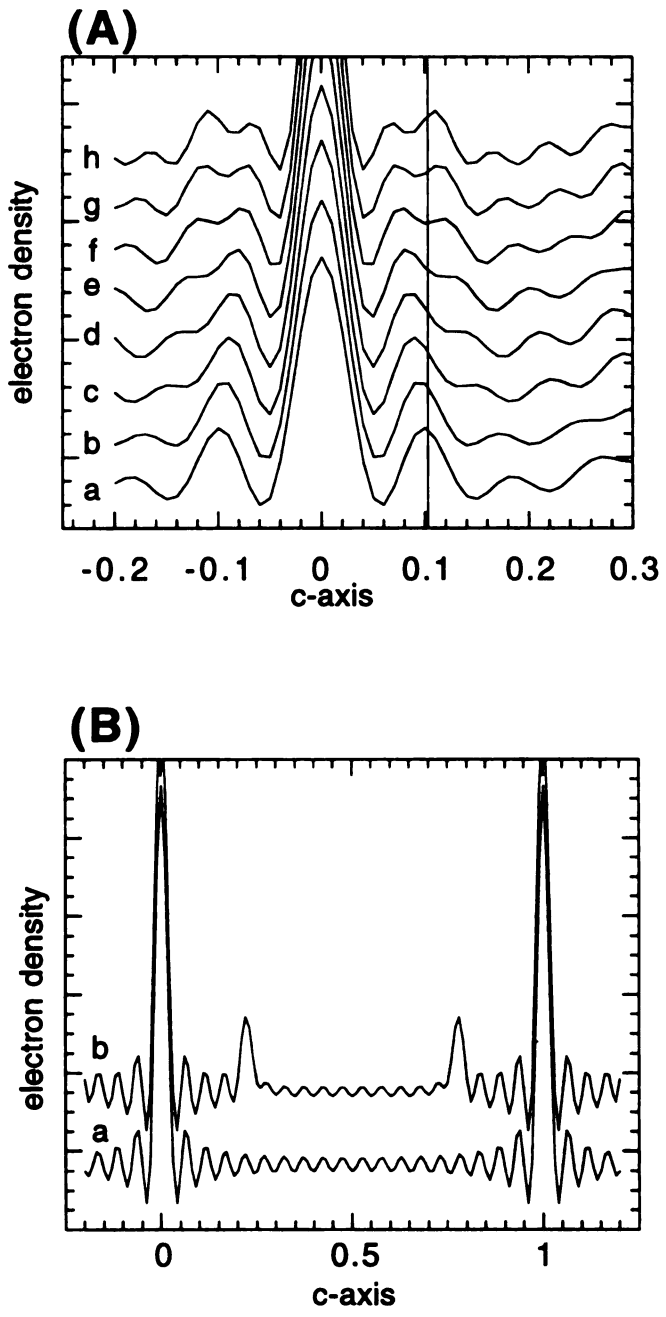

Figure 2.6. (A) Electron density maps calculated from $[Al_{13}O_4(OH)_{24}(H_2O)_{12}]_{0.055}WS_2$ $F(l)_{obs}$ data using 12-19 *00l* reflections (a-h). The S atoms are split and appear to move. (B) Maps calculated from theoretical data for a) a W atom and b) a W atom and a S atom, illustrating the Fourier truncation error and the dynamic range problem.

this case both the patterns from the diffraction data (O) and for the theoretical pattern (A) have somewhat asymmetric peaks for two of the oxygen planes (Figure 2.5b). In addition, the peaks for the sulfur atoms are split. In fact, if the number of reflections used to calculate the map is altered, the sulfur peaks seem to move (Figure 2.6a). This strange feature is due to a combination of a dynamic range problem between the heavy tungsten and lighter sulfur (i.e., the very strong atomic scattering factor of W), and a Fourier truncation caused by the use of a finite number of reflections (Figure 2.6b).

2.3.3 One-Dimensional Rietveld Refinement

In order to confirm the cluster orientation found from the analysis of the electron density maps, a Rietveld refinement of the three structural models was carried out using the program FULLPROF[26], on the powder X-ray diffraction data from intercalated WS_2. The cautious application of the Rietveld method, which uses the raw experimental diffractogram and does not require extensive and error prone data treatment, seems to be a straightforward and efficient way to discriminate between various models of cluster orientation. It is not subject to some of the problems of electron density mapping, such as Fourier truncation errors and lack of resolution due to an insufficient number diffraction peaks. Furthermore, it is possible

to exclude the first diffraction peaks, which are most affected by systematic errors in the geometrical factor because of the high degree of preferred orientation. In electron density calculations, the absence of those peaks could preclude the interpretation of the resulting map.

For this refinement, the first two reflections were excluded because their calculated intensities were 2.7 and 1.7 times higher than the observed reflections. These huge discrepancies are mostly due to the deviation of the Lorentz factor from the ideal random powder case.[27] The experimental data were fit with the Pearson VII peak profile function, and a model for the asymmetry of the peaks was included.[28] Sixteen *00l* reflections were used, falling within the range $13.5° \leq 2\theta \leq 125°$, with a step size of 0.16°. Owing to the small number of Bragg peaks in the diffraction pattern, the number of free structural parameters was kept to a minimum. Reasonable and fixed isotropic displacement parameters were assigned to the various atoms types: $B_W = 1.5$ Å^2, $B_S = 2.0$ Å^2, $B_{Al} = 2.5$ Å^2, $B_O = 3.0$ Å^2, and only an overall temperature factor was refined. The $[Al_{13}O_{40}]^{7+}$ cluster was treated as a rigid body, the z positional parameter of all the atoms in the cluster being constrained to follow the same shift. The population parameter was fixed at the value determined from EDS measurements. The position of the sulfur layer was also refined, giving a total of four free intensity dependent parameters: $B_{overall}$, $z_{cluster}$, z_S, and the scale factor.

Table 2.3. Rietveld refinement summary of $[Al_{13}O_4(OH)_{24}(H_2O)_{12}]_{0.055}WS_2$[a]

	WS_2	orientation A	orientation B	orientation C
R_{wp}	12.0%	7.8%	13.6%	9.4%
χ^2	29.1	12.9	37.6	17.7
R_I	13.6	5.8	16.1	7.3
d_{DW}	0.170	0.391	0.135	0.271
z_S	0.095(3)	0.096(1)	0.094(3)	0.096(1)
$\Delta z_{cluster}$	---	0.010(6)	0.005(5)	0.031(7)

[a] R_{wp} is the weighted agreement factor based on the observations, χ^2 is the goodness of fit, R_I is the agreement indices based on "observed" integrated intensities and d_{DW} is the value of the Durbin-Watson statistic[29], an indicator of the degree of correlation among the residuals. $\Delta z_{cluster}$ is the displacement of the center of the cluster from its original position at z=1/2. The standard deviations given by the refinement program are typically underestimated and they were multiplied by a scale factor in order to be more realistic.[30]

The results of the refinements are summarized in Table 2.3. The WS_2 column corresponds to a model without cluster. Orientation (B) is clearly to be rejected, giving worse results than the WS_2 host alone. Orientation (A), which was favored by the electron density maps, gives better results than orientation (C). There is almost certainly water between the layers as well; however, while including ordered water in the models improves the correlation between the theoretical and experimental patterns, it does not change the relative ranking of the models. A larger d spacing (11Å) and electron density mapping calculations indicate that the cluster has a different orientation ((B) in Figure 2.2) in MoO_3.[31]

2.3.4 Thermal Stability and Absorption Measurements

Thermogravimetric analysis under nitrogen shows continuous gradual weight loss with an inflection point around 300°C (Figure 2.7a). Powder X-ray diffraction indicates that the layers have not collapsed after heating to 120°C (Figure 2.7b, pattern B). After heating to 300°C the layers are still expanded, but the material does not diffract as well and a "restacked" peak at 6.1 Å begins to appear (Figure 2.7b, pattern C). Upon heating the sample to 650°C the cluster degrades and the layers collapse, resulting in a material with a d-spacing only slightly larger than the

restacked, unintercalated material. For $[Al_{13}O_4(OH)_{24}(H_2O)_{12}]_{0.04}MoS_2$, there are about 0.72 water molecules per molybdenum (about 20 per aluminum cluster). The amount of water in the sample can be estimated if one assumes that when heated under oxygen, the aluminum cluster will decompose to form Al_2O_3 and MoS_2 will convert to MoO_3. Additional weight loss can be attributed to the water.

Surface area measurements of the samples were conducted; all exhibited low surface areas (ex. 9.4 m^2/g) relative to restacked MoS_2 (10 m^2/g). Drying under vacuum overnight, over P_2O_5, soaking in ethanol and critical point drying in CO_2, and heating to 100°C, 120°C, or 300°C under flowing nitrogen or vacuum did not improve the surface areas of the samples. For one sample heated to 120°C, the vacuum in the outgassing apparatus even reached ~10^{-5} torr, and powder X-ray diffraction after the measurements showed little change in the d-spacing, but the surface area was no better than restacked MoS_2. Given that there is sufficient space between the clusters to accommodate intercalated water molecules, even in the most fully loaded samples which have been observed, it is surprising that the surface area values of the materials are not better than restacked MoS_2. It indicates that the volume vacated by the departing water molecules becomes inaccessible to the nitrogen molecules. In addition, the

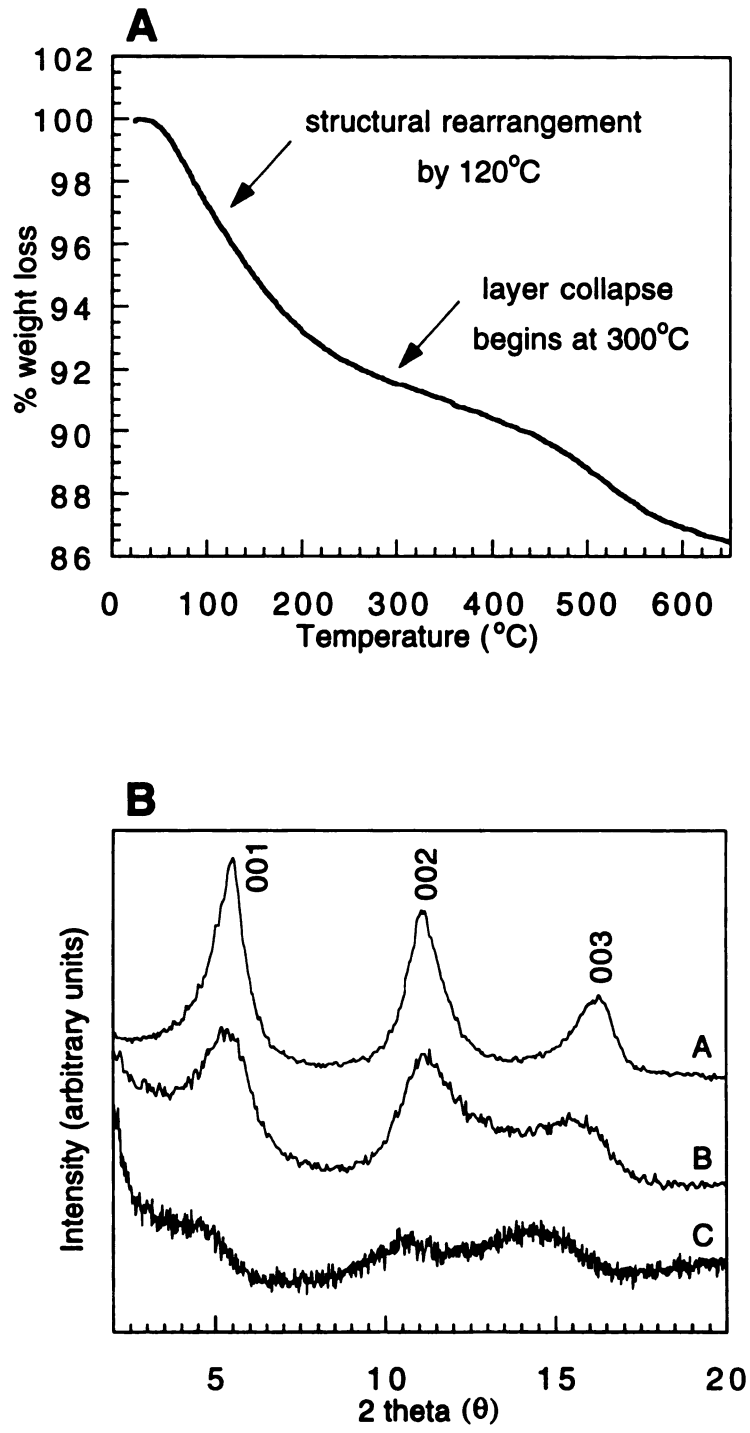

Figure 2.7. (A) TGA of $[Al_{13}O_4(OH)_{24}(H_2O)_{12}]_{0.03}MoS_2$ under nitrogen, showing gradual weight loss with an inflection point near 300°C. (B) XRD patterns of the material (a) at room temperature (b) after heating to 120°C and (c) after heating to 300°C.

collapsed layers at the edges of the particles may inhibit nitrogen absorption.

After conducting surface area measurements on a heated sample (120°C for 18 hours), ^{27}Al solid state MAS-NMR was performed on the product. Although X-ray powder diffraction indicated little change in the d-spacing of the material, the resonance at 64 ppm due to the tetrahedral Al^{3+} atoms disappeared, indicating that the structure of the intercalated species was altered, possibly through oligomerization. This also could result in blockage of void space and may account for the observed low surface areas.

2.4 Conclusions

We have seen through X-ray diffraction, MAS-NMR, and EDS that $[Al_{13}O_4(OH)_{24}(H_2O)_{12}]^{7+}$ can be encapsulated in MoS_2 and WS_2. The cation appears to intercalate without its anion, suggesting a negative charge on the layers. Electron density mapping and Rietveld powder refinement show that the cluster maintains its structural integrity while encapsulated, and it is oriented with its C_3 symmetry axis perpendicular to the layers. The materials are conductive and the layers remain expanded up to 300°C; however, ^{27}Al solid state MAS-NMR of the heated material indicates that

the cluster has decomposed. Surface area measurements indicate that void space in the material (if any exists) is inaccessible.

References

1. Barrer, R.M.; MacLeod,D.L. *Trans. Faraday Soc.*, 1955, **51**, 1290.

2. Barrer, R.M. "Zeolites and Clay Minerals as Sorbents and Molecular Sieves," Academic Press, New York, 1978, 407.

3. (a) Pinnavaia, T.J. "Characterization of Catalytic Materials," Wachs, I.E. (Ed.), Manning Publications Co., Greenwich CT, 1992, 149. (b) Johnson, I.D.; Werpy, T.A.; Pinnavaia, T.J. *J. Am. Chem. Soc.*, 1988, **110**, 8545.

4. Fleischauer, P.D. *Thin Solid Films* 1987, **154**, 309.

5. (a) Harris, S.; Chianelli, R.R. *J. Catalysis* 1984, **86**, 400. (b) Weisser, O.; Landa, S. "Sulfided Catalysts, Their Properties and Applications," Pergamon, New York, 1973. (c) Prins, R.; De Beer, H.J.; Samorjai, G.A. *Cat. Rev. -Sci. Eng.*, 1989, **32**, 1.

6. (a) Julien, C.; Saikh, S.I.; Nazri, G.A. *Mater. Sci. Eng.*, 1992, **B15**, 73. (b) Tributsch, H. *Faraday Discuss. Chem. Soc.*, 1980, **70**, 190.

7. (a) Bissessur, R.; Kanatzidis, M.G.; Schindler, J.L.; Kannewurf, C.R. *J. Chem. Soc. Chem. Commun.*, 1993, 1582. (b) Kanatzidis, M.G.; Bissessur, R.; De Groot, D.C.; Schindler, J.L.; Kannewurf, C.R. *Chem. Mater.*, 1993, **5**, 595. (c) Wang, L.; Schindler, J.L.; Thomas, J.A.; Kannewurf, C.R.; Kanatzidis, M.G. *Chem. Mater.*, 1995, **7**, 1753.

8. Lemmon, J.P.; Lerner, M.M. *Chem. Mater.*, 1994, **6**, 207.

9. (a) Divigalpitiya, W.M.R.; Frindt, R.F.; Morrison, S.R. *Science*, 1989, **246**, 371. (b) Divigalpitiya, W.M.R.; Frindt, R.F.; Morrison, S.R. *J. Mater. Res.*, 1991, **6**, 1103.

10. Tigaya, H.; Hashmoto, T.; Karasu, M.; Izumi, T.; Chiba, K. *Chem. Lett.*, 1991, 2113.

11. Bissessur, R.; Heising, J.; Hirpo, W.; Kanatzidis, M.G. *Chem. Mater.*, 1996, **8**, 318.

12. a) Rudorff, W. *Chimia,* 1965, **19**, 489. b) Bayer, E.; Rudorff, W. *Z. Naturforsch,* 1972, **27b**, 1336. c) Schöllhorn, R.; Bethel, J.; Paulus,

W. *Rev. Chim. Miner.*, 1984, **21**, 545. d) Miremadi, B.K.; Morrison, S.R. *J. Appl. Phys.*, 1988, **63**, 4970.

13. (a) Lerf, A.; Lalik, E.; Kolodziejski, W.; Klinowski, J. *J. Phys. Chem.*, 1992, **96**, 7389. (b) Nazar L.F.; Jacobson, A.J. *J. Chem. Soc. Chem. Commun.*, 1986, 570. (c) Nazar, L.F.; Jacobson, A.J. *J. Mater. Chem.*, 1994, **4**, 149.

14. Brenner, J.; Marshall, C.; Ellis, L.; Tomczyk, N.; Heising, J.; Kanatzidis, M.G. *Chem. Mater.*, 1998, **10**, 1244.

15. Plee, D.; Borg, F.; Gatinau, L.; Fripiat, J.J. *J. Am. Chem. Soc.*, 1985, **107**, 2362.

16. a) Murphy, D.W.; DiSalvo, F.J.; Hull G.W., Jr.; Wasczak, J.V. *Inorg. Chem.*, 1976, **15**, 17. b) Tsai, H.L.; Heising, J.; Schindler, J.L.; Kannewurf, C.R.; Kanatzidis, M.G. *Chem. Mater.*, 1997, **9**, 879.

17. Joensen, P.; Frindt, R.F.; Morrison, S.R. *Mater. Res. Bull.*, 1986, **21**, 457.

18. Fu, G.; Nazar, L.F.; Bain, A.D. *Chem. Mater.*, 1991, **3**, 602.

19. Tsai, P.P.; Hsu, P.H. *Soil. Sci. Soc. Am. J.*, 1985, **49**, 1060.

20. Brunauer, S.; Emmett, P.H.; Teller, Z. *J. Am. Chem. Soc.*, 1938, **60**, 309.

21. Heising, J.; Tsai, H.L.; Kanatzidis, M.G. unpublished results.

22. Gil, A.; Diaz, A.; Montes, M.; Acosta, D. R. *J. Mater. Sci.*, 1994, **29**, 4927.

23. a) Yang, D.; Sandoval, J. J.; Divigalpitiya, W.M.R.; Irwin, J.C.; Frindt, R.F. *Phys. Rev. B*, 1991, **43**, 12053. b) Py, M.A.; Haering, R. R. *Can. J. Phys.*, 1983, **61**, 76.

24. a) Liu, Y.J.; Schindler, J.L.; DeGroot, D.C.; Kannewurf, C.R.; Hirpo, W.; Kanatzidis, M.G. *Chem. Mater.*, 1996, **8**, 525. b) Liu, Y.J. Ph.D. dissertation, Michigan State University, East Lansing, MI, 1994.

25. Pinnavaia, T.J.; Tzou, M.S.; Landau, S.D.; Raythatha, R.J. *J. Mol. Catal.,* 1984, **27**, 195.

26. (a) Rietveld, *J. Appl. Cryst.*, 1969, **2**, 65. (b) Rodriguez-Carvajal, J. "Abstracts of the Satellite Meeting on Powder Diffraction of the XV Congress of the IUCr," Toulouse, France, 1990, 127.

27. (a) Reynolds, R.C. *Clays and Clay Minerals,* 1986, **34**, 359. (b) Bish, D.L.; Post, J.E. (Eds.), "Modern Powder Diffraction, Reviews in Mineralogy," **20**, The Mineralogical Society of America, Washington DC, 1989, Chapter 6. (d) Sheldrick, G.M.; Kruger, C;. Goddard, R. (eds.), "Crystallographic Computing 3: Data Collection, Structure Determination, Proteins, and Databases," Clarendon Press, Oxford, 1985, 247.

28. (a) Young, R.A.; Wiles, D.B. *J. Appl. Cryst.,* 1982, **15**, 430. (b) Cagliotti, G.; Pelotti, A.; Ricci, R.P. *Nucl. Instrum. Methods,* 1958, **35**, 223. (c) Berar, J.F.; Baldinozzi, G. *J. Appl. Cryst.*, 1993, **26**, 128.

29. Durbin, J.; Watson, G.S. *Biometrika* , 1971, **58**, 1.

30. Berar, J.F.; Lelann, P. *J. Appl. Cryst.,* 1991, **24**, 1.

31. Nazar, L.F.; Liblong, S.W.; Yin, X.T. *J. Am. Chem. Soc.,* 1991, **113**, 5889.

CHAPTER 3

Encapsulation of Neutral and Cationic Metal Chalcogenide Clusters in MoS_2 and WS_2

3.0 Abstract

The synthesis of the compounds $[Co_6S_8(PPh_3)_6]_xMoS_2$ (x = 0.02-0.094), $[Fe_6S_8(PEt_3)_y]_xMS_2$ (x = 0.05-0.2, y = 2-3, M = Mo, W), and $[Ni_9S_9(PEt_3)_y]_xMS_2$ (x = 0.04-0.077, y = 6, M = Mo, W) was accomplished by a precipitative encapsulation technique using single layers of MS_2. The products were characterized by X-ray diffraction, energy dispersive spectroscopy (EDS), High Resolution Transmission Electron Microscopy (HRTEM), Thermogravimetric analysis (TGA), direct probe mass spectrometry, room temperature electrical conductivity, and hydrodesulfurization catalytic testing (HDS). Powder X-ray diffraction patterns show an expansion of ~15.3 Å for $[Co_6S_8(PPh_3)_6]_{0.02}MoS_2$, 10.5 Å for $[Fe_6S_8(PEt_3)_2]_{0.096}MoS_2$, 11.4 Å for $[Fe_6S_8(PEt_3)_3]_{0.2}WS_2$, 14.2 Å for $[Ni_9S_9(PEt_3)_6]_{0.07}MoS_2$, and 14.0 Å for $[Ni_9S_9(PEt_3)_6]_{0.077}WS_2$. Variation in cluster loading can result in different expansions. HRTEM micrographs show evidence of localized pillaring in $[Co_6S_8(PPh_3)_6]_{0.02}MoS_2$. The products exhibit metallic conductivity originating from the metallic nature of the MS_2 host. TGA of the samples show weight loss at just below 300°C for $[Co_6S_8(PPh_3)_6]_{0.02}MoS_2$, 140°C and 150°C for $[Fe_6S_8(PEt_3)_2]_{0.096}MoS_2$ and $[Fe_6S_8(PEt_3)_3]_{0.2}WS_2$, respectively, and 160°C for $[Ni_9S_9(PEt_3)_6]_{0.07}MoS_2$. The X-ray powder patterns become amorphous close to the temperature at which weight loss takes place; eventually the layers collapse in all

materials. The unencapsulated $Co_6S_8(PPh_3)_6$ and $[Fe_6S_8(PEt_3)_6](BPh_4)_2$ clusters exhibit weight loss due to departure of the phosphine ligands, whereas $[Ni_9S_9(PEt_3)_6](ClO_4)_2$ loses weight due to loss of triethyl phosphine sulfide. In all encapsulated samples the volatile product was determined by mass spectrometry to be phosphine sulfide. $[Co_6S_8(PPh_3)_6]_{0.02}MoS_2$ was found to be as active as the commercially available catalyst Crosfield 465 (Co-Mo) at normal reaction temperatures, and more active at lower temperatures; however, the product was less selective toward desired byproducts. Catalytic activity of $[Ni_9S_9(PEt_3)_6]_{0.04}MoS_2$ and $[Ni_9S_9(PEt_3)_6]_{0.04}WS_2$ was found to be inferior to Crosfield 504 (Ni-Mo) under all conditions tested. The HDS behavior of these samples has interesting implications for the "rim-edge" model for HDS selectivity.

3.1 Introduction

Zeolites[1], pillared clays[2], and more recently materials such as MCM-41[3] have dominated modern developments in micro and mesoporous materials. These open framework oxides, however, are insulators. The pursuit of non-oxidic porous materials, particularly open framework chalcogenides, is driven by a vision of materials which combine porosity with semiconducting or metallic electronic and optical properties. Strategies to create such a material have mainly involved self-assembly through hydrothermal[4,5,6], molten salt[7], and high temperature[8] synthesis and have led to a rich diversity of new compounds.[9] Recently very promising zeolite-like indium sulfides[10] have been synthesized through this approach, as well as mesostructured metal germanium sulfides through supramolecular self-assembly.[11]

An alternate strategy to create a microporous chalcogenide is through pillaring. Many of the binary sulfides adopt a layered structure and can be intercalated with guest species.[12] The availability and relatively low cost of MoS_2 make it an especially desirable chalcogenide host. MoS_2 has been intercalated with a variety of compounds which include polymers[13,14], small organic molecules[15], ferrocene[16], $[Al_{13}O_4(OH)_{24}(H_2O)_{12}]^{7+}$ [17] and the cobalt clusters $Co_6Q_8(PR_3)_6$ (Q=S, Se, Te;

R=alkyl)[18]. WS_2 is isostructural to MoS_2, with similar intercalation chemistry, although less well explored.[19]

The encapsulation of oxidic clusters such as $[Al_{13}O_4(OH)_{24}(H_2O)_{12}]^{7+}$ into hosts MoS_2 and WS_2 was discussed in the previous chapter and elsewhere.[17] The only precedents for the combination of lamellar dichalcogenides with sulfide pillaring agents are the intercalation of the iron cluster $[Fe_6S_8(PEt_3)_6]^{2+}$ in TaS_2[20] and the pillaring of MoS_2 with the cobalt clusters $Co_6Q_8(PR_3)_6$ (Q=S, Se, Te; R=alkyl) which was initiated in this laboratory.[18] The following data are a continuation and an expansion of this work.

3.2 Experimental

3.2.1 Synthesis

Literature procedures were used in the preparation of $Co_6S_8(PPh_3)_6$,[21] $[Fe_6S_8(PEt_3)_6](BPh_4)_2$,[22] and $[Ni_9S_9(PEt_3)_6](ClO_4)_2$.[23] Chemicals used were Na_2S (Columbus Chemical Industries), PPh_3 (Baker), $CoBr_2$ (Aldrich), dimethylformamide (dmf, Aldrich), H_2S (Aldrich), $[Fe(H_2O)_6](BF_4)_2$ (Alfa Aesar), PEt_3 (Aldrich), dichloromethane (CH_2Cl_2, Aldrich), ethanol (EtOH, Aldrich), $NaBPh_4$ (Lancaster), and $Ni(H_2O)_6](ClO_4)_2$ (Alfa Aesar). $LiMS_2$

(M = Mo, W) was prepared as described in Chapter 2, or by a literature method.[24] Chemicals used were 2H-MS_2 (Cerac, MoS_2; Alfa Aesar, WS_2), n-butyl lithium (Aldrich), hexane Aldrich, and CaH_2 (Fisher).

MS_2 aqueous suspension. Method 1. $LiMoS_2$ (0.1 g, 0.6 mmol) was placed in a 125 ml flask equipped with a stir bar under a nitrogen atmosphere and capped with a rubber septa. The flask was removed from the glove box and 10 ml deionized H_2O was introduced. This results in the exfoliation of MoS_2 by a redox reaction described previously (Chapter 2, equation 1), generating single layers in suspension, H_2 gas, and LiOH. The reaction was then sonicated for 1.5 hours. **Method 2.** The preparation was identical to method 1 (WS_2 = 0.1 g, 0.2 mmol) until H_2O was introduced; then, instead of sonicating, the mixture was stirred for a half hour. The contents of the flask were then transferred to a centrifuge tube and centrifuged for a half hour. The supernatant was decanted, 10 more ml H_2O was added to the product to rinse away the excess LiOH, and the mixture centrifuged again. This rinsing was repeated two more times. To the product 10 more ml H_2O was added, the contents of the centrifuge tube were returned to the 125 ml flask, and stirred for a half hour prior to use.

$[Co_6S_8(PPh_3)_6]_xMoS_2$. To an aqueous suspension of MoS_2 (prepared by method 1) was added a solution of various amounts (ranging from 1/50 to 1/16 cluster:MoS_2 molar ratio) of $Co_6S_8(PPh_3)_6$ in CH_2Cl_2. The flask was shaken to help promote the formation of an emulsion; then stirred for two

days. The product was isolated by filtration and rinsed with H_2O to remove excess LiOH and CH_2Cl_2 to remove unencapsulated cluster.

$[Fe_6S_8(PEt_3)_y]_xMS_2$. An aqueous suspension of MS_2 (prepared by method 2) was added to a solution of various amounts of $[Fe_6S_8(PEt_3)_6](BPh_4)_2$ in acetone (Aldrich) (example: 0.12 g $[Fe_6S_8(PEt_3)_6](BPh_4)_2$, 0.06 mmol in 50 ml for MoS_2; 0.46 g $[Fe_6S_8(PEt_3)_6](BPh_4)_2$, 0.24 mmol in 80 ml acetone for WS_2). Flocculation occurred immediately. The reaction mixture centrifuged and the supernatant decanted. The product was rinsed with acetone until colorless, then rinsed with a little H_2O and deposited on a glass slide to dry.

$[Ni_9S_9(PEt_3)_6]_xMoS_2$. One fifth of an aqueous suspension of MoS_2 (prepared by method 2: ~ 0.02 g $LiMoS_2$, 0.12 mmol) was added to a solution of $[Ni_9S_9(PEt_3)_6](ClO_4)_2$ (0.0516 g, 0.03 mmol) in 5 ml of dimethyl sulfoxide (dmso, Aldrich), acetonitrile (MeCN, Aldrich), or dmf. Flocculation occurred immediately. The reaction mixture was centrifuged and the supernatant decanted. The product was rinsed with the solvent used to dissolve the cluster (dmso, MeCN, or dmf) until colorless, then rinsed with a little H_2O and deposited on a glass slide to dry. Best results were achieved with dmso. Larger scale preparations used to prepare samples for HDS measurements (in dmso) employed 1.2 mmol MoS_2 and 0.2 mmol of $[Ni_9S_9(PEt_3)_6](ClO_4)_2$.

$[Ni_9S_9(PEt_3)_6]_xWS_2$. The reaction procedure was similar except that dmso and acetone were used (0.2 mmol WS_2, 0.02-0.09 mmol $[Ni_9S_9(PEt_3)_6](ClO_4)_2$, 25-50 ml acetone). Best results were achieved with acetone. Larger scale preparations used to prepare samples for HDS measurements (in dmso) employed 2 mmol WS_2 and 0.2 mmol of $[Ni_9S_9(PEt_3)_6](ClO_4)_2$.

3.2.2 Characterization

Powder X-ray diffraction patterns, HRTEM micrographs, Energy Dispersive Spectroscopy (EDS) measurements, Thermogravimetric Analyses (TGAs), Surface Area measurements, and conductivity values were collected as described previously (Chapter 2, section 2.2.2). Hydrodesulfurization (HDS) measurements were conducted by Dr. James Brenner or Dr. Di Wei (post-doctoral associates of Dr. Chris Marshall, Chemical Technology Division) at Argonne National Laboratory using a pilot plant scale HDS unit designed with the help of Dr. John Young of EC Technologies. Conditions were chosen so as to mimic those of an industrial middle distillate desulfurization unit. Weight loadings of samples (0.1 g) and the commercial catalysts (1.0 g) have been adjusted so as to make the total metal (Co or Ni + Mo or W) loadings equivalent. Liquid velocity was

0.25 g/minute (or 0.33 g/minute for $[Ni_9S_9(PEt_3)_6]_{0.04}MS_2$ samples); gas velocity was 700 cm^3/min; ratio of $H_2/H_2S/N_2$ was 5/0/2; pressure was 400 psig; furnace temperature was 300-400°C; tabular alumina diluent was 2.5-3.0 g; and liquid feed was 1.0 weight % sulfur as dibenzothiophene in hexadecane (or 0.75 weight % sulfur feed for $[Ni_9S_9(PEt_3)_6]_{0.04}MS_2$ samples). Reported values were collected at a Liquid Hourly Space Velocity (LHSV) of 20/hr. Prior to catalytic testing the samples were purged in N_2 at 20°C for 30 minutes, dried in N_2 at 150°C for 60 minutes and at 200°C for 60 minutes, then heated in H_2 for 2 hours at 200°C. The commercially available materials were pre-treated in an analogous fashion except the second drying step was at 400°C and the final heating step was in an 5% H_2S/H_2 mixture at 400°C.

3.3 Results and Discussion

3.3.1 Evidence of Cluster Encapsulation

$[Co_6S_8(PPh_3)_6]_xMoS_2$. X-ray diffraction patterns exhibiting an expansion of the MoS_2 layers due to encapsulation of the $Co_6S_8(PPh_3)_6$ cluster can be found in Figure 3.1. As noted during the discussion of the diffraction patterns in Chapter 2, the *00l* reflections predominate due to the tendency of lamellar materials to adopt a preferred orientation. These patterns exhibit d-spacings around 21.6 Å (Figure 3.1a, pattern a), which is a 15.4 Å expansion over the d-spacing of restacked MoS_2, 6.2 Å (Figure 3.1a, pattern b). This expansion is consistent with the dimensions of the cluster. The patterns from contain very broad and weak peaks, in contrast to the diffraction patterns found for $[Al_{13}O_4(OH)_{24}(H_2O)_{12}]_{0.05}MoS_2$. This seems to be particularly true for samples with lower loadings of the cluster (x = 0.02-0.03). EDS measurements indicate a loading of $[Co_6S_8(PPh_3)_6]_{0.024}MoS_2$ for the sample found in Figure 3.1a, pattern b, and $[Co_6S_8(PPh_3)_6]_{0.094}MoS_2$ for the sample in Figure 3.1b.[18c] Samples with higher loadings of the cluster ($x \approx 0.10$) give sharper powder patterns, but are still not as ordered as those found for the encapsulation of cationic species. Only 4 *00l* reflections are observed in Figure 3.1b, and at higher

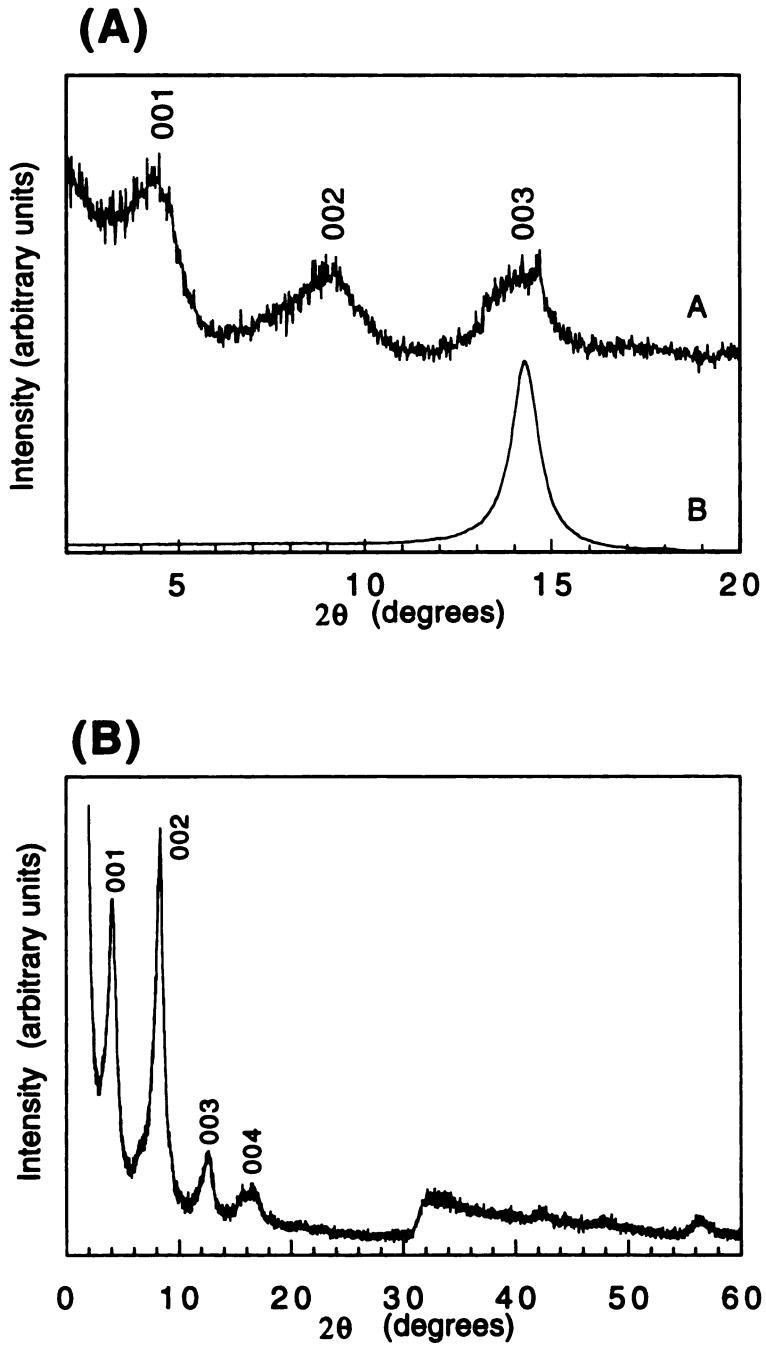

Figure 3.1. X-ray diffraction patterns of (A) $[Co_6S_8(PPh_3)_6]_{0.24}MoS_2$ and restacked MoS_2, showing an expansion of 15.4 Å upon encapsulation of the cluster (B) $[Co_6S_8(PPh_3)_6]_{0.96}MoS_2$, showing only 4 *00l* reflections (in contrast to 18 *00l* in $[Al_{13}O_4(OH)_{24}(H_2O)_{12}]_{0.05}MoS_2$) for even high loadings of the cluster.

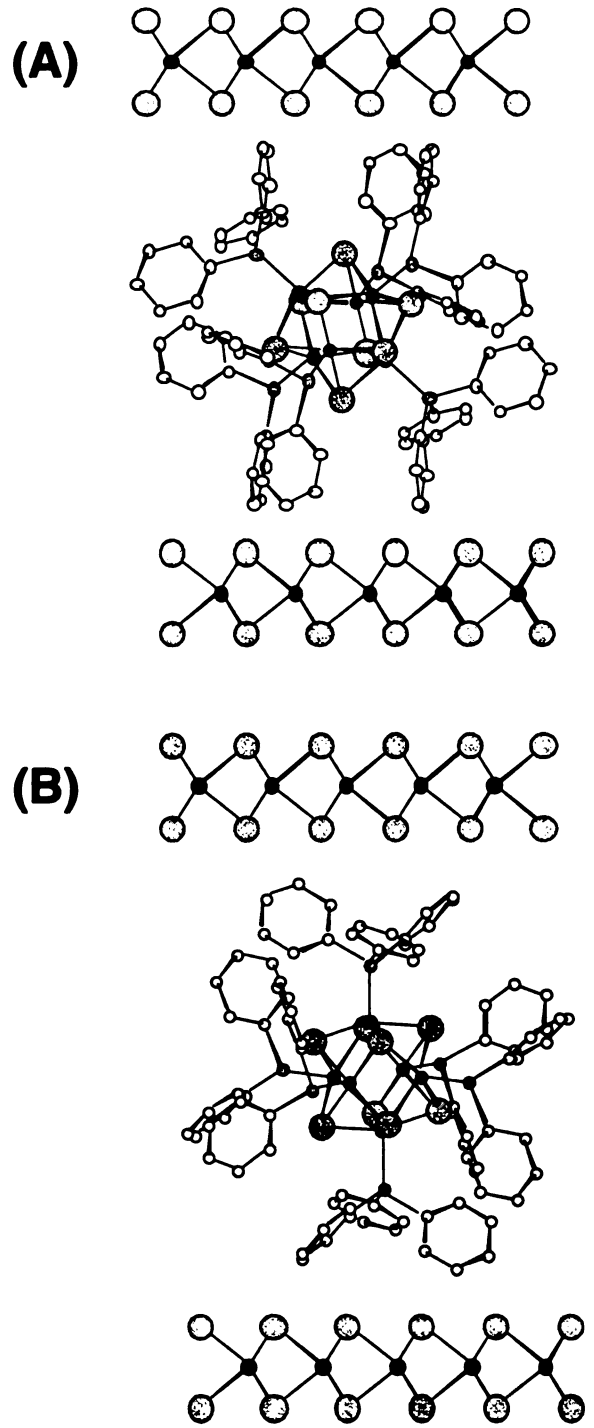

Figure 3.2. The $Co_6S_8(PPh_3)_6$ cluster oriented with its (A) C_3 axis perpendicular to the layers and its (B) C_4 axis perpendicular to the layers. Expansion in (B) is slightly larger than in (A). Black circles represent Mo or W atoms; large light gray circles, S atoms; dark gray circles, Co atoms; small light gray circles, P atoms; open circles, C atoms.

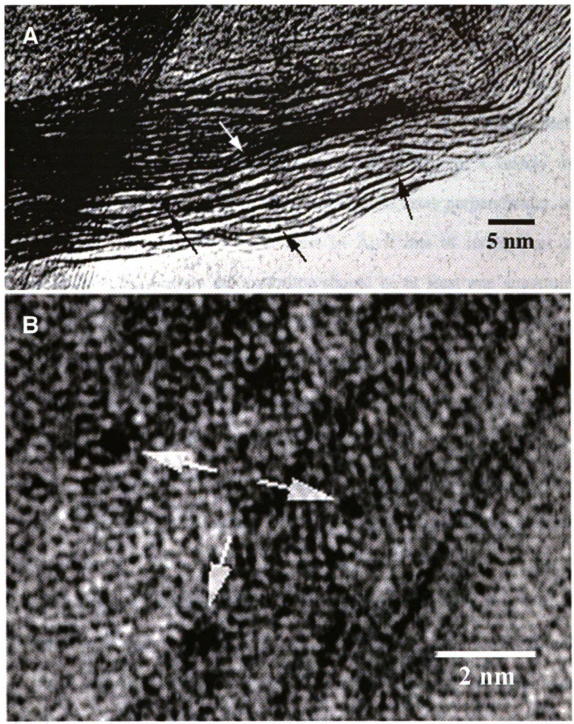

Figure 3.3. HRTEM micrographs of $[Co_6S_8(PPh_3)_6]_{0.02}MoS_2$. (A) Region with lamellar features showing expanded and unexpanded (white arrow) layers. Small scattering centers may be attributed to Co_6S_8 cores (black arrows). (B) Region showing in-plane structure which contains dark grey circles (white arrows) which may be attributed to Co_6S_8 cores.

2θ values the *hk0* reflections predominate. Although some of the broadening of the peaks might be attributed to small particle size, disorder probably contributes to the broadening as well.

A rather broad range of expansions (from 14 - 15.4 Å) has been observed for these samples[18] which might be explained by a variety of factors. If the cluster is oriented with one of its C_3 axes perpendicular to the layers the expansion will be at least 14 Å; if one of its C_4 axes is perpendicular to the layers the expansion should be at least one angstrom greater (Figure 3.2). Also, the phosphine ligands in the $Co_6S_8(PPh_3)_6$ cluster contain phenyl rings which, although not very flexible compared to other phosphine ligands, may move slightly to alter the dimensions of the cluster. Finally, unlike the 12 H_2O ligands in the $[Al_{13}O_4(OH)_{24}(H_2O)_{12}]^{7+}$ cluster, some of the bulky triphenyl phosphine ligands may detach from the cluster. The partially deligated species would have noticeably smaller dimensions.

Room temperature conductivity measurements on pressed pellets of the materials revealed metallic behavior, with conductivity values around 2-3 S/cm. Lithiation results in a structural transformation of the MS_2 from trigonal prismatic coordination about the metal atoms to octahedral coordination[25] which is retained in restacked MS_2 (*vide infra*). The structural transformation results in a change in the electrical properties from semiconducting to metallic behavior.

HRTEM micrographs acquired at the edges of $[Co_6S_8(PPh_3)_6]_{0.02}MoS_2$ particles dusted on a carbon-supported copper grid are found in Figure 3.3. In Figure 3.3a an intimate mixture of expanded and un-expanded lamellar regions is visible. The observed d-spacing in the expanded region (13.9 Å, Δ = 7.7 Å) is smaller than that observed by transmission X-ray diffraction (21.5 Å), which may be attributed to loss of the phosphine ligands and is consistent with the dimensions of the Co_6S_8 core (~8 Å). In the expanded region it is possible to see weak scattering centers which may be interpreted as Co_6S_8 cores (black arrows). Phosphine ligands, even if present, would be too light to scatter sufficiently to be visible. The fact that expansion of the layers is not continuous over the entire sample suggests that pillaring is for the most part localized. In Figure 3.3b a view of the in-plane structure is visible. Superimposed on the scattering due to Mo and S centers are large, spherical scattering centers which may be attributed to in-plane $Co_6S_8(PPh_3)_x$ species (white arrows). This implies that the clusters are dispersed throughout the material, as indicated by X-ray diffraction measurements.

$[Fe_6S_8(PEt_3)_6]_xMS_2$. X-ray diffraction patterns of $Fe_6S_8(PEt_3)_6^{2+}$ encapsulated in MoS_2 and WS_2 are shown in Figure 3.4. The patterns are more well-ordered than those for the neutral $Co_6S_8(PPh_3)_6$ cluster, exhibiting 10 *00l* reflections in the MoS_2-containing sample and 15 *00l*

reflections in the WS_2-containing sample. The d-spacing of $[Fe_6S_8(PEt_3)_6]^{2+}$ in MoS_2 is 16.7 Å, corresponding to an expansion of 10.5 Å (Figure 3.4a), whereas the d-spacing of $[Fe_6S_8(PEt_3)_6]^{2+}$ in WS_2 is 17.6 Å, corresponding to an expansion of 11.4 Å (Figure 3.4b). These expansions are consistent with the dimensions of the cluster (~10.3 Å along the C_3 axis; ~11.7 Å along the C_4 axis). The orientation of the cluster between the layers is not known; however, the cluster was observed to be oriented with its C_3 axis perpendicular to the layers upon intercalation into TaS_2 and gave rise to an 11.5 Å expansion.[20]

EDS measurements indicated that the chemical formulas of the compounds shown in Figure 3.4 are $[Fe_6S_8(PEt_3)_x]_{0.096}MoS_2$ and $[Fe_6S_8(PEt_3)_x]_{0.2}WS_2$. There is no evidence of co-intercalation of the BPh_4^- anion. These represent the upper limit of observed loadings. The values are slightly higher than those observed for the maximum loadings of the $Co_6S_8(PPh_3)_6$ cluster, which is consistent with the smaller dimensions of the $Fe_6S_8(PEt_3)_6^{2+}$ cluster. The maximum observed loading of the $[Al_{13}O_4(OH)_{24}(H_2O)_{12}]^{7+}$ cluster suggested a negative charge as high as 0.35/0.38 per Mo/W atom on the layers; the maximum loadings observed here give rise to comparable negative charge on the layers (0.2/0.4 per Mo/W atom). However, this is not a reliable way to determine the charge per Mo/W atom as the value may be artificially inflated due to partial decomposition of either cluster.

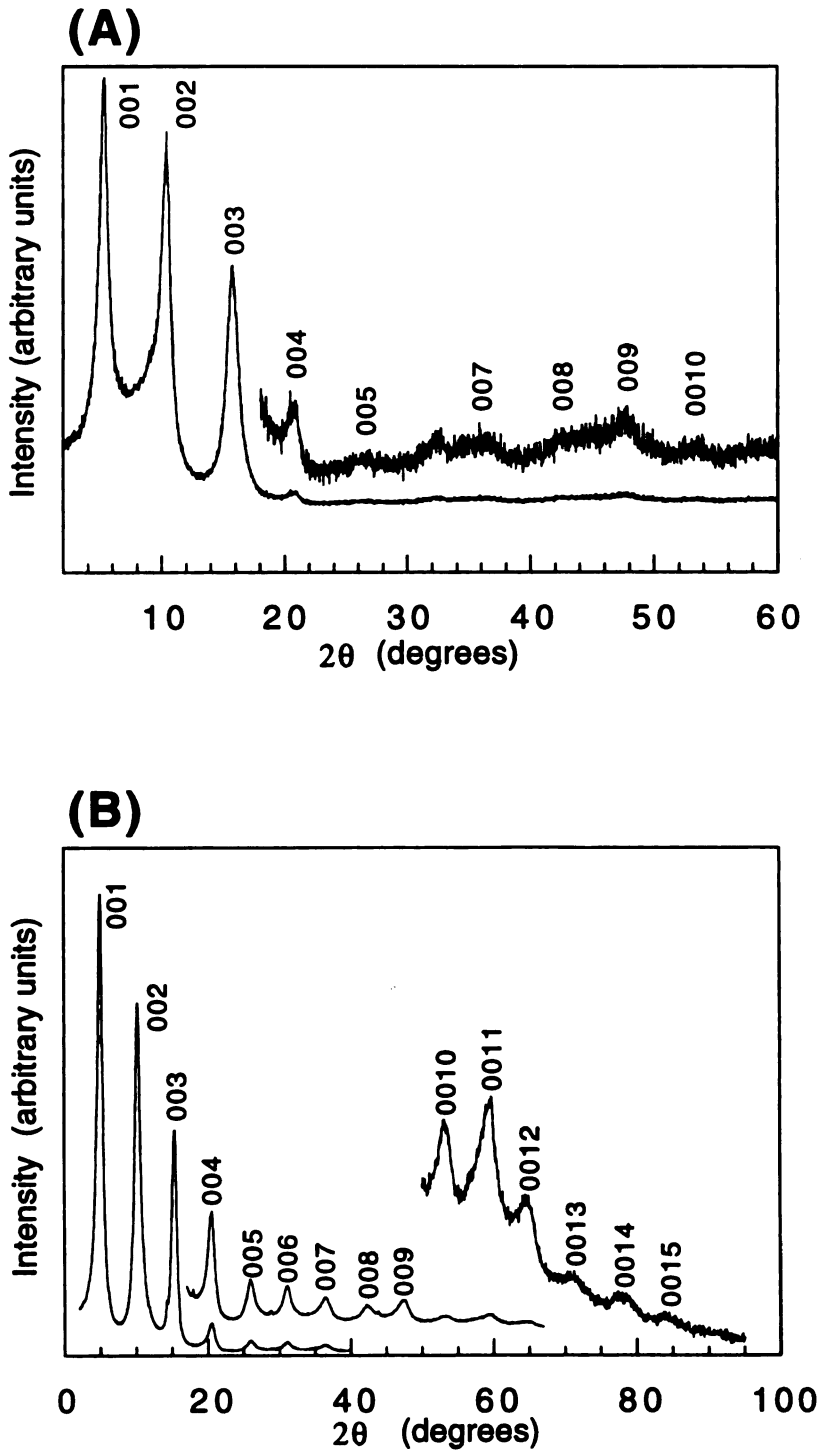

Figure 3.4. X-ray diffraction patterns of (A) $[Fe_6S_8(PEt_3)_2]_{0.096}MoS_2$ (Δ = 10.5 Å) and (B) $[Fe_6S_8(PEt_3)_3]_{0.20}WS_2$ (Δ = 11.4 Å). Both exhibit a predominance of *00l* reflections and greater order than the patterns for $[Co_6S_8(PPh_3)_6]_{0.96}MoS_2$,but less order than for $[Al_{13}O_4(OH)_{24}(H_2O)_{12}]_{0.05}MoS_2$.

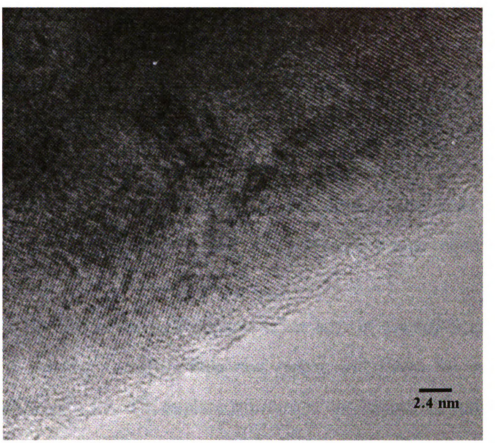

Figure 3.5. HRTEM micrograph of $[Fe_6S_8(PEt_3)_x]_y]_{0.2}WS_2$, showing highly ordered in-plane structure. Large dark grey areas could be attributed to aggregated $[Fe_6S_8]^{2+}$ cores.

The triethyl phosphine ligands are more flexible than the triphenyl phosphine ligands because they are less hindered sterically; hence, a wider range of d-spacings are possible for any given orientation of the cluster. However, given the dimensions of the cluster, it is impossible to observe these loadings in WS_2 (5 W atom per cluster) without loss of some of the triethyl phosphine ligands. It is barely possible to retain them all in the loading observed in MoS_2 (10.4 Mo per cluster). The number of phosphines ligated to the clusters will be discussed in conjunction with the thermal analysis of the materials.

Room temperature conductivity measurements on thin films of the materials indicated metallic behavior, with conductivity values around 0.4 S/cm.

A HRTEM micrograph acquired at the edge of $[Fe_6S_8(PEt_3)_x]_{0.2}WS_2$ particles dusted on a carbon-supported copper grid shows the in-plane structure, Figure 3.5. The in-plane structure in this sample is significantly more ordered than the structure visible in Figure 3.3b, and can be indexed as *110* planes. No discrete scattering centers due to $[Fe_6S_8]^{2+}$ cores are observed; however, larger dark gray regions are visible which may be due to aggregation of $[Fe_6S_8]^{2+}$ cores. Aggregation would be consistent with the higher loading of $[Fe_6S_8(PEt_3)_x]^{2+}$ clusters found in this sample (0.2 per W atom) than $Co_6S_8(PPh_3)_x$ cores in MoS_2 (0.02 per Mo atom).

$[Ni_9S_9(PEt_3)_6]_xMS_2$. X-ray diffraction patterns of $Ni_9S_9(PEt_3)_6^{2+}$ encapsulated in MoS_2 and WS_2 are found in Figure 3.6. As with the other cationic clusters, the patterns are more well ordered than those from samples containing the neutral $Co_6S_8(PPh_3)_6$ cluster. Fourteen *00l* reflections are observed for are $[Ni_9S_9(PEt_3)_6]^{2+}$ in MoS_2, which exhibits an expansion of 14.2 Å; and nine *00l* for $[Ni_9S_9(PEt_3)_6]^{2+}$ in WS_2, which is expanded by 14.0 Å. The dimensions of the cluster are approximately 13 Å perpendicular to and 11.5 Å parallel to the Ni_3S_3 planes (Figure 3.7).

EDS measurements indicated that the chemical formulas of the compounds shown in Figure 3.6 are $[Ni_9S_9(PEt_3)_6]_{0.07}MoS_2$ and $[Ni_9S_9(PEt_3)_6]_{0.077}WS_2$. There is no evidence of co-intercalation of the ClO_4^- ion. These loadings represent the upper limit; lower loadings (down to ~0.04) have been observed. The maximum charge per Mo/W atom is 0.14/0.15, which is lower than that observed for samples containing the $[Fe_6S_8(PEt_3)_6]^{2+}$ and the $[Al_{13}O_4(OH)_{24}(H_2O)_{12}]^{7+}$ clusters. The dimensions, coupled with the observed loadings (13-14 Mo/W atoms per cluster), suggest that the clusters may be packed in the gallery space with the Ni_3S_3 planes parallel to the layers. It is possible to accommodate the cluster in this loading without loss of phosphine ligands. At lower loadings smaller d-spacings have been observed (10.5 Å - 13 Å).

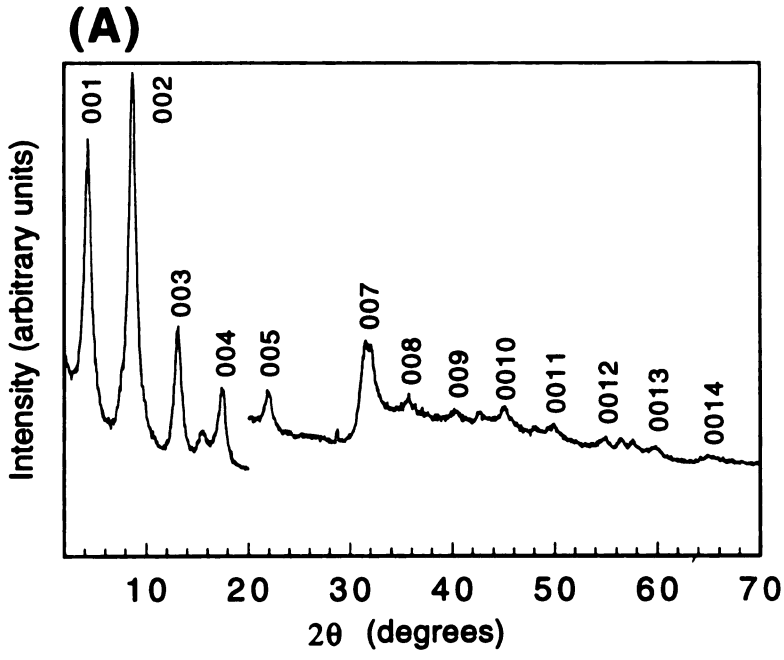

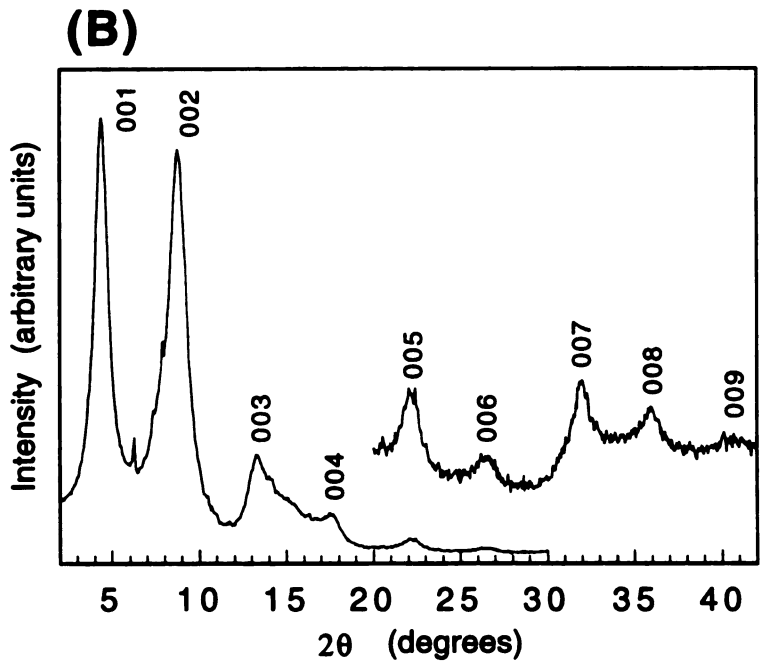

Figure 3.6. X-ray diffraction patterns of (A) $[Ni_9S_9(PEt_3)_6]_{0.07}MoS_2$ (Δ = 14.2 Å) and (B) $[Ni_9S_9(PEt_3)_6]_{0.077}WS_2$ (Δ = 14.0 Å). Again the predominance and number of observed *00l* reflections indicates a greater degree of order than in $[Co_6S_8(PPh_3)_6]_{0.96}MoS_2$.

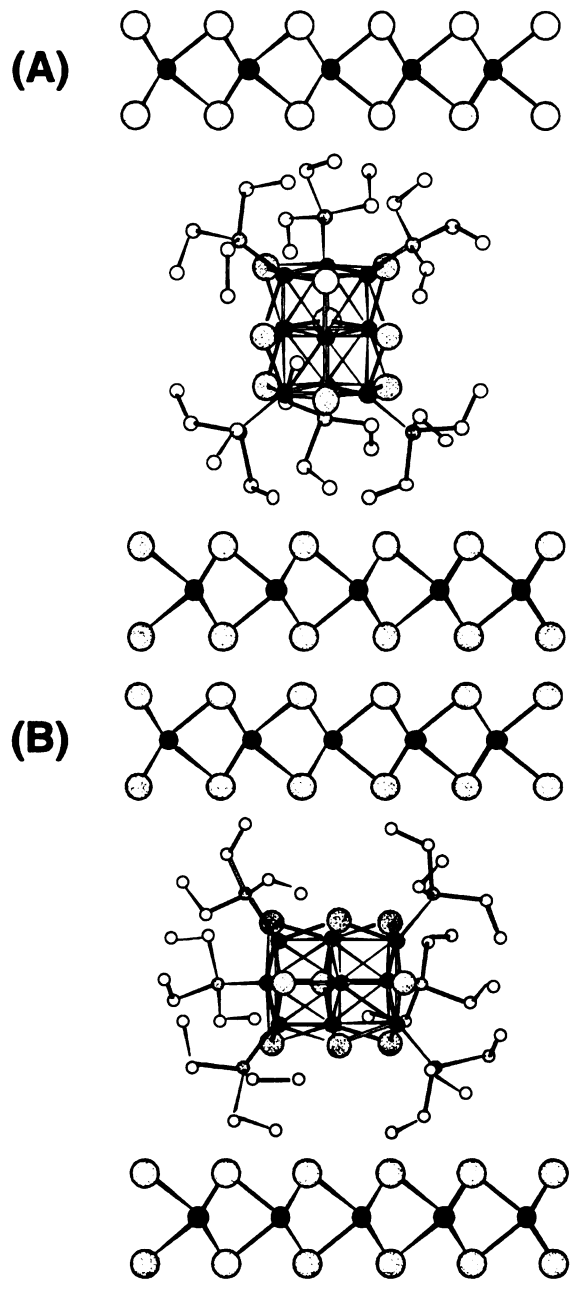

Figure 3.7. A view of the $[Ni_9S_9(PEt_3)_6]^{2+}$ cluster with its Ni_3S_3 planes (A) parallel to and (B) perpendicular to the MS_2 layers. Orientation (A) gives rise to a larger expansion which is consistent with the d-spacing observed in the X-ray diffraction pattern.

3.3.2 Thermal Analysis

$[Co_6S_8(PPh_3)_6]_{0.022}MoS_2$. The TGA of unintercalated $Co_6S_8(PPh_3)_6$ (Figure 3.8a) shows a clean weight loss, beginning at about 250°C, corresponding to the departure of the triphenyl phosphine ligands (expected weight loss, 72%; observed, 70.6%). The identity of the volatile product was confirmed by direct probe mass spectrometry, and the nonvolatile decomposition product is CoS.[18] In contrast, the TGA of $[Co_6S_8(PPh_3)_6]_{0.022}MoS_2$ shows a broad, continuous weight loss, beginning at about 220°C, to 650°C. Our hope was that the triphenyl phosphine ligands could be removed from the cluster by thermal treatment, resulting in a microporous sulfide (Figure 3.9). If all six phosphine ligands are still attached to the cluster core, the expected weight loss due to the departure of triphenyl phosphine ligands is 16.6%; the observed weight loss is 18.9%. Although additional weight loss might be explained by co-encapsulated solvent, direct probe mass-spectrometry indicates that the volatile product is actually triphenyl phosphine sulfide. Predicted weight loss for triphenyl phosphine sulfide is 18.7%. In fact, when the selenide analog $Co_6Se_8(PPh_3)_6$ is encapsulated the volatile product is still triphenyl phosphine sulfide. This surprising result suggests that the phosphine ligands are extracting sulfur from MoS_2 as they depart (Figure 3.10).

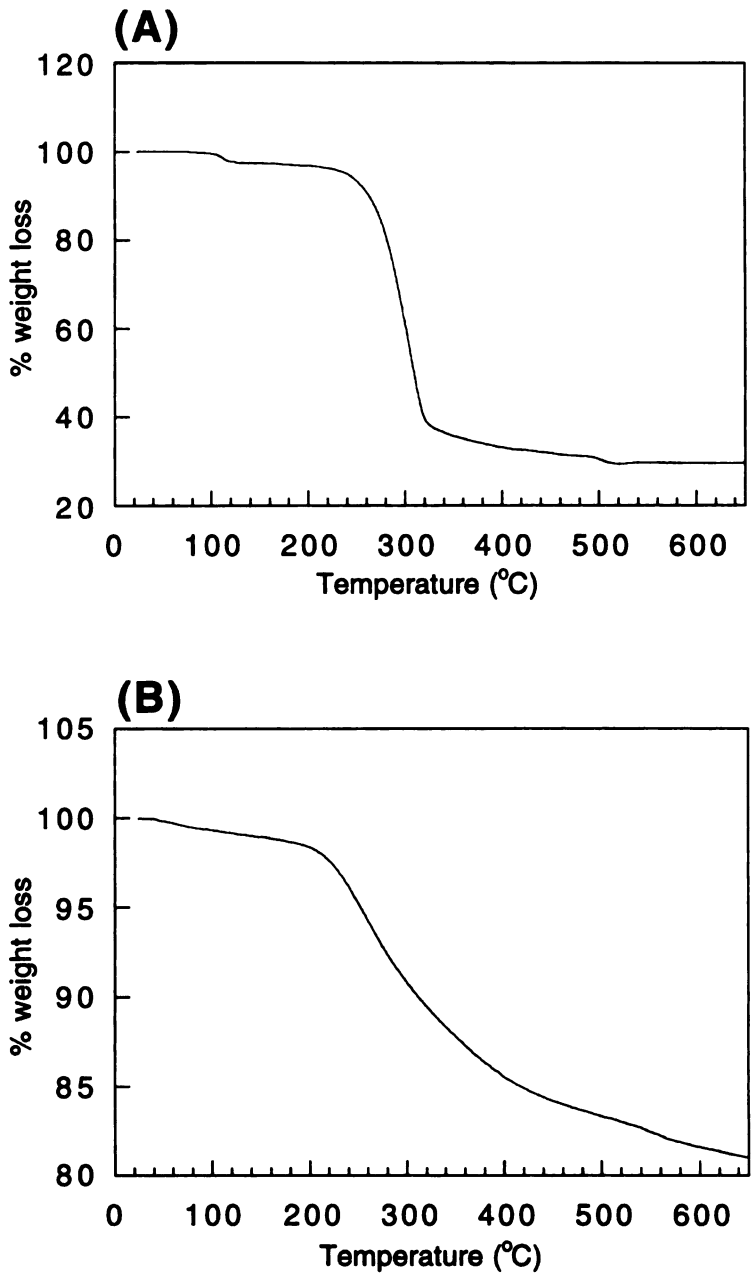

Figure 3.8. TGA of (A) $Co_6S_8(PPh_3)_6$. The PPh_3 ligands depart in a clean step just below 300°C (expected weight loss, 72%; observed, 70.6%). (B) $[Co_6S_8(PPh_3)_6]_{0.22}MoS_2$. The PPh_3 ligands begin to depart at a comparable temperature, but the weight loss is gradual to 650°C (predicted weight loss due to PPh_3 departure, 16.6%; observed, 18.9%).

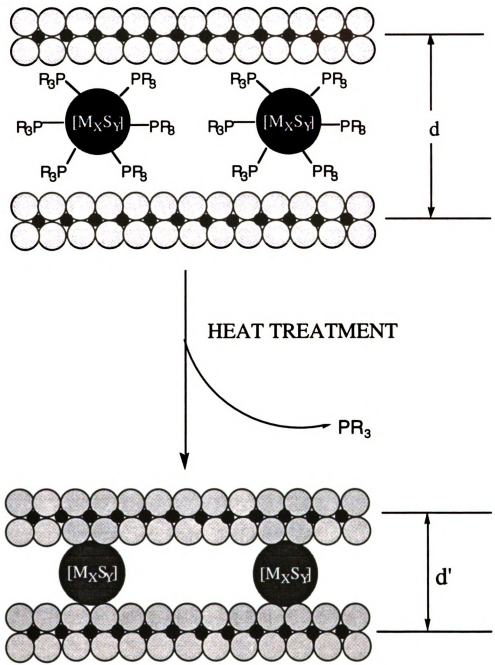

Figure 3.9. An illustration of the original plan to create a microporous sulfide: encapsulation of the cluster with phosphine ligands acting as "spacers", followed by thermal treatment to remove the phosphine ligands.

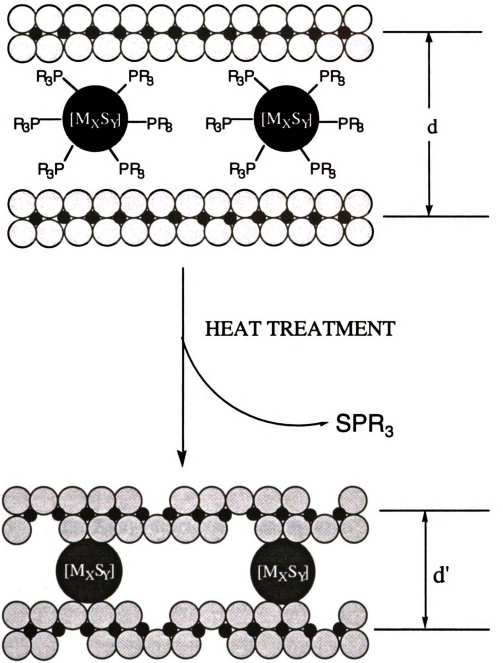

Figure 3.10. An illustration of the observed data: encapsulation of the cluster with phosphine ligands acting as "spacers", followed by thermal treatment. The phosphine ligands attack the layers as they depart, forming SPR_3 species and possible S^{2-} anion vacancies.

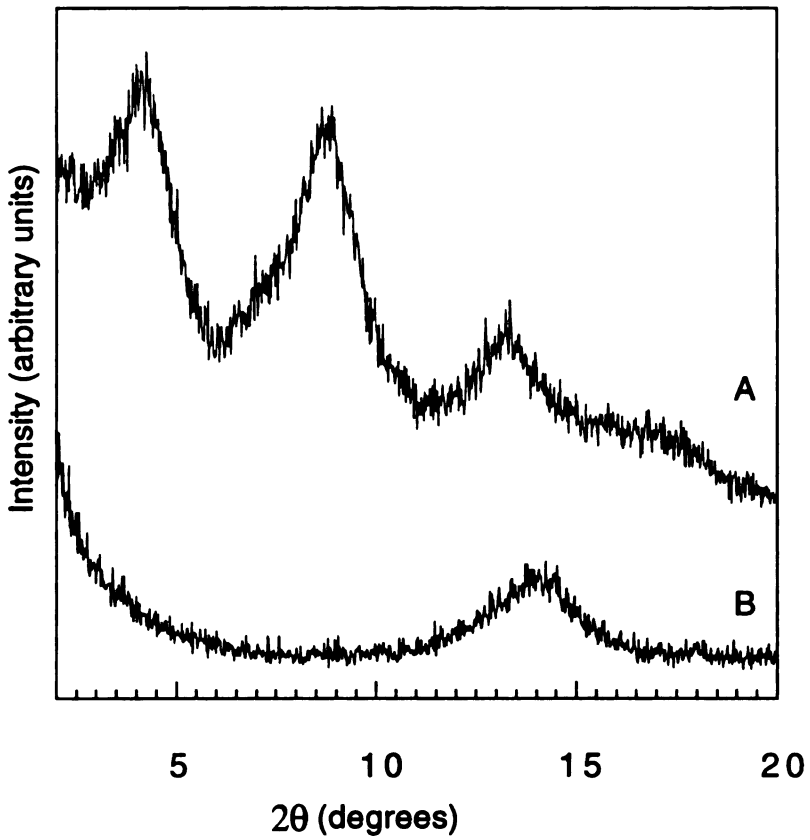

Figure 3.11. X-ray diffraction patterns upon thermal treatment of $[Co_6S_8(PPh_3)_6]_{0.24}MoS_2$. $[Co_6S_8(PPh_3)_6]_{0.24}MoS_2$ becomes amorphous upon heating to 250°C, then collapses to a d-spacing only slightly larger than restacked MoS_2 by 650°C (b).

X-ray diffraction studies upon thermal treatment show that the material becomes amorphous after onset of the removal of the phosphine ligands; if heated to 650°C, the material collapses to a product with a d-spacing only slightly larger than restacked MoS_2 (Figure 3.11). It is likely that, as vacancies are created in the MoS_2 layers by the departing phosphine ligands, sulfur atoms are transferred from the $[Co_6S_8]$ cores:

$$[Co_6S_8(PPh_3)_6]_xMoS_2 \text{ --> } [Co_6S_8]_xMoS_{2-y} \text{ --> } [Co_6S_{8-y}]_xMoS_2 \quad \text{(Eq. 3.1)}$$

$[Fe_6S_8(PEt_3)_y]_xMS_2$. The TGA of $[Fe_6S_8(PEt_3)_6](BPh_4)_2$ (Figure 3.12a) shows weight loss, beginning shortly after 100°C, due to the departure of the BPh_4^- anions as well as the triethyl phosphine ligands (expected weight loss, 69.5%; observed, 69.2%). The majority of the triethyl phosphine appears by mass spectrometry to depart as a non-sulfide product. $[Fe_6S_8(PEt_3)_x]_{0.096}MoS_2$ and $[Fe_6S_8(PEt_3)_x]_{0.2}WS_2$, however, show a gradual weight loss starting at about 140°C for the MoS_2-containing sample and 150°C for the WS_2-containing sample (Figure 3.12b). No BPh_4^- anions were detected by mass spectrometry. If all six phosphine ligands were present in each sample, and the volatile product was only triethyl phosphine, the predicted weight loss for each compound would be 23.9% and 28.0%, respectively; the observed values are 12.7% for $[Fe_6S_8(PEt_3)_x]_{0.096}MoS_2$ and 18.7% for $[Fe_6S_8(PEt_3)_x]_{0.2}WS_2$. It seems that, as

predicted based on the loadings and dimensions of the cluster, the $[Fe_6S_8]^{2+}$ core is not fully ligated. Furthermore, direct probe mass spectrometry revealed that the majority of the volatile product is triethyl phosphine sulfide, analogous to the behavior of the triphenyl phosphine ligand in $[Co_6S_8(PPh_3)_6]_{0.022}MoS_2$. For $[Fe_6S_8(PEt_3)_x]_{0.096}MoS_2$, if there are two triethyl phosphine ligands still attached to the cluster the predicted weight loss (due to $SPEt_3$ loss) is 12.0%. For $[Fe_6S_8(PEt_3)_x]_{0.2}WS_2$, if there are three triphenyl phosphine ligands still attached to the cluster the predicted weight loss (again due to $SPEt_3$ loss) is 20.7%. Loss of three phosphine ligands was observed upon encapsulation of the $[Fe_6S_8(PEt_3)_6]^{2+}$ cluster in TaS_2.[20]

X-ray diffraction patterns probing the thermal stability of $[Fe_6S_8(PEt_3)_2]_{0.096}MoS_2$ are found in Figure 3.13. The material remains pillared up to 100°C (13b), the temperature at which MoS_2 converts from an octahedral geometry about the Mo atom to a trigonal prismatic coordination environment. At 150°C, after which weight loss has begun, the powder pattern is amorphous (13c). By 200°C the pillars have collapsed, resulting in Fe_xMoS_2, a material with a d-spacing only slightly larger than restacked MoS_2 (13d). $[Fe_6S_8(PEt_3)_x]_{0.2}WS_2$ exhibits slightly better thermal stability. At 150°C the material is still expanded; however, by 210°C partial decomposition to Fe_xWS_2 has taken place.

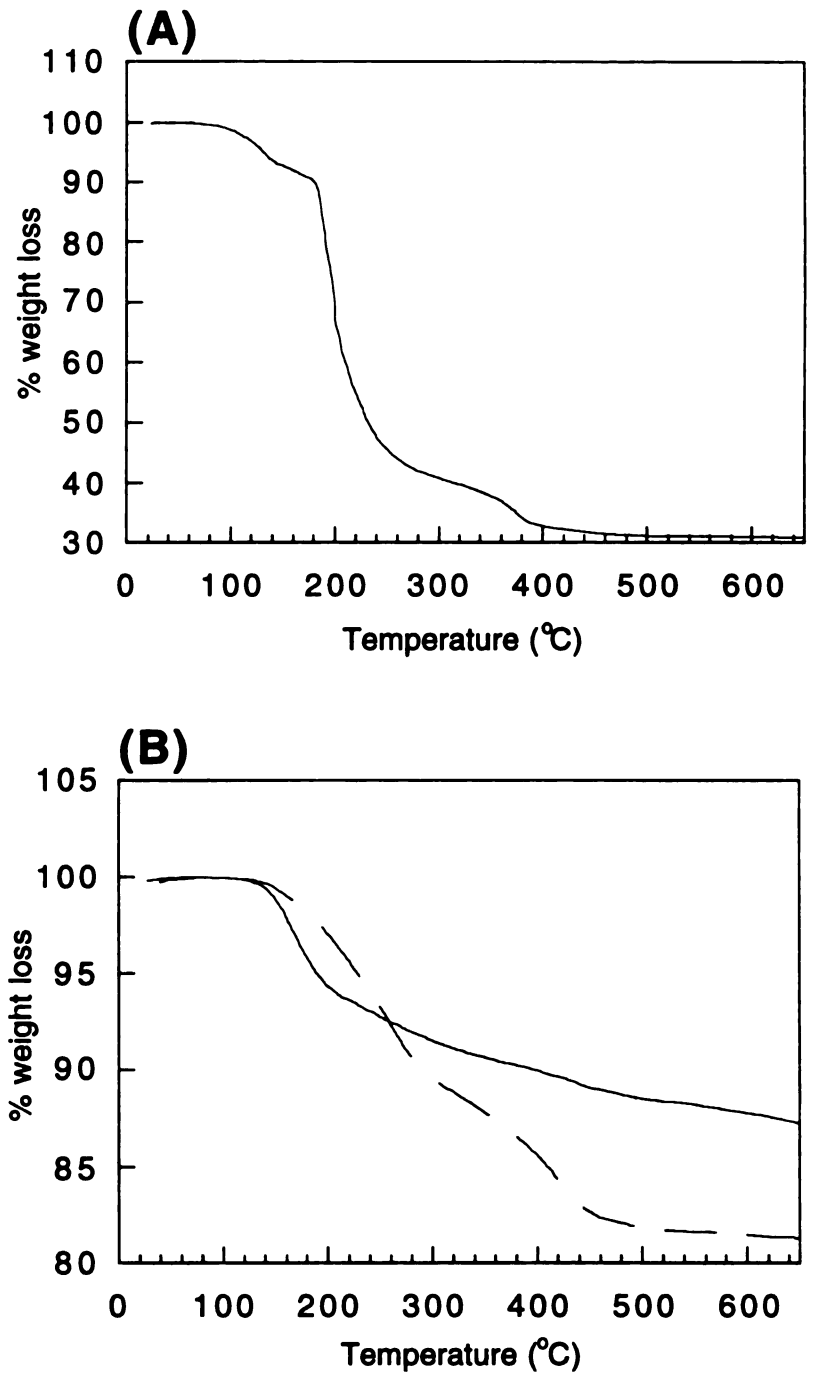

Figure 3.12. TGA of (A) $[Fe_6S_8(PEt_3)_6](BPh_4)_2$, which loses weight due to the departure of the PEt_3 ligands and the BPh_4 anion (expected, 69.5%; observed, 69.15%) and (B) $[Fe_6S_8(PEt_3)_2]_{0.096}MoS_2$ (solid line) and $[Fe_6S_8(PEt_3)_3]_{0.20}WS_2$ (dashed line). The volatile species, $SPEt_3$, is lost more gradually than the PEt_3 ligands in the unintercalated cluster.

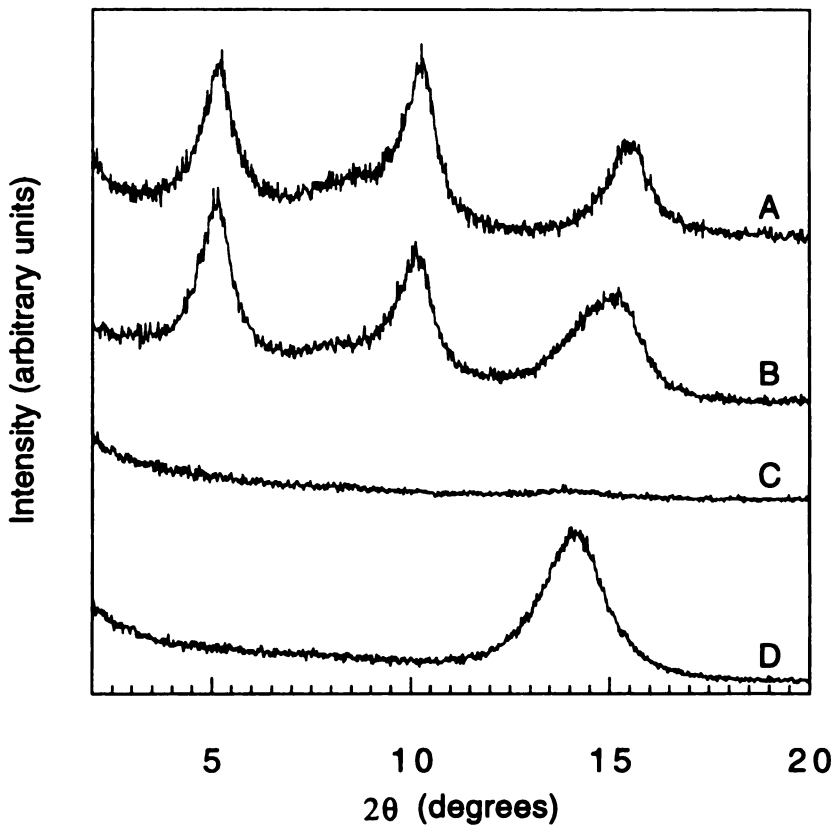

Figure 3.13. X-ray diffraction patterns upon thermal treatment of $[Fe_6S_8(PEt_3)_2]_{0.096}MoS_2$. The room temperature pattern (a) resembles the pattern upon heating to 100°C (b), but becomes amorphous by 150°C (c) and collapses to Fe_xMoS_2 (6.3 Å) by 200°C (d).

$[Ni_9S_9(PEt_3)_6]_{0.047}MoS_2$. The TGA of unintercalated $[Ni_9S_9(PEt_3)_6](ClO_4)_2$ is found in Figure 3.14a. The material loses most of its weight in a sharp step beginning at approximately 240°C, but continues to lose weight gradually until 650°C. Theoretical weight loss due to departure of triethyl phosphine ligands is 41%; the observed weight loss is 56.6%. Direct probe mass spectrometry indicates that the volatile product from the thermolysis of the unintercalated cluster is predominantly triethyl phosphine sulfide; predicted weight loss due to loss of triethyl phosphine sulfide is 52.3%, much closer to the experimentally observed value.

$[Ni_9S_9(PEt_3)_6]_{0.047}MoS_2$ also loses weight gradually all the way to 650°C; weight loss begins sooner but the material exhibits a significant drop around 160°C, a slightly lower temperature than the sharp step observed for the unintercalated cluster. Direct probe mass spectrometry indicates that the volatile product from the thermolysis of the unintercalated cluster is also triethyl phosphine sulfide (predicted weight loss due to $SPEt_3$, 13.4%; observed, 16.5%). The sulfur source in this case is probably the $[Ni_9S_9]^{2+}$ core, as even the unintercalated cluster loses its phosphine ligands as $SPEt_3$, leading to layer collapse. Additional weight loss may be due to co-encapsulated solvent.

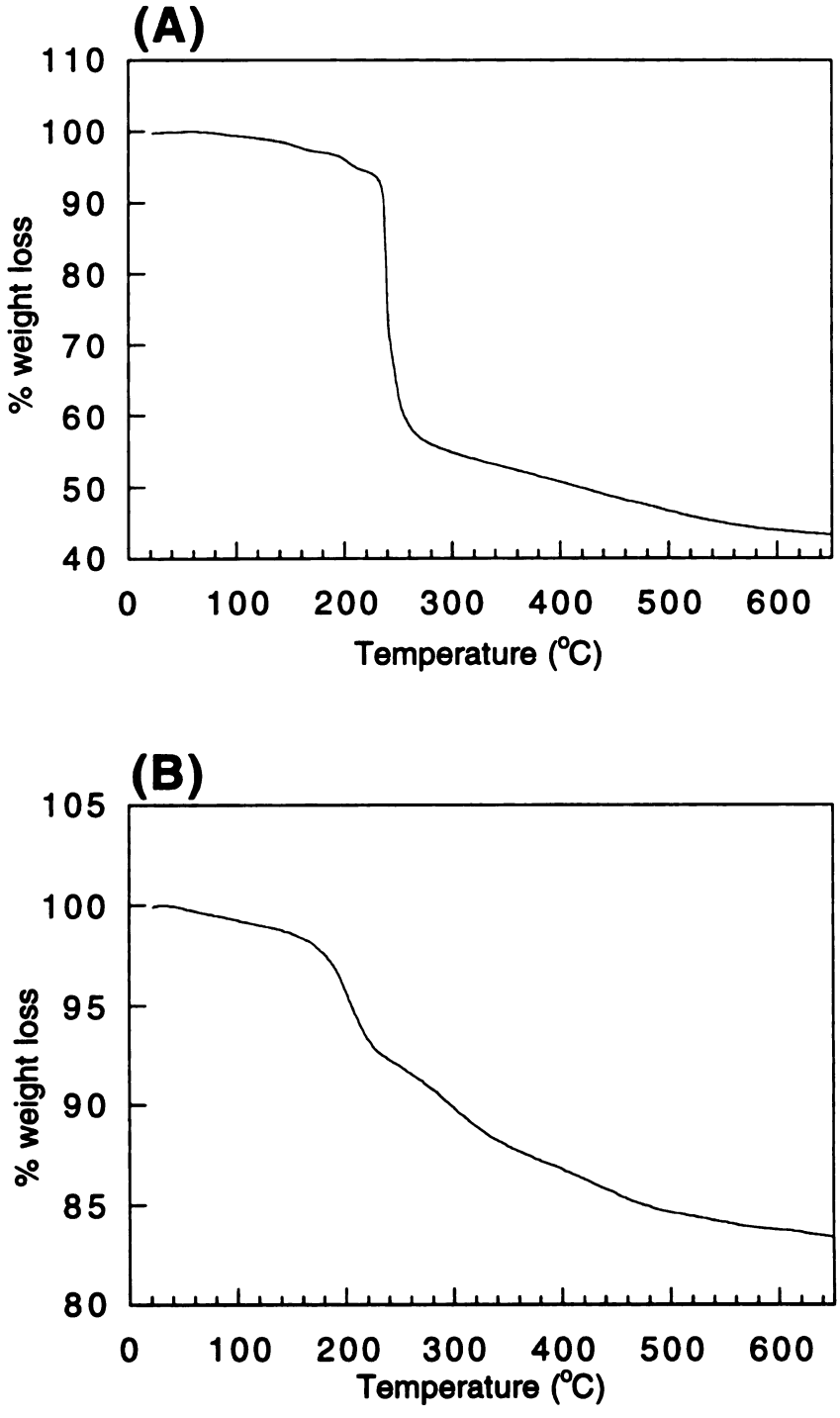

Figure 3.14. TGA of (A) $[Ni_9S_9(PEt_3)_6](ClO_4)_2$. Volatile product, lost in a clean step before 250°C, is $SPEt_3$ (expected weight loss due to $SPEt_3$, 52.3%; observed, 56.6%). (B) TGA of $[Ni_9S_9(PEt_3)_6]_{0.047}WS_2$. The volatile product is also $SPEt_3$ (expected loss, 13.4%; observed, 16.5%).

3.3.3 HDS Activity

HDS, or hydrodesulfurization, is a catalytic process used to remove sulfur-containing impurities from crude oil. The removal of these impurities prevents the formation of sulfur oxides upon combustion, which are precursors to acid rain. For example, an efficient HDS catalyst converts dibenzothiophene to biphenyl:

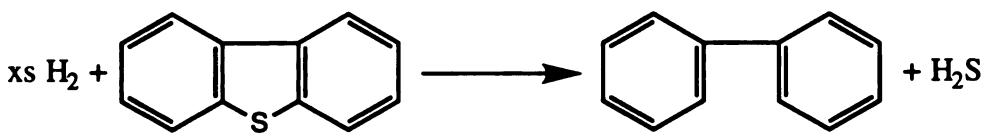

Eq. (3.2)

The effectiveness of an HDS catalyst depends not only on its activity, but also on its selectivity toward certain products. In the desulfurization of dibenzothiophene, the desired product is biphenyl. An undesirable product is cyclohexylbenzene:

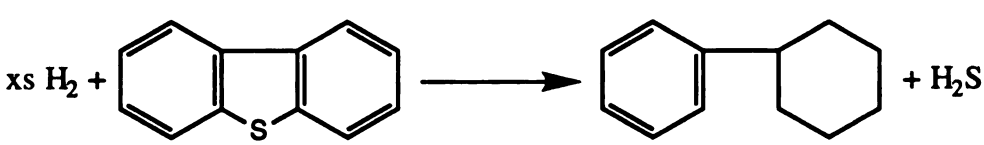

Eq. (3.3)

because it consumes additional H_2 gas.

The transition metal sulfides are a class of compounds which exhibit good HDS activity, with rhenium, osmium, and iridium sulfides being among the most effective.[26] Unfortunately, those particular metal sulfides are rather expensive. It has been known for many years that mixed-metal sulfide catalysts such as Co or Ni promoted MoS_2 or WS_2 (over an alumina

support) can provide comparable or better activity[27]. Although the more reasonable cost of these mixed-metal sulfides has resulted in widespread commercial use, the mechanism for their activity is not well understood, and a variety of models have been developed to try to explain their effectiveness[28, 29, 30, 31]

As mentioned previously, the $Co_6S_8(PPh_3)_6$ and $[Ni_9S_9(PEt_3)_6]^{2+}$ clusters were chosen as pillaring agents due to the similarity in chemical composition of the pillared products to the mixed-metal HDS catalysts. Most of the models place the active sites on the surfaces or edges of the particles; however, a material such as ours, in which the MS_2 layers have been propped apart with these clusters, may allow catalysis to take place in the interior of the particles, thereby enhancing the efficiency of the catalyst. Accordingly, the products were tested for HDS activity by reaction with dibenzothiophene (Eq. 3.2). The activities for a number of reference materials were collected as well. The results are summarized in Table 3.1. The selectivity of each catalyst toward biphenyl is reported in parentheses (as a percentage) next to the overall activity.

The results indicate that $[Co_6S_8(PPh_3)_6]_{0.02}MoS_2$ exhibits comparable catalytic activity to Crosfield 465 (Co-Mo) at 400°C. At 300°C its activity (38%) is actually better than the commercially available catalyst (20%).

Table 3.1. HDS catalytic activity and surface area (SA) of selected samples and references. Reported (as a function of temperature) are the percent conversion of dibenzothiophene to a non-sulfur containing product, and the percentage of biphenyl in the desulfurized products (in parentheses).[a]

Catalyst	400°C	350°C	300°C	200°C	SA (m^2/g)
$[Co_6S_8(PPh_3)_6]_{0.02}MoS_2$	85 (50)		38 (61)	15 (7)	26.8
Crosfield 465 (Co-Mo)	82 (80)	56 (91)	20 (85)	<5	
$0.2[Co_6S_8(PPh_3)_6]$ + restacked MoS_2	25 (73)	10 (76)	<5	<5	9.3
$[Ni_9S_9(PEt_3)_6]_{0.04}MoS_2$	58 (24)	35 (17)	32 (16)		
$[Ni_9S_9(PEt_3)_6]_{0.04}WS_2$	44 (21)	41 (16)	39 (8)		
Crosfield 504 (Ni-Mo)	98 (44)	58 (46)	27 (76)	10 (55)	
$[Al_{13}O_4(OH)_{24}(H_2O)_{12}]_{0.03}MoS_2$	6 (89)	<5	<5	<5	10.0
restacked MoS_2	22 (75)	9 (78)	<5	<5	10.0
2H-MoS_2	8 (88)	<5	<5	<5	5.8

[a]Run-to-run conversion reproducibility = ± 15% (e.g., 20 ± 3%). Amount of "active" metals (Co + Mo) in each run = 0.1 g in all cases.

Unpromoted 2H-MoS_2 is clearly an inferior catalyst, with an activity of only 8% at 400°C. Restacked MoS_2, although better than 2H-MoS_2 (22%), is still not as effective as $[Co_6S_8(PPh_3)_6]_{0.02}MoS_2$. In addition to these reference samples, a material consisting of a physical mixture of restacked MoS_2 and the $Co_6S_8(PPh_3)_6$ cluster in a ratio comparable to the stoichiometry of $[Co_6S_8(PPh_3)_6]_{0.02}MoS_2$ was prepared and tested ($0.2[Co_6S_8(PPh_3)_6]$ + restacked MoS_2). The results are only slightly better than restacked MoS_2 (25%), verifying that the increased catalytic activity in $[Co_6S_8(PPh_3)_6]_{0.02}MoS_2$ requires the insertion of the cluster between the layers. Unfortunately $[Co_6S_8(PPh_3)_6]_{0.02}MoS_2$ is not as selective toward biphenyl as Crosfield 465.

As discussed previously, the structure of $[Co_6S_8(PPh_3)_6]_{0.02}MoS_2$ under HDS conditions is ambiguous. HRTEM micrographs acquired after the catalysis suggest that some regions remain pillared whereas other regions have collapsed (Figure 3.15), but this method cannot probe the structure of the bulk of the sample. If in fact the sample is still pillared, as the micrograph suggests, the increase in activity may be due to the larger surface area of the sample (26.8 m^2/g) as compared to the surface areas of pristine MoS_2 (5.8 m^2/g), restacked MoS_2 (10.0 m^2/g), $[Al_{13}O_4(OH)_{24}(H_2O)_{12}]_{0.03}MoS_2$ (10.0 m^2/g), and ($0.2[Co_6S_8(PPh_3)_6]$ + restacked MoS_2) (9.3 m^2/g). Also, if one compares the surface areas of the

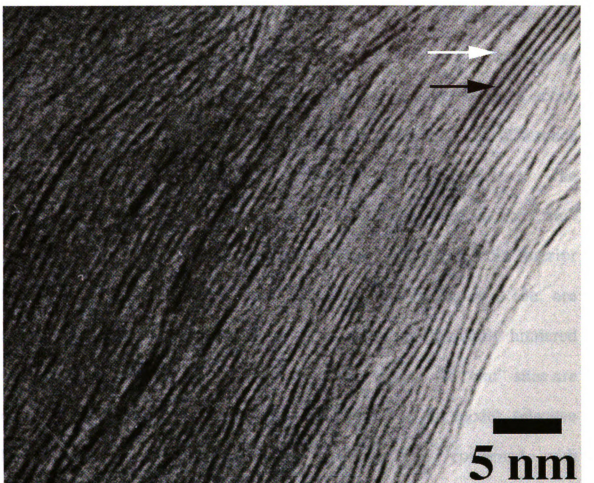

Figure 3.15. HRTEM micrograph of $[Co_6S_8(PPh_3)_6]_{0.02}MoS_2$ after HDS. Although some regions do not appear to be expanded (black arrow), other regions are still separated (white arrow). The observed d-spacing, 14.7 Å, corresponds to an expansion of 8.5 Å, consistent with the dimensions of the Co_6S_8 core.

samples to their selectivities toward biphenyl, it appears that higher surface area coincides with lower selectivity.

This possible relationship between surface area and selectivity supports the rim-edge model[31a] of the active sites. In this model all catalysis takes place on the exterior of the particle, not on the basal planes but at the perimeter of each layer. There are two different kinds of active sites: the "edge" sites and the "rim" sites. To understand the difference between the two, consider a stack of MoS_2 layers (Figure 3.16a). The perimeters of the layers at the top and bottom of the stack are the "rim" sites (much like the rim of a soup can). The perimeters of the interior layers, which comprise the bulk of the active sites in Figure 3.16a, are called "edge" sites. Unlike the "edge" sites, which are sterically hindered on both top and bottom by the presence of other layers, the "rim" sites are unrestricted on one side. According to the authors of this model, selective HDS takes place at "edge" sites, whereas HDS combined with hydrogenation takes place at the "rim" sites. The exfoliation/flocculation process used to synthesize restacked MoS_2 (and $[Co_6S_8(PPh_3)_6]_{0.02}MoS_2$) decreases the particle size (and increases the surface area) relative to 2H-MoS_2, resulting in more "rim" sites, which may explain why restacked MoS_2 shows higher activity (but less selectivity) than 2H-MoS_2. Furthermore, by propping the layers apart with the $Co_6S_8(PPh_3)_6$ cluster,

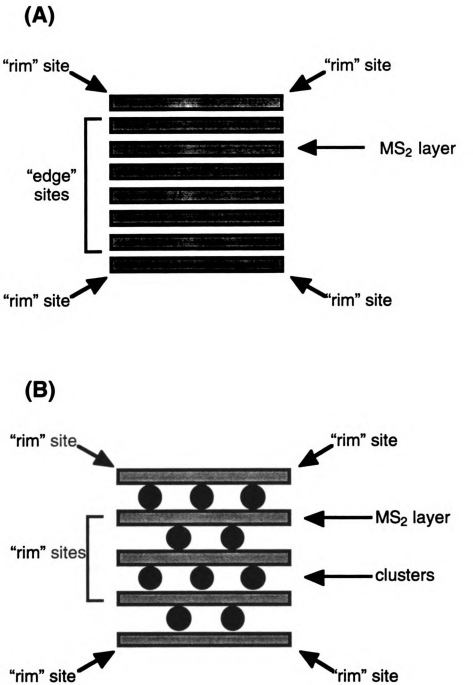

Figure 3.16. Illustration of the "rim-edge" model for (A) unpillared and (B) pillared MoS_2. In unpillared MoS_2, the "rim" sites are less selective toward biphenyl. In pillared MoS_2 the propping apart of the layers results in a higher number of "rim" sites, reducing the selectivity of the catalyst.

the surface area increases and even more "rim" sites are generated, which also results in a decrease in the selectivity (Figure 3.16b). The rim-edge model does not address the effects of Co- or Ni- containing species on the activity, however.

It is interesting to note that, although we considered the attack of the layers by the departing PPh_3 ligand to be a serious liability, in fact it may promote the activity of the material. In the "anion vacancy" model, the HDS active sites are sulfur vacancies in MoS_2 which are stabilized by the promoter species. Although sulfur vacancies induced by phosphine ligand evolution could explain increased activity in $[Co_6S_8(PPh_3)_6]_{0.02}MoS_2$, it does not explain the increase in the activity of restacked MoS_2 relative to 2H-MoS_2.

The activities of $[Ni_9S_9(PEt_3)_6]_{0.04}MoS_2$ and $[Ni_9S_9(PEt_3)_6]_{0.04}WS_2$ were disappointing in comparison to the activity of $[Co_6S_8(PPh_3)_6]_{0.02}MoS_2$. Although they are somewhat increased relative to restacked MoS_2 (58% and 44% over 22%), they are far lower than the activity of the commercially available catalyst Crosfield 504 (Ni-Mo) (98%) and their selectivity is the worst of all the catalysts. This behavior can be understood in terms of several factors. First, at HDS temperatures the encapsulated cluster has degraded (as discussed previously), most likely resulting in a material which is no longer pillared. Second, because the sulfide source of the

volatile triethyl phosphine sulfide is the $[Ni_9S_9]^{2+}$ cluster core, no additional sulfur vacancies are created by the departing ligand upon thermal treatment. The fact that there is any increase in the activity relative to restacked MoS_2 is more of a reflection on the effects of the Ni-containing species on the activity than it is on the rim-edge model or the anion vacancy model.

3.4 Conclusions

In conclusion, $Co_6S_8(PPh_3)_6$, $[Fe_6S_8(PEt_3)_6]^{2+}$, and $[Ni_9S_9(PEt_3)_6]^{2+}$ can be encapsulated in MoS_2 and WS_2 and exhibit expansions of 14.0 - 15.4 Å, 10.5 - 11.4 Å, and ~14 Å, respectively, which are consistent with the dimensions of the clusters. X-ray diffraction patterns from samples containing the neutral $Co_6S_8(PPh_3)_6$ species are weaker than the patterns from samples containing the cationic clusters. Although X-ray diffraction and TGA studies suggest little loss of phosphine prior to thermal treatment in $[Co_6S_8(PPh_3)_6]_{0.02}MoS_2$, HRTEM micrographs show loss of PPh_3 ligands, perhaps due to the ultrahigh vacuum or the limited applicability of the technique, which allows only the examination of the edges of thin particles. Furthermore, expansion of the layers appears to be localized. TGA studies indicate the loss of PEt_3 ligands prior to thermal treatment in $[Fe_6S_8(PEt_3)_2]_{0.096}MoS_2$ and $[Fe_6S_8(PEt_3)_3]_{0.2}WS_2$, and HRTEM micrographs

suggest some aggregation of the clusters. The orientation of the $Co_6S_8(PPh_3)_6$ or the $[Fe_6S_8(PEt_3)_2]^{2+}$ clusters in the layers is not known; it may change with loading and/or degree of phosphine coordination remaining in the encapsulated cluster. The orientation of the cluster in $[Fe_6S_8(PEt_3)_3]_{0.05}TaS_2$[20] is with its C_3 axis perpendicular to the MS_2 layers; this kind of arrangement makes sense, particularly at lower loadings, because it minimizes the observed expansion. The rather large expansion observed for $[Ni_9S_9(PEt_3)_6]_{0.07}MoS_2$ and $[Ni_9S_9(PEt_3)_6]_{0.077}WS_2$, coupled with the high loadings of the cluster and TGA studies revealing no loss of PEt_3 ligands prior to thermal treatment, imply that the clusters are packed with their Ni_3S_3 planes parallel to the MS_2 layers. Metallic conductivity of the samples verifies that the layers have not structurally transformed from the octahedral coordination found in $LiMoS_2$ and restacked MS_2 to the trigonal prismatic coordination found in 2H-MS_2.

The ability of MoS_2 and WS_2 to encapsulate all three of these clusters is both remarkable and perplexing. What is the driving force for the reaction, particularly the encapsulation of neutral species such as the $Co_6S_8(PPh_3)_6$ cluster? This ability of MoS_2 (and WS_2) to accept neutral molecules initially convinced some scientists that the layers were in fact completely oxidized in the exfoliation process.[9] However, increasing evidence of facile encapsulation of cationic species, often with a high degree of order, suggests that the layers retain some negative charge. The

driving force for the encapsulation of cationic species would simply be an electrostatic interaction. The degree of charge remaining on the layers is difficult to determine from these samples, as a range of stoichiometries for all clusters can be observed. Furthermore, residual negative charge on the layers may explain the encapsulation of species such as the $[Fe_6S_8(PEt_3)_6]^{2+}$ and the $[Ni_9S_9(PEt_3)_6]^{2+}$ clusters, but it still does not explain the ability of these layers to also incorporate neutral species. Admittedly, the encapsulation of the neutral cluster is more difficult, requiring sonication and two days of stirring, and is sometimes difficult to reproduce. Encapsulation can be expedited by bubbling oxygen or air through the reaction mixture, or by (cautiously) introducing a neutral oxidizing agent such as I_2. This indicates that the layers may require further oxidation, either with time or with additional oxidizing agents in the reaction, before neutral species can be encapsulated. In addition, it is probable that small amounts of Li^+ cations, which are extremely difficult to detect, are co-encapsulated with the $Co_6S_8(PPh_3)_6$ cluster. However, the driving force for neutral cluster encapsulation remains a mystery.

Thermal treatment combined with mass spectrometry reveals that all phosphine ligands depart from the samples as phosphine sulfide. In $[Co_6S_8(PPh_3)_6]_{0.02}MoS_2$ and $[Fe_6S_8(PEt_3)_y]_xMS_2$ the phosphines appear to attack the layers as they depart; even the unencapsulated $[Ni_9S_9(PEt_3)_6]^{2+}$

cluster decomposes to $SPEt_3$, indicating that the sulfur source in all samples is the $[Ni_9S_9]^{2+}$ core.

The HDS activity of $[Co_6S_8(PPh_3)_6]_{0.02}MoS_2$ is comparable to the commercially available catalyst Crosfield 465 (Co-Mo); however, it is less selective toward desirable products such as biphenyl. Although the poor selectivity prohibits it from becoming commercially viable, the correlation between surface area and activity seems to support the "rim-edge" model to describe a mechanism for selectivity. In addition, the attack of the layers by the departing phosphine ligand does not seem to inhibit catalytic activity; in fact, it may help promote it.

References

1. Barrer, R.M. "Zeolites and Clay Minerals as Sorbents and Molecular Sieves," Academic Press, New York, 1978, p407.

2. a) Pinnavaia, T.J. "Characterization of Catalytic Materials," Wachs, I.E. (Ed.), Manning Publications Co, Greenwich CT, 1992, p149. b) Johnson, I.D.; Werpy, T.A.; Pinnavaia, T.J. *J. Am. Chem. Soc.,* 1988, **110**, 8545. c) Pinnavaia, T.J. *Science*, 1983, **220**, 365.

3. Kresge, C.T.; Leonowizc, M.E.; Roth, W.J.; Vartuli, J.C.; and Beck, J.S. *Nature,* 1992, **359**, 710.

4. a) Hanko, J.A.; Kanatzidis, M.G. *Angew. Chem. Int. Ed.,* 1998, **37**, 342. b), Stephan, H.-O.; Kanatzidis, M.G. *J. Am. Chem. Soc.,* 1996, **118**, 12226. c) Chou, J.-H., Kanatzidis, M.G. *Chem. Mater.,* 1995, **7**, 5. d) Chou, J.-H., Kanatzidis, M.G. *Inorg. Chem.,* 1995, **33**, 1001. e) Parise, J.B. *Science,* 1991, **251**, 293.

5. a) Yaghi, O.M.; Sun, Z.; Richardson, D.A.; Groy, T.L. *J. Am. Chem. Soc.,* 1994, **116**, 807. b) Tan, K.; Darovsky, A.; Parise, J.B. *J. Am. Chem. Soc.,* 1995, **117**, 7039. c) Ahari, H.; Garcia, A.; Kirkby, S.; Ozin, G.A.; Young, D.; and Lough, A.J. *J. Chem. Soc., Dalton Trans.,* 1998, 2023.

6. a) Bedard, B.L.; Wilson, S.T.; Vail, L.D.; Bennet, J.M.; Flanigen, E.M. *Zeolites, Facts, Figures, Future.* Jacobs, P.A.; van Santen, R.A. (Eds.) Elsevier Science Publishers B.; Amsterdam, the Netherlands, 1989, 375-387. b) Jiang, T.; Lough, A.; Ozin, G.A.; Bedard, R.L.; Broach, R. *J. Mater. Chem.,* 1998, **8**, 721. c) Jiang, T.; Lough, A.; Ozin, G.A.; Bedard, R.L. *J. Mater. Chem.,* 1998, **8**, 733. d) Ahari, H.; Bowes, C.L.; Jiang, T.; Lough, A.; Ozin, G.A.; Bedard, R.L.; Petrov, S.; Young, D. *Adv. Mater.,* 1995, **7**, 375. e) Ahari, H.; Ozin, g.A.; Bedard, R.L.; Petrov, S.; Young, D. *Adv. Mater.,* 1995, **7**, 370. f) Bowes, C.L.; Petrov, S.; Vovk, G.; Young, D.; Ozin, G.A.; Bedard, R.L. *J. Mater. Chem.,* 1998, **8**, 711.

7. a) Dhingra, S.; Kanatzidis, M.G. *Science,* 1992, **258**, 1769. b) Chondroudis, K.; Kanatzidis, M.G. *J. Am. Chem. Soc.,* 1997, **119**, 2574. c) Sheldrick, W.S.; Braunbeck, H.-G. *Z. Naturforsch,* 1990, **45b**, 1643. d) Marking, G.A.; Kanatzidis, M.G. *Chem. Mater.,* 1995,

7, 1915. e) McCarthy, T.J.; Tanzer, T.A.; Kanatzidis, M.G. *J. Am. Chem. Soc.,* 1995, **117**, 1294.

8. Eisenmann, B.; Jackowski, J.; Schafer, H. *Rev. Chim. Min.,* 1983, **20**, 295.

9. Bowes, C.L.; Ozin, G.A.; *Adv. Mater.,* 1996, **8**, 13.

10. Li, H.; Laine, A.; O'Keefe, M.; Yaghi, O.M. *Science,* 1999, **283**, 1145.

11. a) Wachhold, M.; Rangan, K.K.; Billinge, S.J.L.; Petkov, V.; Heising, J.; Kanatzidis, M.G. submitted. b) MacLachlan, M.J.; Coombs, N.; Ozin, G.A. *Nature,* 1999, **397**, 681.

12. a) Whittingham, M.S.*Prog. Solid St. Chem.,* 1978, **12**, 41-99. b) Rouxel, J. "Layered Metal Chalcogenides and their Intercalation Chemistry." *Comprehensive Supramolecular Chemistry,* Alberti, G.; Bein, T., Eds. Vol. 7, Pergamon Press, New York, 1996, p77-105.

13. (a) Bissessur, R.; Kanatzidis, M.G.; Schindler, J.L.; Kannewurf, C.R. *J. Chem. Soc. Chem. Commun.* 1993, 1582. (b) Kanatzidis, M.G.; Bissessur, R.; De Groot, D.C.; Schindler, J.L.; Kannewurf, C.R. *Chem. Mater.* 1993, **5**, 595. (c) Wang, L.; Schindler, J.L.; Thomas, J.A.; Kannewurf, C.R.; Kanatzidis, M.G. *Chem. Mater.*, 1995, **7**, 1753.

14. Lemmon , J.P.; Lerner, M.M. *Chem. Mater.*, 1994, **6**, 207.

15. (a) Divigalpitiya, W.M.R.; Frindt, R.F.; Morrison, S.R. *Science* 1989, **246**, 371. (b) Divigalpitiya, W.M.R.; Frindt, R.F.; Morrison, S.R. *J. Mater. Res.* 1991, **6**, 1103.

16. Tigaya, H.; Hashmoto, T.; Karasu, M.; Izumi, T.; Chiba, K. *Chem. Lett.* 1991, 2113.

17. Heising, J.; Bonhomme, F.; Kanatzidis, M.G. *J. Solid State Chem.,* 1998, **139**, 22.

18. a) Bissessur, R.; Heising, J.; Hirpo, W.; Kanatzidis, M.G. *Chem. Mater.*, 1996, **8**, 318. b) Brenner, J.; Marshall, C.; Ellis,L.; Tomczyk,N.; Heising, J.; Kanatzidis, M.G.*Chem. Mater.*, 1998, **10**, 1244. c) Bissessur, R. "Synthesis and Characterization of Novel

Intercalation Compounds of Molybdenum Trioxide and Molybdenum Disulfide." Ph.D. Dissertation, Michigan State University, 1994.

19. a) Rudorff, W. *Chimia* 1965 **19**, 489. b) Bayer, E.; Rudorff, W. *Z. Naturforsch* 1972, **27b**, 1336. c) Schöllhorn, R.; Bethel, J.; Paulus, W. *Rev. Chim. Miner.*, 1984, **21**, 545. d) Miremadi, B.K.;. Morrison, S.R. *J. Appl. Phys.* 1988, **63**, 4970.

20. (a) Nazar, L.F.; Jacobson, A.J. *J. Chem. Soc. Chem. Commun.* 1986, 570. (b) Nazar, L.F.; Jacobson, A.J. *J. Mater. Chem.*, 1994, **4**, 149.

21. Hong, M.; Huang, Z.; Lei, Z.; Wei, G.; Kang, B.; Liu, H. *Polyhedron* 1991, **10**, 927.

22. Agresti, A.; Bacci, M.; Cecconi, F.; Ghilardi, C.A.; Midollini, S. *Inorg. Chem.* 1985, **24**, 689.

23. Cecconi, F.; Ghilardi, C.A.; Midollini, S. *Inorg. Chem.* 1983, **22**, 3802.

24. Murphy, D.W.; DiSalvo, F.J.; Hull, G.W. Jr.; Wasczak, J.V. *Inorg. Chem.* 1976, **15**, 17.

25. Py, M.A.; Haering, R.R.. *Can. J. Phys.* 1983, **61**, 76.

26. a) Pecoraro, T.A.; Chianelli, R.R. *J. Catal.*, 1981, **67**, 430. b) Harris, S.; Chianelli, R.R. *J. Catal.*, 1984, **86**, 400. c) Ledoux, M.J.; Michaux, O.; Agostini, G.; Panissod, P. *J. Catal.*, 1986, **102**, 275.

27. Massoth, F.E. *Adv. Catal.*, 1978, **27**, 265.

28. a) Lipsch, J.M.J.G.; Schuit, g.C.A. *J. Catal.*, 1969, **15**, 179. b) Massoth, F.E. *J. Catal.*, 1977, **50**, 190.

29. a) Farragher, A.L.; Cossee, P. "Proceedings, 5th International Congress on Catalysis, Palm Beach, 1972", Hightower, J.W., Ed., North-Holland, Amsterdam, 1973, 1301. b) Dungey, K.E.; Curtis, M.D.; Penner-Hahn, J.E. *J. Catal.*, 1998, **175**, 129.

30. Topsøe, H.; Clausen, B.S. *Catal. Rev. -Sci. Eng.*, 1984, **26**, 395.

31. a) Daage, M.; Chianelli, R.R. *J. Catal.*, 1994, **149**, 414. b) Del Valle, M.; Cruz-Reyes, J.; Avalos, Borja, M.; Fuentes, S. *Catal. Lett.*, 1998, **54**, 59.

CHAPTER 4

Structure of Restacked MoS_2 and WS_2 Elucidated by Electron Crystallography

4.0 Abstract

There has been a lot of confusion about the nature of restacked MoS_2 and WS_2. The structure has been proposed to be trigonal TiS_2 type with octahedral M^{4+} and called 1T-MoS_2. The presence of a distortion in the metal plane which gives rise to a superstructure has been suggested. We have performed electron crystallographic studies on small (sub micron) single crystal domains of restacked WS_2 and MoS_2 in order to solve their superstructure. We find that what initially seems to be a trigonal crystal is actually a "triplet" of three individual orthorhombic crystals. Using two-dimensional *hk0* data from films for both "triple" and "single" crystals we calculated corresponding Patterson projections, which reveal a severe distortion in the Mo/W plane, forming infinite zigzag chains. The projection of the structure suggests M-M distances of 2.92 Å and 2.74 Å for MoS_2 and WS_2, respectively. Least squares refinement from the single crystal data gives R_1=13.3% for WS_2 and R_1=15.3% for MoS_2. Therefore, we submit that restacked MoS_2 and WS_2 are not 1T-form but rather WTe_2 type.

4.1 Introduction

Due to a unique combination of valuable structural, electronic, and optical properties, the layered dichalcogenides have been studied and used for a litany of practical applications.[1,3-4] One of the most versatile members of this class of compounds is MoS_2. Found in nature in its 2H form as the mineral molybdenite[2], its inexpensiveness and availability have permitted its use as a solid lubricant, a catalyst for hydrodesulfurization[3], a host for intercalation chemistry and an electrode material for solid state batteries[4].

Many layered transition metal chalcogenides can be treated with n-Butyl lithium to form a reduced species in which lithium occupies the space between the layers[5]. (This ability to undergo reduction and accept lithium is one important reason why these materials have been investigated for solid state batteries.) The redox properties of these reduced dichalcogenides vary from one compound to the next, but some have the remarkable ability to form suspensions in water, much like clays. The chemistry of $LiMoS_2$ (and $LiWS_2$) in water is particularly fascinating because, after undergoing a redox reaction with water to form H_2 (g) and LiOH, a suspension of colloidally dispersed single layers is formed, and the layers can remain separated from one another in water for days. The material can be "restacked" by filtration, precipitation, centrifugation, or

evaporation. Due to this remarkable ability, many guest species have been encapsulated between the layers.[6,7,8]

There has been a lot of confusion about the nature of restacked MoS_2 and WS_2. The presence of a distortion in the metal plane which gives rise to a superstructure has been suggested. The reduction of the 2H form appears to induce a structural transformation from trigonal prismatic coordination about the metal to octahedral coordination.[9] The structure has been proposed to be trigonal TiS_2 type[10] with octahedral M^{4+} and called 1T-MoS_2. Originally, 1T-MoS_2 was synthesized by the oxidation of $K_x(H_2O)_yMoS_2$ instead of the exfoliation/restacking method, but the products of both synthetic methods exhibit metallic conductivity and an exothermic transition around 90-100°C which suggests that they are identical.[11] The layered dichalcogenides are prone to a wide variety of structural distortions caused by Charge Density Waves (CDWs), resulting in significant changes in the properties of the materials.[12] The source of confusion is that several superlattices have been reported for 1T-MoS_2 (Figure 4.1).

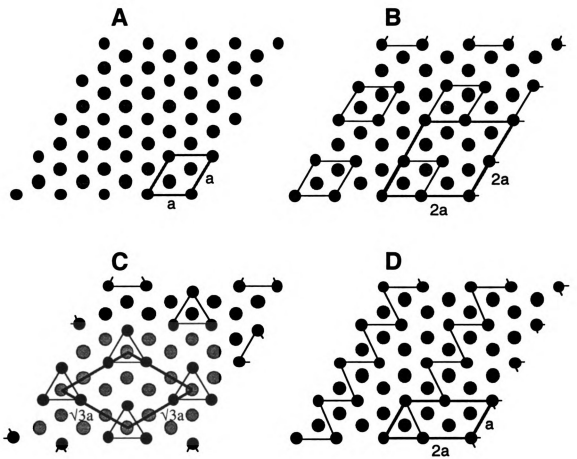

Figure 4.1. Schematic illustrating the proposed superstructures of restacked/1T-MoS_2. The superstructures derive from bonding associations of metal atoms. (A) An ideal undistorted lattice, (B) a tetramerization, (C) a trimerization, and (D) zig-zag chain formation. Black circles represent Mo, gray circles, S.

EXAFS (Extended X-ray Absorption Fine Structure) analyses have indicated M-M associations, but are not able to provide a structural model. X-ray and electron diffraction studies of the restacked MoS_2 (and WS_2) have indicated a *2a x 2a* superstructure in the *ab* plane. A tetramerization model was proposed based on the X-ray diffraction studies.[13,14] The electron diffraction studies on restacked WS_2, however, found that the hexagonal symmetry was preserved, but the proposed tetramerization model is incompatible with this finding.[15] To add to the confusion, another electron diffraction study on $LiMoS_2$ found the same *2a x 2a* superstructure, but the authors attributed it to lithium ordering between the layers.[16] Later, an STM study of the surface layer of restacked MoS_2 suggested a *2a x a* superstructure caused by the formation of zig-zag chains.[17] The original 1T-MoS_2, however, is reported to exhibit a $\sqrt{3}a$ x $\sqrt{3}a$ superstructure, which would be best described by a trimerization model.[11,18] In an effort to clarify the structure, we have performed 2-dimensional *electron crystallographic* studies on restacked WS_2 and MoS_2. This method has enabled us to probe the bulk material, not just the local environments of the atoms or the structure at the surface. Furthermore, it has allowed us not only to directly determine the structure, but to refine it as well.

X-rays are scattered by the electron shells of atoms; electrons, on the other hand, are scattered by the electrostatic potential due to the atomic nuclei and their electron clouds. Despite the different origins of scattering, much of the theory developed for X-ray crystallography can be applied to electron crystallography and thus, in principle, the two techniques provide similar structural information.[19,20] Most experimentalists have avoided electron diffraction as a technique for structure solution, however, because electrons interact more strongly with the sample than X-rays; hence, multiple scattering events (secondary and dynamic scattering) may take place in electron diffraction.[19,20] Because a TEM (Transmission Electron Microscope) is capable of high magnification, it is possible to acquire data for many samples which cannot be investigated by single crystal X-ray methods.[19,20] Furthermore, the wavelength of an electron (at an accelerating voltage of 120kV) is 0.0335 Å; as compared to 0.71 Å for Ka Mo radiation, which (theoretically) can lead to higher resolution data. Because the Ewald sphere is much flatter, many reflections can be observed simultaneously for one orientation of the crystal.[19-21,22]

We have discovered that, despite the presence of Mo/W in our samples, quasi-kinematical data are acquired, from which a plausible projection of the structure can be obtained and refined.

4.2 Experimental

$LiMS_2$ (M=Mo, W) was synthesized by reacting 2H-MS_2 with excess $LiBH_4$ at 300-350°C for 3 days. Restacked MS_2[6,13] was synthesized by reacting $LiMS_2$ with H_2O, rinsing several times to remove the LiOH generated in the exfoliation process, and depositing the solution on a copper carbon coated grid. The grids were examined at 120kV on a JEOL 120CX TEM. Suitable crystals were located and their diffraction patterns captured on film. The negatives of the diffraction patterns were scanned into the computer at 600 dpi. The patterns were indexed to an orthorhombic cell with a =5.56Å and b=3.21Å, related to the subcell by the relation $\sqrt{3}a_{sub} \times a_{sub}$. The "Gel Plotting Macro" in NIH Image 1.60 was used to extract the integrated intensities (I_{hk0}) from the patterns.[23] Accurate cell parameters a and b were determined from powder diffraction data using a Rigaku-Denki/RW400F2 (Rotaflex) rotating anode powder diffractometer.

The data were converted into .hkl file format for use in SHELXTL programs.[24] The two-dimensional Patterson maps were calculated from the data by Equation 4.1:

$$P(u,v) = \frac{2}{A}\sum_h\sum_k |\Phi(hk)|^2 \cos 2\pi(hu+kv) \qquad \text{Eq. (4.1)}$$

Where P corresponds to electron density overlap in the structure (i.e. the Patterson function), A is the unit cell area, and $|\Phi(hk)| = \sqrt{I_{hk}}$.[19] Least squares refinement of the structure in SHELXTL (version 5)[24] were carried out after the coefficients for the electron scattering factors were obtained by fitting the $\sin\theta/\lambda$ curves using the program Curve Expert.[25]

4.3 Results and Discussion

4.3.1 Data Collection

Because restacked MoS_2 and WS_2 are layered compounds with plate-like morphology, they exhibit preferred orientation which causes the *ab* plane to be perpendicular to the electron beam, and the diffraction patterns consistently contained only *hk0* data. Our initial efforts to locate a suitable crystal resulted in pictures similar to Figure 4.2a-4.2b. The patterns suggested a *2a x 2a* superstructure. Upon consideration, however, we recognized that the exfoliation/flocculation process, involved in the synthesis of restacked MoS_2 and WS_2, would result in turbostratic materials, or at least materials susceptible to stacking faults, and that this could result in pronounced twinning phenomena. We then targeted

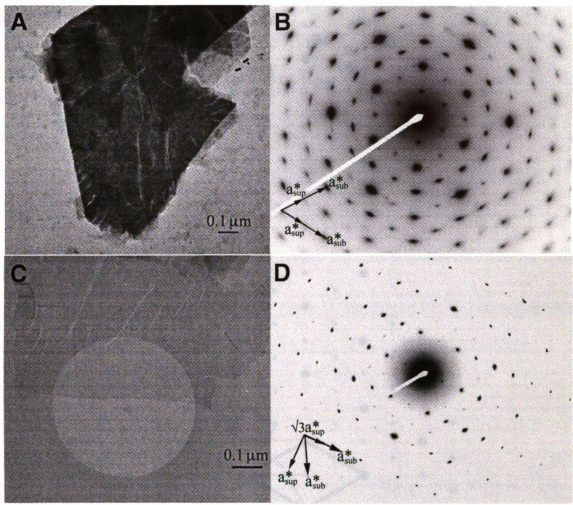

Figure 4.2. (A) Bright field image and (B) selected area electron diffraction pattern from a "triple" WS_2 crystal, giving rise to an apparent *2a x 2a* hexagonal superstructure. (C) Bright field image and (D) selected area electron diffraction pattern from a "single" WS_2 crystal, giving rise to a *2a x a* or $\sqrt{3}a$ *x a* superstructure.

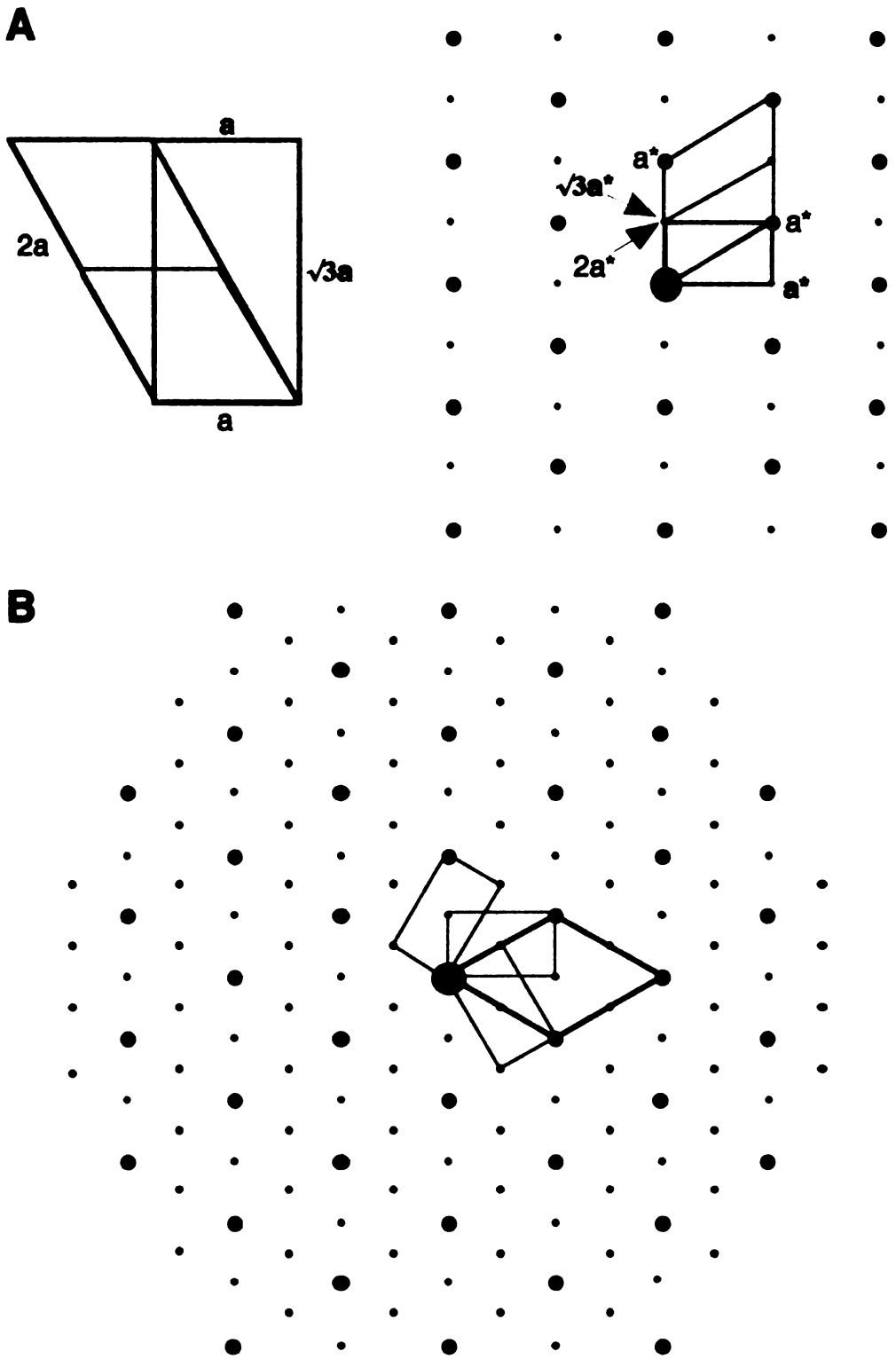

Figure 4.3. (A) Relationship between the *2a x a* and $\sqrt{3}a$ *x a* lattice. (B) Illustration of how three $\sqrt{3}a$ *x a* patterns can be overlapped to form a *2a x 2a* pattern. Note that only the sublattice reflections overlap.

extremely thin crystals in our investigations and found that, in fact, restacked WS_2 and MoS_2 have a *2a x a* superstructure (Figure 4.2c-4.2d), which is consistent with the results of the STM studies of restacked MoS_2.[17] This *2a x a* superstructure can actually be more simply described by an orthorhombic $\sqrt{3}a$ *x a* cell (Figure 4.3a). Note that $a = a$ but $a^* \neq a^*$ in the two unit cells because of the change from a hexagonal to an orthorhombic crystal system. The *2a x 2a* superstructure is in fact a "triplet" of three $\sqrt{3}a$ *x a* crystals rotated by 120 degrees relative to each other. This causes their diffraction spots to be aligned with respect to the sublattice reflections but not the superlattice reflections (Figure 4.3b).

4.3.2 Structure solution from the "triplet" crystal of WS_2

Because a "single" crystal pattern of sufficient quality was not initially available, we proceeded with the structure determination using the twinned crystal depicted in Figure 4.2a-4.2b. Intensities of the reflections were extracted from the diffraction pattern using the "Gel Plotting Macro" of NIH Image 1.60.[23] This Macro was developed to calculate concentrations in gel electrophoresis experiments by a comparison of the

bands in a sample to the same bands in reference samples of known concentrations. In order to make this comparison it is necessary to consider not only how dark (or light) the band, but also the area occupied by the band. Similarly, the intensity of a reflection in an electron diffraction pattern is a function of the area of the spot as well as its optical density. No external standard is required because only the "relative" intensities of the reflections are necessary for structure determination. Accordingly, the diffraction pattern was indexed to the three orthorhombic cells and the relative intensities of the reflections were extracted from the pattern (Figure 4.4). First the macro creates a one-dimensional set of peaks from the data; then the width and baseline of the peaks are specified and a numerical value for the integrated intensity is extracted. A 2-D rolling ball background subtraction suggested in the "Gel Plotting Macros" manual was applied, as well as a Lorentz correction recommended by early electron crystallographers.[19] Intensities of reflections from all three of the "triplet" cells were extracted, but only the cell with the strongest reflections was used. The intensity of the subcell reflections were corrected for the twinning by dividing by three.

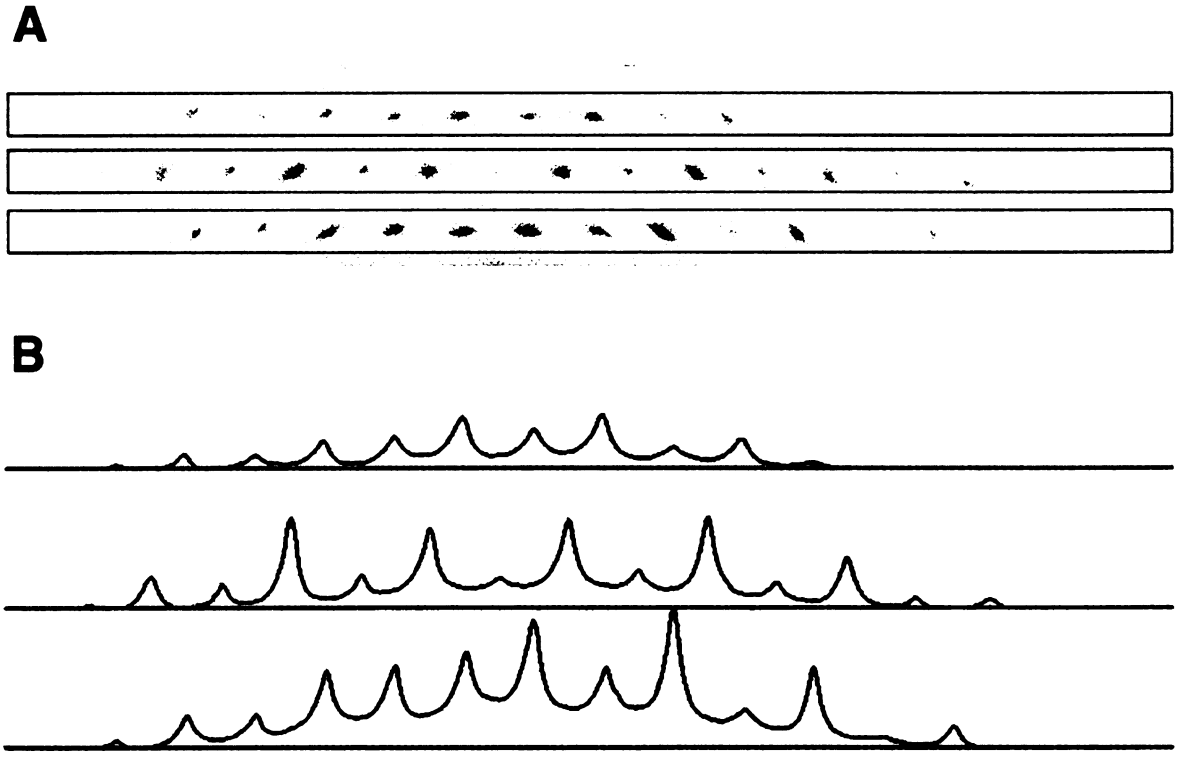

Figure 4.4. Illustration of the "Gel Plotting Macro" in NIH Image 1.60. (A) Lanes of reflections are specified, then (B) converted to a set of one-dimensional peaks from which the integrated intensities of the reflections can be extracted.

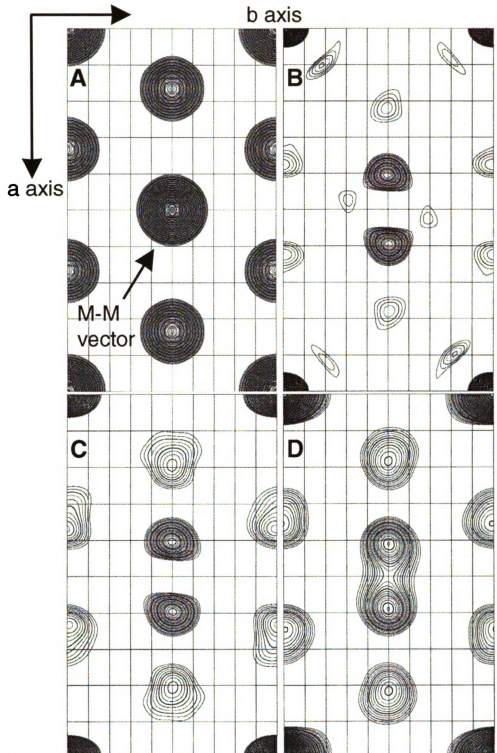

Figure 4.5. Two-dimensional Patterson projections along the c-axis: (A) ideal 1T-MS_2 (from simulated data) (B) restacked WS_2 with background subtraction and Lorentz correction (C) restacked WS_2 with only the Lorentz correction (D) restacked WS_2 with no corrections. All experimental patterns indicate a deviation in the W-W atom vector.

A two-dimensional Patterson contour plot generated from the extracted data clearly indicates a substantial deviation in the metal atom position from the ideal position in the 1T-TiS_2 structure type, which gives rise to a short M-M distance (Figure 4.5b). In an ideal 1T structure the electron density overlap at the center of the Patterson map, which is indicative of the M-M vector in the structure, is circular (Figure 4.5a). This translation of the metal atom along the $\sqrt{3}a$ axis can only be explained by the formation of zig-zag chains. This kind of distortion has been observed in WTe_2,[26] another layered dichalcogenide with (distorted) octahedral coordination about the metal atom, and represents a significant departure from the ideal structure, TiS_2.[10] Distortion of layered octahedral ML_2 d^2 systems to form zig-zag chains due to a charge density wave has been predicted by Rovira and Whangbo.[27] This kind of distortion gives rise to changes in the band structure of the material which are consistent with the properties we have observed.[28]

The Patterson map in Figure 4.5b contains some strange features which had to be addressed before refinement of the structure was possible, however. The M-S vector peaks are very weak, and there are other puzzling features which seem to indicate short atom-atom vectors in the structure. These vectors became more pronounced with the elimination of higher order reflections. They disappeared completely, however, when the

2-D rolling ball background subtraction was eliminated from the data extraction procedure. Electron diffraction patterns have a rather high, sloping background due to diffuse scattering which occurs in all samples. The peaks closest to the main beam are most severely affected. A background subtraction seemed an ideal manner to address this problem; however, use of the background subtraction method in the "Gel Plotting Macro" obviously results in perturbation of the data, particularly the data closest to the main beam, because the contribution of the background is less significant in gel electrophoresis samples than in electron diffraction patterns. The background can be removed manually (with much better results) during the step in which the baseline is specified for each peak. Also, data from two different camera lengths were combined. Use of a larger camera length allows reflections to be collected further away from the main beam on the negative, whereas the smaller camera length allows higher order reflections (which provide better resolution) to be collected. The modified data set gave rise to the Patterson map found in Figure 4.5c.

Least squares refinement of this data set in SHELXTL (version 5)[24] against a WTe_2 type model gives an R_1 value of 36.8% (Tables 4.1 and 4.2). Structures with comparable R_1 values solved by electron diffraction have actually been published by early electron crystallographers.[19] Such a high R_1 value is considered acceptable for many systems due to the

Table 4.1. Crystal data and structure refinement for restacked WS_2.

Empirical formula	WS_2
Formula weight	248.00
Temperature	293 K
Wavelength	0.0335 Å
Crystal system	Rectangular
Plane group	pg (#4)
Unit cell dimensions	a = 5.56 Å
	b = 3.21 Å
	γ = 90 deg.
Area (Å^2)	17.295
Z	2
Φ (000)	46
2θ range for data collection	0.36 to 4.20 deg.
Data resolution	0.09 to 1.1 sinθ/λ
Index ranges	-12<=h<=10, -5<=k<=5
Reflections collected	173
Independent reflections	99
Refinement method	Full-matrix l.s. on Φ^2
Data / restraints / parameters	99 / 0 / 7
Goodness-of-fit on Φ^2	0.874
R indices (all data)[a]	R_1 = 0.3683

[a] $R_1 = \Sigma(||\Phi_o| - K|\Phi_c||) / \Sigma|\Phi_o|$

Table 4.2. Preliminary atomic coordinates (x 10^4) and equivalent isotropic displacement parameters (A^2 x 10^3) for restacked WS_2.

	x	y	U(eq)	Occ.
W(1)	-2022	0	1	1
S(1)	4231	0	724	1
S(2)	997	0	1100	1

U(eq) is defined as one third of the trace of the orthogonalized Uij tensor.

susceptibility of the electron diffraction data to perturbation by multiple scattering events, as mentioned previously. In order to improve the refinement, we attempted a two-beam dynamic scattering correction.

4.3.3 Dynamic Scattering: Two-Beam Approximation

Dynamic scattering has inhibited the widespread use of electron diffraction data for structure determination, particularly in samples containing heavy elements. A schematic depicting the perturbation of the electron diffraction data by dynamic scattering is found in Figure 4.6. In the ideal situation (found in X-ray diffraction), called "kinematic" scattering, the radiation source is diffracted only one time as it passes through the sample. Due to the strong interaction of the electron beam with the sample, however, electrons can be diffracted many times as they pass through the sample. The thicker the sample, the greater its susceptibility to multiple scattering events. One can then consider the intensity of each diffracted beam to be "contaminated" with intensity from the other diffracted beams, and also "contaminated" due to the loss of some of its original intensity to other reflections:

$$I_{dyn} = (I_{kin} - I_{lost}) + I'_{gained} \qquad \text{Eq.(4.2)}$$

Historically, correction for this phenomenon has been attempted in more than one way. The two-beam approximation tries to simplify the problem by treating the data as if the pattern comes from a "mosaic" of small crystals, each with a unique and perfect orientation such that only that one

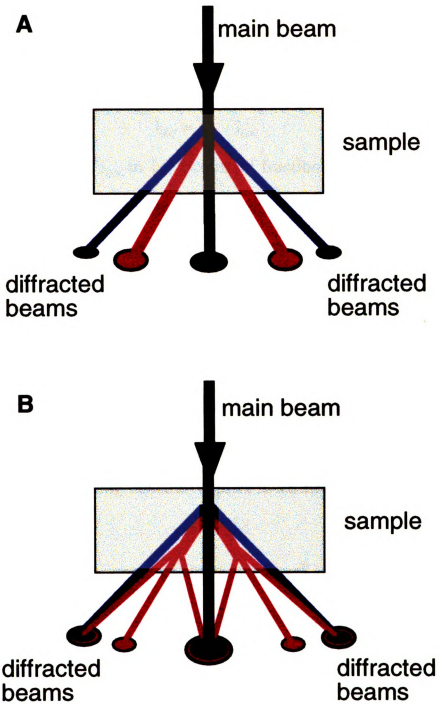

Figure 4.6. Schematic illustrating (A) kinematic scattering, in which the electron beam is diffracted only once as it passes through the sample and (B) dynamic scattering, in which the beam is diffracted multiple times, resulting in "contamination" of the intensity of all the reflections.

reflection is produced per crystal. Each reflection therefore functions completely independently of all the other reflections in the pattern.[19,29,35] In this case, the intensity of each diffracted beam can be conceptualized as

$$I_{diff} = I_{kin} - I_{lost} \qquad \text{Eq.(4.3)}$$

If one imagines I_{lost} to be a constant fraction (say, 30%) of the original intensity of each reflection, it becomes clear that the strongest reflections will be most noticeably affected. The mathematics are actually somewhat more complicated, but the net effect is a homogenization of the diffraction pattern. In order to adjust for this 'homogenization', a method has been developed to correct the experimental data.[29] It operates under the assumption that most reflections scatter kinematically, but a few of the most intense reflections exhibit "deviations toward dynamic scattering."[19]

The following equation applies in a kinematically scattering crystal:

$$I = Q^2\mathcal{L} \qquad \text{Eq.(4.4)}$$

in which Q is a normalized structure factor[30] and $\mathcal{L}$ is a Lorentz correction (in this case, to divide each reflection by its d-spacing). In a dynamically scattering crystal the equation is slightly modified:

$$I = Q^2A_3K(A_3Q)\mathcal{L} \qquad \text{Eq.(4.5)}$$

such that it now includes a term for the thickness of the crystal (A_3) and a function $K(A_3Q)$, shown in Figure 4.7, which describes dynamic scattering

as a function of the product of the thickness and the normalized structure factor.

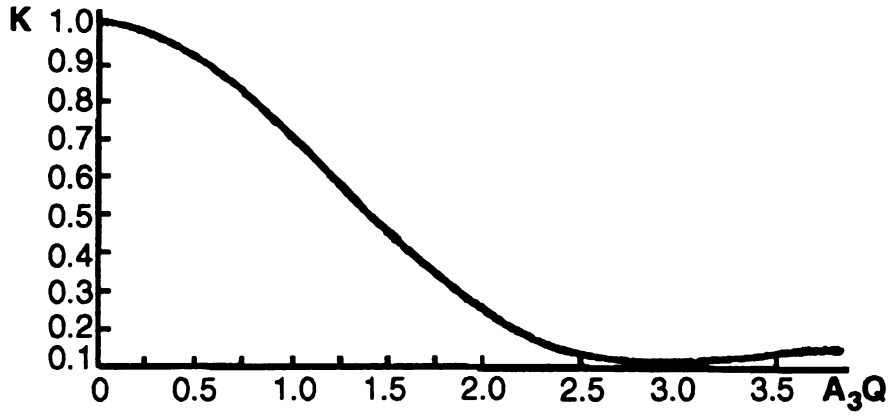

Figure 4.7. Graph of the function $K(A_3Q)$, which describes dynamic scattering as a function of the thickness (A_3) of a crystal and the normalized structure factor (Q) according to the two-beam approximation. In a kinematically scattering crystal K = 1.

After a preliminary refinement has been conducted, the calculated structure factors are used to determine an experimental K value for each reflection:

$$(I_{obs}/\mathcal{L})/\Phi^2_{calc} = K_{exp} \qquad \text{Eq.(4.6)}$$

If $K_{exp} < 1$ the reflection is considered to be decreased in intensity due to dynamic scattering. The purpose of calculating K_{exp} is purely diagnostic, and $K_{exp} < 1$ values are only significant for reflections of large intensity.

Once the reflections in need of correction have been determined, Φ_{calc} and the thickness (A_3) of the crystal can be used to calculate a theoretical A_3Q value for each reflection, and the graph in Figure 4.7 is

used to find a K_{corr} value. The corrected intensity can then be calculated by the following relation:

$$I_{corr} = (I_{obs}/\mathcal{L})/K_{corr} \qquad \text{Eq.(4.7)}$$

Two major drawbacks of this method (aside from the fact that the I'_{gained} term is neglected) are that some knowledge of the structure is required to correct the data, and the thickness of the crystal must be determined. Unfortunately the thickness of the "triplet" crystal used in this structure determination was not known. Several different X-ray diffraction patterns containing *00l* reflections were acquired, and Debye-Scherrer line broadening[31] was used to estimate an average thickness for the particles:

$$D_{hkl} = \frac{0.9 \times \lambda \times 57.3}{\beta_{1/2} \cos\theta} \qquad \text{Eq.(4.8)}$$

where $\beta_{1/2}$ is the full width at half maximum of the *00l* reflection. The results indicated a thickness range of 150 Å to 220 Å. K_{corr} values were calculated for 12 reflections at 150 Å and up to 34 reflections at 220 Å, new Patterson maps were generated, and refinements of the corrected data were conducted.

Table 4.3. Refinement for WS_2 as a function of data correction methods.

	R_1[a]	Goodness of Fit (GOF)
Original data (no background subtraction)	0.3683	0.874
Dynamic scattering correction (2 beam) t = 150 Å	0.3580	0.871
Dynamic scattering correction (2 beam) t = 220 Å	0.3161	0.756
Lorentz correction eliminated	0.2454	1.301

[a] $R_1 = \Sigma(||\Phi_o| - K|\Phi_c||) / \Sigma|\Phi_o|$

The results (Table 4.3) indicated little improvement in the refinement at either thickness (from 36.8% to 35.8% and 31.6%). This led us to re-assess the quality of our integrated data prior to the dynamic scattering correction. As mentioned previously, only data from the strongest supercell was used in the refinement, and subcell reflections were divided by three to correct for the twinning. In reality, this correction results in an underestimation of intensity values of the subcell reflections. The relative intensities of the three different supercells indicated that 50% of the intensities of the subcell reflections are due to that particular supercell. Accordingly the data was adjusted, but the refinement was not much improved (33.66%).

Next the Lorentz correction suggested by Vainshtein was eliminated. This correction, which is simply to divide the intensities of the reflections by their d-spacings, is a crude method to compensate for the curvature of the Ewald sphere (Figure 4.8). Because most crystals examined by TEM are very thin, their reciprocal lattice points are more "cigar"-shaped than spherical along the axis parallel to the electron beam. At the center of the negative the Ewald sphere intersects the lattice points through the center of the cigars, capturing their maximum intensity. Towards the edge of the negative, when the Ewald sphere has begun to curve away from the plane, the sphere no longer intersects the lattice points through the center of the cigars. The end result is that the intensities of the reflections at the limit of the Ewald sphere, which have the smallest d-spacings, are underestimated. In the early days of electron diffraction, smaller accelerating voltages (which give rise to smaller Ewald spheres) were used; hence the effect of the curvature was more significant and a d-spacing correction was more important. Most modern electron microscopists no longer apply this correction, however.[20] With the elimination of the Lorentz correction the intensities of the vectors in the Patterson contour plots generated from the uncorrected data increased, (Figure 4.5d) and the refinement improved to 24.54% (Table 4.3).

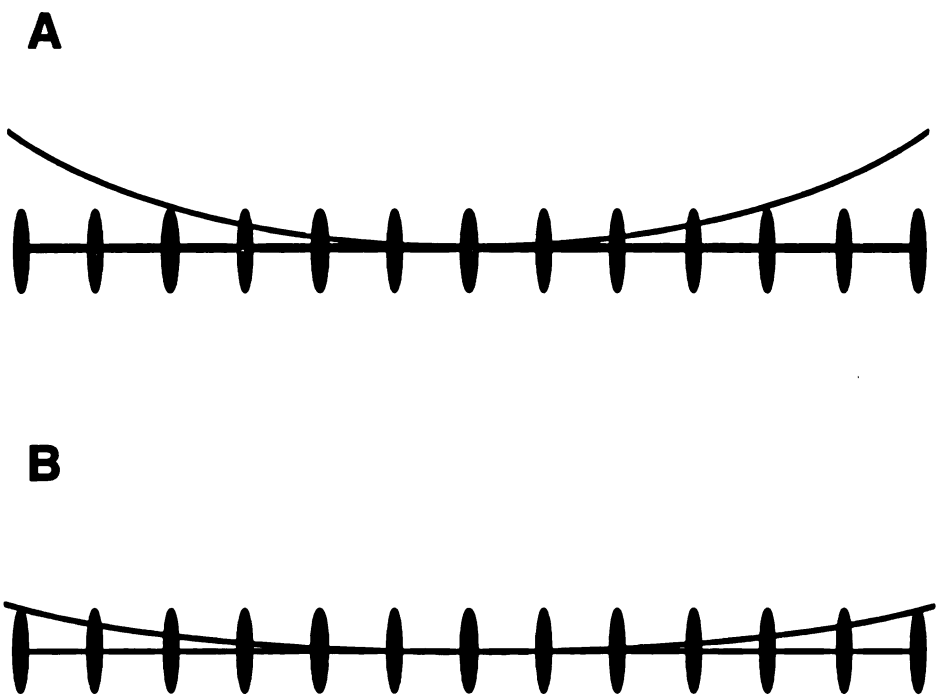

Figure 4.8. The intersection of the Ewald sphere with the reciprocal lattice at an accelerating voltage of (**A**) ~50kV and (**B**) ~100kV. at 100kV the Ewald sphere is much flatter, and the effects of its curvature become significant at smaller d-spacings than at 50kV.

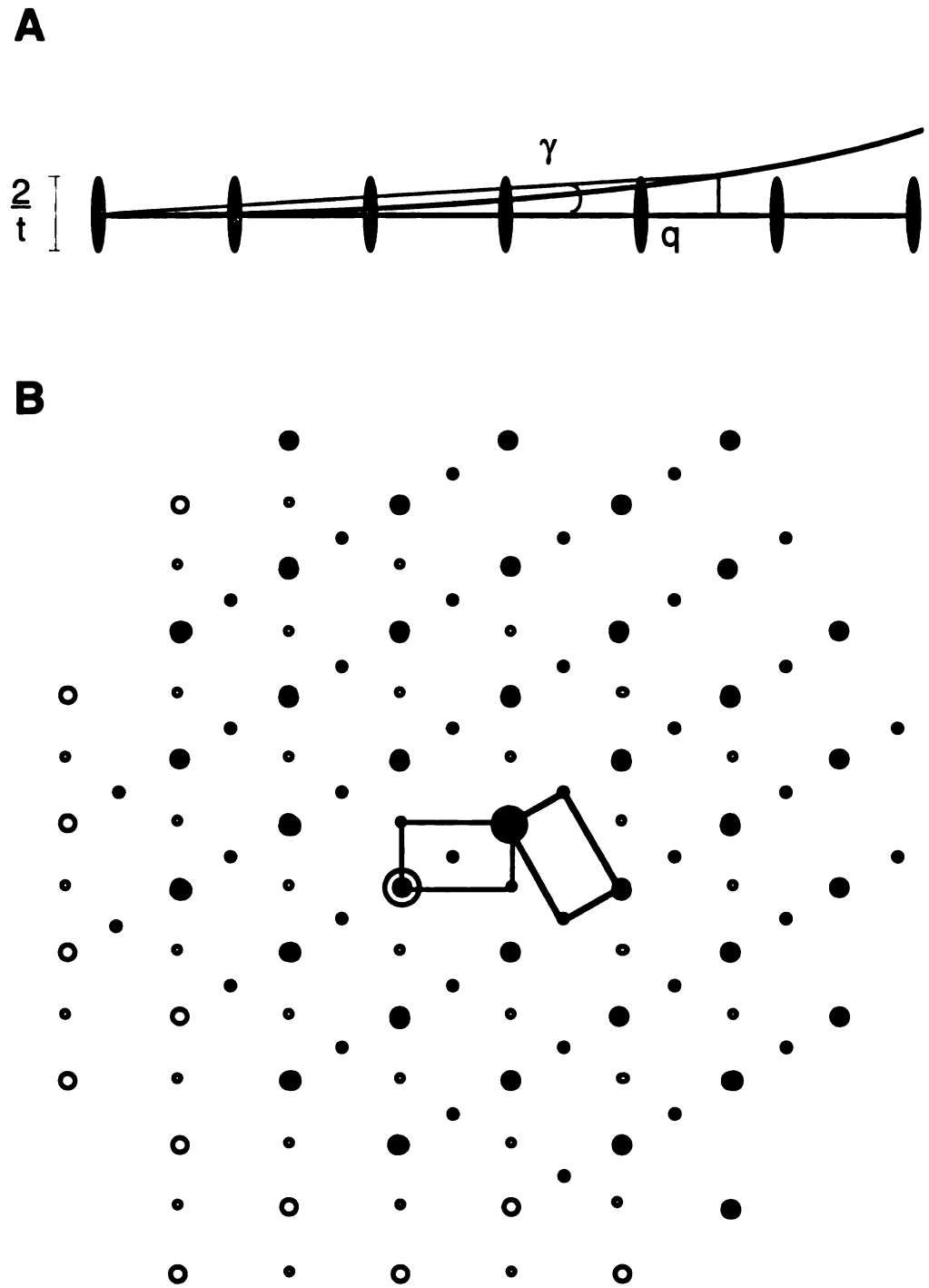

Figure 4.9. **(A)** The limit of detectable reflections (in a perfectly oriented crystal) as a function of the thickness (t) of the sample (q = 1/t), the radius of the Ewald sphere (r), and angle γ. **(B)** An illustration of secondary scattering, in which the diffracted beams from one crystal act as "main beams" as they pass through a second crystal, resulting in the appearance of reflections with artificially small d-spacings.

Based on the accelerating voltage and the d-spacing of the highest order reflections observed it is possible to estimate the thickness (t) of the crystal (Figure 4.9a) through the following relationships:

$$d^*/2r = \sin\gamma$$
$$\tan\gamma d^* = q \qquad \text{Eq.(4.9)}$$

where d* is the reciprocal of the d-spacing of the outermost observed reflection, r is the radius of the Ewald sphere (29.8 $Å^{-1}$), and q is 1/2 the length of the cigar and is equal to the reciprocal of the thickness (t). Based on this calculation, the "triplet" crystal would have to be 4 layers thick or less. This immediately seemed suspicious because in order to observe these higher order reflections it was necessary to examine twinned crystals of "intermediate" thickness, indicating that the crystal is probably more than 4 layers thick. Therefore it seems that, in addition to dynamic scattering, the data is perturbed by secondary scattering.

Secondary scattering, like dynamic scattering, involves multiple scattering of the electrons as they pass through the sample. Unlike dynamic scattering, however, which is a multiple scattering event within a single crystal domain (or, in the approximation, a "mosaic" of independently scattering crystals forming a nearly single crystal domain), secondary scattering involves multiple scattering events encompassing two or more crystals which are significantly dislocated relative to one another. It is possible that the two crystals could even be two different compounds.

Consider two stacked layers rotated by 120 degrees relative to one another, as in the "triplet" crystal. The electron beam is scattered at least once as it passes through the first crystal; but before the pattern reaches the negative the undiffracted and diffracted beams must pass through the second crystal, where they can act as "main beams" and be scattered again. These new "main beams" each have their own Ewald sphere that is slightly shifted relative to the original main beam, which results in a pattern which appears to have higher resolution data than is possible (Figure 4.9b) given the thickness of the sample and the curvature of the Ewald sphere associated with the original main beam. Secondary scattering can be treated mathematically; however, when one combines correction of the data for secondary scattering as well as dynamic scattering the reliability of the experimental data becomes questionable. For this reason, we decided to concentrate our efforts on patterns which were relatively "single" crystal.

4.3.4 Structure solution from "single" crystals of WS_2.

Data was extracted from the diffraction pattern of restacked WS_2 in Figure 4.2d, and also the patterns from restacked WS_2 in Figure 4.10, using the Gel Plotting Macro as described previously. All Patterson maps generated from these data sets indicate a deviation in the M-M vector from

the ideal position (Figure 4.11). The other peaks in the Patterson maps, which contain information about the M-S vectors, are elongated because there are two non-equivalent metal atom positions.

Least squares refinement of the data from Figure 4.2d in SHELXTL (version 5)[24] gave rise to an R_1 value of 13.3% (Tables 4.4,4.5). The structure is non-centrosymmetric, belonging to the plane group *pg* (#4). Due to a convention regarding the cell parameters in this plane group, which contains a glide plane along one axis, $\sqrt{3}a = a_{sup}$ and $a = b_{sup}$. The structure, shown in Figure 4.12, contains the W atoms in distorted octahedral coordination, forming zig-zag chains. The structure of WTe_2, which is very similar, is also shown.[26] It is interesting to note that, in WTe_2, the W atoms are also slightly distorted along the *c*-axis of the structure. Because the electron diffraction data contains only *hk0* reflections, the refinement of the structure of WS_2 produces only a projection of the layer structure. The projection of the short W-W distance in the structure is 2.74 Å, significantly shorter than the 3.16 Å distance found in the ideal 2H-WS_2 structure.

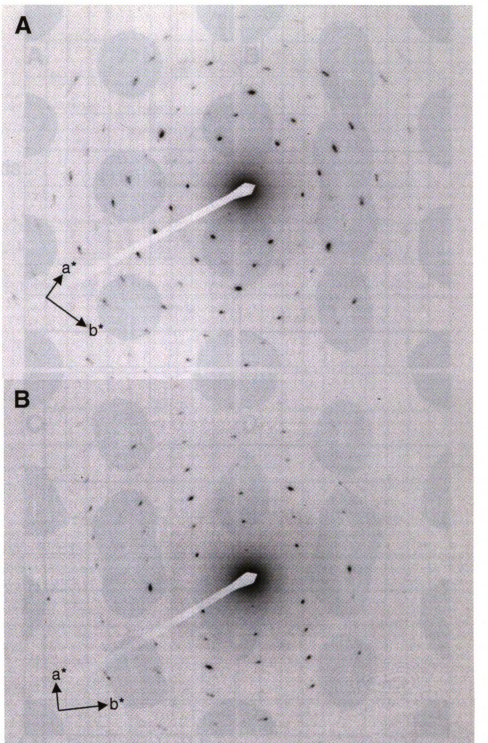

Figure 4.10. Selected area electron diffraction patterns from "single crystal" restacked WS_2 used to generate Patterson contour plots.

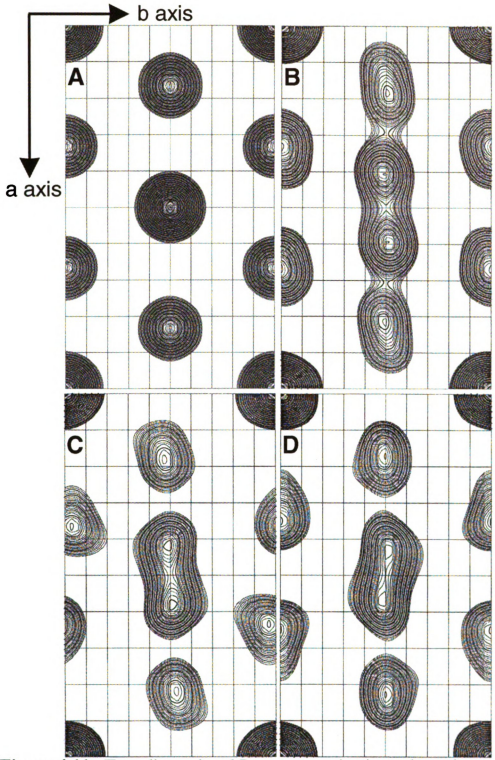

Figure 4.11. Two-dimensional Patterson projections along the c-axis: (A) ideal 1T-MS_2 (from simulated data) (B) restacked WS_2 from the data in Figure 4.2d (C) restacked WS_2 from the data in Figure 4.10a (D) restacked WS_2 from the data in Figure 4.10b. All patterns indicate a deviation in the W-W atom vector.

Table 4.4. Crystal data and structure refinement for crystals of WS_2.

Title	"single" WS_2	"triple" WS_2
Empirical formula	WS_2	WS_2
Formula weight	248.00	248.00
Temperature	293 K	293 K
Wavelength	0.0335 Å	0.0335 Å
Crystal system	Rectangular	Rectangular
Plane group	pg (#4)	pg (#4)
Unit cell dimensions	a = 5.56 Å b = 3.21 Å γ = 90 deg.	a = 5.56 Å b = 3.21 Å γ = 90 deg.
Area (Å^2)	17.295	17.295
Z	2	2
Φ (000)	46	46
2θ range	0.36 to 2.52 deg.	0.36 to 4.20 deg.
Data resolution	0.09 to 0.66 sinθ/λ	0.09 to 1.1 sinθ/λ
Index ranges	--7<=h<=7, 3<=k<=3	-12<=h<=10, -5<=k<=5
Reflections collected	78	173
Independent reflections	43 [R(int) = 0.1556]	99 [R(int) = 0.0870]
Refinement method	Full-matrix l.s. on Φ^2	Full-matrix l.s. on Φ^2
Data / restraints / parameters	43 / 0 / 5	99 / 0 / 7
Goodness-of-fit on Φ^2	1.305	1.301
R indices (all data)[a]	R_1 = 0.1328	R_1 = 0.2456

[a] $R_1 = \Sigma(||\Phi_o| - K|\Phi_c||) / \Sigma|\Phi_o|$

Table 4.5. Atomic coordinates (x 10^4) and equivalent isotropic displacement parameters (A^2 x 10^3) of restacked "single" and "triple" WS_2.

	x	y	U(eq)	Occ.
"single" WS_2				
W(1)	-2021	0	2	1
S(1)	4290	0	8	1
S(2)	950	0	8	1
"triple" WS_2				
W(1)	-2066	0	4	1
S(1)	4182	0	105	1
S(2)	883	0	127	1

U(eq) is defined as one third of the trace of the orthogonalized Uij tensor.

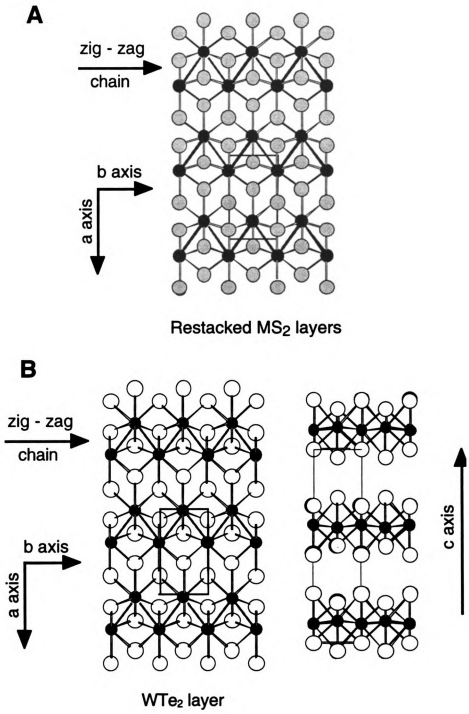

Figure 4.12. **(A)** Two-dimensional projection of a restacked MS_2 layer (M=Mo,W) and one WTe_2 layer. **(B)** View of WTe_2 parallel to *c*-axis. Dark Circles are M; gray circles, S; open circles, Te.

4.3.5 Dynamic Range Correction

One of the challenges in the data collection for this system is balancing the dynamic range in the intensities of the reflections with the limited capability of the film. In the electron diffraction pattern depicted in Figure 4.2d, a number of the strongest peaks (usually sublattice peaks) are overexposed, creating a "flat top" on the negative (Figure 4.13a), but the exposure is a good length of time to capture most of the weaker reflections (Figure 4.13b). Conversely, if a shorter exposure time is used as in the electron diffraction patterns in Figure 4.10, the strongest peaks will not have a "flat top" (Figure 4.13c), but the weaker peaks, which encompass most of the superlattice reflections, are so weak that it is extremely difficult to evaluate their relative intensities (Figure 4.13d). For this reason, the data collected at longer exposures were corrected for this "flat top" problem. The intensities of the *(±020)*, *(±3±10)*, and *(±300)* reflections (8 total, 5 unique) were increased by 30%. Least squares refinement against corrected and uncorrected data sets revealed no differences in positional parameters and only minor changes in thermal parameters; the net result was a virtually identical solution with slightly lower R_{int} (Δ_{max}=0.5%); R_1 (Δ_{max}=1.6%); and wR_2 (Δ_{max}=8%) values.

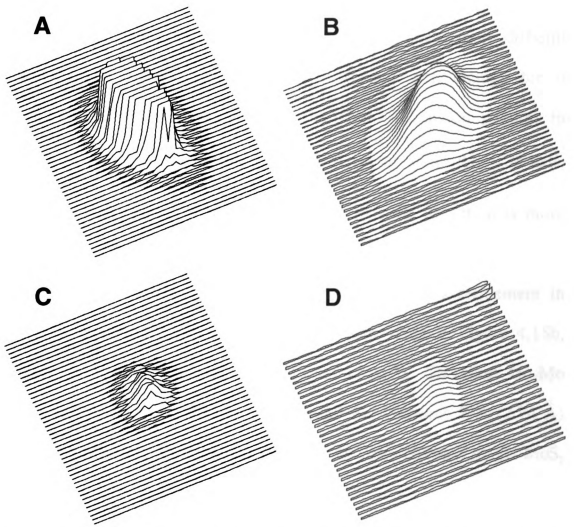

Figure 4.13. Surface plot of the (*3-10*) (A) and the (*-2-20*) (C) reflections in the electron diffraction pattern in Figure 4.2d. The (*3-10*) has a "flat top" due to overexposure. Surface plot of the (*3-10*) (B) and the (*-2-20*) (D) reflections in the electron diffraction pattern in Figure 4.11a. The (*3-10*) is not overexposed, but the (*-2-20*) is very weak.

4.3.6 Structure Solution from "single" crystals of MoS_2.

Data was also collected for restacked MoS_2 (Figure 4.14). The lighter Mo atom does not scatter as well as W; hence, it was more difficult to find "single crystal" patterns which diffracted well enough for a refinement. Patterson maps calculated from both diffraction patterns in Figure 4.14 indicate a distortion in the M-M vector along the $\sqrt{3}a$ axis, forming an oval (Figure 4.15). In restacked WS_2 the distortion is more pronounced, as the M-M vector has split into two resolvable peaks which correspond to two different M-M vectors. Least squares refinement in SHELXTL (version 5)[24] was conducted on the data shown in Figure 4.15b, and gave rise to an R_1 value of 15.3% (Tables 4.6, 4.7). The short Mo-Mo distance is 2.92 Å, longer than the value found for restacked WS_2 (2.74 Å) but still significantly shorter than the ideal Mo-Mo distance in 2H-MoS_2 (3.16 Å).

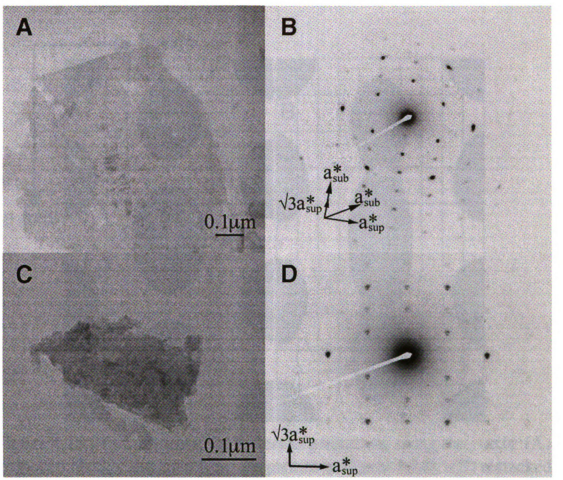

Figure 4.14. Bright field images (A,C) and selected area electron diffraction patterns (B,D) of restacked MoS_2 , giving rise to a $2a \times a$ or a $\sqrt{3}a \times a$ superstructure.

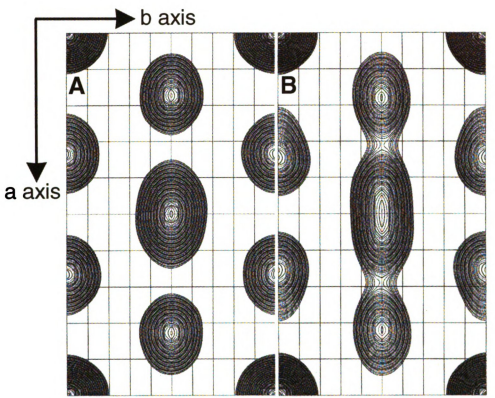

Figure 4.15. Two-dimensional Patterson projections along the *c*-axis: (A) restacked MoS_2 calculated from the pattern in Figure 4.14b. (B) restacked MoS_2 calculated from the pattern in Figure 4.14d.

Table 4.6. Crystal data and structure refinement of restacked MoS_2.

Empirical formula	MoS_2
Formula weight	160.00
Temperature	293 K
Wavelength	0.0335 Å
Crystal system	Rectangular
Plane group	pg (#4)
Unit cell dimensions	a = 5.47 Å
	b = 3.16 Å
	γ = 90 deg.
Area (Å^2)	17.295
Z	2
Φ (000)	40
2θ range for data collection	0.36 to 2.78 deg.
Data resolution	0.09 to 0.73 sinθ/λ
Index ranges	-7<=h<=5, -3<=k<=3
Reflections collected	73
Independent reflections	46 [R(int) = 0.2120]
Refinement method	Full-matrix l.s. on Φ^2
Data / restraints / parameters	46 / 0 / 7
Goodness-of-fit on Φ^2	1.267
R indices (all data)[a]	R_1 = 0.1525

[a] $R_1 = \Sigma(||\Phi_o| - K|\Phi_c||) / \Sigma|\Phi_o|$

Table 4.7. Atomic coordinates (x 10^4) and equivalent isotropic displacement parameters (A^2 x 10^3) in restacked MoS_2.

	x	y	U(eq)	Occ.
Mo(1)	-2251	0	9	1
S(1)	4240	0	38	1
S(2)	925	0	54	1

U(eq) is defined as one third of the trace of the orthogonalized Uij tensor.

The M-M distances have been measured by EXAFS to be 2.74 Å and 2.8 Å for WS_2 and MoS_2, respectively.[32] Shorter M-M distances than those observed by EXAFS might be explained by displacement of the metal atom along the *c*-axis. As mentioned previously, this displacement is actually observed in WTe_2. Longer M-M distances than those observed by EXAFS may be an artifact of dynamic scattering: we have observed by simulation that the M-M distances appear to increase with increasing thickness (*vide infra*).[33] Despite these difficulties, electron crystallography is a more powerful tool for the structure elucidation of these compounds than EXAFS. The latter probes only the local structure, while electron diffraction provides a direct structure determination.

4.3.7 Dynamic scattering: n-beam approximation.

Although including the effects of dynamic scattering in the refinement should improve the results, it is non-essential for determination of the structure of these materials. This suggests that the use of electron diffraction for structure determination of inorganic materials may not be as unrealistic as previously supposed. Nonetheless, an effort was made to address the effects of dynamic scattering in these data sets.

The two-beam approximation is severely limited by the assumption that each diffracted beam functions independently of all the other diffracted beams in the diffraction pattern. The assumption is particularly false when large accelerating voltages are used, resulting in very large Ewald spheres which can excite many reflections at one time. Therefore, alternate approximations, most notably the n-beam approximation, have been developed.[20,34,35] The n-beam approximation permits the calculation of the dynamic contribution to each reflection from multiple beams in a series of slices through the crystal.[36] Although more accurate, it is significantly more complicated than the two-beam approximation, and solving a structure using a dynamical treatment of the electron diffraction data is a mathematically challenging procedure. Some researchers have combined HRTEM (High Resolution TEM) images with the electron diffraction data in order to obtain phase information and then used direct methods.[37]

Others have developed software which enables one to combine least-squares refinement with a multislice calculation.[38]

As part of an effort to include a correction for dynamic scattering, the models which resulted from kinematic refinement in SHELX programs were constructed using the molecular modeling program CERIUS^2.[33] This program contains a HRTEM module which employs the multislice n-beam calculation to simulate high resolution images. One step in this process involves the generation of electron diffraction patterns. Simulated diffraction data for varying thickness of the WS_2 crystal are shown in Figure 4.16. Figure 4.16a contains essentially a kinematic pattern, as it comes from a crystal which is only one layer thick. Note that the *(200)* is less intense than the *(300)*. At three layers thick (Figure 4.16b) the sublattice reflections have increased in intensity, and at six layers thick (Figure 4.16c) the intensity of the *(200)* is equal to the *(300)*. At eight layers thick (Figure 4.16d), the hexagonal sublattice reflections are the most intense reflections in the diffraction pattern. It is interesting to note that, using the two-beam approximation, one might have predicted that the sublattice reflections, which are generally more intense than the superlattice reflections, would have been decreased in intensity with increasing thickness rather than increased. One can qualitatively use the values of the *(200)* and the *(300)* to estimate the degree of dynamic

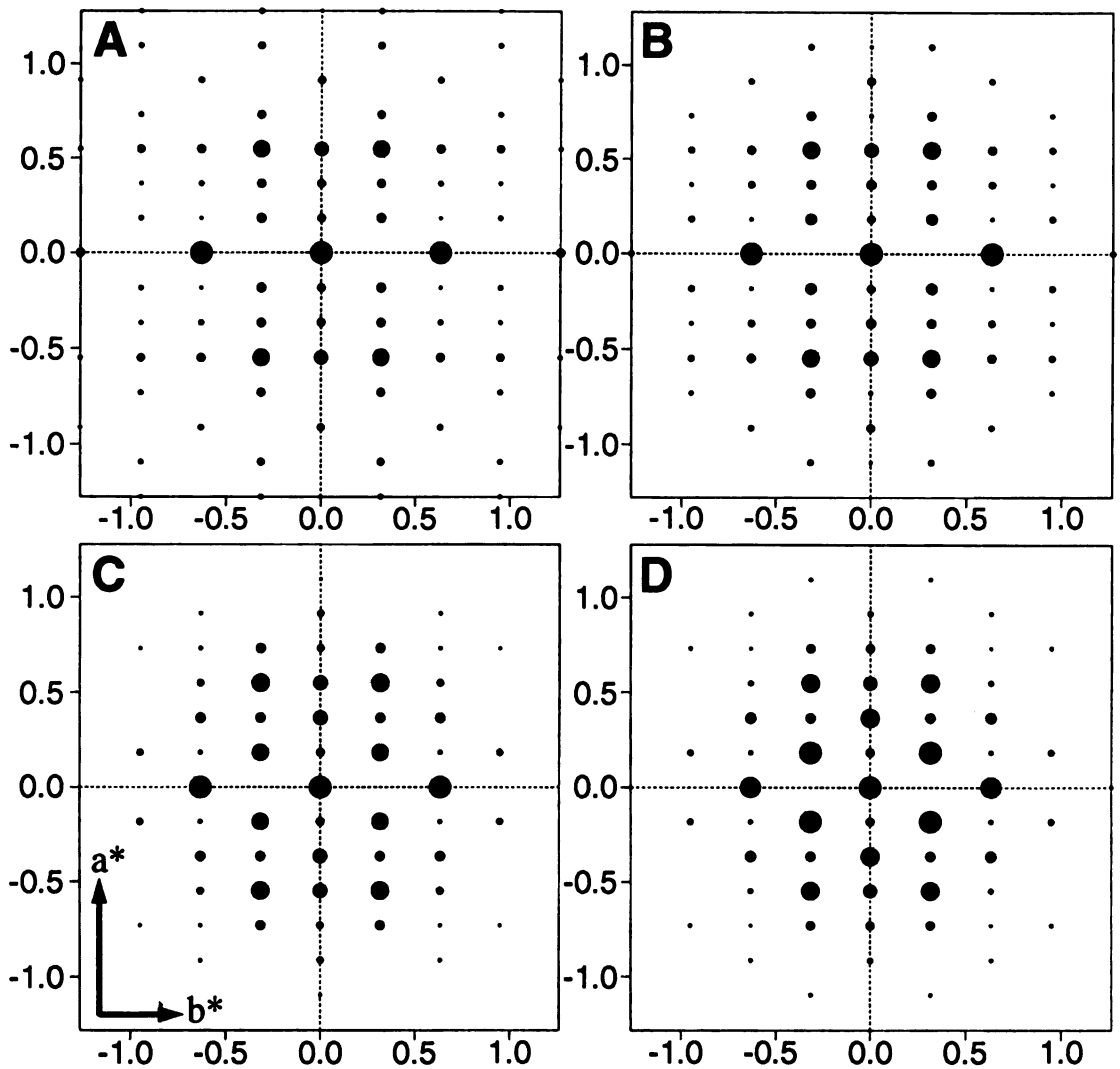

Figure 4.16. Electron Diffraction patterns of restacked WS_2 simulated using the multi-slice dynamic scattering calculation employed in the CERIUS^2 HRTEM module: (A) one layer thick (kinematic scattering) (B) three layers thick (C) six layers thick and (D) eight layers thick. As thickness increases, the relative intensities of the hexagonal sublattice reflections increases.

scattering present in the sample. In this case, the data in Figure 4.2d is the most free of dynamic scattering. Simulations of the diffraction patterns from the models of MoS_2 were comparable, with the exception that the *(200)* surpassed the *(300)* before 5 layers thick rather than after 6 layers thick, as in the simulations involving WS_2. One can also see that in both data sets for MoS_2 the *(200)* is more intense than the *(300)*, suggesting contamination due to dynamic scattering.

The intensities were extracted from these simulated diffraction patterns (an option in CERIUS[2]), and Patterson contour plots were generated (Figure 4.17). In the kinematic pattern (Figure 4.17a), the distortion in the W-W vector can be resolved as two distinct peaks, and the W-S vectors are elongated and fairly intense. At three layers thick (Figure 4.17b) the W-W vectors are slightly more blurred and the W-S vectors are more rounded. At six layers thick (Figure 4.17c) the W-W vectors are no longer resolvable as two separate peaks, and the W-S vectors are significantly reduced in intensity. At eight layers thick (Figure 4.17d) there is almost no intensity in the W-S vectors and the distortion in the W-W vector is only evident as a large, oval peak. If the data from this last Patterson map is refined against the model that was used to create it the W-W distance increases and the temperature factors of all the atoms become very large. Based on the fact that the simulated electron diffraction

patterns for MoS_2 are comparable, would expect it to follow a similar trend, but the deterioration of the data with thickness would be more rapid.

This loss of resolution of the M-M vector with increasing dynamic scattering led us to conduct a kinematic simulation in which the W-W distance was varied from 2.65 Å to 2.90 Å (Figure 4.18). The W-W vector starts to blur between 2.70 and 2.80 Å (Figures 4.18b and 4.18c), and blurs completely into one oval peak between 2.80 and 2.90 Å (Figure 4.18d). The W-S vectors become more rounded due to the decrease in the distortion of the W atoms. The oval which describes the W-W vector in these Patterson contour plots is smaller than the oval in the plots generated as a function of thickness, but the most significant difference is that the W-S vectors are not decreased in intensity with increasing W-W distance. One might expect this feature to manifest itself as elevated temperature factors for the S atoms, which is observed to a small degree in the MoS_2 data.

The CERIUS[2] program is not designed to conduct least squares refinements in conjunction with multislice n-beam calculations. In order to try to evaluate the degree to which our data is contaminated by dynamic scattering, R_1 values were calculated as a method to compare the simulated dynamic data[39] with the experimental data:

$$R_1 = \frac{\sum_{hk} \| \Phi_o | - K | \Phi_c \|}{\sum_{hk} \Phi_o} \qquad \text{Eq.(4.10)}$$

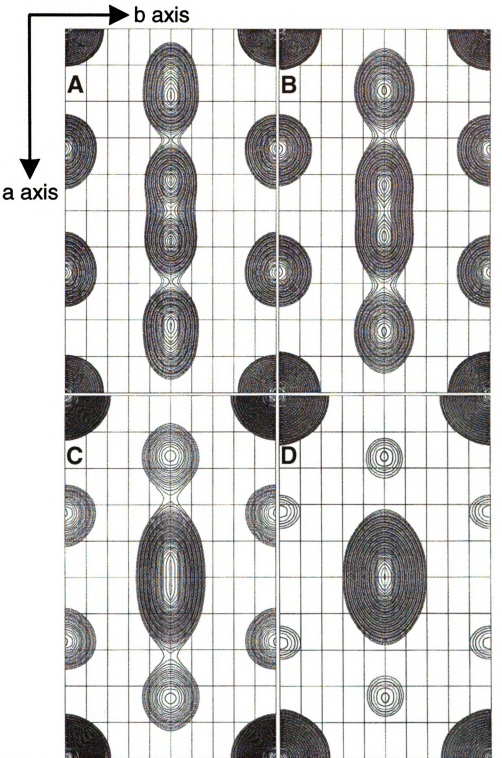

Figure 4.17. Two-dimensional Patterson projections along the *c*-axis calculated from the data in Figure 4.16: (A) one layer thick (kinematic scattering) (B) three layers thick (C) six layers thick and (D) eight layers thick. As thickness increases, the W-W vectors become blurred and the W-S vectors decrease in intensity.

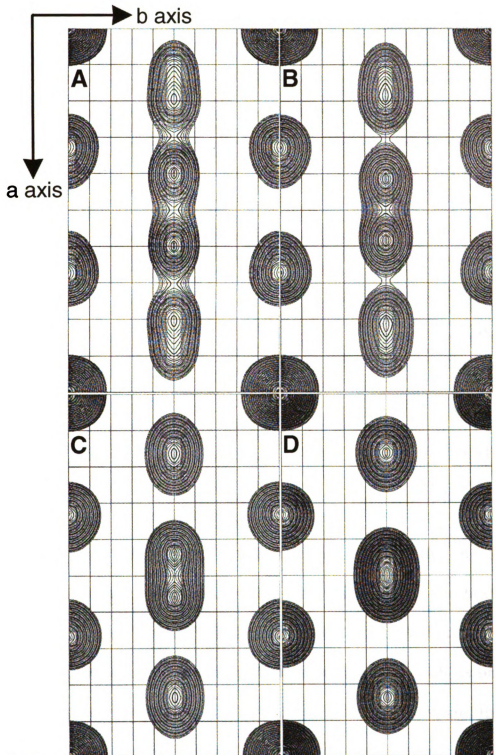

Figure 4.18. Two-dimensional Patterson projections along the *c*-axis calculated from simulated electron diffraction data (kinematic) as a function of W-W distance: (A) 2.65 Å (B) 2.70 Å (C) 2.80 Å and (D) 2.90 Å. As the W-W distance increases, the W-W vectors become blurred, but the W-S vectors retain their initial intensity.

Table 4.8. A comparison of simulated dynamic electron diffraction data to the experimental data for MoS_2 and WS_2 as a function of layer thickness.

Layer thickness	R_1 for MoS_2 (%)	R_1 for WS_2 (%)
1	15.38	13.27
2	14.75	13.21
3	15.44	14.77
4	19.03	19.58
5	23.15	24.98
6	26.19	29.92
7	28.14	34.76
8	30.13	39.81

Unfortunately the simulations did not result in significant improvements over kinematic least squares refinement: the best R_1 value calculated for the "single" WS_2 data set is only ~0.1% lower than the value from the kinematic refinement, and the best value for MoS_2 is only ~0.9% lower. Part of the problem is that the atomic coordinates and the thermal parameters have already been minimized in a kinematic refinement in SHELX; if we had access to a program which would allow those parameters to refine against a dynamic model the R_1 value might

improve.[38] The lack of improvement also suggests that there are other sources of perturbation of the data besides dynamic scattering. For example, the correction which was applied to compensate for the limited dynamic range of the electron microscope film may not have been adequate. Another possible source of perturbation of the data is the flatbed scanner used to digitize the negative, as it is also somewhat limited in dynamic range. Despite these difficulties, meaningful structural information has been extracted from the electron diffraction patterns.

4.3.8 Electron Crystallographic Studies of an alternate superlattice in MoS_2

Recently, STM studies on the original 1T-MoS_2, prepared by the oxidation of $K_x(H_2O)_yMoS_2$ with I_2, indicated that it has a $\sqrt{3}a$ x $\sqrt{3}a$ superstructure[18], as proposed in the original publication reporting the material.[11] It is becoming clear that restacked MoS_2 is not the same as 1T-MoS_2. Other studies have indicated that restacked MoS_2, previously believed to be neutral because of its ability to encapsulate neutral species, has some residual negative charge.[40] The charge balancing species could be Li^+, H^+, or H_3O^+. This residual negative charge apparently stabilizes the

structure of restacked MoS_2. STM studies of $K_x(H_2O)_yMoS_2$ suggest that it has the same superstructure as restacked MoS_2.[41]

As will be discussed in the next chapter, it is possible to produce this alternate $\sqrt{3}a$ x $\sqrt{3}a$ superlattice in restacked MoS_2 upon oxidation of the sample with Br_2. It is very unusual to observe this lattice without the presence of the orthorhombic lattice solved in this chapter, but a few "single crystal" patterns were obtained (Figure 4.19). We attempted to elucidate the structure of this alternate lattice from the electron diffraction patterns.

Figure 4.20a contains the Patterson map of an idealized octahedral species with a $\sqrt{3}a$ x $\sqrt{3}a$ lattice. The M-M vectors can be found at (1/3, 2/3) and (2/3, 1/3). Figures 4.20b and 4.20c are the Patterson maps calculated from the experimental data in Figure 4.19. Although the M-M vector is not spherical, there does not appear to be a splitting or even an elongation of the M-M vectors as seen in the orthorhombic Patterson maps. Actually it seems that, for this system, even if there is a distortion in the M-M distance it will not be visible in the Patterson map. In Figure 4.21a a Patterson map has been simulated from a model (created using the distortion model shown in Figure 4.1c) with a short M-M distance of 2.8 Å. Although the M-M vectors are no longer spherical, there is no evidence of a pair of M-M vectors representing the short and long distances in the

structure, even though the map was generated from a model which contained such distances. In fact, if one distorts the M-M distance to a ridiculously short value, such as 2.2 Å, the M-M vector disappears almost completely and the overall intensity of the peaks in the pattern is reduced (Figure 4.21b). The problem is that the Patterson map is not a plot of the electron density in the structure, but a plot of the atom-atom vectors in the structure. The M-M distortion generates distortion in the M-S vectors as well, which in this case complicates the Patterson map significantly more than in the orthorhombic cell and results in an overall increase in the background noise in the map. When the S atoms are eliminated from the model, the distorted M-M vectors are easily observed (Figure 4.21c).

Although the Patterson did not provide much information about the structure, we attempted unsuccessfully to refine the structure using the proposed trimerization model shown in Figure 4.1c, which belongs to the plane group *p31m* (#15). This unit cell is larger than the orthorhombic cell, and consequently contains more atoms. Even with maximum constraint of the parameters the data:parameter ratio was 4:1, which is insufficient for a refinement. Data collection at higher accelerating voltages, or employing tilt studies to collect higher order reflections, are required for the determination of the structure of this compound from electron diffraction data.

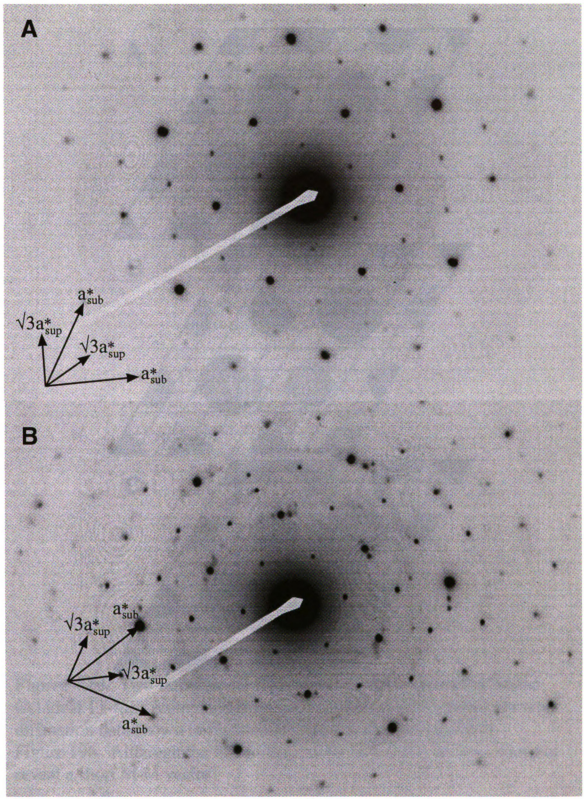

Figure 4.19. Selected area electron diffraction patterns from crystals of restacked MoS_2 which have been oxidized with Br_2, giving rise to a $\sqrt{3}a \times \sqrt{3}a$ superstructure.

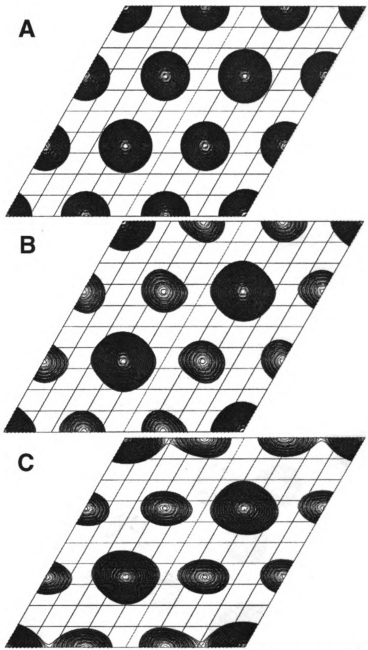

Figure 4.20. Two-dimensional Patterson projections along the *c*-axis: (A) ideal 1T-MS_2 (computed from simulated data) (B) from the electron diffraction data shown in Figure 19a (C) from the data shown in Figure 19b. Although the M-M vector is not spherical, the map does not reveal a short M-M vector.

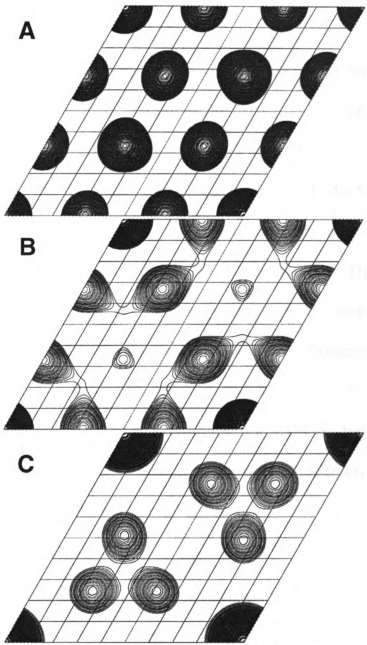

Figure 4.21. Two-dimensional Patterson projections along the *c*-axis calculated from simulated data: (A) a trimerization with a short M-M distance of 2.8 Å (B) a trimerization with a short M-M distance of 2.2 Å and (C) the same model without S atoms.

4.4 Conclusions

In summary, the structure of restacked WS_2 and MoS_2 has been determined from electron diffraction data. The 2-D Patterson projection indicates unequivocally that the metal atoms are distorting to form zig-zag chains with a short W-W distance of 2.74 Å and a short Mo-Mo distance of 2.92 Å. These distortions are in agreement with earlier theoretical predictions for layered octahedral ML_2 d^2 systems.[27] The results are consistent with those from EXAFS studies, and they are more informative because they provide direct structural information. Structure refinement has been conducted to R_1=13.3% for WS_2 and R_1=15.3% for MoS_2. We conclude that restacked MoS_2 and WS_2 are not 1T-TiS_2 type, but rather WTe_2 type, and that quasi-kinematical electron diffraction data are sufficient for meaningful structure elucidation.

References

1. Fleischauer, P.D. *Thin Solid Films*, 1987, **154**, 309.

2. Dickinson, R.G.; Pauling, L. *J. Am. Chem. Soc.*, 1923,**45**, 1466.

3. a) Harris, S.; Chianelli, R.R. *J. Catalysis*, 1984, **86**, 400. b) Brenner, J.; Marshall, C.L.; Ellis, L.; Tomczyk, N.; Heising, J.; Kanatzidis, M.G. *Chem. Mater*, 1998, **5**, 1244.

4. Julien, C.; Saikh, S.I.; Nazri, G.A. *Mater. Sci. Eng.*, 1992, **B15**, 73.

5. Murphy, D.W.; DiSalvo, F.J.; Hull, G.W.,Jr.; Waszczak, J.V. *Inorg. Chem.*, 1976, **15**, 17.

6. a) Divigalpitiya, W.M.R.; Frindt, R.F.; Morrison, S.R. *Science*, 1989, **246**, 369. b) Divigalpitiya, W.M.R.; Frindt, R.F.; Morrison, S.R. *J. Mater. Res.*, 1991, **6**, 1103. c) Gee, M.A.; Frindt, R.F.; Morrison, S.R. *Mater. Res. Bull.*, 1986, **21**, 543.

7. a) Bissessur, R.; Heising, J.; Hirpo, W.; Kanatzidis, M.G.; *Chem. Mater.*, 1996, **8**, 318. b) Wang, L.; Schindler, J.L.; Thomas, J.A.; Kannewurf, C.R.; Kanatzidis, M.G. *Chem. Mater.*, 1995, **7**, 1753. c) Kanatzidis, M.G.; Bissessur, R.; DeGroot, D.C.; Schindler, J.L.; Kannewurf, C.R. *Chem. Mater.*, 1993, **5**, 595.

8. a) Lemmon, J.P.; Lerner, M.M. *Chem. Mater.*, 1994, **6**, 207. b) Dungey, K.E.; Curtis, M.D.; Penner-Hahn, J.E. *J. Catalysis*, 1998, **175**, 129.

9. Py, M.A.; Haering, R.R. *Can. J. Phys.*, 1983, **61**, 76.

10. Chianelli, R.R.; Scanlon, J.C.; Thompson, A.H. *Mater. Res. Bull.*, 1975, **10**, 1379.

11. Wypych, F.; Schöllhorn, R. *J. Chem. Soc., Chem. Commun.*, 1992, 1386.

12. a) Wilson, J.A.; DiSalvo, F.J.; Mahajan, S. *Adv. Phys.*, 1975, **24**, 117. b) Wilson, J.A.; DiSalvo, F.J.; Mahajan, S.; *Phys. Rev. Lett.*, 1974, **32**, 882.

13. Yang, D.; Frindt, R.F. *J. Phys. Chem. Solids*, 1996, **57**, 1113.

14. Yang, D.; Sandovals, S.J.; Divigalpitiya, W.M.R.; Irwin, J.C.; Frindt, R.F. *Phys. Rev. B.* , 1991, **43**, 12053.

15. Tsai, H.L.; Heising, J.; Schindler, J.L.; Kannewurf, C.R.; Kanatzidis, M.G. *Chem. Mater.*, 1997, **9**, 879.

16. Chrissafis, K.; Zamani, M.; Kambas, K.; Stoemenos, J.; Economou, N.A.; Samaras, I.; Julien, C. *Mater. Sci. Eng.*, 1989, **B3**, 145.

17. Qin, X.R.; Yang, D.; Frindt, R.F.; Irwin, J.C. *Ultramicroscopy*, 1992, **42-44**, 630.

18. Wypych, F. Weber, Th. Prins, R. *Chem. Mater.*, 1998, **10**, 723.

19. Vainshtein, B.K. *Structure Analysis by Electron Diffraction*; Pergamon Press, MacMillan Co., New York, 1964.

20. Dorset, D.L. *Structural Electron Crystallography* ; Plenum Press, New York, 1995.

21. Stout, G.H.; Jensen, L.H. *X-ray Structure Determination: a Practical Guide* (2nd ed.); John Wiley & Sons, New York, 1989.

22. Ladd, M.F.C.; Palmer, R.A. *Structure Determination by X-ray Crystallography* (3rd ed.); Plenum Press, New York, 1994.

23. Analysis of integrated intensities was performed on a Macintosh Performa 6214CD computer using the public domain NIH Image 1.60 program (developed at the U.S. National Institutes of Health and available on the Internet at http://7/2/98/rsb.info.nih.gov/nih~image/) using the "Gel Plotting Macros" plug-in.

24. Sheldrick, G.M. "SHELTX™ Version 5", Bruker Analytical X-Ray Instruments, Inc., Madison, WI.

25. Hyams, Daniel. "CurveExpert Version 1.34", 1995-1997. Portions copyright (1993) Microsoft Corporation, Seattle, WA.

26. a) Brown, B.E. *Acta Crystallogr.*, 1966, **20**, 268. b) Mar, A.; Jobic, S.; Ibers, J. A. *J. Am. Chem. Soc.*, 1992, **114**, 9587.

27. a) Rovira, C.; Whangbo, M.-H. *Inorganic Chem.*, 1993, **32**, 4094. b) Whangbo, M.-H.; Canadell, E. *J. Am. Chem. Soc.*, 1992, **114**, 9587.

28. Bissessur, R.; Kanatzidis, M.G.; Schindler, J.L.; Kannewurf, C.R. *J. Chem. Soc., Chem. Commun.*, 1993, 1582.

29. a) Pinsker, Z.G.; Dvoryankina, G.G. *Kristallografiya*, 1958, **3**, 438. b) Nagakura, S. *Acta Crystallogr.*, 1957, **10**, 601.

30. $Q = \lambda |\Phi/ \Omega|$, where Φ is the structure factor, Ω is the volume of the unit cell, and λ is the wavelength of the electrons.

31. Klug, P.; Alexander, L.E. *X-Ray Diffraction Procedures for Polycrystalline and Amorphous Materials*, John Wiley and Sons, New York, 1954.

32. a) Joensen, P.; Crozier, E.D.; Alberding, N.; Frindt, R.F. *J. Phys. C.: Solid State Phys.*, 1987, **20**, 4043. b) Prouzet, E.; Heising, J.; Kanatzidis, M.G. Unpublished results.

33. "CERIUS^2 Version 3.5 HRTEM module", Molecular Simulations, Inc., San Diego, CA.

34. Cowley, J.M.; Moodie, A.F. *Acta Cryst.*, 1957, **10**, 609.

35. Cowley, J.M. *Diffraction Physics*; Elsevier, New York, 1975.

36. Spence, J.C. H. *Acta Cryst.*, 1998, **A54**, 7.

37. Sinkler, W.; Marks, L.D.; Edwards, D.D.; Mason, T.O.; Poeppelmeier, K.R.; Hu, Z.; Jorgensen, J.D. *J. Solid State Chem.*, 1998, **136**, 145.

38. a) Zandbergen, H.W.; Andersen, S.J.; Jansen, J. *Science*, 1997, **277**, 1221. b) Jansen, J.; Tang, D.; Zandbergen, H.W.; Schenk, H. *Acta Cryst.*, 1998, **A54**, 91.

39. "CERIUS^2 Version 3.8 HRTEM module", Molecular Simulations, Inc., San Diego, CA. (According to the company, this newer software version contains an "improved" dynamic scattering calculation,

particularly with regard to the incorporation of the temperature factors of the atoms in the calculation.)

40. Heising, J.; Bonhomme, F.; Kanatzidis, M.G. *J. Solid State. Chem.*, 1998, **139**, 22.

41. Wypych, F.; Weber, Th.; Prins, R. *Surf. Sci.*, 1997, **380**, L474.

CHAPTER 5

Exfoliated and Restacked MoS_2 and WS_2: Ionic or Neutral Species? Encapsulation and Ordering of Hard Electropositive Cations

5.0 Abstract

The relationship between charge and structure in restacked MS_2 (M = Mo,W) has been probed by cation encapsulation and chemical oxidation and characterized by elemental analysis, electron diffraction, X-ray diffraction, and Differential Scanning Calorimetry. Alkali cations have been encapsulated in MoS_2 and WS_2 without the presence of a co-intercalated counter-ion, suggesting a negative charge in the range 0.15-0.25 electrons per M atom. Electron diffraction studies show ordering of these cations between the layers. Chemical oxidation with I_2 or Br_2 results in a change in the structure of restacked MoS_2, giving rise to a $\sqrt{3}a \times \sqrt{3}a$ superlattice, whereas no change is observed in the structure of restacked WS_2. Differential Scanning Calorimetry studies show an irreversible exothermic transition to 2H-MS_2 upon heating, which shifts in temperature with oxidation. Thermopower measurements indicate that restacked MoS_2 and WS_2 are p-type metallic conductors, consistent with an observed structural distortion and residual negative charge.

5.1 Introduction

2H-MoS_2 and 2H-WS_2 are the most stable members of the family of layered dichalcogenides, and find practical application in such processes as hydrodesulfurization (HDS) due to their availability and relatively low cost. [1] Both materials strongly resist attempts to incorporate guest species between their layers.[2] Li atoms can be inserted into MoS_2 (and WS_2) only upon treatment with a strong reducing agent such as n-butyllithium (n-BuLi) or $LiBH_4$.[3,4] $LiMoS_2$ and $LiWS_2$, however, exhibit a remarkable ability to exfoliate in water by the following redox reaction:

$$LiMS_2 + H_2O \text{ ---> } (MS_2)_{\text{single layers}} + LiOH + H_2\,(g) \qquad \text{(Eq. 5.1)}$$

resulting in a colloidally dispersed suspension of single layers.[4,5] The layers can be recovered in a restacked form by filtration, centrifugation, or precipitation. The ability of these materials to exfoliate and to be restacked with relative ease has permitted the encapsulation of a wide variety of guest species which include neutral organic molecules,[6] polymers,[7] metal chalcogenide[8] and metal oxide[9] clusters, metallocenes[10], porphyrins[11], and metal cations.[12,13]

The authors who first reported the exfoliation of MoS_2 believed that the redox reaction between H_2O and MoS_2 resulted in complete oxidation of the layers, returning the molybdenum to a 4+ oxidation state, because many

of the molecules which have been encapsulated are neutral.[6-8,14] A net drift of the suspended layers toward the anode in an electrophoresis apparatus was observed by these authors, but was attributed to OH^- ions associated with the layers which could be displaced by the organic molecules.[15] Subsequent pH studies seemed to support this hypothesis.[16] The increasing number of examples of cationic species which have been encapsulated have suggested to other authors that the layers may retain some negative charge.[8,10-13,17] It is rather curious that restacked MoS_2 (and WS_2) can incorporate both cationic and neutral species. The ambiguity of the situation stems from an abundance of both Li^+ and OH^- generated in the exfoliation process: Li^+, which could counterbalance a negative charge on the layers when neutral species are intercalated, is a notoriously difficult element to detect; OH^-, which could co-intercalate with the cationic species, can be confused with residual co-intercalated H_2O.

In addition to the unresolved issues about the oxidation state of the layers, there has also been confusion about the atomic structure of the layers. Reduction of 2H-MoS_2 with n-BuLi or $LiBH_4$ results in a structural transformation in the layers, causing the geometry around the metal atoms to shift from trigonal prismatic to octahedral.[18] This results in a change in the conductive properties of the material from semiconducting to metallic.[18,19] This structural change appears to be retained in exfoliated

MoS_2, with a structural distortion which results in a $a \times \sqrt{3}a$ orthorhombic superlattice.[20,21] Restacked MoS_2 has also been called 1T-MoS_2 because of the octahedral coordination of the Mo atom. Restacked WS_2 appears to be analogous to restacked MoS_2.[4,21] Another material which has been called 1T-MoS_2 is prepared by high temperature synthesis and subsequent oxidation of $K_{0.33}(H_2O)_yMoS_2$.[22] Restacked MoS_2 and 1T-MoS_2 were thought to be the same material because both appear to have octahedral metal coordination and both undergo an irreversible exothermic transition to 2H-MoS_2 at around 100°C.[22,23] 1T-MoS_2, however, exhibits a $\sqrt{3}a \times \sqrt{3}a$ superlattice.[22,24] The $a \times \sqrt{3}a$ superlattice found in restacked MoS_2 is due to M-M associations resulting in the formation of zig-zag chains, whereas a $\sqrt{3}a \times \sqrt{3}a$ superlattice would involve M-M trimerization.

Are these layers neutral or cationic? Why do 1T-MoS_2 and restacked MoS_2 have different superlattices? What is the impact of negative charge on the structure of these materials? If the MoS_2 layers are slightly reduced, how does it affect the conductivity? In this chapter we describe our experimental efforts toward answering these questions. The encapsulation of hard, electropositive alkali metal cations is described, chosen due to their relatively poor affinity for OH^- which make them perhaps the best

species for chemical analyses to determine negative charge. The materials are characterized by X-ray diffraction, electron diffraction, TGA, and elemental analyses. The treatment of $LiMS_2$ and exfoliated MS_2 with the oxidizing agent Br_2 and concentrated HCl has also been conducted and the products characterized by X-ray diffraction, electron diffraction, and DSC measurements. Thermopower measurements of restacked MoS_2 and WS_2, which address the effects of structure and charge on the nature of their conductivity, are also presented.

5.2 Experimental

5.2.1 Synthesis

$LiMoS_2$ and $LiWS_2$ were synthesized by the $LiBH_4$ method.[4] Acetonitrile, RbCl, CsF, and CsI were purchased from Aldrich. KCl and were purchased from J.T. Baker. Br_2 and NaCl were purchased from EM Science. I_2 was purchased from Mallinckrodt. HCl was purchased from Columbus Chemical Industries. All compounds were used as received.

MoS_2 aqueous suspension. In a glove box under nitrogen atmosphere $LiMoS_2$ (0.1 g, 0.6 mmol) was placed in a 125 ml Erlenmeyer flask equipped with a stir bar and rubber stopper. The flask was removed from

the glove box and 10 ml deoxygenated deionized H_2O was added. The mixture was allowed to stir for 0.5 hr, then the contents of the flask were transferred to a centrifuge tube and centrifuged for 0.5 hr. The supernatant was decanted (pH >12) and to the black gooey solid at the bottom of the tube 10 ml fresh deoxygenated deionized H_2O was added to rinse away the LiOH. The tube was agitated to re-suspend the product, and the mixture again centrifuged for 0.5 hr. This rinsing was conducted three times, the supernatant having pH ~12, pH ~9, and pH ~7 after each rinse. Then 10 ml more deoxygenated deionized H_2O was added, the tube was agitated to re-suspend the product, and the contents of the centrifuge tube were returned to a 125 ml Erlenmeyer flask with stir bar. The suspension was stirred for at least 0.5 hr before further use.

WS_2 aqueous suspension. In a glove box under nitrogen atmosphere $LiWS_2$ (0.1 g, 0.39 mmol) was placed in a 125 ml Erlenmeyer flask equipped with stir bar and rubber stopper. The flask was removed from the glove box and 10 ml deoxygenated deionized H_2O was added. The material was then centrifuged, rinsed, and re-suspended in the same manner as MoS_2.

$Na_{0.14}(H_2O)_{0.45}MoS_2$. NaCl (0.11 g, 1.8 mmol) was dissolved in about 3.5 ml H_2O. To this solution was added an aqueous suspension of MoS_2 (3:1 excess Na^+). Flocculation occurred immediately. The reaction mixture was stirred for one half hour, centrifuged and the supernatant decanted.

The product was rinsed and centrifuged three times as described in the preparation of aqueous MoS_2, then deposited on a glass slide to dry.

$K_{0.23}(H_2O)_{0.4}MoS_2$. KCl (0.13 g, 1.8 mmol) was dissolved in about 3.5 ml H_2O. To this solution was added an aqueous suspension of MoS_2 (3:1 excess K^+). Flocculation occurred immediately. The product isolation was analogous to that used for $Na_{0.14}(H_2O)_{0.45}MoS_2$.

$Rb_{0.15}(H_2O)_{0.3}MoS_2$. RbCl (0.22 g, 1.8 mmol) was dissolved in about 3.5 ml H_2O. To this solution was added an aqueous suspension of MoS_2 (3:1 excess Rb^+). Flocculation occurred immediately. The product isolation was analogous to that used for $Na_{0.14}(H_2O)_{0.45}MoS_2$.

$Cs_{0.23}(H_2O)_yMoS_2$. CsF (0.27g, 1.8 mmol) was dissolved in about 2 ml H_2O. To this solution was added an aqueous suspension of MoS_2 (3:1 excess Rb^+). Flocculation occurred immediately. The product isolation was analogous to that used for $Na_{0.14}(H_2O)_{0.45}MoS_2$.

$Ba_x(H_2O)_yMoS_2$. $BaCl_2 \cdot 2H_2O$ (0.88g, 3.6 mmol) was dissolved in about 5 ml H_2O. To this solution was added an aqueous suspension of MoS_2 (6:1 excess Ba^{2+}). Flocculation occurred immediately. The product isolation was analogous to that used for $Na_{0.14}(H_2O)_{0.45}MoS_2$.

$Na_{0.19}(H_2O)_{0.45}WS_2$. NaCl (0.14 g, 2.4 mmol) was dissolved in about 3.5 ml H_2O. To this solution was added an aqueous suspension of WS_2 (6:1 excess Na^+). Flocculation occurred immediately. The product isolation was analogous to that used for $Na_{0.14}(H_2O)_{0.45}MoS_2$.

$K_{0.21}(H_2O)_{0.41}WS_2$. KCl (0.18 g, 2.4 mmol) was dissolved in about 5 ml H_2O. To this solution was added an aqueous suspension of WS_2 (6:1 excess K^+). Flocculation occurred immediately. The product isolation was analogous to that used for $Na_{0.14}(H_2O)_{0.45}MoS_2$.

$Rb_{0.24}(H_2O)_{0.34}WS_2$. RbCl (0.15 g, 1.2 mmol) was dissolved in about 3.5 ml H_2O. To this solution was added an aqueous suspension of WS_2 (3:1 excess Rb^+). Flocculation occurred immediately. The product isolation was analogous to that used for $Na_{0.14}(H_2O)_{0.45}MoS_2$.

$Cs_{0.13}(H_2O)_yWS_2$. Method 1. An aqueous suspension of WS_2 was added to 5 ml of a concentrated CsF solution in H_2O. To this solution was added an aqueous suspension of WS_2 (7:1 excess Cs^+). Flocculation occurred immediately. The product isolation was analogous to that used for $Na_{0.14}(H_2O)_{0.45}MoS_2$.

Method 2. CsI (0.73 g, 2.8 mmol) was dissolved in about 5 ml H_2O. To this solution was added an aqueous suspension of WS_2 (7:1 excess Cs^+). Flocculation occurred immediately. The product isolation was analogous to that used for $Na_{0.14}(H_2O)_{0.45}MoS_2$.

$Ba_{0.08}(H_2O)_yWS_2$. $BaCl_2 \cdot 2H_2O$ (0.29 g, 1.2 mmol) was dissolved in about 5 ml H_2O. To this solution was added an aqueous suspension of WS_2 (3:1 excess Ba^{2+}). Flocculation occurred immediately. The product isolation was analogous to that used for $Na_{0.14}(H_2O)_{0.45}MoS_2$.

H_xMoS_2. In a glove box under nitrogen atmosphere $LiMoS_2$ (0.3 g, 1.8 mmol) was placed in a 125 ml Erlenmeyer flask equipped with a stir bar and rubber stopper. The flask was removed from the glove box and 30 ml cold concentrated HCl was added. The reaction mixture was stirred for a few minutes, then was transferred to a centrifuge tube and centrifuged for a few minutes. The supernatant was decanted, then 30 ml cold H_2O was added to the solid to rinse, and the slurry was centrifuged again. This rinsing was repeated two more times, the supernatant after each rinse having pH~1, pH~1, and pH~7, respectively. The solid was then slurried in a few ml of H_2O and deposited on a glass slide to dry overnight.

H_xWS_2. In a glove box under nitrogen atmosphere $LiWS_2$ (0.3 g, 1.2 mmol) was placed in a 125 ml Erlenmeyer flask equipped with a stir bar and rubber stopper. The reaction procedure and rinsing was the same as the one used to prepare H_xMoS_2, with the supernatant after each rinse having pH~1, pH~4, and pH~7, respectively. The solid was then slurried in a few ml of H_2O and deposited on a glass slide to dry overnight.

Oxidized $LiMoS_2$. Method 1. In a glove box under nitrogen atmosphere $LiMoS_2$ (0.3 g, 1.8 mmol) was placed in a 125 ml Erlenmeyer flask equipped with a stir bar and rubber stopper. The flask was removed from the box, and 50 ml of a 0.18 M solution of I_2 in acetonitrile or 50 ml of a 45 mM solution of Br_2 in acetonitrile was added to the solid (5:1 excess I_2/Br_2). The mixture was stirred for different amounts of time

ranging from 15 minutes to 4 days, then was centrifuged and the supernatant decanted. The product was rinsed by re-suspending it in 15 ml acetonitrile and re-centrifuging 2 times and then deposited on a glass slide and a saran wrapped transmission XRD slide to dry.

Method 2. In a glove box under nitrogen atmosphere $LiMoS_2$ (0.15 g, 0.9 mmol) was placed in a 125 ml Erlenmeyer flask equipped with a stir bar and rubber stopper. The flask was removed from the box and an exfoliated suspension of MoS_2 was prepared as described previously, then centrifuged and rinsed once with acetonitrile. To the solid 50 ml of a 0.18 M MeCN solution of I_2 or 50 ml of a corresponding 45 mM MeCN solution of Br_2 was added (5:1 excess I_2/Br_2). The mixture stirred for different amounts of time ranging from 15 minutes to a week, was centrifuged and the supernatant decanted. The product was rinsed by re-suspending in acetonitrile, re-centrifuging and decanting the supernatant. The product was then deposited on a glass slide and a Saran™ wrapped transmission X-ray Diffraction (XRD) slide to dry.

Oxidized $LiWS_2$. Method 1. In a glove box under nitrogen atmosphere $LiWS_2$ (0.3 g, 1.2 mmol) was placed in a 125 ml Erlenmeyer flask equipped with a stir bar and rubber stopper. The flask was removed from the box, and to the solid 50 ml of a 0.12 M MeCN solution of I_2 or corresponding 75 ml 80 mM MeCN solution of Br_2 was added (10:1 excess I_2/Br_2). The mixture stirred for varying amounts of time from ~15

minutes to a week, was centrifuged and the supernatant decanted. The product was isolated as described for oxidized $LiMoS_2$.

Method 2. In a glove box under nitrogen atmosphere $LiWS_2$ (0.15 g, 0.6 mmol) was placed in a 125 ml Erlenmeyer flask equipped with a stir bar and rubber stopper. The flask was removed from the box and an exfoliated suspension of WS_2 was prepared as described previously, then centrifuged and rinsed with acetonitrile. To the solid 50 ml of a 0.12 M MeCN solution of I_2 or corresponding 75 ml 80 mM MeCN solution of Br_2 was added (10:1 excess I_2/Br_2). The reaction time and product isolation was the same as described above.

Method 3. $LiWS_2$ (0.15g, 0.6mmol) was used to prepare an exfoliated suspension as described previously. Next 100ml of a saturated aqueous solution of Br_2 was added. The product was centrifuged immediately for a few minutes, then rinsed with water and centrifuged three times. It was deposited on a glass slide and a Saran™ wrapped transmission XRD slide to dry.

5.2.2.Characterization.

Selected Area Electron Diffraction patterns were collected using a JEOL 120 CX Transmission Electron Microscope (TEM). Transmission and reflection powder X-ray diffraction patterns were collected using a Rigaku-Denki/RW400F2 (Rotaflex) rotating anode X-ray diffractometer using Cu-Kα radiation. Differential Scanning Calorimetry (DSC) measurements were conducted using a Shimadzu DSC-50 instrument under nitrogen flow in sealed aluminum containers at a heating rate of 5°C/minute. Thermogravimetric Analyses (TGA) employed a Shimadzu TGA-50 instrument under nitrogen flow in quartz containers at a heating rate of 2°C/minute. Energy Dispersive Spectroscopy (EDS) was used to determine the alkali metal to Mo/W ratio, and employed a JEOL-JSM-6400V Scanning Electron Microscope was operated at an accelerating voltage of 30kV using a Tracor Northern 5500 X-ray microanalysis attachment. Thermopower measurements utilized a MMR Technologies Seebeck System.

5.3 Results and Discussion

5.3.1 Cation encapsulated MS_2.

Addition of exfoliated MoS_2/WS_2 to the alkali halide solution results in immediate flocculation of the suspension. This rapid precipitation, which is not usually observed upon addition of neutral species, strongly suggests that the interaction of the layers with the alkali cations is ionic in nature. Similar behavior is observed upon addition of exfoliated MoS_2/WS_2 to solutions containing $Al_{13}O_4(OH)_{24}(H_2O)_{12}^{7+}$ or tetraphenylphosphonium cations.[9a,25]

The samples were characterized by reflectance X-ray diffraction (Figure 5.1a) and were found to be well ordered, particularly compared to the X-ray diffraction patterns of samples containing neutral species such as the cobalt chalcogenide clusters.[8] The predominance of the *00l* reflections in the pattern is due to the tendency of lamellar materials to adopt a preferred orientation. All samples exhibited interlamellar d-spacings in the range 9.3-9.7 Å (an expansion of 3.1 - 3.5 Å), indicating co-encapsulation of approximately one monolayer of water with the cations.

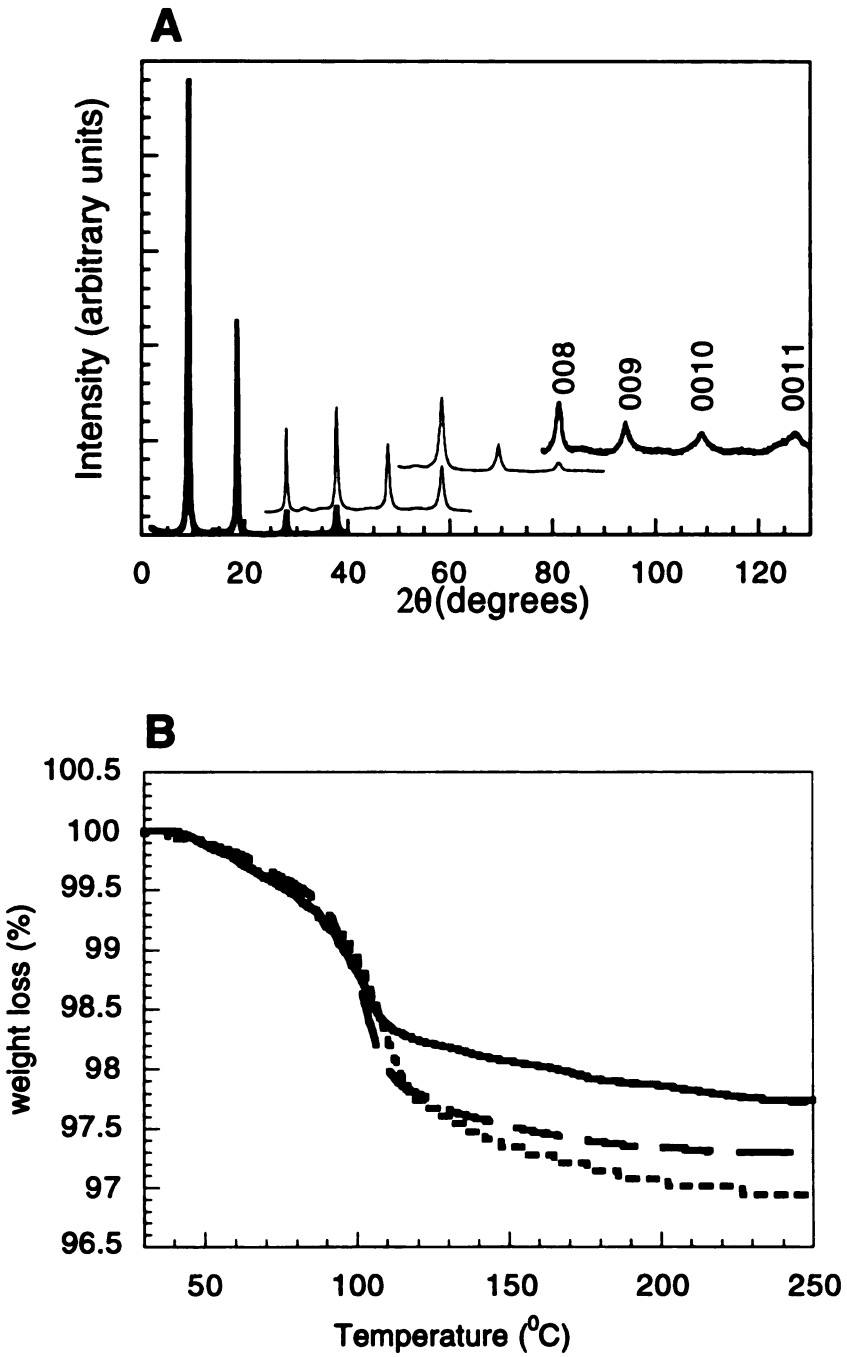

Figure 5.1. (A) X-ray diffraction pattern of $Na_{0.18}(H_2O)_{0.45}WS_2$., exhibiting a d-spacing of 9.7 Å (Δ= 3.5 Å). (B) TGA of $Na_{0.18}(H_2O)_{0.45}WS_2$ (dotted line), $K_{0.21}(H_2O)_{0.40}WS_2$ (dashed line), and $Rb_{0.24}(H_2O)_{0.34}WS_2$ (solid line). Weight loss corresponds to H_2O loss.

The flocculated products were found to have the following formulas: $Na_{0.14}(H_2O)_xMoS_2$, $K_{0.23}(H_2O)_xMoS_2$, $Rb_{0.15}(H_2O)_xMoS_2$, $Cs_{0.23}(H_2O)_xMoS_2$, $Na_{0.18}(H_2O)_xWS_2$, $K_{0.21}(H_2O)_xWS_2$, $Rb_{0.24}(H_2O)_xWS_2$, $Cs_{0.13}(H_2O)_xWS_2$, and $Ba_{0.08}(H_2O)_xWS_2$. . TGA (Thermal Gravimetric Analysis), performed in order to determine the amount of co-encapsulated water, indicates a range of 0.3-0.45 for x (Figure 5.1b). Higher x values were found for samples containing Na^+ and K^+; lower values for those containing Cs^+ and Rb^+. No halide counter-ions were detected. Although the presence OH- ions cannot be completely discounted, the pH of the suspension (~7) and the relatively poor affinity of the alkali cations for OH- ions make their co-encapsulation unlikely.

5.3.2 Electron diffraction studies of (cation)$_x$MS$_2$.

The cation intercalated MoS_2 and WS_2 samples were also examined by electron diffraction. Both restacked MoS_2 and WS_2 give rise to electron diffraction patterns which appear to be more simple than they actually are.[21] In Chapter 4, we solved and refined the structure of restacked MoS_2 and WS_2 from electron diffraction data.[21] The materials exhibit a superlattice caused by metal-metal associations to form zig-zag chains, similar to those observed in WTe_2.[26] This zig-zag distortion results in the

doubling of one axis of the hexagonal sublattice. As the hexagonal symmetry is destroyed, the new lattice is best described by an $\sqrt{3}a \times a$ orthorhombic cell (Figure 4.2d, Figure 4.3). Due to their turbostratic nature and the disorder introduced by the exfoliation/flocculation process, the diffraction patterns of exfoliated and restacked MoS_2 and WS_2 are often a "triplet" of these orthorhombic cells, forming an apparent $2a \times 2a$ superlattice (Figure 4.2b). Failure to recognize this twinning can lead to incorrect interpretations of the M-M interactions.

The cation intercalated samples are represented by an array of diffraction patterns (Figure 5.2) which contain an *additional superlattice* due to ordering of the electropositive cations in the gallery. The high vacuum found in a TEM (~10^{-7} torr) probably results in the removal of most of the co-encapsulated water from the samples. The majority of the patterns appear at first glance to contain a weak $6a \times 6a$ superlattice relative to the hexagonal sublattice, with distinct variations in the reflections present and the intensity distribution from one pattern to the next. Because of the propensity of these materials for twinning, however, the diffraction patterns are actually quite complicated.

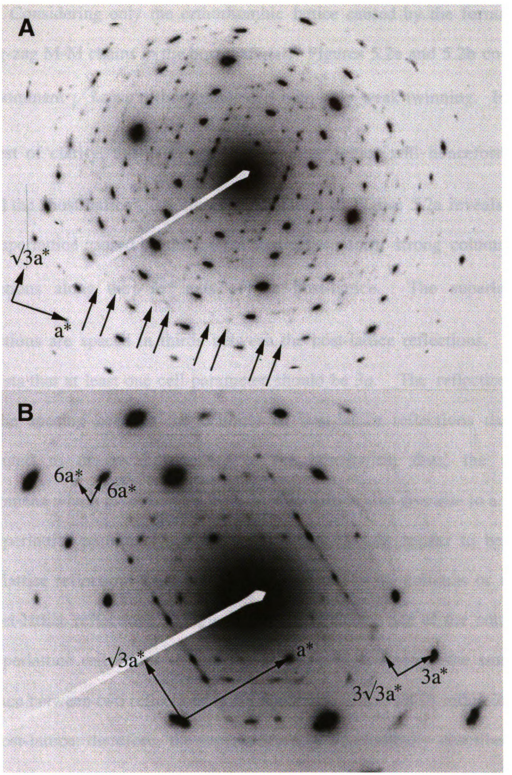

Figure 5.2. SAED patterns of (A) $Cs_{0.23}MoS_2$ and (B) $Cs_{0.13}WS_2$. Superlattice reflections caused by Cs^+ ordering indicate a tripling of the *a* axis and the $\sqrt{3}a$ axis, indicating a $3\sqrt{3}a \times 3a$ supercell. Twinning of the lattice projects a $6a \times 6a$ unit cell.

Considering only the orthorhombic lattice caused by the formation of zig-zag M-M chains in the host material,[21] Figures 5.2a and 5.2b contain one dominant $\sqrt{3}a \times a$ orthorhombic cell with only weak twinning. In the interest of clarity, this $\sqrt{3}a \times a$ orthorhombic lattice will henceforth be called the "host-lattice". A closer examination of Figure 5.2a reveals that the superlattice caused by the intercalated cations form strong columns of reflections along the $\sqrt{3}a^*$ axis of the host-lattice. The superlattice reflections are spaced in thirds between the host-lattice reflections. This suggests that at least one cell parameter should be $3a$. The reflections at 1/2 the spacing between the columns of host-lattice reflections can be attributed to the weak twinning of the host-lattice; thus, the same phenomena which give rise to a false $2a \times 2a$ lattice also give rise to a false $6a$ superlattice parameter. Interestingly, there do not appear to be any superlattice reflections from the cations contained in the columns or rows of host-lattice reflections in Figure 5.2a. Considering one of the columns of superlattice reflections to find the second cell parameter, the smallest distance between two reflections is 1/3 the length of the (*010*) reflection of the host-lattice; therefore, the superlattice may be minimally described by the orthorhombic cell $3a' \times 3b$ relative to the host-lattice ($a' = \sqrt{3}a$; b =

3a), and $3\sqrt{3}a \times 3a$ (orthorhombic) relative to the hexagonal sublattice of the host material (Figure 5.2b).

It is logical to conclude that, if the host-lattice is somewhat twinned, the superlattice will also be somewhat twinned. In this manner the variations in the other diffraction patterns (Figures 5.3 and 5.4) can be explained by the degree of twinning of the $\sqrt{3}a \times a$ orthorhombic host-lattice and the $3a' \times 3b$ cation superlattice. Figure 5.3a is very similar to Figures 5.2a and 5.2b, but comes from $K_{0.23}MoS_2$ rather than $Cs_{0.23}MoS_2$ (Figure 5.2a) or $Cs_{0.13}WS_2$ (Figure 5.2b). The host-lattice is more twinned than the pattern in Figure 5.2a, but the pattern of cation ordering is essentially the same. Figures 5.3b and 5.3c are from crystals of $K_{0.23}MoS_2$ and $Rb_{0.14}MoS_2$, respectively, that are twinned but are still relatively thin. The distribution of orthorhombic host-lattice cells is uneven, appearing to be stronger in one direction. Consequently, the cation superlattice in these pictures is still stronger in one direction, but does show evidence of twinning. Unlike the previous patterns, the cation superlattice reflections are now found in the columns of reflections along the $\sqrt{3}a^*$ axis of the dominant orthorhombic host-lattice (arrows, Figure

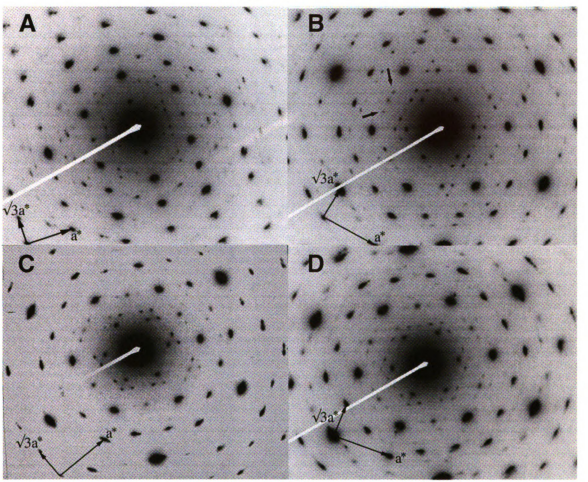

Figure 5.3. SAED patterns of (A) $K_{0.23}MoS_2$, which resembles the patterns in Figure 5.2 but the degree of twinning is slightly greater; (B) $K_{0.23}MoS_2$ and (C) $Rb_{0.15}MoS_2$, in which the host-lattice is more twinned but the crystals are still relatively thin; and (D) $K_{0.23}MoS_2$, from a thick crystal with a very twinned host-lattice and a "halo" of cation superlattice reflections. As twinning of the host-lattice increases, twinning of the cation superlattice increases, leading to a variety of diffraction patterns.

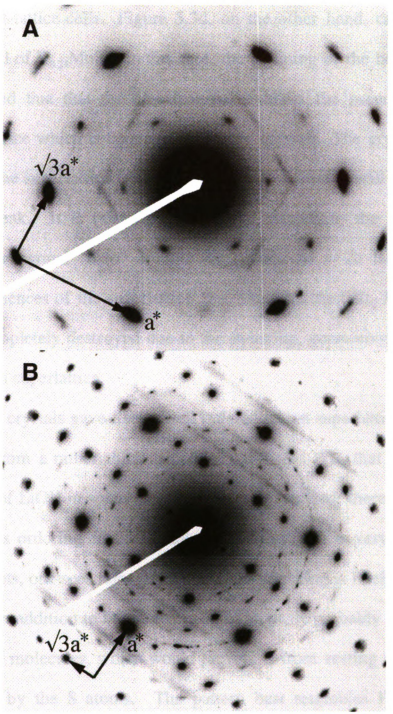

Figure 5.4. SAED patterns from (A) a thick crystal of Li_xWS_2 and (B) a thin crystal of $Rb_{0.15}MoS_2$. Streaking is observed due to disorder of the cations. The cations are more susceptible to disorder along the $\sqrt{3}a$ axis.

5.3b). This seems to be due to cation superlattices associated with the other (weaker) host-lattice cells. Figure 5.3d, on the other hand, came from a thicker crystal of $K_{0.23}MoS_2$. In this case, the twinning of the host-lattice is so pronounced that that the host material exhibits the pseudo *2a x 2a* hexagonal lattice which is common in thicker crystals. The crystal is thin enough that the superlattice from the intercalated cations is still visible, but extremely weak. It is twinned in the same manner as the host-lattice, creating a hexagonal "halo" around the pseudo *2a x 2a* lattice. The systematic absences of the superlattice (for example, the *020, 130,* and the *310*) are completely destroyed due to the twinning, generating the pseudo *6a x 6a* cation superlattice.

Not all crystals gave rise to well ordered cation superlattices. Figure 5.4a comes from a rather thick sample of exfoliated WS_2 that contained a large excess of LiOH in solution when it was flocculated; there is evidence of Li^+ cations ordering in the sample, but the pattern is very weak and, instead of spots, one sees faint streaking. The streaking is likely due to the fact that Li, in addition to being a very light atom, is probably coordinated by four water molecules, which would prevent it from resting easily in the sites created by the S atoms. The pattern best resembles Figure 5.3d. Crystals which contain discrete superlattice spots are somewhat unusual;

more common are patterns which contain disorder or streaking along the $\sqrt{3}a^*$ axis of the host lattice, as in the $Rb_{0.14}MoS_2$ crystal in Figure 5.4b.

5.3.3 Modeling the cation ordering.

It is virtually impossible to obtain a diffraction pattern which is completely "single crystal" with respect to the host-lattice and the cation superlattice so that this manner of indexing the patterns might be confirmed; however, it is the best available indexing which can account for the variations in intensities and reflections from one diffraction pattern to the next, all of which can be found within one sample. As such, we have developed a cation ordering model from which an electron diffraction pattern was simulated. It has been designed to resemble the diffraction patterns in Figures 5.2a, 5.2b, and 5.3a, since they are the closest to a "single crystal" pattern (Figure 5). As noted previously, no superlattice reflection is found within a column or row of host-lattice reflections (Figure 5.2a). The model of cation ordering, depicted in Figure 5.5a, gives rise to such an electron diffraction pattern (Figure 5.5b).[27]

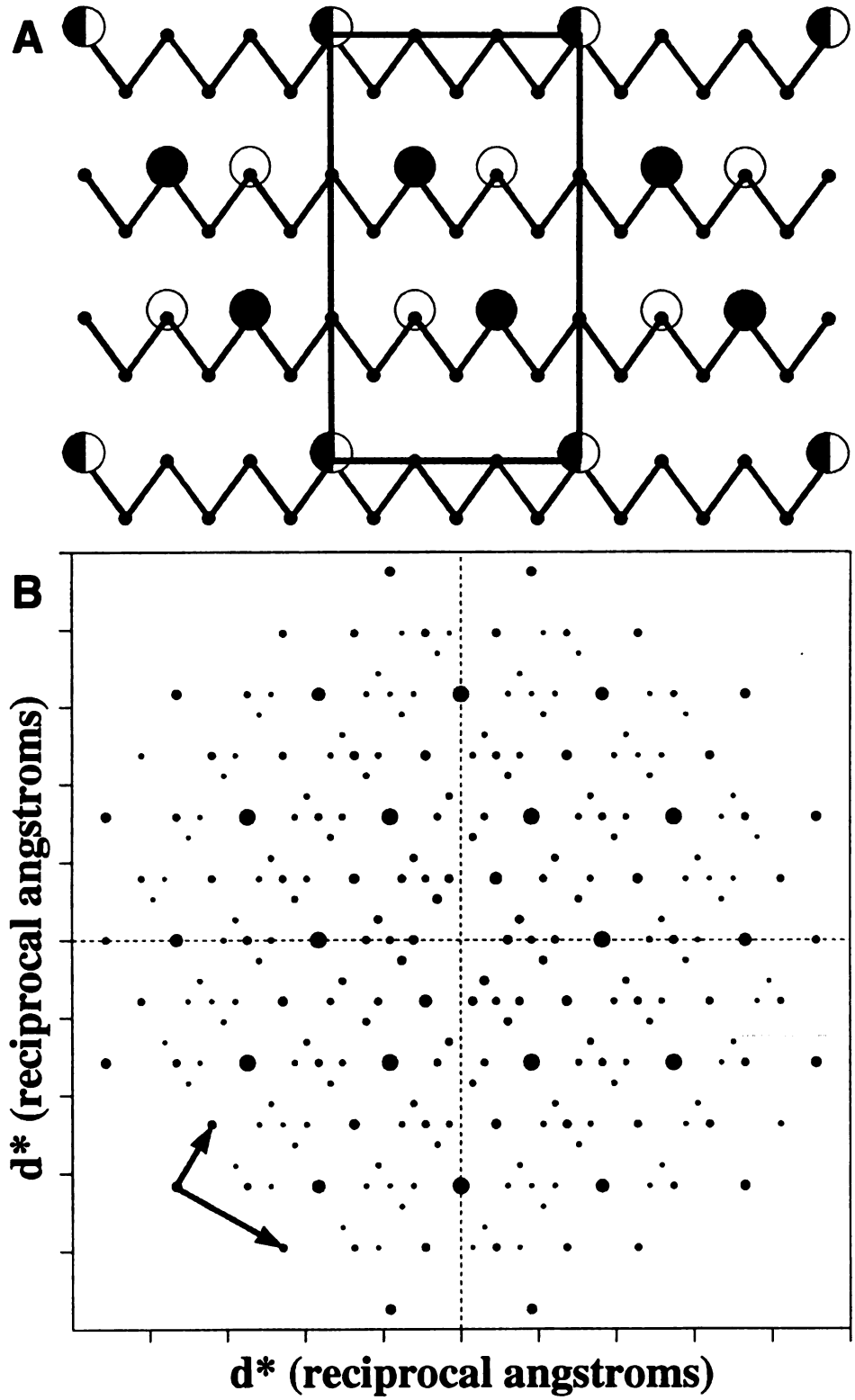

Figure 5.5. (A) Structural model and (B) simulated electron diffraction pattern to explain the observed SAED patterns in Figures 5.2-5.4. Filled circles represent cations in one layer; open circles represent cations in a second layer. The projection of the two results in a $3\sqrt{3}a \times 3a$ supercell.

The cell contains three chains. Alkali cations are placed along the chains in pockets defined by sulfur atoms, where a cation would be expected to reside in the gallery. One third of the sites are empty in two of the chains; two thirds of the sites are empty in the third chain. So many alkali cations would not normally be in such close proximity to one another within one layer, however, particularly when one considers the elemental analyses of these samples. More likely this picture represents the superposition of two alternating layers of cations, depicted as white and black. Hence, four of the cations have an occupancy of 0.5 and one cation is fully occupied. This results in a stoichiometry of $A_{0.167}MS_2$, which is consistent with the experimentally determined formula. Note that it is a necessary condition of the systematic absences that all the alkali cations be in the same kind of site, either "down" or "up" relative to the zig-zag chain. The alkali cations occupy only sites which are pointing "up" in the model presented in Figure 5.5a; however, the sites which are pointing "down" are equally valid sites, so it becomes apparent that this is a possible source of disorder in the samples. The streaking which is observed along the $\sqrt{3a}$ * axis in Figure 5.4b indicates that the cations are more disordered along the $\sqrt{3a}$ axis of the host-lattice. This is reasonable when one considers that the M atom distorts from its ideal octahedral position along this axis, causing an accompanying shift of the S atoms and distorting the site on which the

alkali cation sits. Also, the fact that there seems to be no disorder along the *a* axis indicates that the cations are better ordered along the zig-zag chains than between zig-zag chains.

A few of the electron diffraction patterns did not have this *3a x 3b* superlattice, but had a rather different pattern (Figure 5.6) corresponding to a $\sqrt{3}a \times \sqrt{3}a$ lattice combined with the pseudo *2a x 2a* lattice of the host material, forming a "honeycomb" pattern. The projection of this $\sqrt{3}a \times \sqrt{3}a$ unit cell occupies a smaller area than the previous superlattice (31 $Å^2$ vs. 161 $Å^2$), which is puzzling when one considers that it is most readily observed for samples in which Ba^{2+} is encapsulated. To reconcile such a lattice with the observed loading of cation one must again employ alternating layers of cations and consider their projection onto the *ab* plane. For example, in Figure 5.7a a model has been constructed with four layers of cations, depicted as white, black, gray, and striped circles. The unit cell per MS_2 layer is $2\sqrt{3}a \times 2\sqrt{3}a$ (solid line), but the projection is the smaller $\sqrt{3}a \times \sqrt{3}a$ lattice (dashed line). This gives a stoichiometry of $A_{0.09}MS_2$. The simulated diffraction pattern generated from this cation model (Figure 5.7b) resembles the experimental data.[27] It is now possible to understand why cations of different charge can have the same diffraction pattern - they can occupy half as many sites and require twice as many

layers to project the appropriate unit cell. This is consistent with the fact that the superlattice is weaker in the samples containing Ba^{2+} than it is in the samples containing Na^{+} or Rb^{+}.

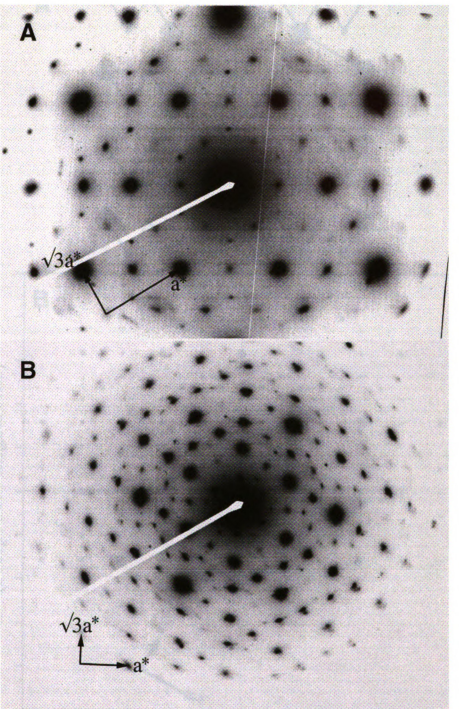

Figure 5.6. SAED patterns of (A) $Ba_{0.08}MoS_2$ and (B) $Na_{0.14}MoS_2$. The combination of a $\sqrt{3}a \times \sqrt{3}a$ cation superlattice with a pseudo $2a \times 2a$ host-lattice gives rise to a "honeycomb" pattern. This alternate cation superlattice, although most common for samples with encapsulated Ba^{2+}, was also observed within samples which exhibited the $3\sqrt{3}a \times 3a$ superlattice.

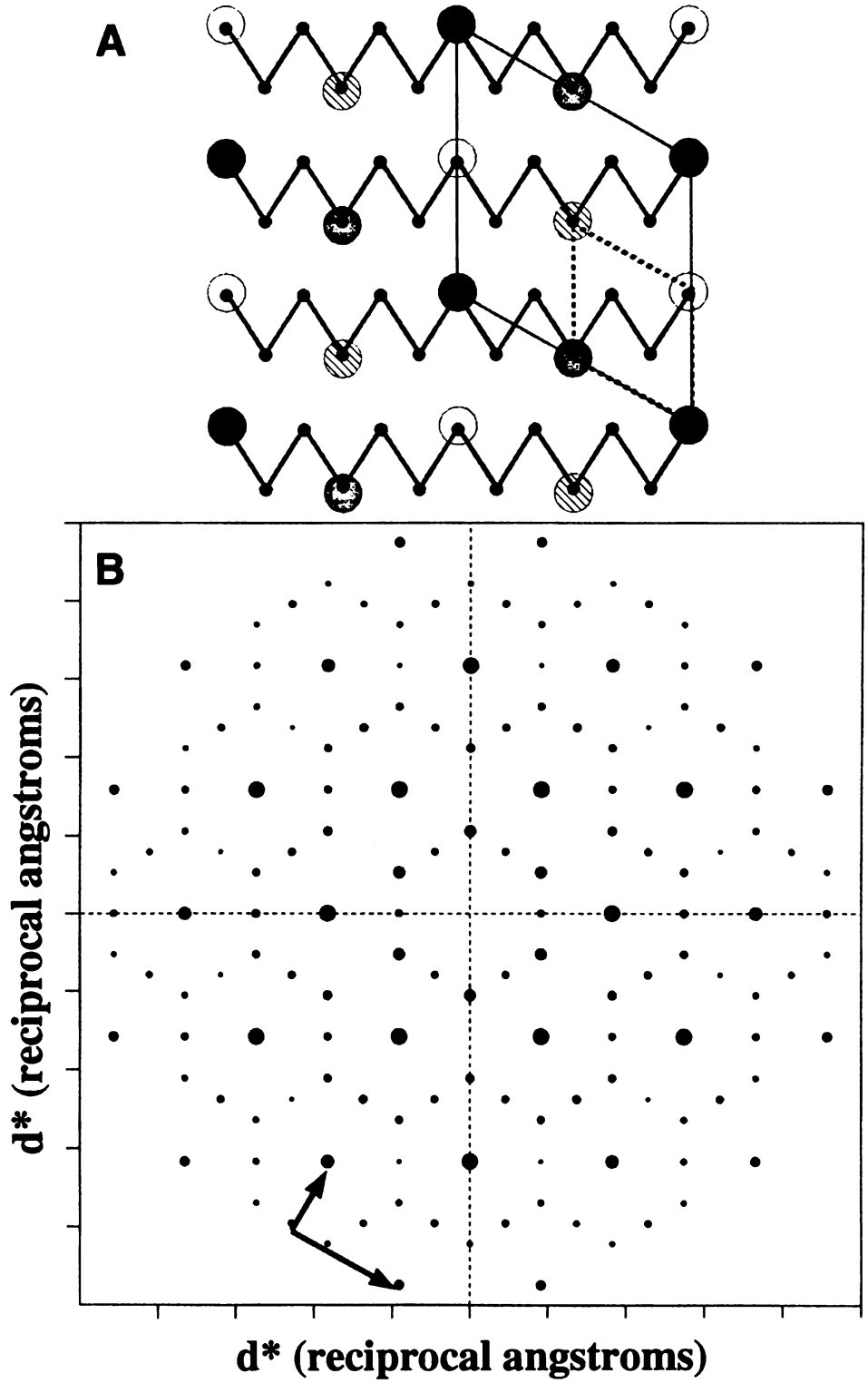

Figure 5.7. (A) Structural model and (B) simulated ED pattern to explain the SAED patterns in Figure 5.6. Black circles represent one cation layer; open circles a second; grey a third; and striped a fourth. Each layer has a $2\sqrt{3}a \times 2\sqrt{3}a$ lattice, but the $\sqrt{3}a \times \sqrt{3}a$ lattice is formed by the projection.

5.3.4. Oxidation state of M (M = Mo,W) and the charge of the layers.

The fact that one can see ordering of alkali cations in the MoS_2 and WS_2 layers without co-intercalation of the halide counter-ions supports the conclusion that the exfoliated and restacked layers retain residual negative charge. The layers in suspension behave as if they are solvated macroanions, precipitating readily in the presence of most cationic species. The hypothesis that the charge is due to the association of OH^- ions with the basal planes seems unlikely because the driving force for the association of the OH^- ions with the layers is not obvious. Furthermore, the pH of the exfoliated suspension has been reduced to ~7 by repeated rinsing. It seems surprising that any remaining OH^- ions would not be at least partially displaced in a solution with an excess of halide ions, resulting in materials with co-encapsulated halide ions. Unfortunately the high degree of disorder and the propensity of the systems for twinning make it impossible to determine the degree of negative charge on the layers based on the cell parameters of the samples with encapsulated cations.

The amount of negative charge on exfoliated and restacked MoS_2 has been studied rather extensively by a group of Russian scientists.[13,17] They assert that MoS_2 which has been freshly exfoliated under an inert atmosphere has a negative charge of approximately 0.15-0.29 per Mo atom

(Li^+ counter-ion), but if the dispersion is allowed to sediment over time the value decreases to 0.07-0.12 per Mo atom.[17a] This slow, continuous oxidation of MoS_2 suspensions in solution over time may explain how it is possible to intercalate the neutral cobalt chalcogenide clusters, which require stirring for at least 2 days before encapsulation is observed.[8] This same group has also observed that in some transition metal systems it is possible to co-intercalate OH^- anions, thereby increasing the number of cations which may be encapsulated between the layers beyond the range of negative charge attributed to MoS_2.[13c] The ability of MoS_2 and WS_2 to accept co-intercalated OH^- ions hinders the quantitation of the negative charge through chemical analyses, as the exfoliation process creates an abundance of OH^- ions. These difficulties necessitate the use of "innocent" cations such as alkali metals, as they have poor affinity for OH^-. This is particularly true for the heavier alkali cations Rb^+ and $Cs,^+$ and they are easier to quantify than Li^+, Na^+ or K^+. Although the external OH^- ions can largely be removed by rinsing, it is difficult to be certain of their total removal without acidification of the solution. This complicates the situation by increasing the ionic strength of the solution and providing protons, a competing cation which is virtually impossible to unambiguously detect. In addition, if the MoS_2 is in fact slowly oxidized further in solution over time, more OH^- ions will be generated. Even restacked MoS_2 or MoS_2 with encapsulated hydrated alkali cations may continue to undergo

redox chemistry with intercalated H_2O (see Eq. (5.1)). Presumably the cations/OH^- pairs would remain trapped between the layers, indicating at least the oxidation state at the time of flocculation, but would not reflect the continuum of oxidation states possible for the material over time.

The results of our chemical analyses, which indicate a negative charge in the range 0.10-0.25 per Mo/W atom, are consistent with the results of the analysis of fresh Li^+ encapsulated samples[13,17] and are more reliable due to the use of the heavier alkali metal cations. Other studies involving the selective encapsulation of heavy metal ions in such as Ag^+ and Pb^{2+} into MoS_2 and WS_2 have been conducted, and the results indicate a higher negative charge (0.5-0.8 per Mo/W atom).[28] These chalcophilic cations, like the alkali cations, have a poor affinity for OH^-; however, the samples have been prepared under significantly different experimental conditions, in which $LiMS_2$ was exfoliated in the presence of the cations under anaerobic conditions in solutions of moderate ionic strength, resulting in extremely rapid precipitation of the layers. These results suggest that a continuum of oxidation states are possible for MoS_2 and WS_2, depending on the experimental conditions.

5.3.5 Oxidation reactions of $LiMS_2$.

In light of increasing evidence that these materials have a negative charge, $LiMS_2$ and exfoliated MS_2 were treated with oxidizing agents to see if truly neutral MS_2 could be obtained by oxidizing with I_2 or Br_2. The oxidized products were characterized by X-ray and electron diffraction studies and their thermal behavior.

Figure 5.8a contains the Selected Area Electron Diffraction pattern of $LiMoS_2$ oxidized with Br_2 in acetonitrile (MeCN). If $LiMoS_2$ is first exfoliated in water, then rinsed with acetonitrile, forming $Li_{1-n}(MeCN)_xMoS_2$ (n=0.75-0.85), and subsequently oxidized with Br_2 in acetonitrile, similar patterns can be observed. The pattern resembles the one found for the sample $Ba_{0.08}MoS_2$, in which a hexagonal array of diffraction spots resembling a "honeycomb" is formed by the superposition of the twinned $\sqrt{3}a \times a$ lattice caused by Mo-Mo distortions and a $\sqrt{3}a \times \sqrt{3}a$ lattice formed by the ordering of the Ba^{2+} cations. The SAED pattern from oxidation of MoS_2 with Br_2 is caused by a superposition of two types of lattices as well; however, in this case the $\sqrt{3}a \times \sqrt{3}a$ lattice is not due to Li^+ cations ordering between the layers, but different Mo-Mo associations. Wypych and coworkers have reported that, upon treatment with I_2 or

$H_2Cr_2O_7$, $K_{0.33}(H_2O)_yMoS_2$ is oxidized to a material which contains a $\sqrt{3}a$ x $\sqrt{3}a$ lattice attributed to Mo-Mo associations.[22] This material has a smaller *a* parameter than restacked MoS_2. A closer inspection of Figure 5.8a reveals that the hexagons become increasingly distorted as one moves further away from the center spot (Figure 5.8b), indicating a mismatch in the two lattices. The $\sqrt{3}a$ x $\sqrt{3}a$ lattice has a smaller *a* parameter than the $\sqrt{3}a$ x *a* lattice. If $Li_{1-n}(MeCN)_xMoS_2$ is treated with Br_2 it is possible to find electron diffraction patterns of a few crystals which contain only the $\sqrt{3}a$ x $\sqrt{3}a$ lattice (Figure 5.8c), but the majority of the sample is a decomposition product. The material with the $\sqrt{3}a$ x $\sqrt{3}a$ lattice is metastable and appears to be more susceptible to conversion to 2H-MoS_2 than the material with the $\sqrt{3}a$ x *a* lattice. If one treats $LiMoS_2$ with Br_2 for a longer period of time or with sonication, the $\sqrt{3}a$ x $\sqrt{3}a$ lattice disappears, leaving a mixture of 2H-MoS_2 and material with the $\sqrt{3}a$ x *a* lattice (Figure 5.9).

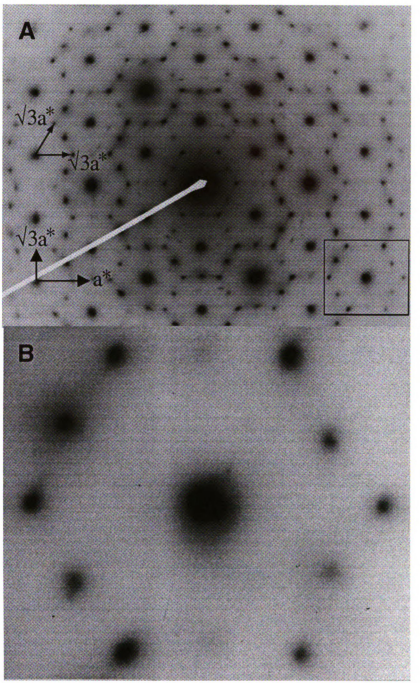

Figure 5.8. (A) SAED pattern of $LiMoS_2$ oxidized with Br_2 in MeCN. The pattern, which resembles those in Figure 5.6, is a combination of a twinned $\sqrt{3}a \times a$ orthorhombic lattice and a $\sqrt{3}a \times \sqrt{3}a$ hexagonal lattice of MoS_2. The two lattices have slightly different cell parameters, which results in a distortion of the honeycomb as one moves away from the center of the pattern (B).

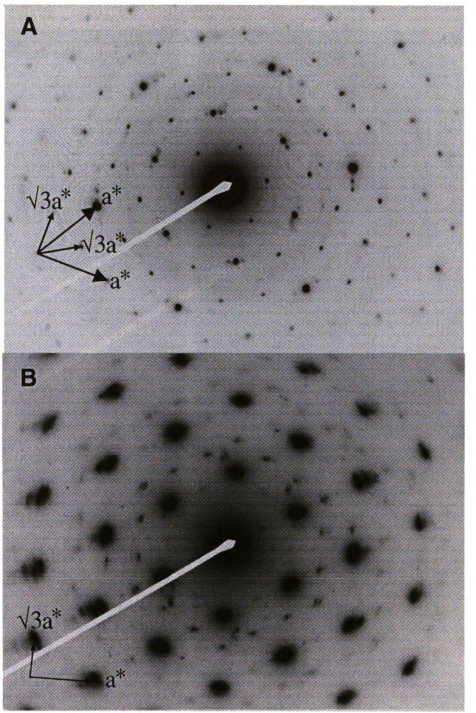

Figure 5.9. Oxidation of $Li_{1-n}(H_2O)_xMoS_2$ with Br_2 results in some particles which contain only the $\sqrt{3}a \times \sqrt{3}a$ lattice (A). If $Li_{1-n}(H_2O)_xMoS_2$ or $LiMoS_2$ is oxidized over a longer period of time, or with sonication, the $\sqrt{3}a \times \sqrt{3}a$ lattice disappears, leaving a mixture of 2H-MoS_2 and MoS_2 with the twinned $\sqrt{3}a \times a$ orthorhombic lattice (B).

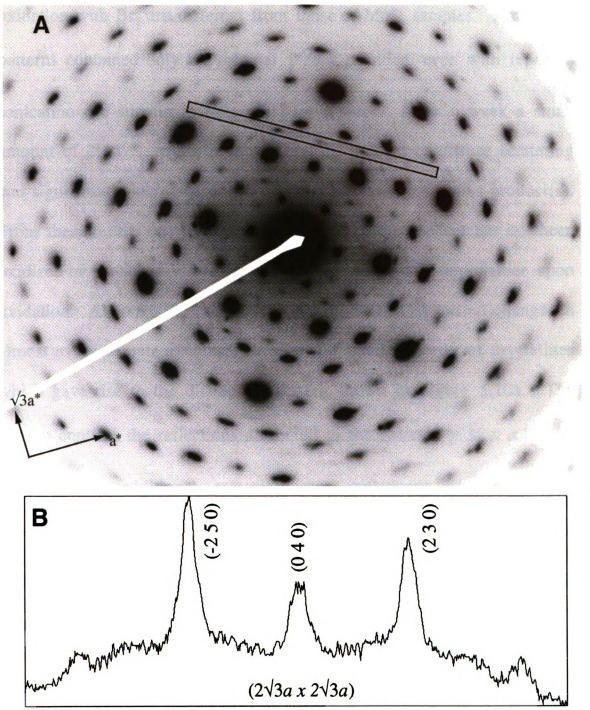

Figure 5.10. SAED pattern of a minority phase formed upon oxidation of $LiWS_2$ with Br_2 in MeCN which exhibits a $2\sqrt{3}a \times 2\sqrt{3}a$ lattice.

The electron diffraction patterns of WS_2 samples obtained upon oxidation with Br_2 are different from those of MoS_2 samples. Almost all patterns contained only the original $\sqrt{3}a \times a$ lattice, even with repeated sonication and stirring in excess Br_2 for a week. After a week a small amount of 2H-WS_2 could be found, and the amount of diffuse scattering was significantly increased due to decomposition to amorphous product(s). From these results one can conclude that either the product has not been oxidized or restacked WS_2 does not exhibit an alternate superlattice upon oxidation. Although the majority of the product exhibited no change, in almost every sample examined there was a small minority of crystallites which gave rise to the diffraction pattern shown in Figure 5.10a. The pattern contains the reflections attributed to the twinned $\sqrt{3}a \times a$ lattice, but there are additional, extremely weak reflections which could be indexed as a $2\sqrt{3}a \times 2\sqrt{3}a$ lattice (Figure 5.10b). This suggests that even if WS_2 is able to have an alternate superlattice upon oxidation it is not the same as the lattice found in oxidized MoS_2.

5.3.6 X-ray diffraction studies of oxidized MS_2.

$LiMS_2$ and $Li_{1-n}(MeCN)_xMS_2$ were also examined by transmission X-ray diffraction (Figures 5.11, 5.12). Due to the turbostratic nature of these samples induced by the exfoliation/flocculation process, only *hk0* reflections are visible from the $\sqrt{3}a \times a$ lattice. Interpretation of the X-ray diffraction patterns is more difficult than the electron diffraction patterns in part because the peaks are broad. Furthermore, some *h0l* reflections of the 2H form of the dichalcogenide overlap with the unique *hk0* reflections from the $\sqrt{3}a \times a$ lattice and the $\sqrt{3}a \times \sqrt{3}a$ lattice. For example, the *200* of the $\sqrt{3}a \times \sqrt{3}a$ lattice overlaps with the *103* of 2H-MS_2. In fact, the presence of the $\sqrt{3}a \times \sqrt{3}a$ lattice cannot be reliably determined by powder X-ray diffraction because the only reflection which is not subject to an overlap problem is the *100*, which is extremely weak. The presence of the $\sqrt{3}a \times a$ lattice is more easily monitored because the *120*, a moderately strong reflection at d=2.10 Å, does not overlap with peaks from either of the other two phases which may be present in the sample.

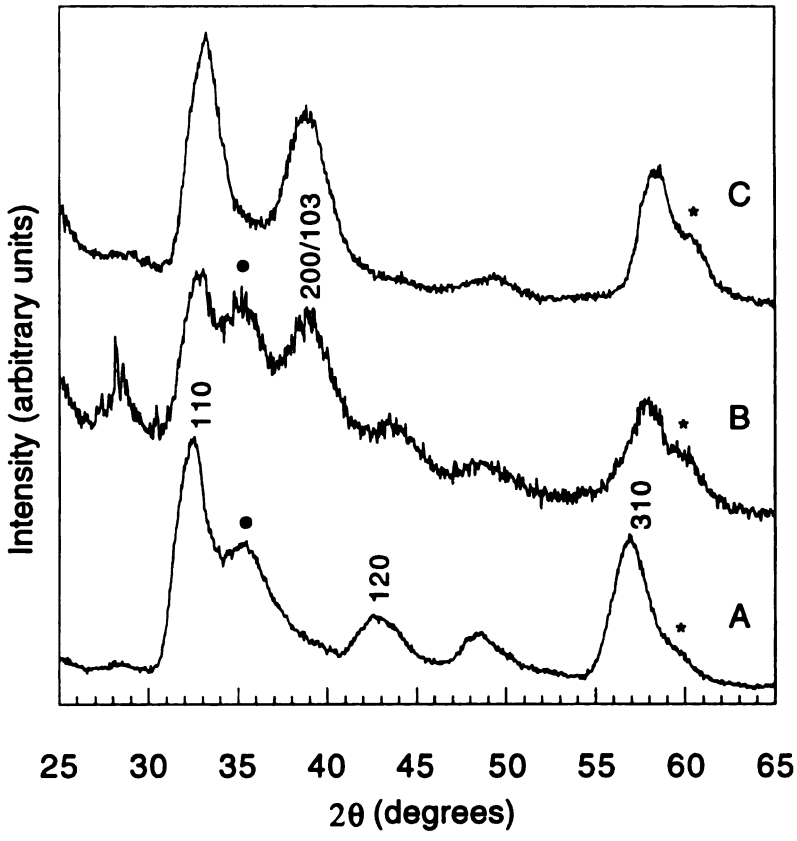

Figure 5.11. Transmission X-ray diffraction (XRD) pattern of $LiMoS_2$ oxidized in MeCN with increasing time. (A) Initially the pattern contains the $a \times \sqrt{3}a$ lattice with two new peaks at 2.55 Å (solid black circle) and 1.56 Å (asterisk). (B) a peak at 2.3 Å appears, indexed as either the *200* of the $\sqrt{3}a \times \sqrt{3}a$ lattice or the *103* of 2H-MoS_2. (C) The *120* of the $a \times \sqrt{3}a$ lattice has disappeared. The pattern is mostly 2H-MoS_2.

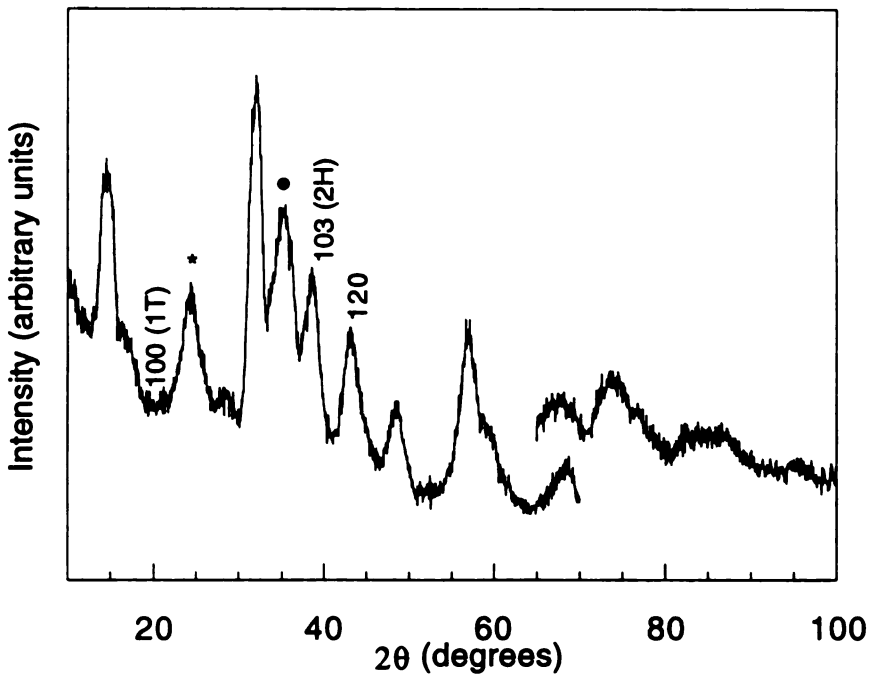

Figure 5.12. Transmission XRD pattern of $LiWS_2$ oxidized with Br_2 in MeCN. The black circle marks a peak at 2.55 Å which does not appear to be an *hk0* reflection of any of the three expected lattices. The asterisk marks a contribution from the Saran™ wrap substrate.

The time dependent behavior of the oxidation of restacked MoS_2 (and $LiMoS_2$) is illustrated in Figure 5.11. Initially the $\sqrt{3}a \times a$ lattice dominates (Figure 5.11a), with the appearance of a shoulder (d = 1.56 Å) on the *310* reflection at 2θ = ~59 degrees and a new peak at 2θ = 35° (d = 2.55 Å) which is not visible in the electron diffraction patterns and is not readily indexed to any of the 3 phases which may be present. At an intermediate stage a new peak appears at 2θ = ~38° (d = 2.35 Å) which, as mentioned previously, can be indexed as either the *200* of the $\sqrt{3}a \times \sqrt{3}a$ lattice or the *103* of 2H-MoS_2 (Figure 5.11b). The *110* and the *310* reflections begin to shift to smaller d spacings (d = 2.78 to 2.71 Å and 1.61 to 1.59 Å). This is not surprising, because the $\sqrt{3}a \times a$ lattice has the largest *a* parameter at 3.21 Å; the $\sqrt{3}a \times \sqrt{3}a$ lattice is slightly contracted, as evidenced by the electron diffraction patterns; and in 2H-MoS_2 *a* = 3.16 Å. The *120* peak of the $\sqrt{3}a \times a$ lattice at 2θ = ~38° (d = 2.10 Å) is still present, and the shoulder at 2θ = ~59° has become more pronounced. In the final stage the diffraction pattern no longer contains the peak at 2θ = 35° (d = 2.55 Å) or the *120* peak of the $\sqrt{3}a \times a$ lattice at 2θ = ~38° (d = 2.10 Å), and the *110* and the *310* reflections have shifted to even smaller d

spacings (d = 2.69 Å and 1.58 Å). The pattern at this stage contains mostly MoS_2 which has converted to the 2H form.

The transmission X-ray diffraction patterns of restacked WS_2 upon treatment with Br_2 (Figure 5.12) resemble those of oxidized restacked MoS_2. The peak at $2\theta = 35^\circ$ (d = 2.55 Å) appears but, unlike in MoS_2, does not disappear with time. Under more rigorous conditions or with time the peak at $2\theta = \sim 38^\circ$ (d = 2.35 Å) appears. Given that there is no evidence of a $\sqrt{3}a \times \sqrt{3}a$ lattice by electron diffraction, that peak is probably best indexed as the *103* reflection of 2H-WS_2. The disappearance of the *120* peak of the $\sqrt{3}a \times a$ lattice at $2\theta = \sim 38^\circ$ (d = 2.10 Å) and the new peak at $2\theta = 35^\circ$ (d = 2.55 Å) happens upon heating the material, which converts it to 2H-WS_2 (Figure 5.13).

The reflection X-ray diffraction patterns contain the basal *001* reflection at 6.05 Å for WS_2 and 6.21 Å for MoS_2, indicating the de-intercalation of most or all of the lithium cations. The basal spacing of WS_2 is slightly contracted (0.1 Å) relative to 2H-MS_2, but expands upon heating.

Residual negative charge on MoS_2 is also substantiated by these electron diffraction patterns. The structure of restacked MoS_2 and WS_2, which we recently solved from electron diffraction data and found to be WTe_2 type, consists of metal-metal associations to form zig-zag chains.[21]

As mentioned previously, a material called '1T-MoS_2' has been prepared by the oxidation of $K_{0.33}(H_2O)_yMoS_2$ and found to have a $\sqrt{3}a \times \sqrt{3}a$ lattice by X-ray diffraction and also by STM studies.[22,24] The starting material $K_{0.33}(H_2O)_yMoS_2$, however, has also been studied by STM and found to have the same structural distortion as restacked MoS_2 and WS_2.[29] Furthermore, it is evident by the electron diffraction studies presented here that restacked MoS_2 can be at least partially converted to "1T-MoS_2" upon treatment with Br_2 or I_2. The exterior of the particle appears to be oxidized, forming the $\sqrt{3}a \times \sqrt{3}a$ lattice, whereas the interior of the particle retains the original $\sqrt{3}a \times a$ structure. Actually in their STM studies of 1T-MoS_2 the authors conceded that occasionally they observed the $\sqrt{3}a \times a$ lattice found in their starting material and concluded that it was symptomatic of incomplete oxidation of those samples.

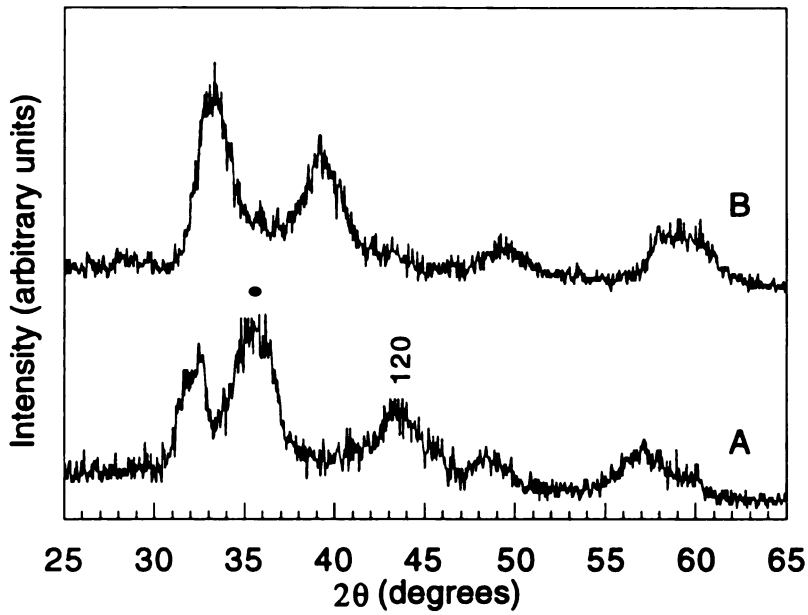

Figure 5.13. Transmission XRD pattern of $LiWS_2$ oxidized with Br_2 (A) before and (B) after heating. The peak at 2.55 Å (black circle) disappears, leaving 2H-WS_2.

5.3.7 DSC studies of oxidized MS_2.

As mentioned earlier, restacked MoS_2 and WS_2 are metastable, and can be converted to 2H-MS_2 by an irreversible exothermic transition upon heating. The 1T- form of MoS_2 with the $\sqrt{3}a \times \sqrt{3}a$ lattice has also been reported to be metastable with a comparable conversion.[22] Figure 5.14 contains a DSC measurement of oxidized MoS_2, which has been identified by electron diffraction to contain both the $\sqrt{3}a \times a$ and $\sqrt{3}a \times \sqrt{3}a$ lattices, and a DSC measurement of restacked MoS_2 for comparison. Restacked MoS_2 undergoes conversion to 2H-MoS_2 at 98°C (at a heating rate of 5°C/min). The transition in the MoS_2 obtained by oxidizing $LiMoS_2$ with Br_2 in acetonitrile occurs at a lower temperature, the broad peak reaching a maximum at 90°C. Although by TEM it is evident that the material contains more than one kind of lattice, it is not possible to resolve two separate transitions. $Li_{1-n}(MeCN)_xMoS_2$ oxidized with Br_2 converts rapidly, and a DSC measurement of the material could not be obtained.

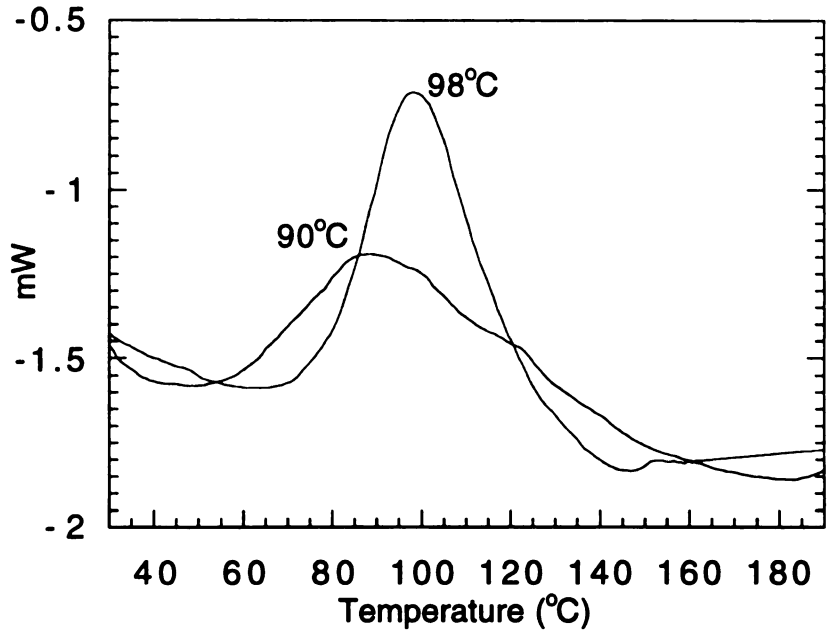

Figure 5.14. Differential Scanning Calorimetry (DSC) plots of restacked and $LiMoS_2$ oxidized with Br_2. Restacked MoS_2 exhibits an irreversible exothermic phase transition at 98°C, corresponding to its conversion to 2H-MoS_2. $LiMoS_2$ oxidized with Br_2 undergoes a similar transition at 90°C.

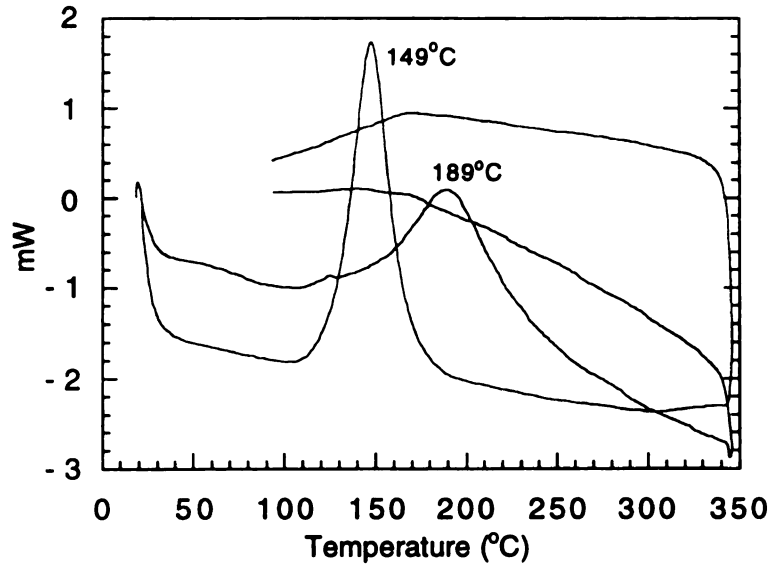

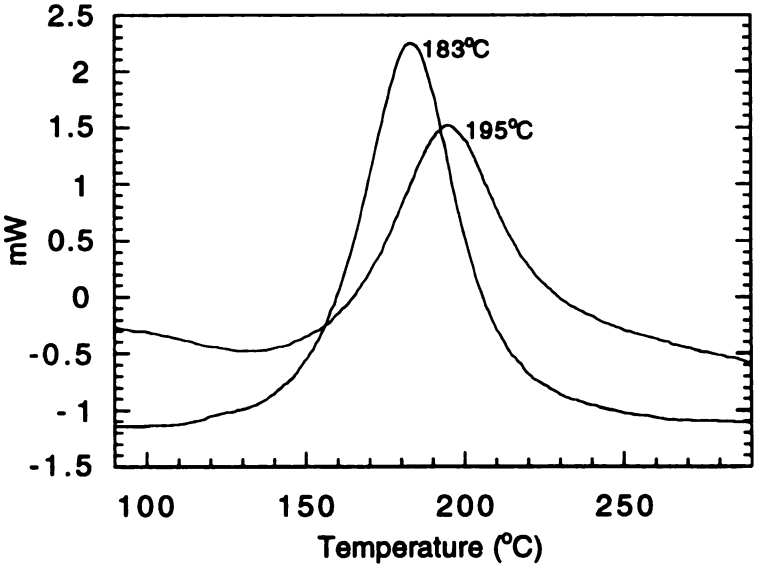

Figure 5.15. DSC plots showing the irreversible exothermic phase transition to 2H-WS_2. (A) $LiWS_2$ (149°C) and $Li_{1-n}(MeCN)_xWS_2$ (189°C) oxidized with Br_2 in MeCN (B) $Li_{1-n}(H_2O)_xWS_2$ oxidized with Br_2 in H_2O (183°C) and restacked WS_2 (195°C).

The situation is different and somewhat more complicated for the oxidation of WS_2 samples (Figure 5.15). Restacked WS_2 undergoes conversion to 2H-WS_2 at 195°C (at a heating rate of 5°C/min). WS_2 obtained by treating $LiWS_2$ with Br_2 in acetonitrile converts at 149°C, whereas $Li_{1-n}(MeCN)_xWS_2$ treated with Br_2 in acetonitrile converts at 189°C (Figure 5.15a). By electron diffraction and transmission X-ray diffraction the materials are structurally identical, containing the $\sqrt{3}a \times a$ lattice. The oxidation was carried out in acetonitrile because aqueous exfoliated WS_2 decomposes fairly rapidly upon exposure to Br_2, but if the aqueous reaction is isolated within a few minutes it is possible to see a shift in the transition to lower temperatures (Figure 5.15b). By transmission X-ray diffraction this material has the $\sqrt{3}a \times a$ lattice with a small shoulder at 2.55 Å, indicating that it has the same structure as the products of the oxidation of $Li_{1-n}(MeCN)_xWS_2$ and $LiWS_2$.

The structural behavior of restacked WS_2 and $LiWS_2$ is clearly different from that of restacked MoS_2 and $LiMoS_2$ upon treatment with Br_2. Despite the lack of a $\sqrt{3}a \times \sqrt{3}a$ phase in the WS_2 system, there is a dramatic shift in conversion temperature, from 195°C to 149°C, which is reminiscent of the shift in the transition temperature observed in the MoS_2 system. This shift suggests that oxidation has in fact taken place.

Furthermore, reflection X-ray diffraction indicates no residual cations between the layers (i.e., the d spacing is 6.1 Å). The fact that both restacked and oxidized WS_2 have the $\sqrt{3}a \times a$ lattice implies that, at least in WS_2, the shift in conversion temperature is not dependent on a structural rearrangement, but rather the degree to which the sample is oxidized. The discrepancy in transition temperature between Br_2 treated $LiWS_2$ and Br_2 treated $Li_{1-n}(MeCN)_xWS_2$ is probably due to limited diffusion in $Li_{1-n}(MeCN)_xWS_2$. In $LiWS_2$ the acetonitrile can solvate the lithium cations, swelling the layers apart and allowing the oxidant to access the layers more intimately, whereas $Li_{1-n}(MeCN)_xWS_2$ does not swell in acetonitrile; hence the interior of the particles is inaccessible to the oxidizing agent and the material remains trapped in the incompletely oxidized state that it achieved upon exfoliation in water.

Studies of the structure dependence upon oxidation state in MoS_2 (and WS_2) are complicated in part because 2H-MoS_2 undergoes a phase transition upon lithiation in which the coordination environment changes from trigonal prismatic to octahedral. If only a small amount of lithium is introduced the material can remain in the 2H-MoS_2 structure.[30] It has also been observed that the material does not convert to the octahedral structure homogeneously with small amounts of lithium, resulting in a two phase system.[18a] Electrochemical studies which start with 2H-MoS_2 are difficult

to interpret due to this problem.[31] The $\sqrt{3}a$ x a octahedral phase can be used as a starting point, however. Electrochemical studies of Li_xMoS_2, $K_x(H_2O)_yMoS_2$, and $K_x(H_2O)_yWS_2$ which start from the octahedral structure indicate the presence of 4-6 different phases in the range x = 0 to x = 1.[18b, 32] Although some authors have attributed these many phases to cation ordering in the gallery[31], others have attributed them to charge density waves.[32] The different observed superlattices in MoS_2 suggest that charge density waves are responsible for at least some of these phases. Wypych and coworkers have proposed a scheme containing three different lattices: a $2a$ x $2a$ for $K_{0.7}MoS_2$, $\sqrt{3}a$ x a for $K_{0.33}(H_2O)_yMoS_2$, and a $\sqrt{3}a$ x $\sqrt{3}a$ for 1T-MoS_2.[24] A comparison of the electrochemical behavior of $K_x(H_2O)_yMoS_2$ and $K_x(H_2O)_yWS_2$ reveals that the two materials behave differently at low x values[32], consistent with the different electron diffraction results observed in the reaction of $LiMoS_2$ and $LiWS_2$ with Br_2.

5.3.8 Acid restacked MS_2.

When $LiMS_2$ is exfoliated in concentrated acid the product should form a proton bronze, H_xMS_2. The transmission X-ray diffraction patterns for the reaction of $LiMoS_2$ and $LiWS_2$ with concentrated HCl (Figure 5.16) show that the materials retain the $\sqrt{3}a \times a$ lattice and a peak appears at 2.55 Å. The products were examined by electron diffraction and exhibited only the $\sqrt{3}a \times a$ lattice with no evidence of an additional reflection at 2.55 Å. In this case, the structure of H_xMoS_2 is the same as that of H_xWS_2, exhibiting no evidence of a $\sqrt{3}a \times \sqrt{3}a$ lattice. The reflection X-ray diffraction patterns exhibit basal *00l* spacings of 6.05 Å.

If $LiWS_2$ is exfoliated directly in concentrated HCl the DSC shows an exothermic transition at 155°C, whereas if it is first exfoliated in H_2O and then concentrated acid is added it exhibits a transition temperature of 191°C (Figure 5.17). Presumably the x values in the products of each reaction, H_xWS_2, are different. The discrepancy in the behavior of $LiWS_2$ and $Li_{1-n}(H_2O)_xWS_2$ in acidic conditions is similar to the discrepancy upon oxidation with Br_2, in which the difference in conversion temperatures

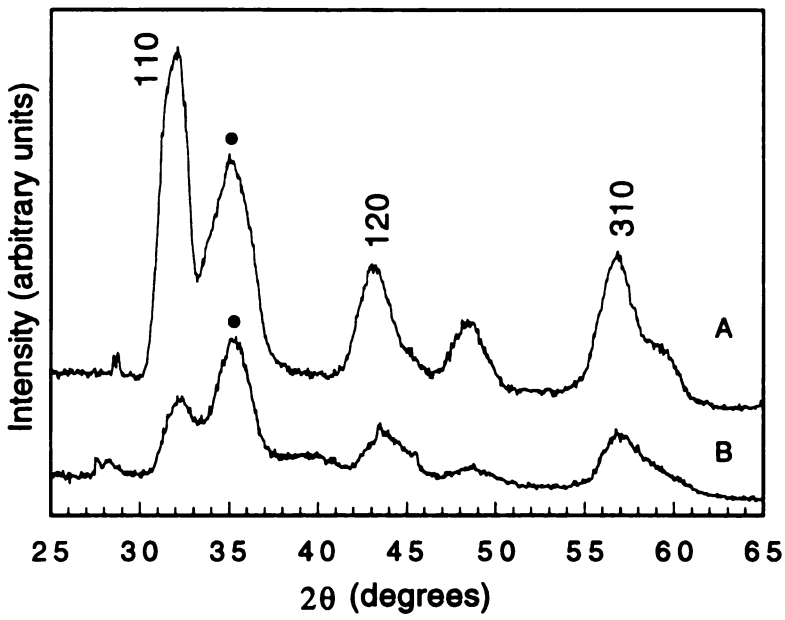

Figure 5.16. Transmission XRD pattern of (A) $LiWS_2$ and (B) H_xMoS_2 obtained from $LiMoS_2$ exfoliated in concentrated HCl. Black circle marks peak at 2.55 Å.

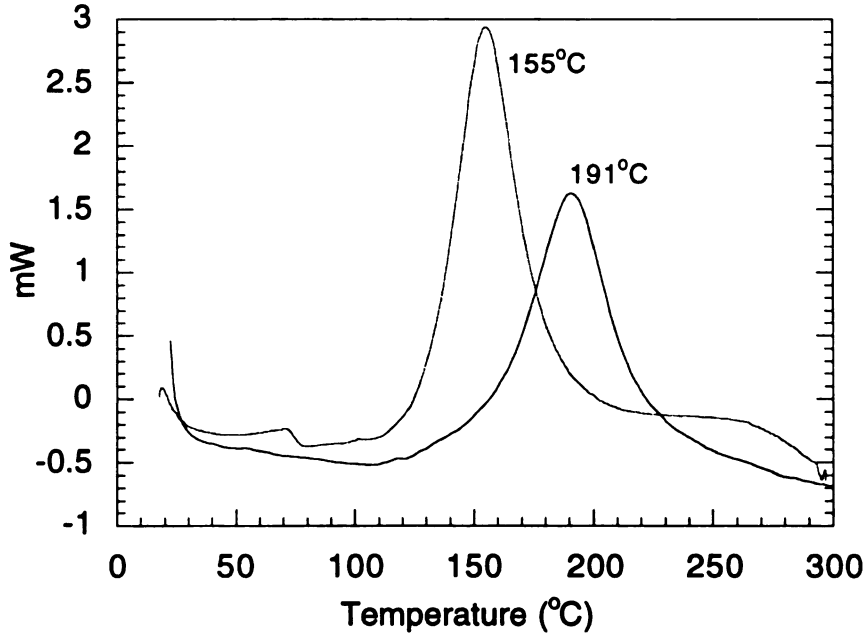

Figure 5.17. DSC plots of H_xWS_2 obtained from the reaction of HCl with (A) $LiWS_2$ (155°C) and $Li_{1-n}(H_2O)_xWS_2$ (191°C).

could be attributed to a diffusion problem. Exfoliation in concentrated acid provides more oxidizing conditions than exfoliation in H_2O before addition of acid. The amount of oxidation during the exfoliation process is important because there is a competition between oxidation and proton encapsulation. Once the material has flocculated its oxidation is limited by diffusion; hence the discrepancy in transition temperatures.

$LiMoS_2$ exfoliated in concentrated acid does not exhibit a shift in its exothermic transition to a lower temperature. The structure of H_xMoS_2 samples prepared from the reaction of $LiMoS_2$ and $Li_{1-n}(H_2O)_xMoS_2$ with acid resembles that of their W analogues more than in Br_2 solution. There is no evidence of the $\sqrt{3}a \times \sqrt{3}a$ phase in acidic conditions. This suggests that the Russian scientists' hypothesis that MoS_2 is fully oxidized upon treatment with acid is not correct; only that protons are now the encapsulated counter-ion.[17]

As mentioned previously, the authors who first reported the exfoliation of MoS_2 believed that the negative charge of the layers was due to OH^- groups associated with the basal planes of the layers. It was believed that exfoliated MoS_2 (and WS_2) has a point of zero charge (PZC) upon acidification. The authors used the different PZC to create a restacked composite material with alternating MoS_2 and WS_2 layers, forming a superstructure along the *00l* axis.[16c] Their evidence for a

superstructure of alternating MoS_2 and WS_2 layers was poor, however; a better interpretation of these results is that the introduction of protons to a homogeneous mixture of exfoliated layers resulted in rapid flocculation, creating a homogeneous mixture of MoS_2 and WS_2 in the product. They also developed the concept that the PZC occurs at slightly different pH for the edge OH^- sites and basal OH^- sites, and used this to create a House-Of-Cards structure for MoS_2.[16b] Their evidence for this kind of structure was a decrease in the intensity of the *00l* reflections in the X-ray diffraction pattern. However, the intensity of the *00l* reflections, which is indicative of the degree of order in the flocculated layers, can be influenced by a variety of factors (the ionic strength of the solution, for example), and does not constitute proof of a point of zero charge on the layers.

The mysterious peak at 2.55 Å in the transmission X-ray diffraction patterns of H_xMS_2 and $LiMS_2$ oxidized with Br_2 is puzzling, but shifting of the layers relative to one another could allow *h0l* reflections to appear. A *102* reflection has been observed in some samples of 2H-MoS_2 at that d spacing. The peak at 2.3 Å is almost certainly the *103* of 2H-MS_2.

An illustration of the different superlattices observed in MoS_2 and WS_2 due to M-M associations can be found in Figure 5.18. An ideal 1T-MS_2 lattice (not experimentally observed) can distort to form zig-zag

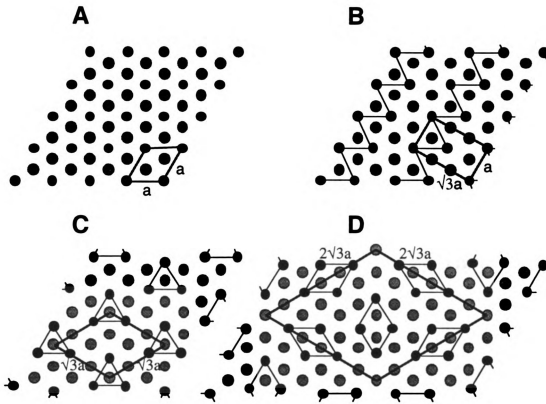

Figure 5.18. Schematic illustrating (A) an ideal 1T-MS_2 lattice, (B) a $\sqrt{3a}$ *x a* lattice with infinite zig-zag metal chains, (C) a $\sqrt{3a}$ *x* $\sqrt{3a}$ lattice with trimers, and (D) a $2\sqrt{3a}$ *x* $2\sqrt{3a}$ lattice with possible tetramers formed due to M-M distortions.

chains, giving rise to the orthorhombic $\sqrt{3}a \times a$ lattice found in restacked MoS_2 and WS_2. It can trimerize, giving rise to a $\sqrt{3}a \times \sqrt{3}a$ lattice found in MoS_2 upon oxidation with Br_2 or I_2 (Figure 5.18c). Finally, when WS_2 is treated with Br_2, a minority phase with a $2\sqrt{3}a \times 2\sqrt{3}a$ lattice is formed. This distortion could be due to a number of M-M associations, perhaps a trimerization similar to Figure 5.18c or a tetramerization (Figure 5.18d).

5.3.9 Thermopower measurements.

As mentioned previously, the reduction of 2H-MoS_2 with lithium results in a structural transformation from trigonal prismatic to octahedral metal coordination and a change in properties from semiconducting to metallic. These changes have been explained using a depiction of the band structures for $LiMoS_2$ in both coordination environments, which revealed that there was a net stabilization in energy upon conversion to octahedral that resulted in a half-filled band with predominantly d orbital character.[18]

Restacked MoS_2 and WS_2 retain octahedral coordination about the metal atom,[21] and their conductivity has been reported elsewhere[4,7b] to be metallic. If one simply removes electrons from the half filled band which was published for $LiMoS_2$, an idealized octahedral d^3 system, one should

expect an n-type conductor for the d^2 system (Figure 5.19). Thermopower measurements on restacked MoS_2 and WS_2, however, indicate that they are p-type (hole) conductors (Figure 5.20), with room temperature values of 50 and 20 μV/K, respectively. The structural distortion in restacked MoS_2 and WS_2 to form zig-zag chains obviously should result in a change in the band structure. In fact, distortion of octahedral ML_2 d^2 systems to form zig-zag chains has been predicted by Extended Huckel Tight Binding calculations[33] and, for a fully oxidized d^2 system, results in a half filled band (Figure 5.19). If, however, the system is actually d^{2+n}, as is the case with restacked MoS_2 and WS_2, residual negative charge results in a material with p-type conductivity, consistent with our experimental observations (Figure 5.19).

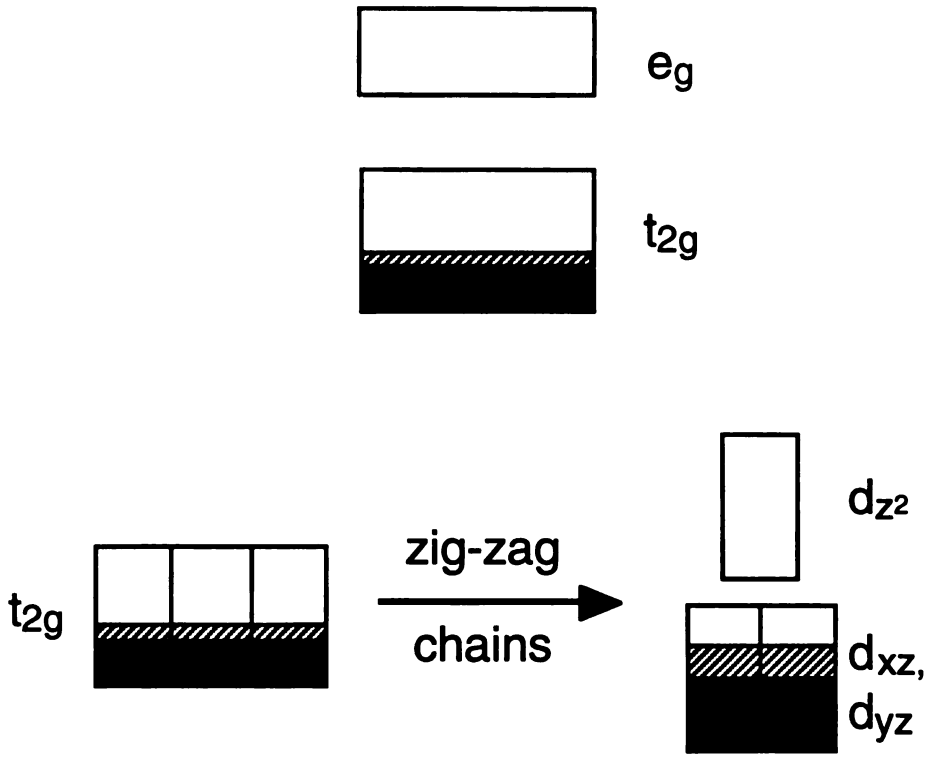

Figure 5.19. Schematic band diagram illustrating the distortion of an ideal octahedral system to form zig-zag chains. The ideal system describes an n-type conductor whether it is d^2 (black fill) or d^{2+x} (black fill + stripes). The distorted system is half filled for d^2 and more than half filled for d^{2+x}, resulting in a p-type metallic conductor.

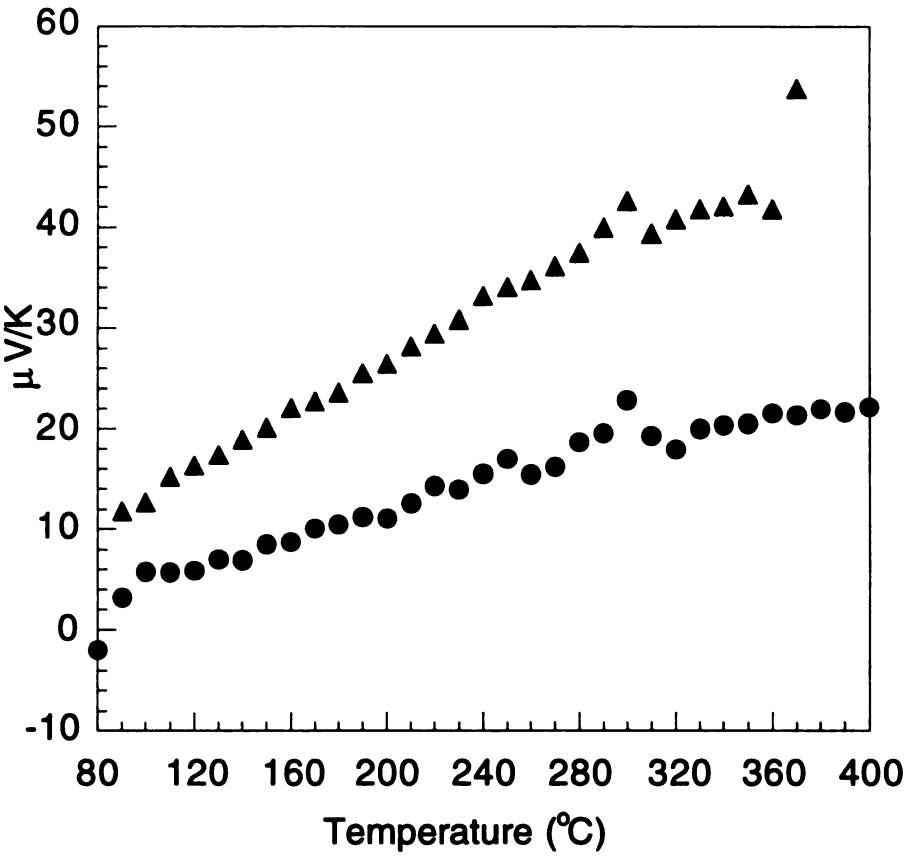

Figure 5.20. Thermopower measurements of restacked MoS_2 (triangles) and WS_2 (circles). The relatively small magnitude and slope of the data is consistent with that of a p-type metallic conductor.

5.4 Conclusions

MoS_2 and WS_2 retain some negative charge upon exfoliation and flocculation. Although it is possible to incorporate neutral species, cations can also be encapsulated without a detectable co-encapsulated anion, usually giving rise to very ordered reflectance X-ray diffraction patterns.[9-13,17] In the studies presented here hard, electropositive alkali cations have been encapsulated in MoS_2 and WS_2 under neutral synthetic conditions. The choice of these cations and these synthetic conditions minimizes the risk of co-encapsulation of OH^- ions. The cations order in the gallery, forming additional superlattices. The range of negative charge on the layers appears to be 0.15-0.25 for both MoS_2 and WS_2, which is consistent with measurements on samples prepared in a similar fashion by other researchers.[17]

Structural characterization of restacked MoS_2 also supports a negative charge. Restacked MoS_2 and WS_2 have been found by electron diffraction to have the same superlattice as $K_x(H_2O)_yMoS_2$.[21,24] Treatment of restacked MoS_2 with Br_2 results in a change from a $\sqrt{3}a \times a$ superlattice to a $\sqrt{3}a \times \sqrt{3}a$ superstructure, which is analogous to the superstructure observed in "1T-MoS_2", the oxidation product of $K_{0.7}MoS_2$.[22] This change in structure upon exposure to an oxidizing agent implies that restacked

MoS_2 is incompletely oxidized, and is probably better formulated as Li_xMoS_2 or $Li_x(H_2O)_yMoS_2$.

Restacked WS_2 does not appear to exhibit a structural change upon exposure to Br_2. However, both restacked MoS_2 and WS_2 exhibit irreversible exothermic transitions which are shifted to lower transition temperatures upon treatment with Br_2. The shift is quite significant in WS_2, from 195°C to 149°C in the Br_2-treated sample, indicating that oxidation has taken place. It is somewhat surprising, however, that oxidation of restacked WS_2 does not result in an alternate superlattice analogous to the $\sqrt{3}a \times \sqrt{3}a$ superstructure observed in oxidized MoS_2.

The products of all thermal conversions are the semiconducting phase 2H-MS_2, which requires an expulsion of the residual negative charge and explains why the oxidation state affects the transition temperature. The expulsion of the residual negative charge likely results in the reduction of residual H_2O (or H^+ in H_xMS_2), forming H_2 gas.[34]

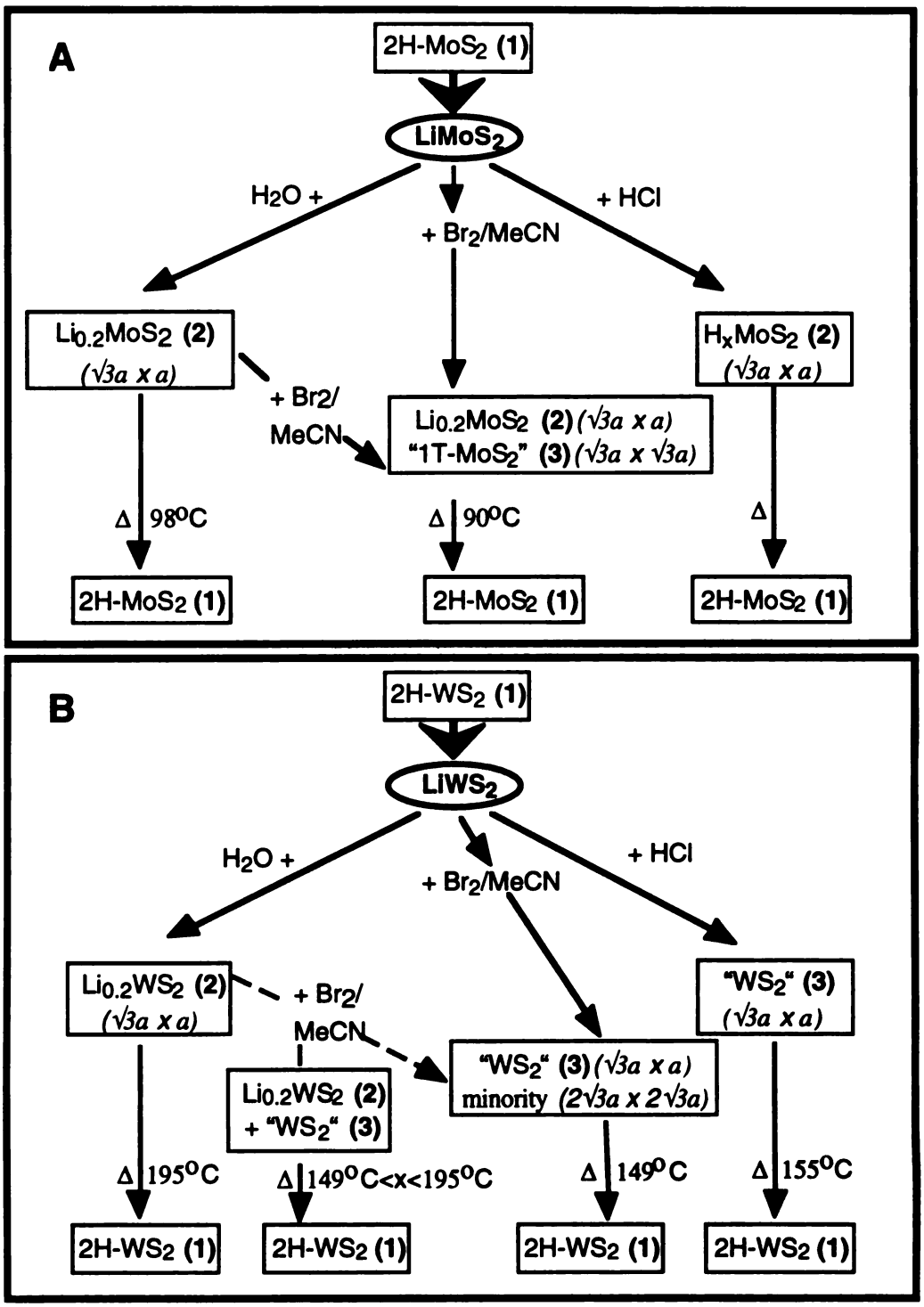

Figure 5.21. Reaction scheme illustrating the different phases obtained with various treatment of (A)MoS_2 and (B) WS_2.

The different phases of MoS_2 produced under various experimental conditions are illustrated in Figure 5.21a. This scheme is intended to correlate all forms of MoS_2 and the inter-conversion between forms, and to help clear up any remaining confusion regarding the nature of this system. Exfoliation and flocculation of $LiMoS_2$ in water results in restacked MoS_2, which can be more accurately formulated as $Li_{0.2}MoS_2$ (**2**) based on the chemical analyses of the alkali cation encapsulated products. Oxidation of $LiMoS_2$ in Br_2/MeCN results in a mixture of "1T-MoS_2" (**3**) and $Li_{0.2}MoS_2$. $LiMoS_2$ exfoliated in H_2O can be converted to the same mixture upon treatment with Br_2/MeCN. If $LiMoS_2$ is exfoliated in concentrated HCl it forms H_xMoS_2, a material with the same superstructure as $Li_{0.2}MoS_2$ which does not appear to be oxidized. A similar scheme in Figure 5.21b illustrates the analogous phases of WS_2. A principal difference is that the product of the oxidation of $LiWS_2$ with Br_2 in MeCN, called "WS_2" (**3**), is not structurally different from $Li_{0.2}WS_2$. Depending on the preparation, it is possible to isolate products exhibiting a continuum of transition temperatures between 149°C and the transition temperature of $Li_{0.2}WS_2$ (195°C). Another difference is that, unlike in MoS_2, when $LiWS_2$ reacts with concentrated HCl, the transition temperature of the product (155°C) is closer to that of the oxidized material (**3**) rather than $Li_{0.2}WS_2$. Given the higher energy of the d orbitals of W, it is not surprising that WS_2 is more readily oxidized than MoS_2 under comparable experimental conditions.

Clearly the MoS_2 and WS_2 systems are rather complicated, and the nature of the phase obtained is very sensitive to the experimental conditions used to prepare the product. The term "restacked MoS_2" has been used casually in the literature to represent material which has been converted to the 2H form as well as the metastable compound with the $\sqrt{3}a \times a$ lattice, and is usually written without a formulation of the negative charge present. In addition, MoS_2 and WS_2 resemble one another, but there are distinct differences between the two systems. To prevent future confusion researchers should take special care to formulate their products precisely, and also to recognize that restacked MoS_2 (and WS_2) which has been heated above its conversion temperature is better described by the formula 2H-MoS_2 (and 2H-WS_2).

References

1. Brenner, J.; Marshall, C.L.; Ellis, L.; Tomczyk, N.; Heising, J.; Kanatzidis, M.G. *Chem. Mater.,* 1998, **10**, 1244.

2. Whittingham, M.S. *Prog. Solid State Chem.*, 1978, **12**, 41.

3. a) Dines, M.B. *Mater. Res. Bull.*, 1975, **10**, 287. b) Yang, D.; Frindt, R.F. *J. Phys. Chem. Solids*, 1996, **57**, 1113.

4. a) Tsai, H.L.; Heising, J.; Schindler, J.L.; Kannewurf, C.R.; Kanatzidis, M.G. *Chem. Mater.*, 1997, **9**, 879. b) Wang, L.; Kanatzidis, M.G. manuscript in preparation.

5. Joensen, P.; Frindt, R.F.; Morrison. S.R. *Mater. Res. Bull.*, 1986, **21**, 457.

6. a) Divigalpitiya, W.M.R.; Frindt, R.F.; Morrison, S.R. *Science,* 1989, **246**, 369. b) Zhou, X.; Yang, D.; Frindt, R.F. *J. Phys. Chem. Solids*, 1996, **57**, 1137. c) Kosidowski, L.; Powell, A.V. *Chem. Commun.*, 1998, 2201.

7. a) Divigalpitiya, W.M.R.; Frindt, R.F.; Morrison, S.R. *J. Mater. Res.* 1991, **6**, 1103. b) Kanatzidis, M.G.; Bissessur, R.; DeGroot, D.C.; Schindler, J.L.; Kannewurf, C.R. *Chem. Mater.*, 1993, **5**, 595. c) Wang, L.; Schindler, J.L.; Thomas, J.A.; Kannewurf, C.R.; Kanatzidis, M.G. *Chem. Mater.*, 1995, **7**, 1753. d) Ruiz-Hitzky, E.; Jimenez, R.; Casal, B.; Manriquez, V.; Santa Ana, A.; Gonzalez, G. *Adv. Mater.*, 1993, **5**, 738. e) Lemmon, J.P.; Lerner, M.M. *Chem. Mater.*, 1994, **6**, 207.

8. Bissessur, R.; Heising, J.; Hirpo, W.; Kanatzidis, M.G. *Chem. Mater.*, 1996, **8**, 318.

9. a) Heising, J.; Bonhomme F.; Kanatzidis, M.G. *J. Solid State Chem.*, 1998, **139**, 22. b) Ollivier, P.J.; Kovtyukhova, N.I.; Keller, S.W.; Mallouk, T.E. *Chem. Commun.*, 1998, 1563.

10. Tagaya, H.; Hashimoto, T.; Karasu, M.; Izumi, T.; Chiba, K. *Chemistry Lett.*, 1991, 2113.

11. Nakagaki, S.; Mangrich, A.S.; Wypych, R. *Inorganica Chimica Acta*, 1997, **254**, 213.

12. a) Dungey, K.E.; Curtis, M.D.; Penner-Hahn, J.E. *J. Catalysis,* 1998, **175**, 129 . b) Gee, M.A.; Frindt, R.F.; Morrison, S.R. *Mater. Res. Bull.*, 1986, **21**, 543.

13. a) Golub, A.S.; Shumilova, I.B.; Zubavichus, Y.V.; Jahncke, M.; Süss-Fink, G.; Danot, M.; Novikov, Y.N. *J. Mater. Chem.*, 1997, **7**, 163. b) Danot, M.; Mansot, J.L.; Golub, A.S.; Protzenko, G.A.; Fabritchnyi, P.B.; Novikov, Y.N.; Rouxel, J. *Mater. Res. Bull.*, 1994, **29**, 833. c) Golub, A.S.; Payen, C.; Protzenko, G.A.; Novikov, Y.N.; Danot, M. *Solid State Commun.*, 1997, **102**, 419.

14.. Divigalpitiya, W.M.R.; Frindt, R.F.; Morrison, S.R. *Appl. Surf. Sci.*, 1991, **48-49**, 572.

15. Divigalpitiya, W.M.R.; Morrison, S.R.; Frindt, R.F. *Thin Solid Films*, 1990, **186**, 177.

16. a) Miremadi, B.K.; Morrison, S.R. *J. Appl. Phys.*, 1988, **63**, 4970. b) Miremadi, B.K.; Cowan, T.; Morrison, S.R. *J. Appl. Phys.*, 1991, **69**, 6373. c) Miremadi, B.K.; Morrison, S.R. *J. Appl. Phys.*, 1990, **67**, 1515.

17. a) Golub, A.S.; Protsenko, G.A.; Gumileva, L.V.; Buyanovskaya, A.G.; Novikov, Y.N. *Russ. Chem. Bull.*, 1993, **42**, 632. b) Golub, A.S.; Shumilova, I.B.; Novikov, Y.N.; Mansot, J.L.; Danot, M. *Solid State Ionics*, 1996, **91**, 307.

18. a) Py, M.A.; Haering, R.R. *Can. J. Phys.*, 1983, **61**, 76,. b) Mulhern, P.J. *Can. J. Phys.*, 1989, **67**, 1049.

19. Bissessur, R.; Kanatzidis, M.G.; Schindler, J.L.; Kannewurf, C.R. *J. Chem. Soc., Chem. Commun.,* 1993,1582.

20. a) Yang, D.; Sandoval, S.J.; Divigalpitiya, W.M.R.; Irwin, J.C.; Frindt, R.F. *Phys. Rev. B.*, 1991, **43**, 12053. b) Joensen, P.; Crozier, E.D.; Alberding, N.; Frindt, R. F. *J. Phys. Solid State Phys.*, 1987, **20**, 4043. c) Qin, X.R.; Yang, D.; Frindt, R.F.; Irwin, J.C. *Ultramicroscopy*, 1992, **42-44**, 630. d) Qin, X.R.; Yang, D.; Frindt, R.F.; Irwin, J.C.

Phys. Rev. B., 1991, **44**, 3490. e) Sandoval, S.J.; Yang, D.; Frindt, R.F.; Irwin, J.C. *Phys. Rev. B.*, 1991, **44**, 3955-3962.

21. Heising, J.; Kanatzidis, M.G. *J. Am. Chem. Soc.*, 1999, **121**, 638.

22. a) Wypych, F.; Schöllhorn, R. *J. Chem. Soc., Chem. Commun.*, 1992, 1386. b) Schöllhorn, R.; Kümpers, M.; Plorin, D. *J. Less-Common. Metals,* 1978, **58**, 55.

23. a) Yang, D.; Frindt, R.F. *Mol. Cryst. Liq. Cryst.*, 1994, **244**, 355. b) Bissessur, R.; Kanatzidis, M.G.; Schindler, J.L.; Kannewurf, C.R. *J. Chem. Soc., Chem. Commun.*, 1993, **20**, 1582.

24. Wypych, F.; Weber, Th.; Prins, R. *Chem. Mater.*, 1998, **10**, 723.

25. Heising, J.; Kanatzidis, M.G. unpublished results.

26. a) Brown, B.E. *Acta Crystallogr.*, 1966, **20**, 268. b) Mar, A.; Jobic, S.; Ibers, J.A. *J. Am. Chem. Soc.,* 1992, **114**, 8963.

27. Twinning of the host-lattice has been included in the simulation of the diffraction patterns in Figures 5.5b and 5.7b to give rise to patterns which better resemble the experimental data. For clarity, the M-M (M=Mo, W) zig-zag chains of these other cells, which would be rotated 120 degrees relative to one another, have been omitted from Figures 5.5a and 5.7a.

28. Gash, A.E.; Spain, A.L.; Dysleski, L.M.; Flashenreim, C.J.; Kalaveshi, A.; Dorhout, P.K.; Strauss, S.H. *Environ. Sci. Techn.*, 1998, **32**, 1007.

29. Wypych, F.; Weber, Th.; Prins, R. *Surf. Sci. Lett.*, 1997, **380**, L474.

30. Papageorgopoulos, C.A.; Jaegermann, W. *Surf. Sci.*, 1995, **338**, 83.

31. Julien, C. "Lithium Insertion in Chalcogenides: Electrochemical Properties and Electrode Applications." *Microionics: Solid State Integrable Batteries.* M. Balkanski (ed.) Elsevier Science, New York, 1991, 309-341.

32. Wypych, F.; Sollmann, K.; Schöllhorn, R. *Mater. Res. Bull.*, 1992, **27**, 545.

33. a) Rovira, C.; Whangbo, M.-H. *Inorganic Chem.*, 1993, **32**, 4094. b) Whangbo, M.-H.; Canadell, E. *J. Am. Chem. Soc.*, 1992, **114**, 9587.

34. Proton NMR studies of the gaseous species released upon conversion of restacked MoS_2 to 2H-MoS_2 indicated the presence of hydrogen gas. J. Heising, M.G. Kanatzidis, unpublished results.